UNIVERSITÀ
degli STUDI
di CATANIA

Nearshore wave-current interaction

Hydrodynamic effects of rough and sloping beds

Doctoral thesis

Ph.D. candidate

Massimiliano Marino

University of Catania
Department of Civil Engineering and Architecture
Doctoral course in *Evaluation and mitigation of urban and territorial risks*
XXXIII cycle

Nearshore wave-current interaction

Hydrodynamic effects of rough and sloping beds

Doctoral thesis

Ph.D. candidate
Massimiliano Marino

Supervisor
Prof. Rosaria Ester Musumeci

Contents

Abstract

Anthropic pressure on the coastal environment has increased sensibly in the last decades. Human activities and interventions on the coastline may trigger significant modifications of the natural physical processes, such as the coastal sediment transport, which may lead to important erosive phenomena. In recent years, the interest in the understanding of the large and small scale mechanisms that take place in the near-shore has grown significantly, from both a scientific and an engineering standpoint. Among those processes, particular attention has been given to the study of waves and currents, which are usually simultaneously present in coastal waters and interact with each other at an orthogonal or near-orthogonal angle. Their hydrodynamic interaction is rather complex and plays a major role in the sediment transport phenomenon.

Although progress has been achieved in this area of research, some critical open questions still remain. For instance, most of the existing studies focuses mainly on the influence of waves on the current mean flow. Extensive studies on the combined flow turbulent field, which has a fundamental role in the current bottom friction, are indeed rather limited. Moreover, interaction of currents with nonlinear waves has been investigated mostly considering currents and waves propagating in the same direction, which is an unrepresentative scenario in the case of longshore currents.

In the present work, an investigation on the hydrodynamics of wave-current orthogonal combined flow has been carried out. The work focuses on the effects of the oscillatory flow superposed on the current steady boundary layer, and on how the oscillatory flow affects the current velocity distribution. Two laboratory experimental campaigns of wave-current orthogonal interaction have been performed. The first one (called WINGS campaign) has been carried out in a shallow water basin at

DHI Water and Environment (Hørsholm, Denmark), in order to investigate the orthogonal combined flow in the presence of different roughness beds. Tests of current only, wave only and combined flow have been carried out. Two currents have been generated (with nominal current velocity $U = 0.140$ m/s and 0.210 m/s) and a series of regular wave conditions have been performed (with wave height $H = 0.05 \div 0.18$ m, and wave period $T = 1.0 \div 2.0$ s). Two types of bed configurations have been used: fixed sand ($d_{50} = 0.0012$ m) and fixed gravel ($d_{50} = 0.025$ m).

The second laboratory campaign (called ACCLIVE campaign) has been carried out in a wave basin at the Hydraulics Laboratory of the University of Catania (Italy). The combined flow has been generated over a gentle sloping 1:25 fixed bottom, in order to investigate the current velocity profile interacting with shoaling waves at a right angle. Three currents ($U = 0.060$, 0.110 and 0.140 m/s) and a regular wave condition ($H = 0.085$ m, $T = 1.0$ s) have been generated. Experiments in the presence of a lone current and combined flow have been performed.

For both laboratory datasets, wave surface elevation and flow velocity measurements have been carried out. Velocity measurements have been performed both inside and outside of the current boundary layer. Mean flow has been investigated by computing time- and space-averaged velocity profiles. Friction velocity and equivalent roughness have been inferred from the velocity profiles by best fit technique (Sumer, 2007), in order to quantify the shear stress experienced by the current mean flow. Tests in the presence of only current, only waves and combined flow have been performed. Instantaneous velocities have been Reynolds-averaged in order to obtain turbulent fluctuations time series and compute turbulence related quantities, such as turbulence intensities and Reynolds stresses. The mean current velocity profiles have been also compared with a selection of analytical models in order to assess their validity for the case of wave-current orthogonal flow for the considered wave and current condition ranges.

Moreover, a series of CFD simulations have been carried out to investigate wave-current interaction, and highlight the limits of the numerical models. Two setups have been developed, a one-dimensional one and a three-dimensional one. Both models solve for Reynolds-Averaged Navier-Stokes equations for incompressible fluids, coupled with a k-ω Shear Stress Transport model (Menter et al., 2003)

to achieve turbulence closure. Cyclic boundary conditions coupled with body forces generated by sources in the momentum equations have been employed to generate the flow dynamics. The 1D model solves the bottom roughness through the use of both smooth and rough wall functions, whereas the 3D setup features a reconstruction of the real gravel bed used within the WINGS campaign. Current only, wave only and waves plus current tests have been conducted for the 1D model, whereas a preliminary current only flow for 3D model has been carried out. The models have been validated by means of the WINGS mean velocity profiles over sand and gravel bed.

The analysis of the mean flow revealed a complex interaction of the waves and currents combined flow. Depending on the relative strength of the current with respect to the waves, the superposition of the oscillatory flow may determine an increase or a decrease of the bottom friction experienced by the current. Such a behavior is also strictly related to the bed physical roughness. Analysis of the turbulence intensities and Reynolds stresses seems to confirm the results of the mean flow investigation. Moreover, the application of the quadrant analysis provides an insight on the dynamics of ejections and sweeps in the presence of superposed waves.

In the presence of shoaling waves, the effects on the current determined by the increase of wave orbital velocity are counteracted by the increment of the current Reynolds number and current boundary layer turbulence. Moreover, phase-averaged velocity analysis reveals an oscillating behavior of the velocities in the current direction determined by the presence of waves. The current oscillatory motion is characterized by a phase-shift, whose behavior is investigated as the waves shoal.

Results of the CFD simulations show that the 1D model is able to reproduce correctly smooth and rough bed mean velocities in the presence of a lone current. However, in the presence of a superposed wave field, the use of wall functions in the bottom boundary condition induces the predicted bed shear stresses to deviate, which determines an overall underestimation of the velocity profile.

Chapter 1

Introduction

1.1 Position of the problem

The anthropic pressure on coastal and marine areas increased significantly in the last decades. Among the most important human activities that are located in the coastline there are the maritime transport sector, aquaculture and fishery industry, oil and gas exploitation, marine renewable energy sector and tourism. The exploitation of coastal resources and the pursuing of these activities require a series of related infrastructures, and determine coastal communities to grow.

However, coastal areas pay a high price for their attractiveness. The increasing urbanisation impacts the ecosystem under different aspects, e.g. water quality, effects on marine biota and physical processes. The latter can be heavily influenced by human activities. Local hydro-morphological characteristics of the coast can be altered significantly due to human intervention, inducing alterations on important natural phenomena such as longshore sediment transport. Modifications of the natural sediment transport cycle can trigger significant erosive processes and induce the retreat of the shoreline, which, in turn, may threaten natural habitats and expose coastal communities to an increased marine storm risk (Nicholls and Cazenave, 2010). Climate change also plays a major role, affecting the sea level rise and increasing the frequency of extreme events. The combination of these two effects is indeed known to increase the occurrence of erosive processes (Glavovic et al., 2014). It is however difficult for scientists to separate climate effects from the ones that result from human activity.

Therefore, the interest of the scientific community in the study of the coastal hydro-morphodynamic mechanisms grew significantly in the last decades, alongside the demand for engineering solutions for coastal defense and the preservation of marine habitats. The contribution of engineering occur by means of the design and construction of coastal structures and the formulation of territorial strategies for the management of coastal communities and ecosystems. However, any mitigation measure to counteract erosion requires a deep knowledge of the coastal processes dynamics that occurs therein.

The physical processes occurring in the near-shore region are characterized by very different spatial and temporal scales. The understanding of the larger scale ones, such as shoreline morphology and coastal circulation, requires a thorough knowledge of the smaller scale hydrodynamics.

Within this scale, coastal hydrodynamics is mainly dominated by two forcings: waves and currents. Waves generation is generally due to wind stresses, they can be either locally generated, or being originated by distant storms and travel long distances until reaching the shore. Coastal currents could be instead generated by wind stresses, tides, wave radiation stress, density stratification, atmospheric pressure gradients, estuarine density currents, etc. The two phenomena feature very different dynamics. Waves usually propagate with a nonzero angle towards the coast, whereas currents are usually longshore oriented. The two flows are also characterized by two different time scales, which is in the order of hours for currents, and in the order of 10^1 seconds for wind-generated waves.

Waves and currents usually coexist in the coastal environment, and their combined flow gives rise to a rather complex hydrodynamics. The effect of the presence of waves on the characteristics of a current is strongly related to the processes that takes place within the bottom boundary layer, which plays an important role in determining the characteristics of the flow field. Moreover, the bottom boundary layer is the place where waves, currents and bottom sediments interact, and where the most of the sediment transport occur. The problem is further complicated by the characteristics of the seabed, which can be movable, present bed forms (e.g. ripples), biota or a complex bathymetry.

Notwithstanding its complexity, the comprehension of such a phenomenon

is vital from both a scientific and engineering standpoint. Our knowledge of the wave-current combined flow hydrodynamics directly impacts our ability to predict sediment transport and shoreline morphology.

The present work aims to contribute to the scientific and technical knowledge on the interaction between current and waves, with a specific focus on how the presence of waves alters the current velocity vertical distribution, and consequently its sediment transport capacity. More specifically, the study focuses on the the combined flow that occur when currents propagate at an orthogonal angle with respect to the current, which is the norm more than the exception in the near-shore region. The study is conducted by means of physical and numerical models, which are meant to reproduce a simplified version of the natural phenomena. The complexity and nonlinearity of the problem requires indeed drastically simplified models, which however do not invalidate the results if the assumptions are well posed and the approximations lead to reasonable margins of error.

1.2 Objectives

During the past decades many studies have contributed to the present knowledge of wave-current interaction, however the present state of the art still shows some criticalities.

Although many studies have shed light on the current knowledge of the phenomenon, there is a significant lack of experimental data on orthogonal or near-orthogonal wave-current interaction (Lim and Madsen, 2016). Investigations pursued by means of field data is difficult to perform. Due to the continually varying flow conditions, alongside the unknown factors that could influence the field measurements, only certain parameters can be measured accurately, such as bed bathymetry and wave surface elevation. Hence, a reasonable methodology is to consider the prevalent natural conditions and to reproduce them in a more controlled environment such a laboratory, which is the more suitable context to achieve a proper setup and obtain accurate measurements. Nevertheless, laboratory facilities which are able to simulate combined wave-current flow are limited, and the studies on this specific field of research rather scarce (Musumeci et al., 2006; Faraci et al.,

2018). Moreover, the existing works present a quite heterogeneous focus of study, with investigations concentrating on sediment transport, evolution of bed forms, effect of wave mass-transport etc. The instrumentation and quantities used within those studies is also quite diversified.

The consequence of this occurrence is that the existing analytical and numerical models that have been developed to predict the wave-current interaction hydrodynamics, have been mostly validated with tests carried out in wave flumes, i.e. with waves and currents propagating in the same or opposite direction, which is an exception rather than the norm in the nearshore. Recent studies revealed that some of these models' prediction may under or overestimate wave effects when the angle between the oscillatory and the current flow is nonzero (Fernando et al., 2011; Lim and Madsen, 2016).

By means of a wave-current orthogonal interaction experimental dataset, Fernando et al. (2011) revealed, after a comparison of a selection of models with velocity data, that none of them was adequately in agreement with its laboratory measurements without a change in the model coefficients, especially for the larger performed waves.

Lim and Madsen (2016) carried out a series of experiments on combined near-orthogonal current and waves over smooth and uniform ceramic-marbles bed, for orthogonal and near-orthogonal angle. Results show that the model examined in the paper (Grant and Madsen, 1986) tends to overpredict influence of the wave field on the current, especially in the wave-dominated regime, when the angle of attack is orthogonal or near-orthogonal.

Notwithstanding the large amount of literature on wave–current interaction, attention has been focused almost exclusively on the mean flow. Little has been reported to understand the combined flow with respect of the boundary layer turbulence activity. Nevertheless, a quantitative analysis of the turbulent properties of the wave–current flow is necessary to understand the bottom friction generation in proximity of the bed. The majority of the investigations dealing with sediment transport problems take into account turbulence only through time averaged velocities or shear stress. Among these, only few studies have shed light on the properties of turbulence in orthogonal combined flow (Faraci et al., 2018).

In the light of the above, the present study is aimed to purse the following objectives:

1. **Provide new experimental datasets for orthogonal wave-current interaction** Two laboratory experimental campaigns have been conducted in order to investigate the hydrodynamics of the combined flow, in the presence of different rough beds and plane sloping bottom. The objective is to obtain new high-quality velocity and wave surface elevation datasets in order to assist the validation of analytical and numerical models for the case of orthogonal combined flow.

2. **Contribute to the understanding of the wave-current orthogonal hydrodynamics.** To this aim, a study on the time-averaged characteristics of the combined flow has been conducted. Moreover, the present work pursue an attempt to analyze turbulence related quantities in the combined flow. This is carried out by means of recovering turbulent fluctuations from velocity time series and through analysis of turbulence intensities, Reynolds stresses and the application of quadrant analysis (Wallace, 2016).

3. **Validate the use of a selection of analytical models for the case of orthogonal combined flow.** The experimental velocity profiles and shear related quantities, such as friction velocity and equivalent roughness, of the dataset are compared with the prediction of a selection of analytical models, in order to provide experimental validation in the case of orthogonal interaction.

4. **Provide insights on wave-current numerical modeling**. A numerical investigation has been carried out in order to investigate the capability of state-of-the-art numerical models to correctly reproduce the combined flow boundary layer physical processes. Specifically, numerical results have been compared with our laboratory experimental results.

1.3 Methodology

The orthogonal wave-current combined flow has been studied by means of laboratory and numerical investigations. Experimental data have been gathered

from two laboratory campaigns. The first one, named WINGS campaign, has been carried out in a shallow water basin at DHI Water and Environment (Hørsholm, Denmark) and investigates the effects of the waves on an orthogonal current velocity profile over fixed sand and fixed gravel beds. The second one, called the ACCLIVE campaign, has been conducted in a wave basin at the Hydraulics Laboratory of the Department of Civil Engineering and Architecture of the University of Catania (Italy) and is focused on current and waves propagating at a right angle over a gently sloping bottom, in order to investigate the effects of shoaling waves on the combined flow boundary layer.

An array of Acoustic Doppler Velocimeters and resistive wave gauges have been deployed in the wave basins, in order to recover three-dimensional flow velocity and wave surface elevation, respectively. Moreover, a three-dimensional replica of the gravel bottom used within the WINGS experiments has been reconstructed by means of a stereoscopic technique, from which the bed geostatics have been computed and analyzed. The recovered data are processed in order to perform an extensive data analysis. Results of the analysis are intended to better understand wave-current interaction at a right angle over different types of beds in terms of: (i) characterization of mean and turbulent flow field, (ii) influence of oscillatory flow on current boundary layer, (iii) alteration of bottom shear stresses due to the superposition of the waves on the current. Once the data analysis is finalized, the next phase of the work has been to carry out a comparison with a selection of analytical wave-current interaction models, in order to assess their for orthogonal wave-current orthogonal interaction.

Finally, a numerical investigation of wave-current orthogonal interaction has been carried out, in order to test the capability of state-of-the-art CFD numerical models to correctly reproduce the dynamics of the combined flow, with a particular focus on the alteration of shear experienced by the current due to the presence of waves in the boundary layer. The numerical simulation has been carried out in OpenFOAM and solves for Reynolds-Averaged Navier Stokes (RANS) governing equation for incompressible fluids, coupled with a $k - \omega$ Shear Stress Transport turbulence closure model. Steady and oscillatory body forces are imposed in the domain as momentum sources to simulate current and waves respectively. Cyclic

boundaries provide flow inlet and outlet for both waves and current.

The WINGS experimental velocity and shear velocity data have served as benchmark results for testing the numerical model. Two numerical setups have been tested: a one-dimensional model and a three-dimensional one. The 1D model has been employed in order assess the capability of bottom wall functions to reproduce correctly the wave-current boundary layer and to have a fast testing ground for the, more computationally expensive, 3D simulation. Rough and smooth condition tests have been conducted. A reconstruction of the real gravel bed of the WINGS campaign has been used as the bottom boundary of the 3D model, in order to reproduce the physical roughness of the bed is reproduced by means. The development of the numerical setup has been described, and a preliminary results are presented.

1.4 Limits

Laboratory and numerical investigations are both subject to limits. For what concerns laboratory investigations, the simulated experimental conditions do not allow a full similarity between the model and the prototype, due to the inherent nonlinearity of the problem. This problem is usually overcome by choosing the appropriate nondimensional parameters which describes the phenomenon, renouncing to a perfect correspondence between the model and the real scale problem. With regards to numerical investigations, the conditions most adherent to the phenomenon should be simulated, ideally. However, the limits of computational power and the difficulty to define appropriate boundary conditions, require to introduce simplified assumptions for the formulation of the problem.

In the specific case of our laboratory experiments, it must be considered the relatively small size of the two wave basins used in the present work. Moreover, the resolution and sensibility of the instruments may limit the accuracy of the measurement. However, the flow measuring equipment used within all the experiments have an accuracy of $\pm$ 0.001 m/s, which is reasonably smaller than the main reference velocities of the study, such as freestream and orbital velocities, which are in the order of $O(10^{-1})$ m. Hence, at least for what concerns this study, sensitivity errors made by the instruments are considered negligible. Another instrument limit is that

shear related quantities have not been measured directly, such as shear stresses and equivalent roughness. However, advanced techniques to infer those quantities have been adopted in the present work (Sumer, 2007).

Moreover, the conducted experiments represent a drastic simplification of the field condition. For instance the generated waves are monochromatic, the topography of the bottom is plane, current and waves interact with the same angle. Therefore, it must be taken into account that results may differ from a field experiment due to the intrinsic limitations of the model. This simplification is fundamental to the understanding of the nonlinear aspects of the phenomenon, which requires the complex field case to be decomposed into more elementary problems (Smith and McLean, 1977).

With regard to numerical investigations, the numerical setup has been designed by considering the available computational power. This occurrence limited the possibilities in terms of domain size, test duration, mesh resolution in the correspondence of the larger spatial gradients (i.e., in proximity of the wall). The model is monophase and is provided with a slip rigid 'lid' as the top boundary, thus it ignores any free surface effects, which is considered a reasonable assumptions in wave modeling (Baykal et al., 2017). The numerical model features momentum sources applied at the cell centroids to generate flow dynamic field, coupled with cyclic boundary conditions. This particular setup does not accurately reproduces an orbital wave motion, as oscillatory flow velocity is uniform in the wave direction. Nevertheless, the size of the domain in the wave direction is in the order $O(10^{-2} \pm 10^{-1})$ m, and considering the wavelength of the simulated waves 3.70 m, this should be a reasonable approximation. Although the aforementioned limitations of the experimental and numerical setups, in the opinion of the author the present work still provides an interesting insight on the study of wave-current interaction and contributes to the scientific knowledge of the phenomenon.

1.5 Phases of work

In Chapter 2 a literature review of the state-of-the-art knowledge on wave-current interaction, with a particular focus on orthogonal combined flow is presented.

It is subdivided in two main sections, one dedicated to laboratory investigations in wave flumes and basins, and one to analytical and numerical modeling.

Chapter 3 describes the experimental setup of the two laboratory campaigns carried out within the present study. One section is dedicated to the WINGS laboratory campaign, which investigates wave-current orthogonal interaction over different roughness beds. The other section is dedicated to the ACCLIVE campaign, which investigates the combined flow hydrodynamics in the presence of a gently varying slope. In both sections, the wave basins, the measuring instruments and the experimental plans are described in detail.

In Chapter 4, the results of the WINGS campaign (waves plus current over rough beds) experiments are presented. The first section is dedicated to a preliminary data analysis on the wave surface elevation, velocity measurements and rough bottom surface elevation, which has been carried out in order to characterize the laboratory simulated conditions and highlights limits and strengths of the experimental setup. The second section is dedicated to the presentations of the results of the mean flow analysis, i.e. the investigation carried out on the time- and space-averaged velocity profiles. The section is further subdivided into four subsections: analysis of tests in the presence of pure current, pure waves, combined waves plus current and finally a comparison of the velocity profiles with a selection of analytical models. The third section presents the results of the turbulent flow data analysis, therefore analyses those quantities that are related to fluctuating velocities, such as turbulent intensities and Reynolds stress. Moreover, a turbulent quadrant analysis is also carried out. A final section discusses the results presented in the Chapter.

Chapter 5 presents the results of the ACCLIVE campaign (waves plus current over a sloping bed). The structure of the Chapter is similar to Chapter 5, having a preliminary analysis section for wave surface elevations and velocity measurements. Subsequently, mean flow, phase-averaged and turbulent flow results are presented and analyzed. A final section summarizes and discusses the results.

Chapter 6 is dedicated to a numerical investigation on wave-current orthogonal interaction over smooth and rough beds. Two numerical setups have been tested: a one-dimensional model and a three dimensional one. First, the numerical setups of the two models is presented, in terms of governing equations, boundary condi-

tions and numerical domain and mesh. Then, the results of the 1D numerical setup are presented. Simulations with current only, wave only and combined flow have been carried out and compared with the WINGS velocity profile dataset. Then, an attempt of validation of the 3D numerical setup is shown. A final section discusses the results presented in the Chapter.

Chapter 7 provides a conclusive discussion on the work, summarizes the results and discusses some suggestions for future investigations.

Chapter 2

Background on wave-current interaction

2.1 Overview

Historically, the wave-current combined flow has been investigated by focusing on (i) the effects of current on waves or, (ii) the effects of waves on the current.

Effects of current on waves include influence on wave energy dissipation, radiation stress and wave refraction. Accounting for these effects is important in those fields in which an accurate wave modelling is relevant, such as the study of loads on coastal structures. In this type of investigations, current characteristics are usually considered unaffected by the superposition of waves.

Effects of waves on current are instead of major importance in the study of suspended sediment transport and coastal morphology. Since the prevalent condition in the near-shore is with orbital velocities being in the same order of magnitude of the current velocity, i.e. with strong waves interacting with relatively weak currents, effect of current on waves is usually neglected.

Influence of waves on a current is strongly related to the processes taking place within the bottom boundary layer. Specifically, two boundary layers develop under a combined flow of waves and currents: an oscillatory boundary layer associated with waves, and a steady boundary layer generated by the current. The two flows feature very different time and length scales, resulting in a thin wave boundary layer close to the bed, being embedded in a larger, steady current boundary layer.

The presence of the wave boundary layer has been found to significantly affect the bottom flow, determining the current to experience an 'apparent' roughness increase (Grant and Madsen, 1979), which affects its velocity vertical distribution. The interaction between the two bottom flows is however rather complex and highly nonlinear, therefore any scientifically relevant investigation should consider the simultaneous presence of both. Moreover, in order to accurately investigate how the two boundary layers interact, accurate measurements of the flow velocities and bed shear related quantities are required. Moreover, in the near-shore, wave-current hydrodynamics is furtherly complicated by the interaction with the sea bed, which can be fixed or movable and feature the presence of time-evolving bedforms (e.g. ripples). Based on the above considerations, it is important that wave-current hydrodynamics is studied in a controlled conditions environment, where a proper instrument setup can be achieved and accurate near-bed measurements can be carried out. It is also important that the combined flow is studied by means of simplified models, in which the prototype-scale problem is decomposed in simpler cases and the contribution of all the variables at stake can be individually analyzed. The laboratory has been considered the most suitable environment for this type of investigations, although some successful field studies exist (Cacchione and Drake, 1982; Trowbridge and Agrawal, 1995). Within the same assumptions, drastic simplifications of the flow field equations in the development of mathematical models are required.

In the last decades several studies contributed to the current knowledge of the wave-current interaction hydrodynamics (Grant and Madsen, 1986; Soulsby et al., 1993), which includes laboratory, field and numerical investigations. These works has been used for validation of mathematical and numerical models. In the following Sections a selection of these studies are presented.

2.2 Physical modeling studies

Wave-current interaction experiments can be carried out in different types of facilities. The most common and widely used is the wave flume, which consists of an open channel provided with a wave generation device (also known as wavemaker) on one side, and an absorbing beach on the opposite. Wavemakers are relatively

simple devices, which consist of one or more oscillating paddles or hinged flaps, which are able to generate different type of waves (Dean, 1970). If provided with water recirculation systems, wave flumes are able to generate a steady current. Current generation systems are usually pump-driven and consists of an inlet and an outlet, to make the water inflow and outflow the flume, and a series of external pipes/channels.

Another device is the oscillating water tunnel, which consists of a closed channel and two risers, one provided with a vertical moving piston, which is meant to generate the oscillatory flow, and one open in the atmosphere. Wave motion can also be achieved by means of other devices like oscillating water plates (Bagnold, 1946). Oscillating water tunnels do not reproduce accurately orbital wave motion, as velocity is uniform in the wave propagation direction, although they can achieve acceptable results for sufficiently long periods. The oscillating water tunnel is sometimes provided of a recirculation system to generate the steady current.

One of the earliest experimental campaign on a wave-current flume is the one by Bakker and Van Doorn (1978), which carried out a series of experiment of following waves and current over rough beds in a wave flume. Accurate bed shear stress measurements have been obtained. The investigation was mostly focused on the comparison of the suspended sand concentration observations with the predictions of a mathematical model by Bakker (1975).

Kemp and Simons (1982, 1983) conducted two experimental studies in a 10.00 m long wave flume, with waves propagating in the same and opposite direction with respect to the current. The investigation revealed that when waves and currents propagate in the same direction, the superposition of waves determines an increase of current mean velocities in proximity of a smooth bed, whereas over rough beds a reduction is always observed. Instead, when waves propagate opposite to the current, a reduction of the current intensity near the bed has been observed. The different behavior between smooth and rough beds has been explained as a change in the eddy pattern inbetween the rough elements.

According to Kemp and Simons' study, variations on the steady current profile is also related with wave amplitude and water depth. Indeed, the current logarithmic layer profiles over the rough bed show an increase in the bed shear stress and roughness length scale, which has been found to be related to wave height. Moreover,

they found that wave surface profiles are not significantly altered by the presence of the current, remaining close to Stokes second-order theory profile if appropriately scaled on wavelength and height. A study on turbulent turbulence activity in the boundary layer has been conducted aswell, which showed that the presence of waves always determine an increment of turbulence intensities and Reynolds stresses. Near smooth bed turbulence intensities increase more rapidly as wave height increase for waves alone case than for waves propagating on a following current.

Other experiments in the same setup have been conducted by Simons et al. (1993) which showed that co-directional and opposite waves over currents flowing on a fixed and sand movable bottom induce a significant decrease of the mean flow in the superior part of the water column and an increase close to the bed.

Mathisen and Madsen (1996a,b) carried out experiments of combined flow on a fixed ripple bed, showing that the bottom roughness for current alone, waves alone and wave–current bottom boundary layer flow can be characterised by a single roughness scale.

Lodahl et al. (1998) carried out experiments in a smooth oscillating water tunnel showing different shear stress patterns. If the flow regime is current dominated, i.e. the current mean velocity is larger than the wave orbital velocity, a linear relation between the wave-current shear stress and the wave motion Reynolds numbers occurs, whereas if the flow is wave dominated two different scenarios may follow. If the wave motion regime in the boundary layer is laminar a shear stress decrease occur, while if wave motion regime is turbulent, a bottom shear stress increase happens in comparison with the only current case. This behavior is qualitatively shown in Figure 2.1.

Experiments in wave flume with a detailed analysis of turbulent Reynolds stresses has been conducted by Umeyama (2005), which observed that, as distance from the bed increases, the wave-current Reynolds stress profile decreases progressively in the case of waves opposing the current, but it decreases rapidly and invert its sign at relative mid depth in the case of waves following the current.

An experimental campaign on an oscillating tunnel where co-linear waves and currents are generated over smooth, sandpaper and round marbles bottom has been carried out by Yuan and Madsen (2014). Results show that in the presence

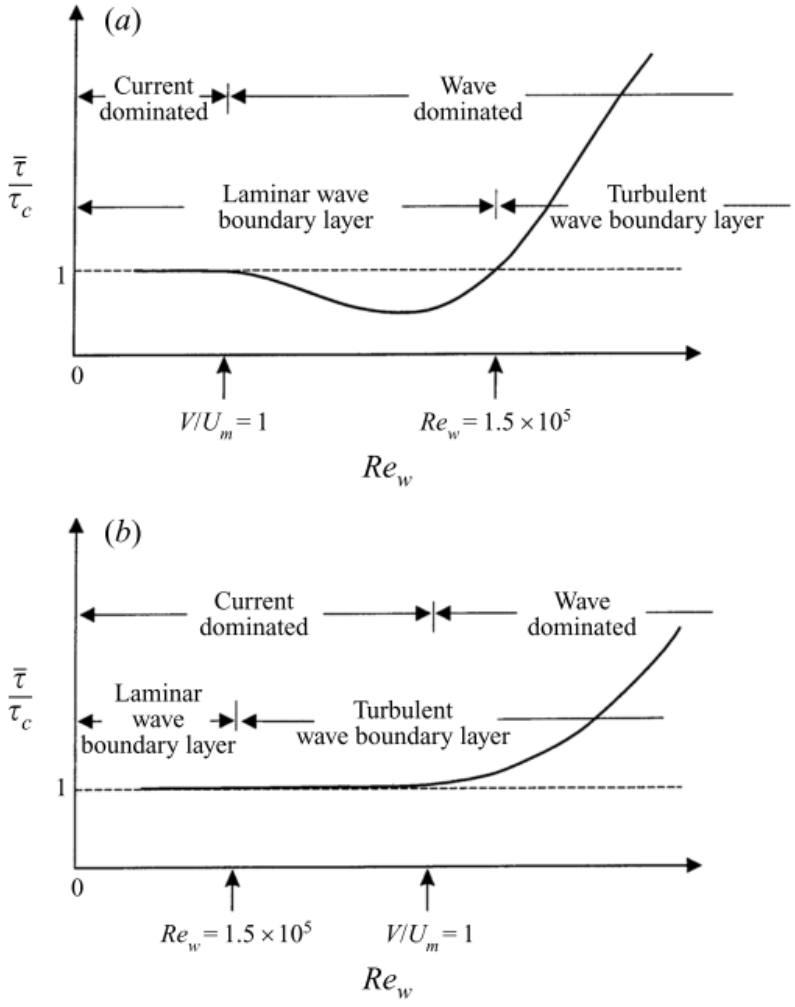

Figure 2.1: Schematization of the two (a and b) normalized mean shear stress patterns observed by Lodahl et al. (1998)

of regular waves a two-logarithmic structure of the velocity profile is observed, as predicted by the original Grant and Madsen (1979) model, whereas in the presence of weak currents opposing to nonlinear waves the two-logarithmic profile is suppressed by the boundary layer streaming induced by the asymmetric turbulence determined by the nonlinear waves. Thus, Yuan and Madsen (2014) conclude, the Grant and Madsen (1979) model is not able to accurately predict the current profile in presence of nonlinear waves. In the frame of the same work, a semi-analytical model is proposed. Other studies in wave flumes include Asano and Iwagaki (1985); Simons et al. (1988); Klopman (1994).

The abovementioned investigations have been carried on wave flumes or oscillating tunnels, which are able to generate waves and currents propagating only in the same or opposite direction. Although they provided a valuable contribution in the study of the wave-current interaction phenomenon, such a condition is not the norm in the coastal environment.

A facility which allows the generation of waves and currents propagating at angles different than 0 and 180 is the wave basin, which consists of a water tank, a wavemaker and water recirculation system positioned in such a way to make the waves superpose on the current with a nonzero angle. To the knowledge of the author, these facilities are less common with respect to wave flumes and oscillating water tunnels, and consequently the studies which involves them are relatively limited in comparison. Moreover, experimental setups, performed conditions, measurement instruments and the overall focus of the investigation are often quite heterogeneous between the available experimental studies on 3D wave basins.

The first combined flow experiments at a right angle reported are the ones by Bijker (1967). These experiment have been conducted in a 27.00 m x 17.00 m wave tank, in which tests have been performed in presence of fixed and movable beds. Detailed velocity measurements have not been carried out, although bed shear stresses have been measured and bedload sediment transport has been quantified by means of sediment traps. Based on the the results of these experiments, Bijker (1967) proposed empirical formulations for both shear stresses and sediment transport.

Visser (1987) presented a set of data of wave-current orthogonal interaction experiments in a wave basin, with a focus on the increase of the mean bottom

stress due to the presence of waves. Mean and orbital velocity measurements have been carried out by means of a laser Doppler anemometer. The results were compared with the prediction of models by Bijker (1967) and Fredsøe (1984), with both models resulting to underestimate bottom shear stresses in comparison with the experimental evidence.

Sleath (1991) carried out experiments in a steady flow flume with a oscillating bed moving perpendicularly to the current, and measured velocity profiles by means of a laser Doppler anomemeter. Mean velocity profiles show agreement with the predictions of the models of Grant and Madsen (1979) and Christoffersen and Jonsson (1985) in the current boundary layer, with larger deviations in the wave boundary layer.

Perpendicular wave and current experiments have been carried out by Arnskov et al. (1993) in a wave basin. In comparison with previous studies, measurements of bed shear stresses have been carried out directly with a hot-film probe. The experimental results revealed that, for relatively large values of the wave amplitude to equivalent roughness ratio a/k_s, no maximum bed shear stress enhancement occurs due to the presence of waves. Moreover, superposition of wave determines the fluctuations of the bed shear stress to be significantly reduced, and this becomes more and more pronounced, as the wave height increases. Results have been compared with the Fredsøe (1984) model, although outside the model limitations. Predictions of the model showed a considerable deviation with the experimental data.

Musumeci et al. (2006) performed experiments of wave-current interaction at a right angle in a 18.00 x 3.60 m wave tank, over small and large roughness beds. The analysis on velocity profiles suggested that when waves are superposed to the current, an increase of near-bottom velocities occurs over smooth bed, the opposite happens in presence of a rough bed. Moreover, larger current velocities have been observed in proximity of the bottom in the waves plus current case and smaller in the current only case, in presence of small and the large roughness, respectively. Effects of current on waves have been investigated aswell. The strong turbulence induced by the current on the waves determines an homogenization of the wave velocity profile and reduces, or sometimes suppress, the steady streaming in the boundary layer.

Moreover, in the small roughness case, apparent roughness k_s may decrease when waves are superposed on the current, whereas over large roughness beds, increase of k_s up to an order of magnitude has been observed. A phase-averaged analysis showed current velocity oscillates with an out of phase behavior with respect to the waves. This lag is not spatially constant, as it changes along the current direction axis. Such an occurrence may be related to the free surface slope determined by the presence of waves, and the relative distance from the inlet/outlet.

Fernando et al. (2011) carried out perpendicular wave-current laboratory experiments in a 24.00 x 10.00 x 0.90 m wave basin over a movable bed. The evidences show that the current is always significantly modified by the superposition of waves, which induces a reduction of the near-bed current velocities due to an increase of the bed shear stress and apparent roughness. Moreover, Fernando et al. (2011) compared the experimental velocity data with a selection of analytical models. In presence of relatively small waves, with wave height to water depth ratio less than 0.25, all of the considered models agree well with experimental mean current velocity profiles, alongside the predictions of current bed shear stresses. For relatively larger waves, with wave height to water depth ratio up to 0.45, models based on the reference point (such as Grant and Madsen (1986)) agree well with experimental findings, whereas the other generally underestimate the bed shear and apparent roughness. For waves with wave height to water depth ratio larger than 0.45 current velocity deviates significantly in the near-surface from the logarithmic law, which cannot be predicted by any of the considered models.

Lim and Madsen (2016) carried out a series of experiments on combined near-orthogonal current and waves over smooth and uniform ceramic-marbles bed. Three different condition are examined and compared (only currents, only waves and waves plus currents) and three different wave-current angles tests are performed (60, 90, 120 degrees) into a 3D experimental basin. The wave motion superimposed to an orthogonal smooth turbulent current determines an increase of the bottom mean velocity and a decrease of the bottom roughness. Over rough beds, the wave-current combined flow induce a reduction of the bottom mean velocity, as Grant and Madsen (1986) model predicts. However, results show that the model tends to overpredict influence of the wave motion on the current, especially in wave dominated regime,

when the angle of attack is different from collinear or near-orthogonal. This effect is amplified by the presence of bedforms which induce the current to veer at the bottom along the ripples direction.

Other studies investigates wave–current flows at right angle over movable beds (Van Rijn and Havinga, 1995; Khelifa and Ouellet, 2000; Andersen and Faraci, 2003; Faraci et al., 2018), which mainly focus on bedload transport, ripple formation or flow-bedform interaction.

Few studies with wave-current angles different than 0, 90 and 180 degrees exist, the already mentioned Arnskov et al. (1993), which included angles of 72 and 108 degrees, and Havinga (1992) and Lim and Madsen (2016), which performed experiments with 60 and 120 degrees angles.

2.3 Analytical and numerical models

Several analytical and numerical models have been developed in the last five decades. Although simple analytical models have been preferred for long time due to their simplicity of use and effectiveness, the increase of computational power in the last two decades induced an increment in the development of CFD models and numerical investigations on wave-current interaction.

One of the earliest analytical model is the one of Lundgren (1973), in which a linear wave-current interaction was assumed. Subsequent theoretical models accounted for the nonlinear effects of wave-current interaction, The first theoretical model for a wave-current combined flow at an arbitrary angle is the one proposed by Grant and Madsen (1979) in which the apparent roughness concept is introduced. An oscillatory motion superimposed to a current determines an increase of the bottom roughness experienced by the current, called apparent roughness. This apparent roughness is larger than the physical one and induces an increase of the bottom shear stress.

The model solves for a 1D wave–current interaction problem, in which the vertical structure of the combined flow is solved, assuming a simple vertical turbulence structure A simple time-invariant linearly-varying eddy viscosity method is adopted by Grant and Madsen (1979), which relates the Reynolds stress to the veloc-

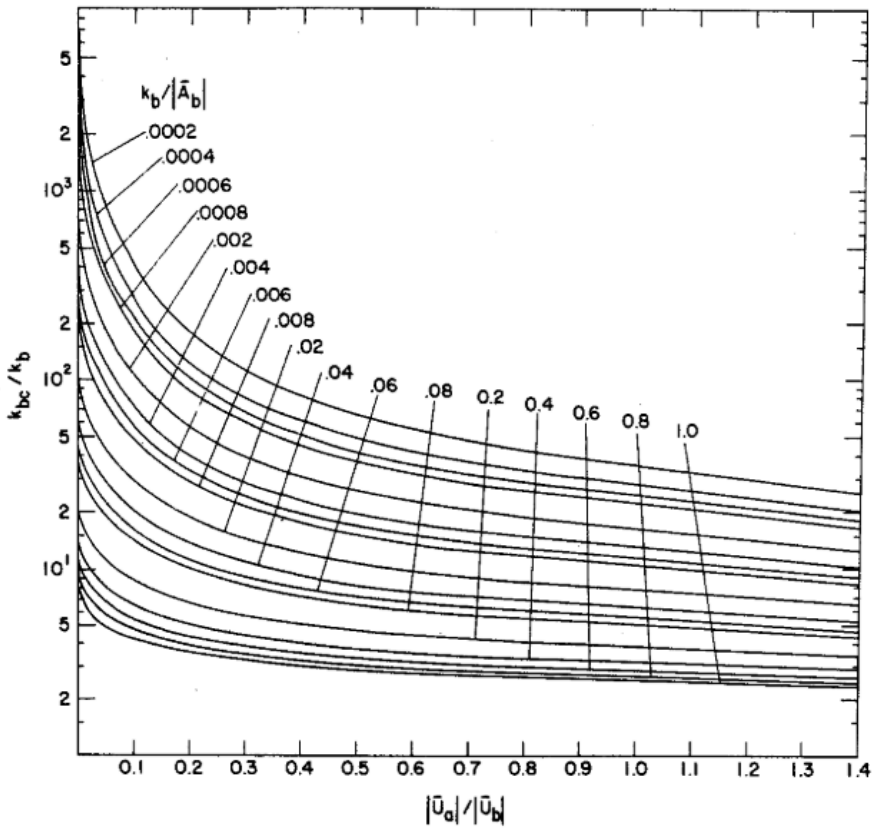

Figure 2.2: Apparent and physical roughness ratio versus the wave orbital and current velocity ratio for co-directional flow according to the Grant and Madsen (1979) model.

ity gradient using an eddy viscosity term ν_t. In Figure 2.2 the apparent to physical roughness ratio versus the wave orbital to current velocity ratio for co-directional flow is shown.

The Grant and Madsen (1979) model is later improved by the Grant and Madsen (1986). In the original model, the combined flow shear velocity is associated with the maximum bed shear velocity of wave–current combined flow, whereas in the improved one, both the bottom shear stress due to current and the maximum shear stress of combined flow are considered. Moreover, in the Grant and Madsen (1986) continental shelf model, the pure wave friction factor relationship for rough turbulent flow was modified with the addition of a coefficient larger than unity to represent the friction factor equation for the combined wave–current flow.

The time-invariant eddy viscosity approach has been adopted by several other studies (Tanaka and Shuto, 1984; Christoffersen and Jonsson, 1985; Myrhaug

and Slaattelid, 1990). Other formulations include the turbulent kinetic energy closure methodology (Bakker and Van Doorn, 1978) and the momentum-deficit method (Fredsøe, 1984).

Fredsøe proposed a model based on the depth-integrated momentum equation, used to compute the mean current profile of the combined flow. The velocity profile is logarithmic both inside and outside of wave boundary layer, but having different slopes. The model relates the apparent bed roughness to the ratio of near-bed wave orbital velocity to mean current friction velocity and the wave orbital amplitude. Coffey and Nielsen (1986) suggested that the apparent roughness may be related to the ratio of maximum to mean friction velocity.

Soulsby et al. (1993) provided a thorough review of the state of the art on combined flow modelling at the time, and performed a comparison with 8 analytical and semi-empirical models, with a broad range of formulations. The considered models have been compared by performing a range of reference current, wave orbital velocities and angle of attack between the currents. Figure 2.3 shows the comparison between the maximum and mean bed shear stresses predicted by the considered models. The comparison showed that generally all the examined models performed similarly in predicting the mean and maximum bed shear stress, although variations of τ_{max} up to 30% have been observed. Moreover, a standard algebraic formulation has been developed in order to fit the examined wave-current models, with the purpose of reducing computational cost in their implementation with sediment transport and morphological models and easing further comparisons. By means of a parameterisation procedure, a series of fitting coefficients have been found for each model.

Numerical models have been developed aswell. One of the earliest formulations is the one by Davies et al. (1988), which used a one-equation turbulent energy closure model, in order to compute the wave-current flow over the whole water column, with the assumption of parallel streamlines. Time-averaged profiles of velocities, turbulence related quantities and shear stresses were presented, for a range of wave–current conditions. The enhancement of the bottom shear stress, due to the current, as well as the nonlinearity of the wave–current interaction in the bottom boundary layer, were both observed in Davies' simulations.

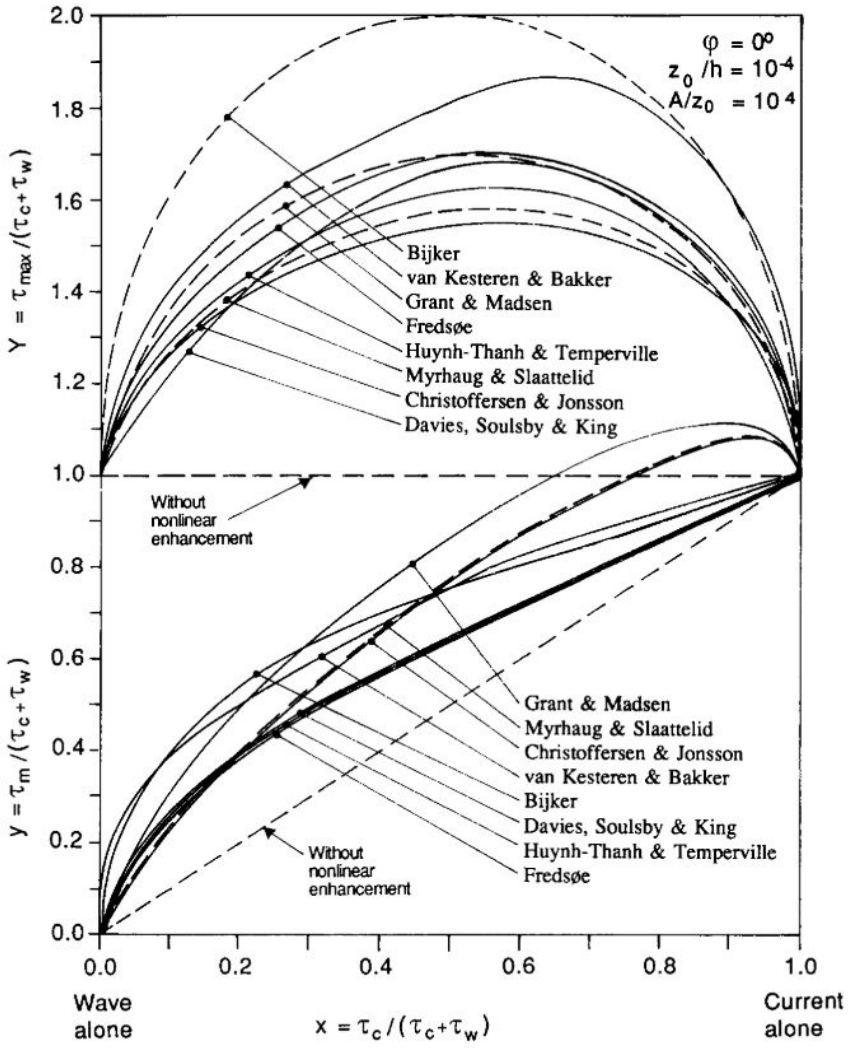

Figure 2.3: Intercomparison between models prediction of maximum and mean bed shear stresses. (Soulsby et al., 1993)

Another approach was undertaken by Hyunh Thanh and Temperville (1991), which used a two-equation model to solve the bottom boundary layer beneath regular waves and current. Boundary values for the velocity and the turbulent quantities were specified at a given height above the bed.

Olabarrieta et al. (2010) developed 2D non-hydrostatic model in order to analyze the effects of wave–current interaction on the mean current profile. The model is able to reproduce currents flowing at different angles with respect to the waves. The model introduces the effects of the free surface elevation variation due to the oscillatory flow, thus without assuming the lid approach. Results of the model have been compare with current velocity profiles obtained from different laboratory campaigns, for both regular and spectral waves. In the orthogonal case, Olabarrieta found a decrease of the velocity in the upper part of the water column, compensated by an increment in the lower part, as already observed by (Musumeci et al., 2006). Indeed, in presence of relatively strong waves with respect of the mean current velocity, the flow resistance in the wave boundary layer is smaller than the resistance in the upper part of the water column, as an effect of large vertical Reynolds stresses closer to the surface, therefore with a consequent acceleration in proximity of the bed.

Some studies have also investigated the superposition of random/spectral waves on currents (Madsen, 1995; Holmedal et al., 2000; Myrhaug et al., 2001). Holmedal et al. (2003) examined the effects of a random wave field on the current bottom boundary using a dynamic turbulent boundary layer model based upon the linearised boundary layer equations, with horizontally uniform forcing. The turbulence closure is provided by a high Reynolds number $k - \epsilon$ model.

More recently, three-dimensional effects of wave-induced streaming on the current boundary layer has been investigated numerically by Afzal et al. (2015) for following and opposing waves and current with zero and nonzero angle interaction. The model has been validated by means of the experimental data of Yuan and Madsen (2014). The effect of streaming on the boundary layer flow has been investigated for different wave-current conditions and bottom roughnesses, with a particular focus on the veering induced by the wave steady streaming on the current. Observations of velocity profiles showed that the influence of the streaming

decreases as the flow is closer to a current-dominated regime, i.e. with a relatively larger current freestream velocity with respect of the wave orbital velocity, but even for the most current-dominated condition, the mean velocity veering is altered by the presence of streaming.

Chapter 3

Experiments

3.1 Overview

In the present Chapter the experimental setup of the laboratory campaigns carried out in this work are presented, and the experimental plan and procedure are thoroughly described. First, the WINGS experimental campaign, which investigates wave-current interaction over horizontal smooth and rough beds, carried out in the Shallow Water Basin of DHI Water and Environment (Denmark), is presented. Second, the ACCLIVE experimental campaign, carried out in a wave basin at the Hydraulics Laboratory of the University of Catania (Italy), which investigates the combined flow in presence of shoaling waves, is described in detail.

3.2 The WINGS campaign

A laboratory campaign has been carried out at DHI Water and Environment (Hørsholm, Denmark) in a three dimensional Shallow Water Basin, in the framework of an Hydralab+ Transnational Access project WINGS (Waves plus currents INteracting at a right anGle over rough bedS), funded by the EU Commission through the Hydralab+ programme. The Shallow Water Basin is a large scale 3D wave facility in which DHI ordinarily performs laboratory testing meant to study the effects of both waves and currents on structures and vessels. Hydrodynamic forces on foundations prompted by waves, wave run-up, run-down and overtopping, scour around pile foundations, stresses and vibrations induced on cables and pipelines, are just

some examples of the possible experimental application fields. More in general, the presence of a current generation system makes the basin ideal for those situation in which accounting the mutual presence of waves and currents is significant. A selection of pictures of the basin is shown in Figure 3.1.

The basin (schematized in Figure 3.2) is 35 m long and 25 m wide, with a maximum depth of 1.00 m. Along the longer side, the basin is provided with a multi-paddle piston-type wavemaker. The wavemaker front is 18.00 m wide, and consists of 36 paddles, with each paddle being 1.20 m high and 0.50 m wide. Paddle movement is controlled by an electro-servo motor through the software *WSproject*. The presence of several independent paddles allows the wavemaker to reproduce different types of wave conditions: regular and irregular waves, 2D and 3D waves, sinusoidal or cnoidal, faced forward or inclined by a defined angle ranging from 30° to 90°. The wavemaker is able to generate waves from 0.05 up to 0.45 m of wave height.

In order to reduce wave reflection, a 18.75 m barrier made up by 15 parabolic steel absorbers is positioned 12.00 m away from the wavemaker. For the same purpose, a C-shaped coarse-grained material beach (d_{50} in the order of $O(10^{-2} \div 10^{-1}$ m) is located at the onshore end of the wave tank.

The water, for both filling and recirculation purposes, is brought from a local lake to a subterranean tank, in which three submerged pumps brings water into the tank. A recirculation system allows the generation of a current, which is conveyed into (out of) the basin through a 12 m inlet (outlet). An electromagnetic flowmeter having a 10^{-4} m^3s^{-1} precision allows to monitor the recirculation discharge. The still water level in the tank is measured by means of a physical meter stick.

The bottom of the basin is horizontal. In order to reproduce two different bottom rough conditions, a series of wood panels with fixed grains glued on top, are positioned on the tank bottom. Specifically, a series of panels with sand (SB) and a series with gravel (GB), with a grain diameter of $d_{50} = 0.0012$ m and $d_{50} = 0.025$ m respectively were installed. The panels cover a rectangular area of 7.50 x 5.00 m, which is called within the text the controlled roughness area. The position of the controlled roughness area has been determined by means of a preliminary investigation which is described in Section 4.2. The controlled roughness area, for

(a)

(b)

Figure 3.1: Pictures of the Shallow Water Basin: (a) empty basin from the coarse beach side, (b) full basin from the current outlet side.

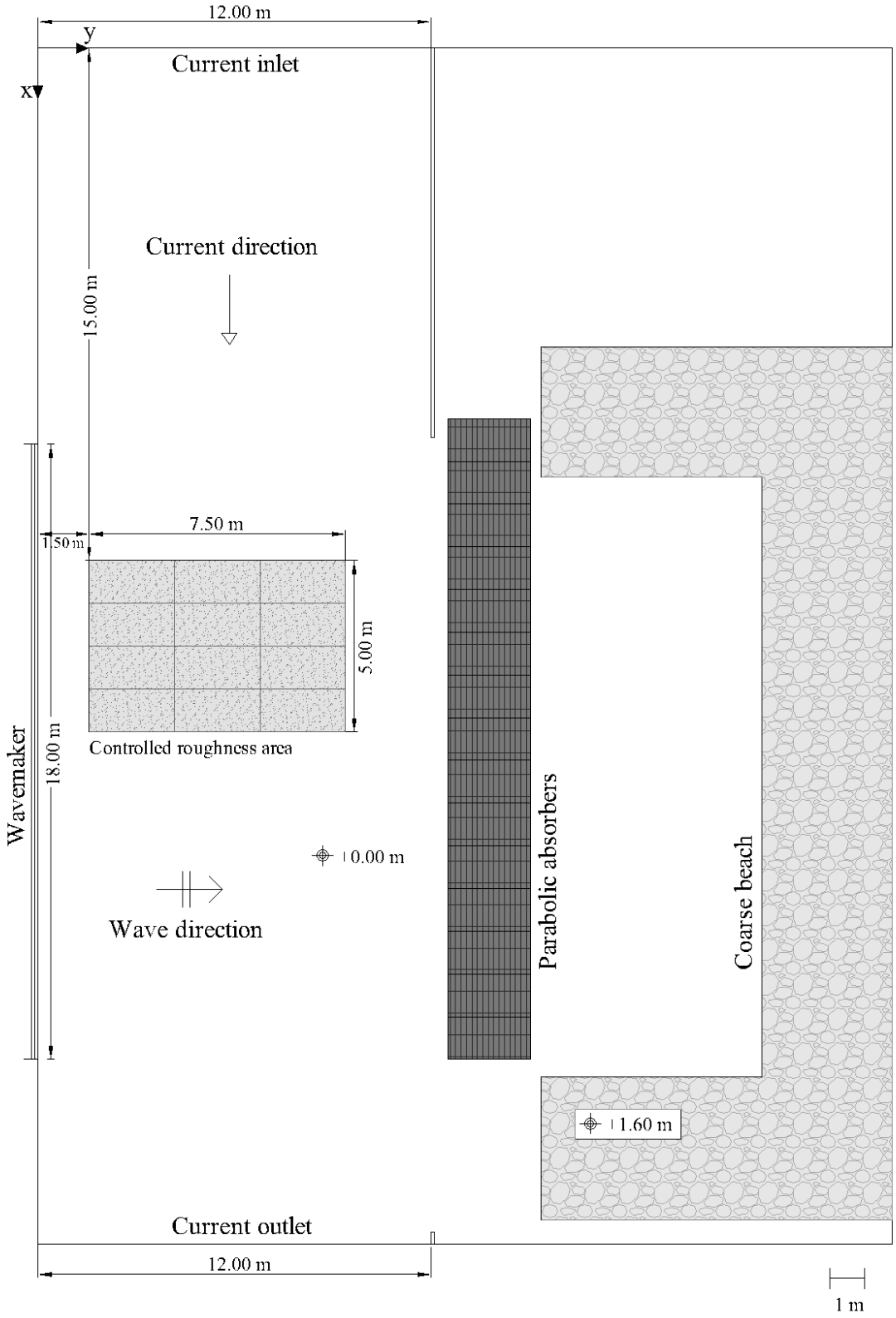

Figure 3.2: Top-view of the Shallow Water Basin.

Table 3.1: Positions of the resistive wave gauges in the Shallow Water Basin.

Wave gauge	x [m]	y [m]	Wave gauge	x [m]	y [m]
WG1	13.50	4.00	WG13	18.00	7.02
WG2	13.50	6.00	WG14	18.00	7.46
WG3	13.50	8.00	WG15	18.00	8.00
WG4	16.00	4.00	WG16	19.00	6.20
WG5	16.00	5.00	WG17	19.50	4.00
WG6	16.00	6.00	WG18	19.50	5.00
WG7	16.00	7.00	WG19	19.50	6.00
WG8	16.00	8.00	WG20	19.50	7.00
WG9	18.00	4.00	WG21	19.50	8.00
WG10	18.00	5.02	WG22	21.50	4.00
WG11	18.00	6.60	WG23	21.50	6.00
WG12	18.00	6.78	WG24	21.50	8.00

both sand and gravel panels, is shown in Figure 3.3.

Water surface elevation is measured by means of 24 resistive wave gauges (WG, Figure 3.4a). The wave gauges are connected to a series of analog data loggers, which allows the adjustment of gauges resolution and sensitivity. The wave gauges are distributed all over the area in front of the wavemaker in order to give detailed spatial information about the wave field. Four out of 24 gauges (WG11 to 14) are positioned in order to measure wave reflection by means of the Faraci 4-probes reflection method (Andersen and Faraci, 2003). The wave gauges are shown in Figure 3.4a, whereas their coordinates in the basin are listed in Table 3.1.

Flow velocities have been measured by means of 5 Acoustic Doppler Velocimeters (ADV), the model is the Vectrino, manufactured by Nortek (Nortek, 2009). The ADVs are held together onto a square chassis attached to a micrometer with a 0.0001 precision m, which allows them to be slided vertically. The micrometer is then fixed to a bridge above the acquisition area. The ADVs positioning is shown in Figure 3.4b. The ADVs are able to measure velocities within a cylindrical sampling volume of 0.001 m in height, with a resolution of 0.001 m/s, the accuracy is $\pm 0.5\%$ of the measured value. Sampling frequency is set to 200 Hz.

(a)

(b)

Figure 3.3: Fixed grain panels positioned in the DHI Shallow Water Basin: (a) sand bed, (b) gravel bed.

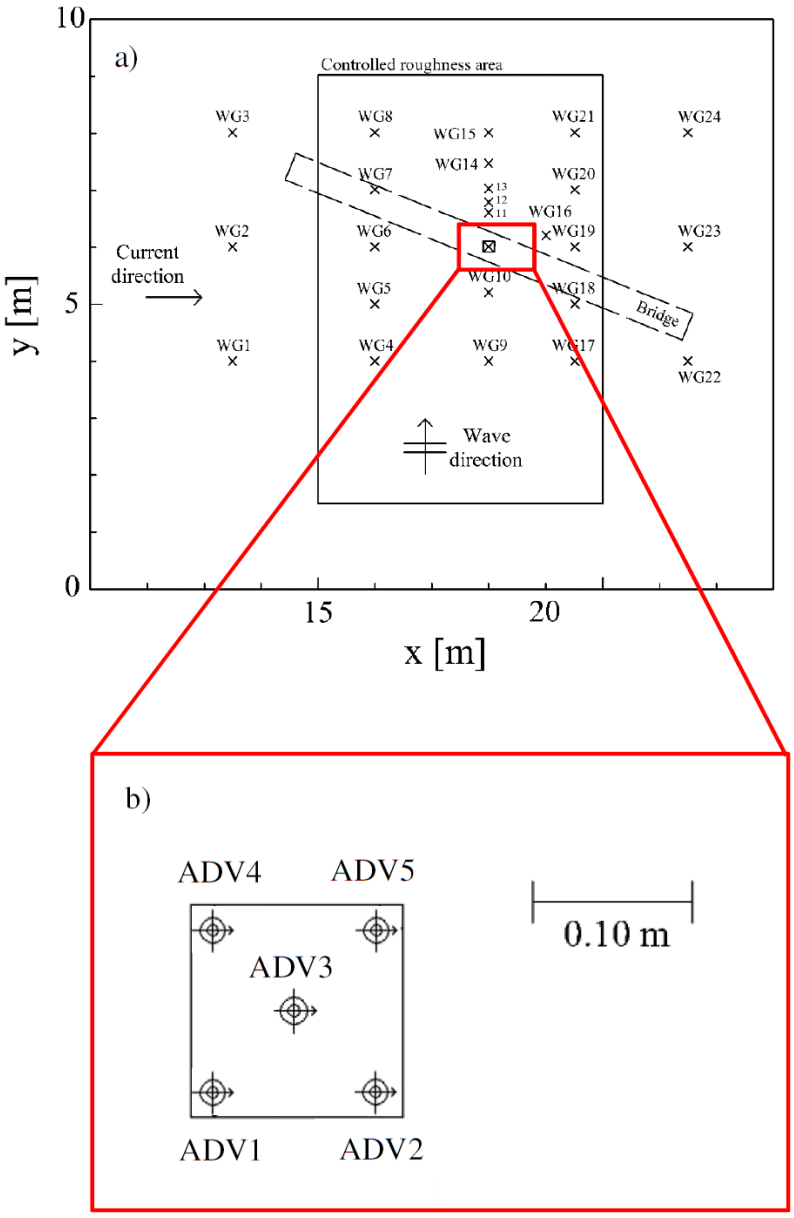

Figure 3.4: (a) Positioning of the wave gauges (crosses) and Acoustic Doppler Velocimeters (square) in the WINGS Shallow Water Basin; (b) close-up view of the ADV positioning.

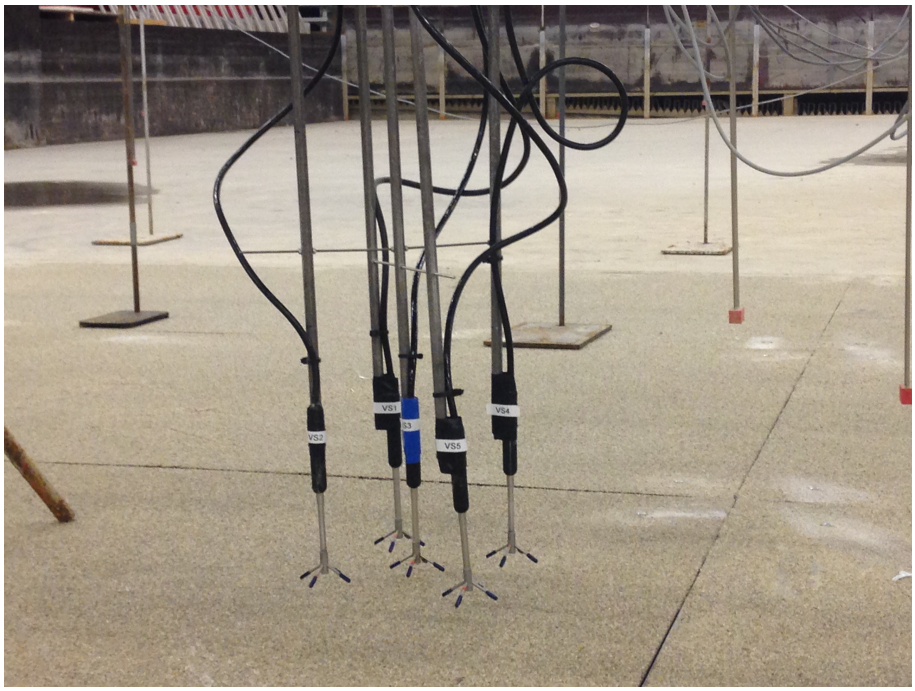

(a)

(b)

Figure 3.5: Pictures of the ADV measurement system: (a) ADVs over the sand bed panels, (b) micrometer for the accurate setting of the ADV distance from the bottom.

Table 3.2: ADVs position in the Shallow Water Basin.

ADV	x [m]	y [m]
ADV1	17.88	5.88
ADV2	18.12	5.88
ADV3	18.00	6.00
ADV4	17.88	6.12
ADV5	18.12	6.12

The data acquisition is remotely controlled by two terminals, one connected to the wave gauges data logger, collecting the water surface elevation, and one connected via USB to the ADVs, collecting flow velocity data. The wave gauges, the ADVs and the wavemaker are activated all together by means of the same signal from one of the two terminals, so that the measurements are synced with the start of the wavemaker movement. The ADVs position in the tank is shown in Figure 3.4b, their coordinates is shown in Table 3.2.

The performed experiments are listed in Table 3.3. The experimental plan included current only (CO), wave only (WO) and waves plus current (WC) conditions. A total of 36 runs have been carried out, Runs 1-18 over SB whereas runs $19 \div 36$ over GB. Two different steady currents have been generated by mantaining the current discharge constant ($Q = 1$ m^3/s) while varying the water level h to 0.40 m and 0.60 m, corresponding to a mean current velocity of $U = 0.21$ m/s and 0.14 m/s respectively. A range of regular wave conditions have been carried out, with wave height H $= 0.05 \div 0.18$ m and wave period T $= 1 \div 2$ s.

Each Run consists of 16 tests, with each test having velocity measurements carried out at a different z, in order to recover 16 positions for each run with a specific wave - current configuration. During the same Run, wave and current conditions are unchanged. A total of 576 tests have been carried out. The measurement distance from the bed z for each Test is shown in Table 3.4. In order to achieve a steady current, the current recirculation system is activated 1 hour before starting the experiments. Sampling duration for CO Tests is equal to 2 minutes. Sampling duration of WO and WC Tests is 2 minutes for Tests with wave period $T = 1.0$ s and 4 minutes for Tests with $T = 2.0$ s, in order to collect 120 wave cycles. Wavemaker

Table 3.3: Experimental plan of the WINGS campaign.

Run	Type	h [m]	U [m/s]	H [m]	T [s]	Run	Type	h [m]	U [m/s]	H [m]	T [s]
Sand bed (SB)						Gravel bed (GB)					
1	CO	0.40	0.21	-	-	19	CO	0.60	0.21	-	-
2	WO	0.40	-	0.18	2.0	20	WC	0.60	0.21	0.05	1.0
3	WO	0.40	-	0.12	2.0	21	WC	0.60	0.21	0.08	1.0
4	WO	0.40	-	0.08	2.0	22	WC	0.60	0.21	0.08	2.0
5	WO	0.40	-	0.08	1.0	23	WC	0.60	0.21	0.12	2.0
6	WC	0.40	0.21	0.18	2.0	24	WO	0.60	-	0.05	1.0
7	WC	0.40	0.21	0.12	2.0	25	WO	0.60	-	0.08	1.0
8	WC	0.40	0.21	0.08	2.0	26	WO	0.60	-	0.08	2.0
9	WC	0.40	0.21	0.08	1.0	27	WO	0.60	-	0.12	2.0
10	CO	0.60	0.21	-	-	28	WC	0.40	0.21	0.05	1.0
11	WC	0.60	0.21	0.08	2.0	29	WO	0.40	-	0.08	2.0
12	WC	0.60	0.21	0.12	2.0	30	WO	0.40	-	0.08	1.0
13	WC	0.60	0.21	0.18	2.0	31	WO	0.40	-	0.05	1.0
14	WC	0.60	0.21	0.08	1.0	32	CO	0.40	0.21	-	-
15	WO	0.60	-	0.08	2.0	33	WC	0.40	0.21	0.08	2.0
16	WO	0.60	-	0.08	1.0	34	WC	0.40	0.21	0.12	2.0
17	WO	0.60	-	0.12	2.0	35	WC	0.40	0.21	0.08	1.0
18	WO	0.60	-	0.18	2.0	36	WO	0.40	-	0.12	2.0

Table 3.4: ADV measurement distance from the bed z for each Test.

Test	z [m]	Test	z [m]
1	0.001	9	0.025
2	0.002	10	0.035
3	0.003	11	0.050
4	0.005	12	0.075
5	0.008	13	0.120
6	0.011	14	0.150
7	0.015	15	0.200
8	0.020	16	0.250

is turned on 2 minutes before the start of the sampling process in order to achieve a stable wave field. Results of the WINGS campaign are described in Chapter 4.

3.3 The ACCLIVE campaign

An experimental campaign (called the ACCLIVE campaign) has been carried out within the wave tank at the Hydraulics Laboratory of the University of Catania (Catania, Italy). This facility has been already employed in the past to study wave-current combined flow at a right angle (Musumeci et al., 2006; Faraci et al., 2008, 2018). The wave-current tank is shown in Figure 3.6.

The tank (schematized in Figure 3.7) is 3.40 m long in the current direction (x), 18.00 m long in the wave direction (y) and 1.00 m high in the vertical direction (z). On one end of the tank, a flap-type wavemaker generates monochromatic regular waves. Waves are generated over an horizontal bottom (water depth $h_0 = 0.30$ m) and then shoal on a 1:25 fixed planar beach. At the opposite end a coarse material beach acts as a wave reflection absorber.

A current recirculation apparatus generates a steady current, which crosses the wave field at a near-orthogonal angle. The current generation device consists of an underground reservoir, a submerged pump and a series of channels, which conveys the water from the reservoir to the wave tank through an inlet, and a channel beyond the outlet of the tank which brings the water back into the same reservoir. The pump is meant to reproduce low head and large discharge conditions. The nominal power of the pump is 11.0 kW, while the maximum discharge is about 0.25 m^3/s.

The pump is monitored during the experiments in order to check that the flow discharge remains constant. The channels act also as a stabilizer of the turbulent flow that comes out of the pump. A weir with a trapezoidal section is employed in order to measure the discharge. A grid made of equally spaced vertical lamellae adjusts the direction of the current and uniform the velocity profile. The lamellae are 0.20 m long in the current direction and 0.01 m spaced. The current enters the wave tank through a 2.50 m wide inlet at a right angle with respecto to the waves. The 2.50 m outlet is symmetric in front of the inlet, on the opposite of

(a)

(b)

Figure 3.6: A selection of pictures of the wave tank used within the ACCLIVE campaign: (a) view of the tank from the onshore side, (b) offshore side with the wavemaker in action.

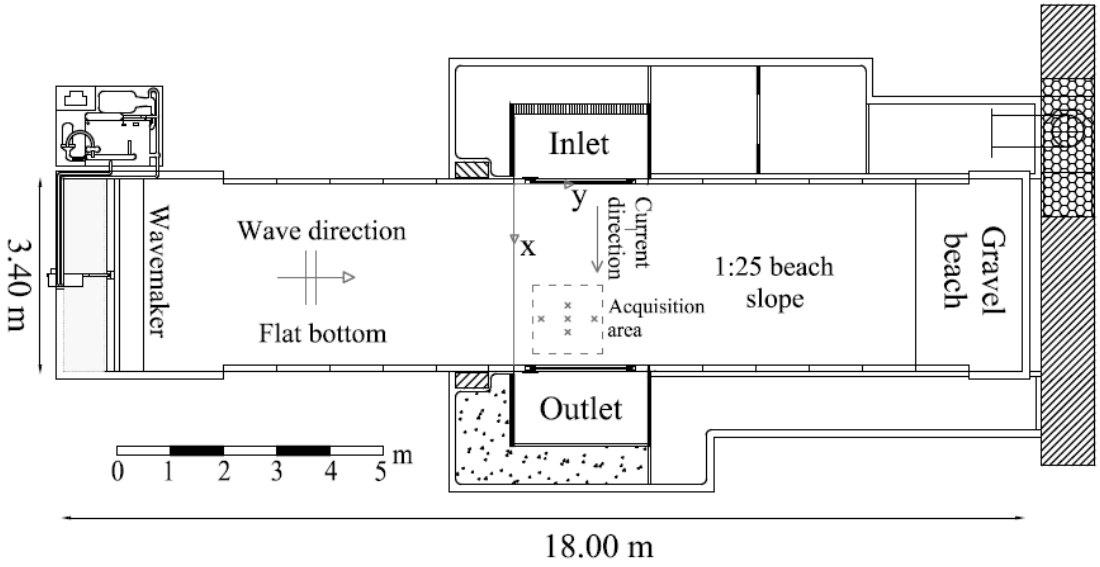

Figure 3.7: Experimental tank for wave-current interaction used within the ACCLIVE campaign.

the tank. Moreover, polystyrene mattresses attached to the channel walls act as a spurious wave reflection absorber. Beyond the outlet, the current flows back through a channel into the reservoir by means of a sluice gate.

Water surface elevation is measured by means of 5 resistive wave gauges, with one wave gauge located near the wavemaker, and 4 wave gauges right in proximity of the slope, positioned in order to compute wave reflection through the 4-probes method by Andersen and Faraci (2003).

Velocity measurements are gathered by means of a Nortek Vectrino+ ADV, which measured velocities u, v and w velocities in the x (current-), y (wave-) and z (vertical upward-) direction respectively. The resolution of the ADV is 0.001 m/s, the accuracy is $\pm 0.5\%$ of the measured value. Sampling frequency is 50 Hz for the WGs and 100 Hz for the ADVs. Positions of the ADV in the tank are shown in Figure 3.8.

Table 3.5 shows the experimental plan and ADV positions of the ACCLIVE campaign experiments. A total of 13 Runs have been carried out. For each Run, 12 velocity acquisitions have been performed at a different distance from bed z. The experimental plan included current only (CO) and waves plus current (WC) conditions. Runs 1-7 are in CO condition, whereas Runs 8-13 are in WC condition.

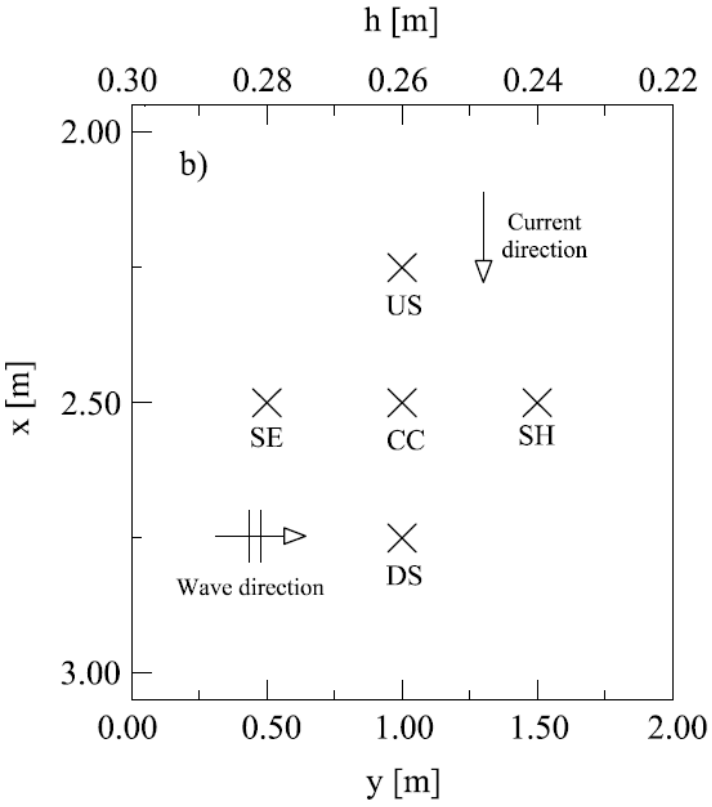

Figure 3.8: Different positions of the ADV in the tank.

Different mean current velocity (U = 0.06, 0.11 and 0.14 m/s) and one wave condition (wave height H = 0.085 m, wave period T = 1.0 s) have been performed. Mean velocity U is computed by dividing the flow discharge of the current recirculation system by the area of the inlet section.

For every Run, the ADV has been positioned at a different location within the tank, in terms of distance from the inlet x and from the wavemaker y, in order to spatially characterize the flow field. Five positions have been considered (see Figure 3.8): central position (CC, x = 2.50 m, y = 1.00 m; h = 0.26 m, where h is the local water depth); upstream position (US, x = 2.25 m, y = 1.00 m; h = 0.26 m); downstream position (DS, x = 2.75 m, y = 1.00 m; h = 0.26 m); shoreward position (SH, x = 2.50 m, y = 1.50 m; h = 0.24 m); seaward position (SE, x = 2.50 m, y = 0.50 m; h = 0.28 m). All Runs at US, DS, SH, SE have the same mean velocity U = 0.11 m/s, whereas three different mean current velocities have been performed for the CC (U = 0.06, 0.11 and 0.14 m/s). Test sampling duration is 10 minutes. Each Run consists of 14 Tests, with each Test having the ADV sampling point at a

different distance from the bed z (Table 3.6). Results of the ACCLIVE campaign are described and discussed in Chapter 5.

Table 3.5: Experimental plan of the ACCLIVE campaign: current only (CO) or waves plus current (WC), coordinates of the location of the ADV, local water depth h, mean current velocity U, wave height H and wave period T.

Run	Condition	ADV Pos.	x [m]	y [m]	h [m]	U [m/s]	H [m]	T [s]
1	CO	CC	2.50	1.00	0.26	0.06	-	-
2	CO	CC	2.50	1.00	0.26	0.11	-	-
3	CO	CC	2.50	1.00	0.26	0.14	-	-
4	CO	US	2.25	1.00	0.26	0.11	-	-
5	CO	DS	2.75	1.00	0.26	0.11	-	-
6	CO	SH	2.50	1.50	0.24	0.11	-	-
7	CO	SE	2.50	0.50	0.28	0.11	-	-
8	WC	CC	2.50	1.00	0.26	0.11	0.085	1.0
9	WC	CC	2.50	1.00	0.26	0.14	0.085	1.0
10	WC	US	2.25	1.00	0.26	0.11	0.085	1.0
11	WC	DS	2.75	1.00	0.26	0.11	0.085	1.0
12	WC	SH	2.50	1.50	0.24	0.11	0.085	1.0
13	WC	SE	2.50	0.50	0.28	0.11	0.085	1.0

Table 3.6: ADV measurement distance from the bed z for each Test.

Test	z [m]	Test	z [m]
1	0.0005	9	0.0100
2	0.0010	10	0.0150
3	0.0020	11	0.0200
4	0.0030	12	0.0400
5	0.0040	13	0.0700
6	0.0150	14	0.1100

Chapter 4

Wave-current interaction at a right angle over rough beds

4.1 Overview

In the following Chapter the results of the WINGS campaign are discussed. First, preliminary investigations on water surface elevation, flow velocities and geostatistics of the bed reconstruction are presented. Second, results of the data analysis is shown concerning mean and turbulent flow, alongside a comparison between experimental data and a selection of combined flow boundary layer models. A discussion Section summarizes the main findings and closes the Chapter.

4.2 Preliminary data analysis

4.2.1 Water surface elevation

Water surface elevation in the WINGS campaign has been measured by an array of 24 wave gauges distributed all over the measurement area within the wave basin. Water elevation timeseries, η, have been used to obtain measured wave height H_m, and to monitor fluctuations of the average water level. The nominal wave height, H, is the target wave height used as input into the wavemaker, the measured wave height H_m is obtained as $\max(\tilde{\eta}) - \min(\tilde{\eta})$, where $\tilde{\eta}$ is the phase-averaged wave surface elevation.

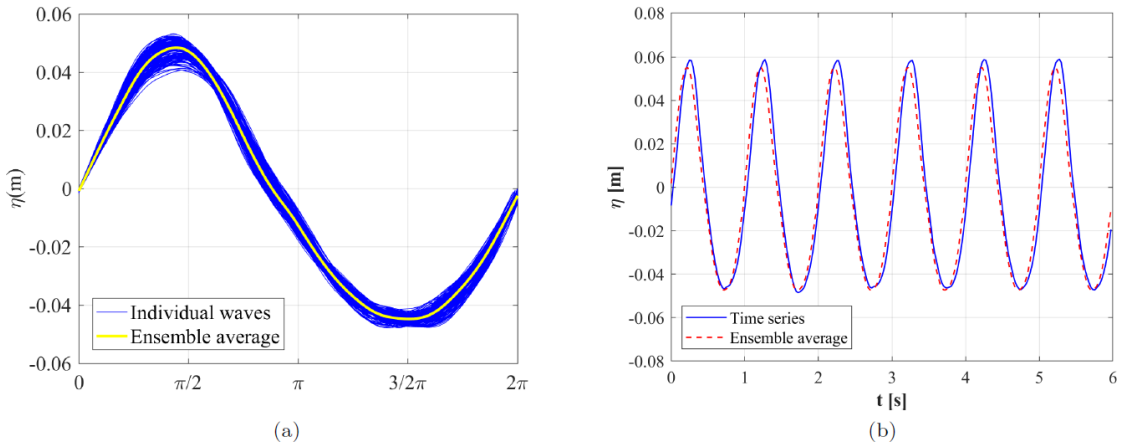

Figure 4.1: Surface elevation timeseries for Run 16 ($U = 0.140$ m/s, $H = 0.08$ m, $T = 1.0$ s) for WG11. (a) All individual waves plus ensemble average wave; (b) extract of a timeseries with the superposed phase-averaged wave.

An example of the acquired signal is reported in Figure 4.1, where the phase-averaged wave is plotted above each single recorded wave during Run 16 (WO, SB, $h = 0.60$ m, $U = 0.140$ m/s, $H = 0.08$ m, $T = 1.0$ s). The chosen wave gauge (WG11, $x = 18.00$ m, $y = 6.60$ m) is the one closest to the velocity measurement point. Figure 4.1(a) shows that the wave signal is regular and with a good repeatability, being the average crest-trough variability, estimated as the displacement of the maximum crest elevation or minimum trough position with respect to the ensemble average, equal to 0.096 of H_m. A trunk of the timeseries along with the phase average is also reported in Figure 4.1(b).

Table 4.1 shows the nominal wave height, measured wave height and the wave height standard deviation σ_H/H_m computed using data recorded at WG11. The difference between H and H_m is always below 20% of H, except for Run 2, in which some error occurred probably in the input into the wavemaker. For this reason no further analysis will be carried out for Run 2. Standard deviation of the measured timeseries is always lower than 1.7%, showing that, except for the above mentioned Run 2, the generated waves are satisfactorily regular and wave reflection within the basin is minimum. as demonstrated by the reflection coefficients listed in Table 4.2.

Every run consists of 16 Tests, in which velocity measurements have been performed with the ADVs at a different bed distance during each Test, while keeping

Table 4.1: Target wave height H, measured wave height H_m and standard deviation of the wave height timeseries σ_H/H for all the Runs of the WINGS campaign.

Run	H [m]	H_m [m]	σ_H/H	Run	H [m]	H_m [m]	σ_H/H
1	-	-	-	19	-	-	-
2	0.180	0.579	0.039	20	0.050	0.046	0.007
3	0.120	0.124	0.008	21	0.080	0.072	0.010
4	0.080	0.091	0.001	22	0.080	0.084	0.005
5	0.080	0.085	0.003	23	0.120	0.121	0.008
6	0.180	0.179	0.012	24	0.050	0.053	0.005
7	0.120	0.139	0.014	25	0.080	0.093	0.003
8	0.080	0.088	0.009	26	0.080	0.086	0.002
9	0.080	0.078	0.012	27	0.120	0.118	0.002
10	-	-	-	28	0.050	0.049	0.008
11	0.080	0.120	0.009	29	0.080	0.099	0.002
12	0.120	0.175	0.010	30	0.080	0.073	0.003
13	0.180	0.182	0.009	31	0.050	0.047	0.002
14	0.080	0.078	0.017	32	-	-	-
15	0.080	0.085	0.002	33	0.080	0.100	0.006
16	0.080	0.097	0.007	34	0.120	0.147	0.008
17	0.120	0.122	0.002	35	0.080	0.077	0.013
18	0.180	0.175	0.003	36	0.120	0.155	0.003

the same current and wave configuration throughout the entire Run.

Figure 4.2 shows the variability of the wave height during Run 14 for each of the 16 tests, for WGs 1-10 and 15-24 (a) and WGs 11-14 (b). The Figure shows that wave height (crosses) remain constant during the Run and for each wave gauge position. Wave gauge offset (pluses), shows the still water level position measured by each wave gauge. Monitoring the offset is important to check variations in the water level or changes in water temperature, which may require wave gauge calibration to be redone. Results indicate that the wave gauge offset is circa zero for all the duration of the Test. Nevertheless, looking at the measured wave heights at the different positions, differences between the WGs are observed.

Figure 4.3 shows the iso-lines of the measured wave height over the sand bed. The grey circles indicate the WGs location, the square indicates the ADVs position. More in detail, Figure 4.3(a) and (b) shows the spatial distribution of H_m/H in the WO and WC cases respectively (Runs 16 and 14, $H = 0.08$ m, $T = 1.0$ s). Looking at Figure 4.3(a) it is possible to observe that the measured wave height is amplified of about 20% around $x = 18.00$ m and $y = 6.50$ m, whereas a "shadow zone" is observed close to $x = 19.50$ m, $y = 7.00$ m, i.e. close to WGs 19-21, where the wave propagation is sheltered by the presence of the instrumentation bridge. Here the measured wave height is about 20% smaller than the target value. Elsewhere the average wave height is close to its target value. In the wave plus current case, (Figure 4.3(b), the shelter effect at WG19-21 is counteracted by the current, which spreads and makes more uniform the mean wave height spatial distribution. Indeed measured wave height is approximately constant everywhere apart from a side area at $x = 14 \div 15$ m, close to WGs 1-3, where the wavemaker fronts end. Similarly, Figure 4.4 reports the time-averaged wave height measured over the gravel bed, for WO (Figure 4.4(a), Run 25) and WC (4.4(b), Run 21). Results are similar to the case of sand bed.

Figures 4.3 and 4.4 furtherly shows that in the correspondence of the ADVs, the ratio H_m/H is always between $0.90 \div 1.15$, while reaching larger values apart from the velocity measurement area.

Figure 4.5 shows WINGS experimental conditions in the context of wave theories validity according to Le Mehaute (1979), in terms of the parameters h/T^2

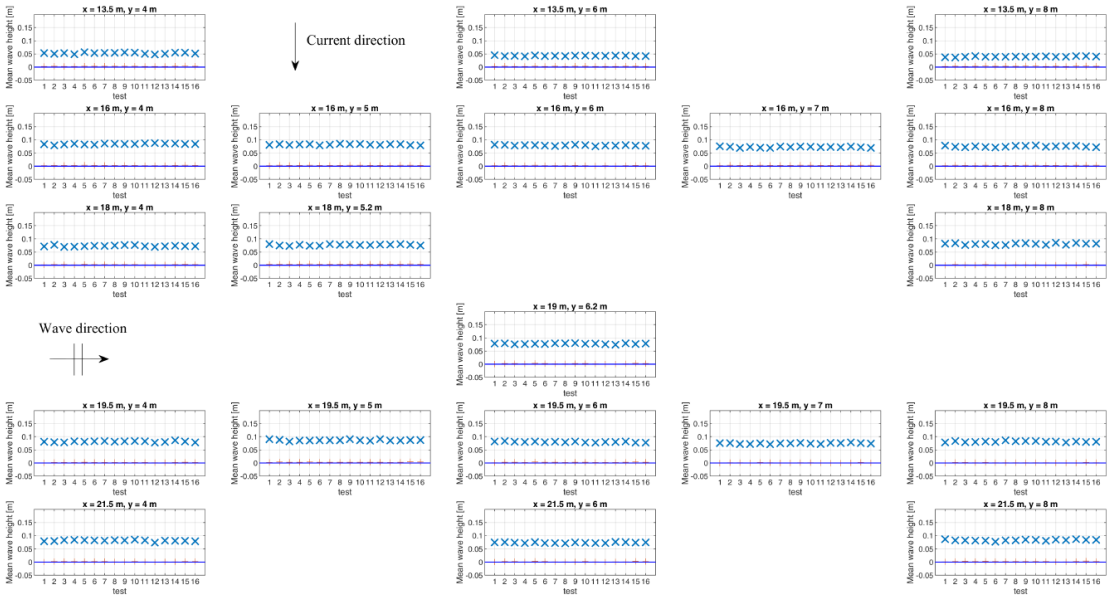

(a)

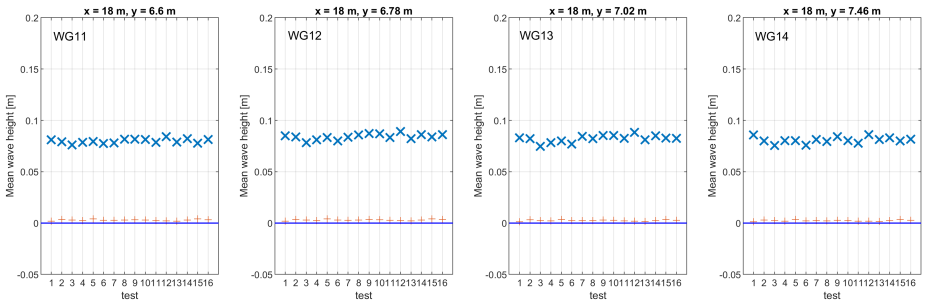

(b)

Figure 4.2: Wave height time variability within the tank at each gauge during all Tests of Run 14 (WC, SB, $h = 0.60$ m, $U = 0.140$ m/s, $H = 0.08$ m, $T = 1.0$ s): (a) wave gauges 1-10 and 15-24, (b) wave gauges 11-14. The blue line indicates the zero level, the $\times$ refer to the average wave height during each test, the $+$ symbols refer to the gauge offset.

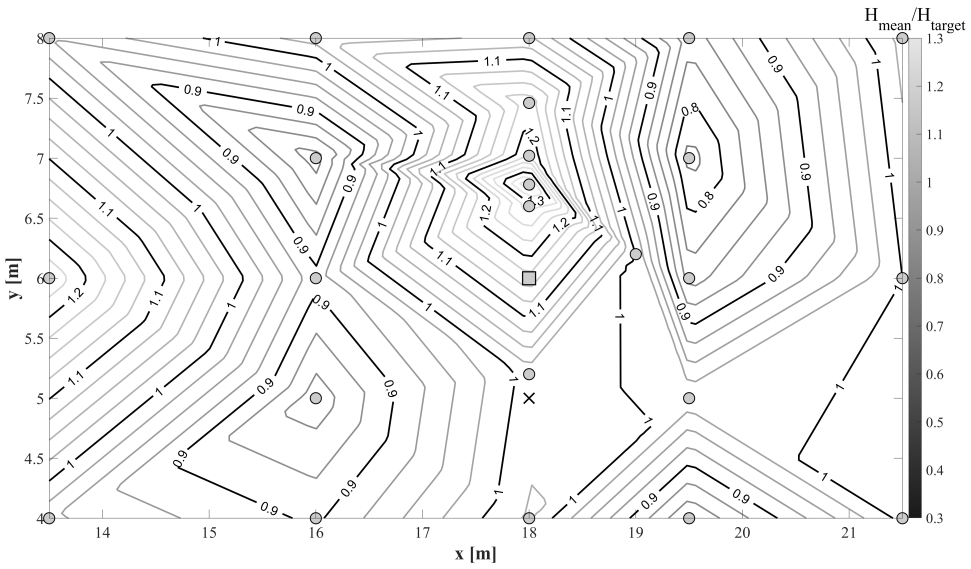

(a)

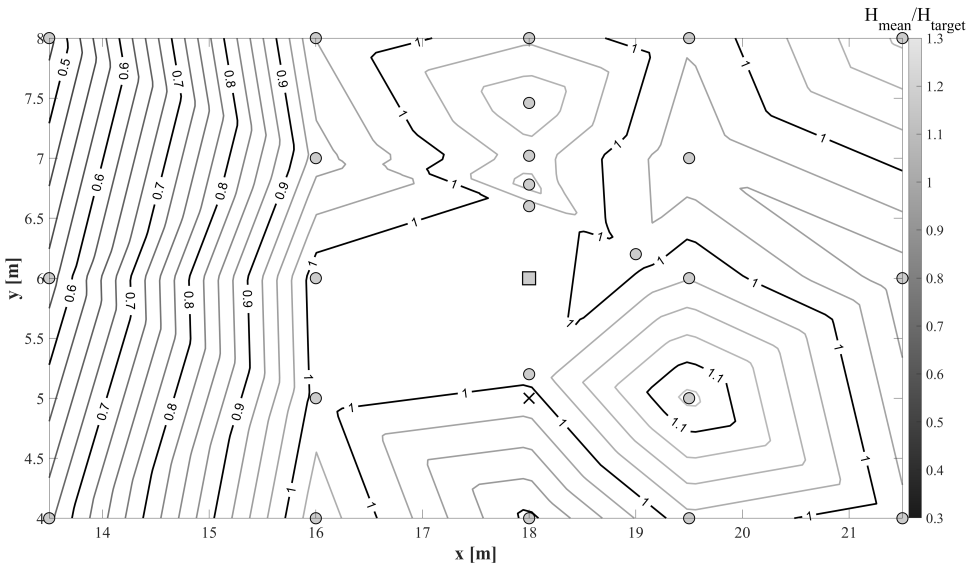

(b)

Figure 4.3: Contour iso-lines of H_m/H in the SB, $U = 0.140$ m/s case: a) Run 16 (WO, $H = 0.08$, m $T = 1.0$ s); b) Run 14 (WC, $H = 0.08$, m $T = 1.0$ s). The grey circles indicate the position of the wave gauges, the square indicates the location of the ADVs.

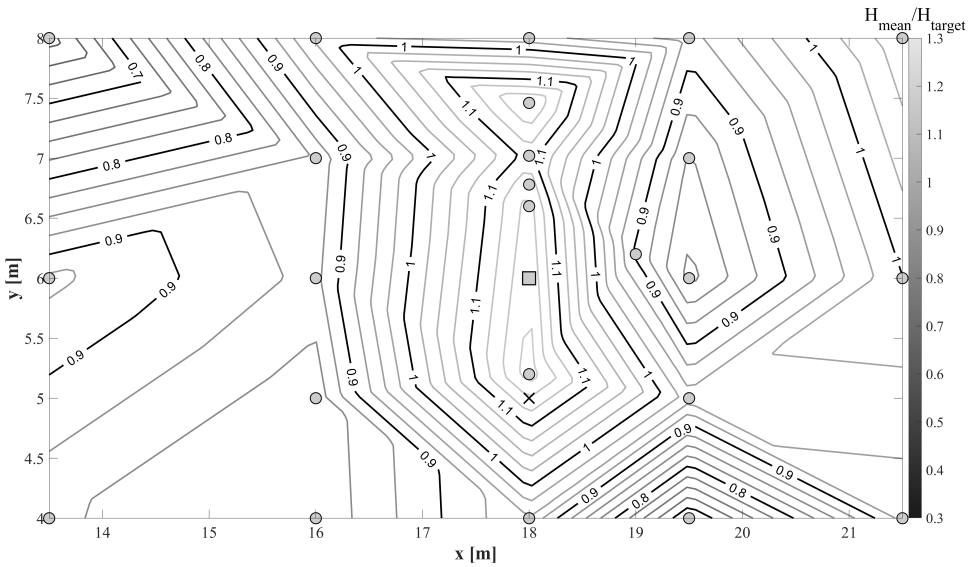

(a)

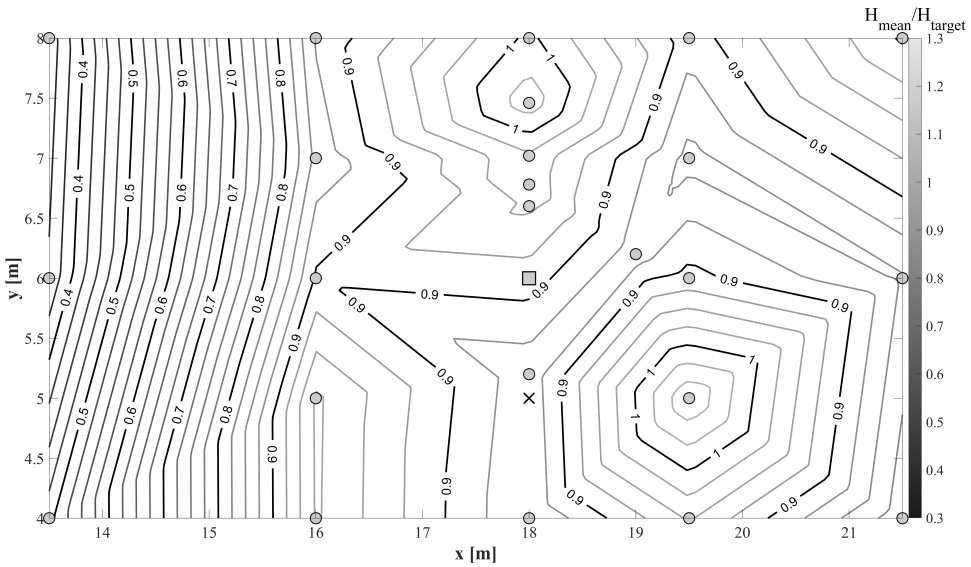

(b)

Figure 4.4: Contour iso-lines of H_m/H in the GB, $U = 0.210$ m/s case: a) Run 25 (WO, $H = 0.08$, m $T = 1.0$ s); b) Run 21 (WC, $H = 0.08$, m $T = 1.0$ s). The grey circles indicate the position of the wave gauges, the square indicates the location of the ADVs.

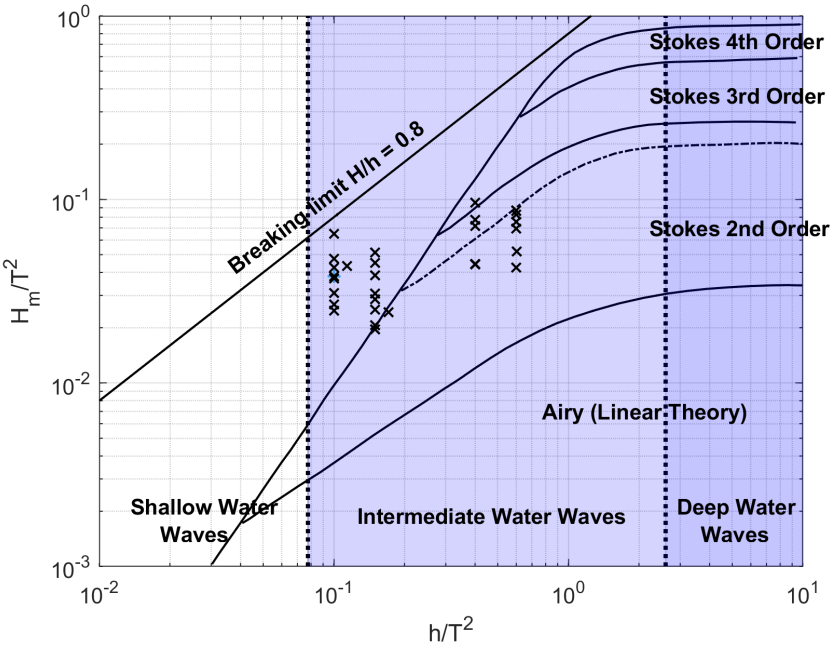

Figure 4.5: WINGS Runs wave height to water depth ratio (crosses) in the context of wave theories validity according to Le Mehaute (1979).

and H_m/T^2. Results refer to WG11 which is the closer to the velocity measurement area. All the performed runs fall into the intermediate water waves region. Runs with shorter waves ($T = 1.0$ s) fall into the 2^{nd} order Stokes wave theory validity region, whereas the remaining the remaining longer wave runs ($T = 2.0$ s) fall into the 5^{th} order/streamfunction wave theory validity region.

Reflection coefficients k_r for all WINGS Runs have been computed by means of the Faraci and Liu (2014) 4-probes methods and are shown in Table 4.2. Wave reflection is generally lower for $h = 0.60$ m cases (Runs 11-27), and except for a few cases that are close to 30%, most of the cases have a reflection coefficient smaller than 20%.

4.2.2 Velocity measurements

Preliminary tests in the basin have been performed in order to: (i) check the uniformity of the flow velocity within the test area, (ii) set both the location of the rough bottom panels and the position of the instrumentation inside the basin. First, a Lagrangian particle tracking analysis, making use of plastic buoyant particles, allowed the large scale wave-current interaction to be monitored and secondary flows

Table 4.2: Reflection coefficients for the WINGS campaign

Run	k_r	Run	k_r
1	-	19	-
2	-	20	0.09
3	0.21	21	0.11
4	0.27	22	0.09
5	0.26	23	0.10
6	0.24	24	0.15
7	0.10	25	0.09
8	0.10	26	0.10
9	0.18	27	0.07
10	-	28	0.13
11	0.17	29	0.33
12	0.16	30	0.10
13	0.33	31	0.07
14	0.12	32	-
15	0.06	33	0.18
16	0.08	34	0.18
17	0.06	35	0.15
18	0.08	36	0.29

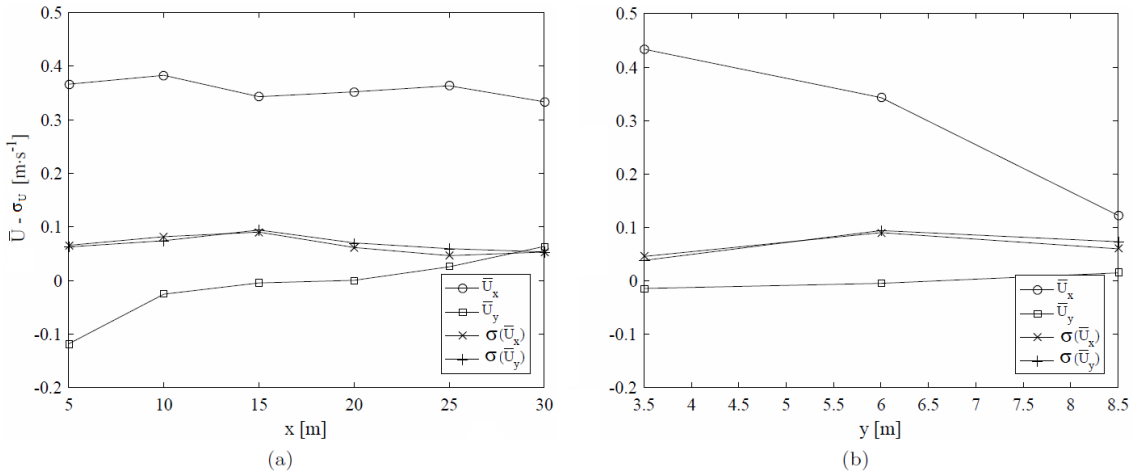

Figure 4.6: Current only preliminary flow measurements ($h = 0.40$ m) at $z = 0.10$ m from the bed: a) x-direction ($y = 6$ m); b) y-direction ($x = 20$ m).

to be investigated by means of visual inspection. One water depth ($h = 0.40$ m), i.e. one current condition ($U = 0.210$ m/s), and one wave condition ($H = 0.12$ m and $T = 2.0$ s) have been chosen in order to run a current only case and a wave plus current one, the latter obtained by superimposing the wave on the existing current. After that, an analysis both in the current and in the wave direction of the flow conditions within the basin at one vertical position located 0.1 m above the bed was carried out by means of an ADV.

The main goal has been to check to which extent the velocity in the outer flow could be influenced by the local coordinate of the measuring station. The measurements explored the area where the waves interact with the current, acquiring measurements at 14 positions in the current only case and 12 positions in the wave plus current case (in the range of 5 m $< x <$ 30 m, 3.5 m $< y <$ 8.5 m). Figure 4.6 shows the results for the current only case.

Preliminary current experiments feature the same discharge of the experimental campaign runs, but with a smaller water depth, i.e. with a smaller inlet/outlet section area, determining an almost doubled current velocity (nominal current velocity $U = 0.40$ m/s) with respect to the maximum value used during the WINGS experimental campaign ($U = 0.21$ m/s). The reasons behind such a choice are related to the will to test the capabilities of the experimental setup to determine the optimal wave-current interaction measuring area and the accuracy of the flow

measurement instruments. Specifically, one reason of concern was the generation of internal circulation cells in the tank, which is a common problem to be taken into account when reproducing wave-current interaction in three-dimensional water basins. Similar issues have been observed in Musumeci et al. (2006) in the same tank used in the ACCLIVE campaign but over a flat bottom. Such circulation cells are determined by the presence of quiescent fluid in certain regions of the tank that lead to velocity gradients, and thus to a shear layer, where the quiescent fluid meets the flowing current. This circulation phenomena may determine spurious flows that may propagate and contaminate the flow in the measurement area. Naturally, such circulation becomes more significant as the velocity difference between the current and quiescent fluid increases. This is the reason why we preliminary tested the experimental setup with the significantly large current velocity of 0.40 m/s. Secondly, our aim was also to test the capabilities of acoustic velocimeters to correctly measure the velocity in the tank. One of our concerns was the lack of reflective particles in the water, which may notoriously lead to a noisy signal. Such noise is usually more significant when the lack of particle occurs in the presence of an higher velocity flow McLelland and Nicholas (2000). Finally, a larger velocity generally lead to a more readable tracking of the trajectory of the buoyant tracking particles in the preliminary tracking study.

Depth- and time-averaged velocities in the current direction ($\bar{U_x}$) and wave direction ($\bar{U_v}$), along with their standard deviation, are plotted along the x and y coordinates. The two plots highlight that a small anticlockwise rotation of the velocity field is present (Figure 4.6(a), along with a deceleration of the current flow along the y direction (Figure 4.6(b), induced by the presence of the dissipating basin and by the outlet geometry. Based on these preliminary results, the velocity measurement area has been set at x between 15 and 20 m and precisely at x = 18.00 m, and at y = 6.00 m, in order to minimize the influence of the velocity reduction shown by Figure 4.6(b), and guarantee at the same time to be at least 1.5 wavelengths far away from the wavemaker.

Additionally, a time variability analysis has been performed for the current only runs in order to investigate variability of the current velocity depending on the timeseries length. The 2-minutes timeseries have been splitted into two 1-minute

Table 4.3: Depth-averaged current velocity standard deviation for CO Runs. Original 2-minutes timeseries have been splitted in two 1-minute long timeseries (*a and *b, with * being the run number).

Run	$\sigma_{u,1}$ [m/s]	$\sigma_{u,3}$ [m/s]	$\sigma_{u,4}$ [m/s]	$\sigma_{u,5}$ [m/s]
1	-	0.021	0.018	-
1a	-	0.018	0.015	-
1b	-	0.018	0.015	-
10	0.013	0.022	0.013	0.041
10a	0.013	0.021	0.012	0.039
10b	0.011	0.020	0.013	0.038
19	0.018	0.021	0.016	0.045
19a	0.016	0.020	0.015	0.044
19b	0.017	0.021	0.016	0.039
32	0.053	0.036	0.023	0.043
32a	0.033	0.033	0.021	0.042
32b	0.057	0.035	0.020	0.040

timeseries (a and b) and current velocity standard deviation has been computed. Table 4.3 shows the depth-averaged standard deviation of the current velocity $\sigma_{u,ADV}$, where $_{ADV}$ is the ADV number. For all the chosen ADVs, it appears that even halfing the length of timeseries lead to change of variability in the order of 10^{-3} m/s, which correspond to a variability of the velocity always below 5% of the target current velocity U.

Flow velocity data are treated in order to remove spikes in the timeseries. Presence of spikes is a common issue in acoustic flow velocimetry and their removal (known as *despiking*) is considered an essential operation in velocity data processing. Several despiking methods have been developed in the last decades. Goring and Nikora (2002) developed a phase-space threshold, which follows the principle that velocity derivative enhances spikes and makes them easily identifiable. Velocity and its first and second derivative are plotted in a tridimensional space, then an ellipsoid which axes are defined by Universal threshold by Donoho and Johnstone (1994) is plotted. All the projections of the points that lies outside the ellipses formed by the

intersection between the ellipsoid and the xy xz and yz planes are considered spikes.

Wahl (2013) modified the phase-space method using a true threshold ellipsoid rather then its projections. Moreover, it uses robust statistics like the median as a location estimator and median absolute deviation as a spread estimator. Chauvenet criterion (Coleman and Steele, 1995) is applied instead of the universal threshold as a cutoff value.

Cea et al. (2007) applied a correlation filter method, in which in the 3D map instead of u velocity components and derivatives, flow velocities are plotted. Universal threshold is used as a cutoff value.

Parsheh et al. (2010) applies a preconditioning to the Goring and Nikora (2002) phase-space threshold method and applies robust statistics (statistics that are resistant to outliers, like the median in comparison with the mean). Parsheh et al. (2010) reported that their method significantly improve power spectra.

Islam and Zhu (2013) developed a kernel-based despiking method, in which a bivariate density estimate of velocity – velocity first derivative via diffusion (Botev et al., 2010) is computed, then a threshold based on the slope of the density estimation "bell" is set, which defines the limit over which velocity data are considered outliers.

Goring and Nikora (2002) and Islam and Zhu (2013) despiking methods were chosen to be compared. The former is a well-established method, widely used in hydraulics physical modeling; the latter one is a new method purposely developed to deal with velocity data series heavily contaminated by spikes. The Islam and Zhu method, despite dealing better with spikes, it was found to cut the crest and troughs, such an occurrence seems related to the wave steepness but it has not been investigated further. Therefore, the Goring and Nikora method has been used to remove spikes on velocity data in order to obtain time-averaged and phase-averaged velocities. Once the velocity data have been phase-averaged, turbulent velocities are obtained by Reynolds decomposition, and the Islam and Zhu method has been used in order to remove spikes. Data identified as spikes are then substituted by means of a cubic polynominal interpolation in both Goring and Nikora and Islam and Zhu methods. The percentage of removed data is up to 15%.

Sharp thresholds on Correlation (COR < 70) and Signal-to-Noise Ratio

(SNR < 15) are applied on velocity timeseries in order to remove uncorrelated and noisy signal, values smaller than those thresholds have been removed. COR and SNR are computed by means of the internal algorithm of the ADV. Moreover, velocity data that showed an acceleration larger than 9.81 m/s^2 are recognized as spikes and removed from the timeseries.

Recirculation system generated a non-perfectly steady current, determining low frequency oscillations of the water level h in the order of $10^{-1} \div 10^{-2}$ Hz. A sharp highpass filter with a cutoff frequency of 0.8 Hz is applied in order to remove low frequency oscillation whilst mantaining the ones determined by the wave field (which starts at 0.5 Hz).

Phase averaging is operated by the following procedure: a lowpass filter is applied to the timeseries in order to easily identify zero-up crossings, timeseries is then cut wave-by-wave from a zero-up crossing to the next, phase averaged wave is then obtained by averaging every wave. The Phase averaged wave is obtained from 4 minutes time series for $T = 2.0$ s tests and 2 minutes time series for $T = 1.0$ s tests, in order to have in both cases 120 waves. The number of waves is set considering Sleath (1987) which states not less than 50 waves should be used for phase averaging.

4.2.3 Bed surface geostatistics

Three-dimensional surface reconstruction mesh of the bottom have been obtained through Structure-from-Motion (SfM) technique (van Gent and van der Werf, 2014; Hofland et al., 2018), i.e. several photos of the bottom are taken (reference square markers ensures the scaling and set the referencing system), images are then processed by the software Photoscan by Agisoft, which generates a triangular high-resolution in the order of $O(10^{-4})$ m mesh out of the images. Markers positioning is shown in Figure 4.7.

As the area of major interest is the one in proximity of the velocity measurement system, the markers have been placed around the area interested by the ADVs. The origin of the mesh reference system lies at the center of one of the markers. In order to characterize the bottom surface, statistics have been gatherered through a random field approach i.e. by considering the bed as a 2D field of surface

Figure 4.7: Markers position over the gravel bed for the application of the Sfm technique to recover bed morphology.

elevations (Aberle and Nikora, 2006; Qin et al., 2019). The geostatistical analysis is carried out on the gravel bed reconstruction mesh recovered before carrying out the experiments. The reconstruction has been interpolated linearly over an evenly spaced grid with 0.0002 m spacing, the grid extends over an area of 2.66 x 1.66 m, the longer side is parallel to the wave direction, whereas the shorter one is parallel to the current direction.

The surface reconstruction is contaminated by the presence of the markers and other part of the instrumentation, not easily removable by a surface elevation filter. Thus, a square area of the grid (0.41 x 0.41 m), corresponding to the surface right below the single-point ADVs, has been cropped out from the original surface in which no markers or instrument supports are present; the analysis is then carried out only considering this area. The bed surface elevation frequency distribution is shown in Figure 4.8.

The bin size of the frequency distribution is set to 0.0002 m, equal to the resolution of the interpolated grid. The frequency of distribution of the bed surface elevation has a median value of 0.0135 m and a standard deviation of 0.004 m. The distribution is slightly asymmetric towards smaller values, as shown by the positive skewness value $Sk(z) = 0.493$, while a longer tail in the larger elevations direction,

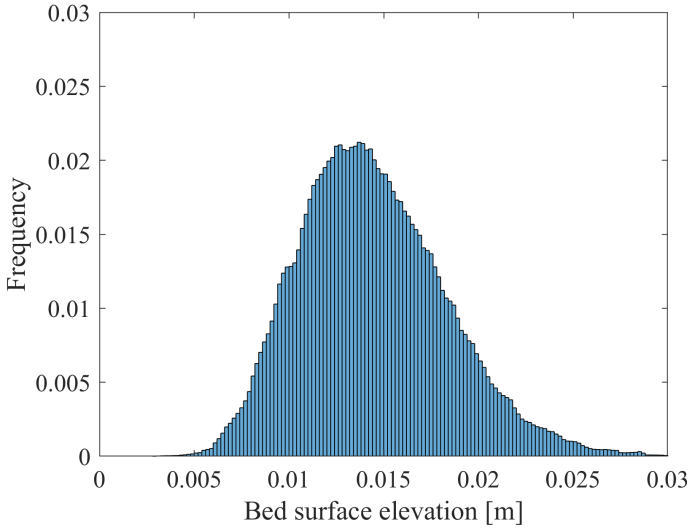

Figure 4.8: Frequency distribution of surface elevation for a 0.41 x 0.41 area

in which the maximums elevations of the larger grains are stored, appears. The distribution kurtosis $Ku(z) = 3.25$, which is close to a normal distribution (3.00).

Frequency distribution provides an overview of the bottom characteristics, however it does not give any information about its spatial distribution and how the grains are clustered. In order to characterize spatially the bottom surface, a one dimensional structure function like the one used by (Nikora et al., 1998) is computed:

$$D_1(l) = \frac{1}{N_z - n} \sum_{N-n}^{i=1} [z(x_i + n\delta x) - z(x_i)]^2; \tag{4.1}$$

where N_z is the total number of considered bed elevation, n is the lag length within which spatial deviation is computed, z is the surface elevation and δx is the lag step. The structure function is meant to provide information about the spatial correlation of a one-dimensional profile. Although, a two-dimensional structure function would be preferable as the surface elevation reconstruction is a 2D array, the 1D profile analysis provides easily readable results, while the physical interpretation of the 2D structure function data may be a challenging task (Nikora and Walsh, 2004). For this reason, a 1D structure function has been computed here for several 1D profiles in the x and y direction. The structure function is calculated for 20 profiles in total, 10 in the current direction and 10 in the wave direction. Only 6 out of 20 profile structure function are here examined, 3 along the current direction (a, c, e) and 3 along the wave direction (b, d, f), their position is shown in Figure 4.9.

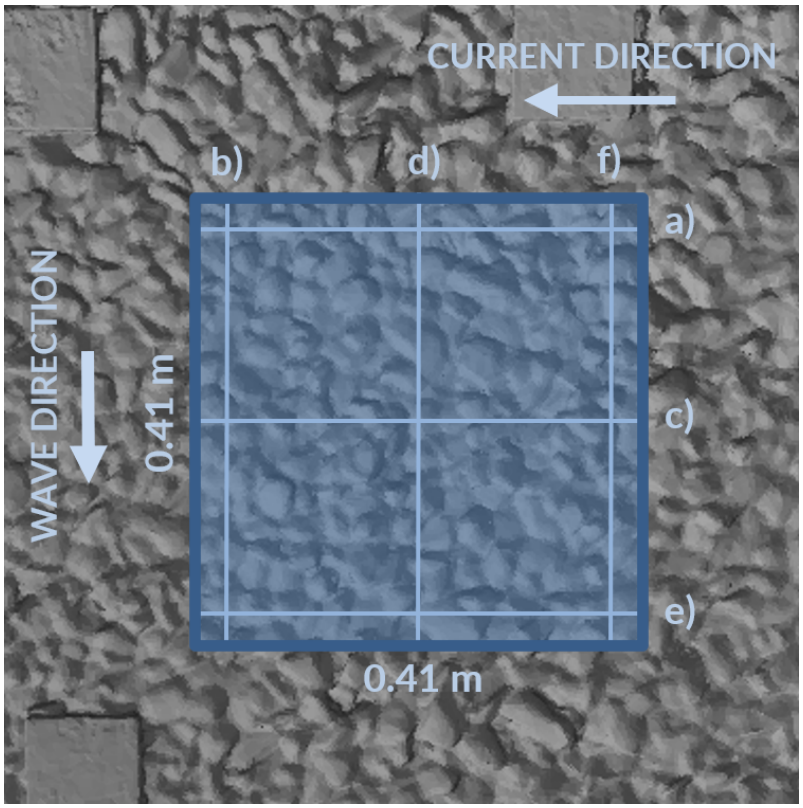

Figure 4.9: Top view of the structure function profiles examined in Figure 4.10

The 1D structure function values are shown in Figure 4.10 plotted in semio-variograms, i.e. versus the lag length. As long as the structure function shows a linear non-constant trend, elevation data shows a spatial correlation. Once it reaches the value of two times the variance of the elevation, or become constant, from that point on space correlation is lost and further structure function values have no physical meaning (Qin et al., 2019).

Results show that, in the subgrain scale ($0.0002 \div 0.012$ m) a strong correlation is found in all cases, showing that the gravel texture is uniform and smooth for all the examined profiles. Within the grain scale, defined by the nominal range of the gravel diameter $0.012 \div 0.036$ m, a smaller correlation is found, as the slope of the structure function gradually decreases and reaches constant value, showing that gravel grains have different sizes and shapes. All the subfigures show that spatial correlation is always lost within the grain scale range, by becoming constant or because the structure function reaches values larger than 2 times squared standard deviation limit. Then, in the larger topographic scale, correlation is always lost. This has been observed for all the examined profiles in both x and y directions.

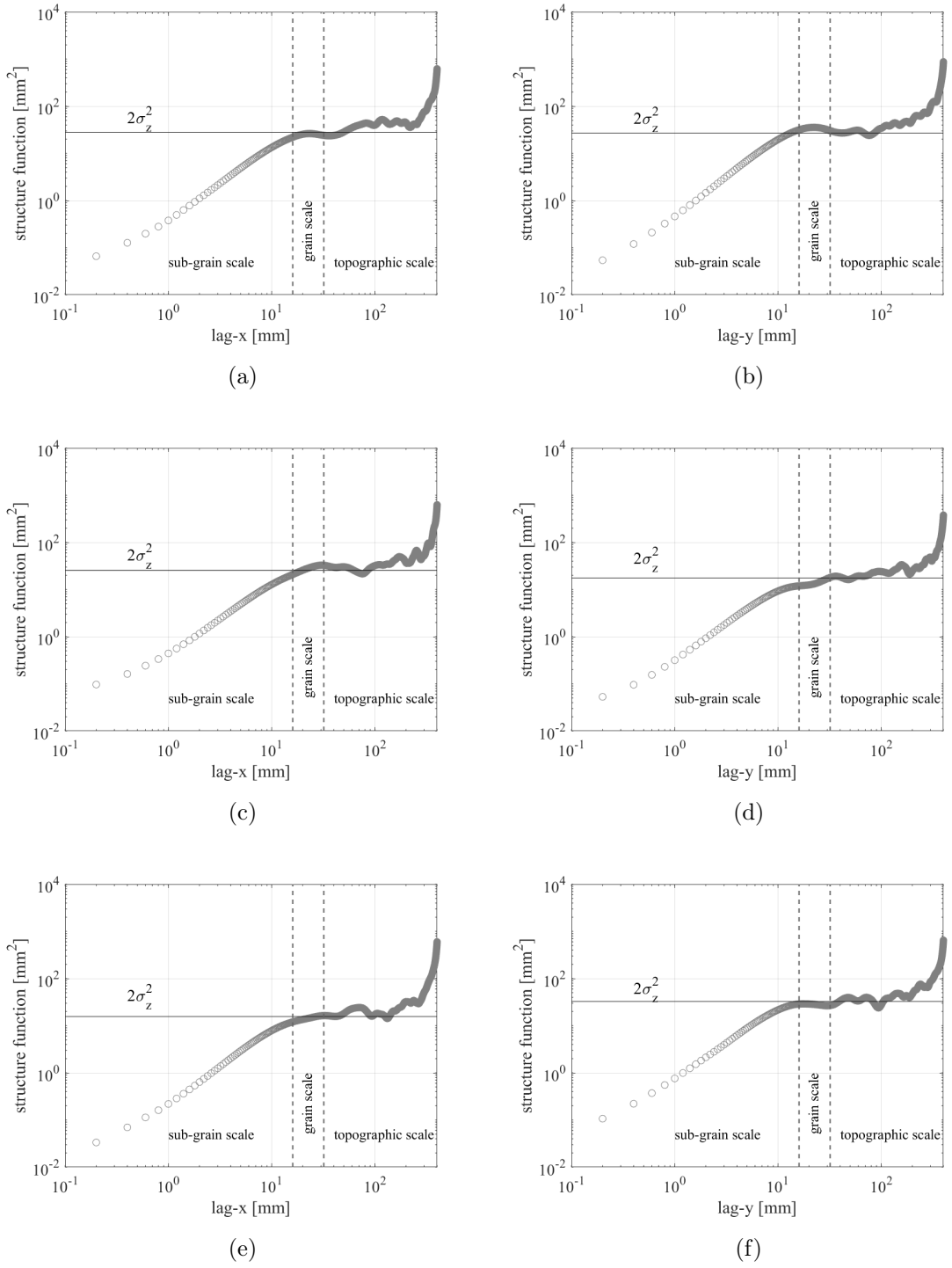

Figure 4.10: One-dimensional structure function (Nikora et al., 1998) applied on bottom surface elevation, profiles along current direction (a, b, c) and wave direction (d, e, f). Right side profiles (a, b); central profile (b, c), left side profile (e, f).

The loss of correlation within the grain scale shows that the grains are randomly clustered, and this seems to occur in a very similar way for all the examined profiles in the two examined directions. This result suggests that no 'bedform' or geometrical pattern were formed during the realization of the rough panels, or at least not within the examined spatial scale and direction.

Previous studies of wave-current over rough beds mostly employed uniform roughness elements, such as semispheres or marbles (Yuan and Madsen, 2014; Lim and Madsen, 2016). A concern about the use of non-uniform grains in our experiments then arised, in the sense that the measured flow characteristics could be highly dependant on the position where the velocity instrument is deployed. Nevertheless, this result seems to suggest that the grains are packed in a sufficiently random way, and that the choice of the positioning of the ADV should not make substantial differences on the resultant velocity profile. Small local differences which are dependant on the position of the velocity measurement can anyway be filtered out by means of space-averaging, as explained in the following Section.

4.3 Mean flow analysis

In spatially non-homogeneous rough flows, mean and turbulent fields are strictly related to the location of the measurement point. Nevertheless, flow near a rough boundary can be made globally homogeneous by means of space averaging, which allows to characterize flow dynamics through its spatially averaged properties.

The idea of space averaging in hydraulics was introduced by Smith and McLean (1977), who averaged open-channel flow velocities measured along a line over a fixed ripples bed. Wilson and Shaw (1977) developed a methodology based on spatially averaged equations for atmospheric flow-canopies interaction. Other studies include Raupach and Shaw (1982), Finnigan (1985), Raupach et al. (1991) who derived new equations for atmospheric boundary layer. Giménez-Curto and Lera (1996) applied a analogous approach in oscillatory turbulent flows over very rough bottoms. Space averaging in open-channel rough flows is relatively recent. Nikora et al. (2001) obtained continuity and momentum equations by double averaging Navier-Stokes equations, providing a link between space-averaged roughness

parameters and double-averaged flow quantities. A physical interpretation of space-averaged Reynolds stress terms has been carried out by Pokrajac et al. (2008).

In the present work, the time-averaged velocities $\bar{u}$, $\bar{v}$ and $\bar{w}$, obtained by time-averaging the instantaneous velocities measured by all the ADVs, have been averaged in order to obtain time- and space-averaged $\langle\bar{u}\rangle$, $\langle\bar{v}\rangle$ and $\langle\bar{w}\rangle$. The procedure of averaging by time and space is referred in the text as double-averaging. The double-averaging is performed in order to filter out the heterogeneous flow characteristics that belongs to the specific position of the ADV, in order to consider only the flow characteristics common to all the measurement points. The space averaging consists of averaging $\bar{u}$, $\bar{v}$ or $\bar{w}$ measured by each ADV at a specific measurement point, the values in between the measured points are obtained by linear interpolation with a vertical step Δz of 0.001 m. In the following plots only the double-averaged values at the measurement positions are shown.

Significant dimensional and nondimensional parameters have been computed to characterize the flow field. Current freestream velocity has been computed by depth averaging the double-averaged current velocities above the expected current boundary layer upper limit ($z = 0.3h$). Wave orbital velocity has been computed by considering the phase-averaged velocity maximums at the first measurement point above the wave boundary layer thickness. According to Fredsøe (1984), the expected wave boundary layer thickness in rough flows depends on the relative wave orbital amplitude A_{bm}/k, where the k is the bottom roughness. Once the expected wave boundary layer thickness is computed, the wave orbital velocity is measured considering the lowest measurement point above the wave boundary layer thickness in the crest velocity profile. The individuation of the measurement point where to compute has been also aided by graphical considerations on the crest velocity profile, to more easily identify the potential flow region. Then, the orbital velocities measured by each ADV have been averaged in order to obtain space-averaged orbital velocity U_w.

Once U_c and U_w are obtained, current and wave Reynolds numbers have been computed by the following;

$$Re_c = \frac{U_c h}{\nu}; \qquad Re_w = \frac{U_w A_{bm}}{\nu}; \tag{4.2}$$

where a is the wave orbital amplitude ($= U_w/\omega$). A nondimensional wave-current

Table 4.4: Dimensional and nondimensional parameters for the WINGS campaign Runs over sand bed: target current velocity U, wave height H, wave period T, current Reynolds number Re_c, wave Reynolds number Re_w, freestream current velocity U_c, orbital velocity U_w, wave-current regime parameter U_w/U_c.

Run	Bed	Type	U [m/s]	H [m]	T [s]	U_c [m/s]	U_w [m/s]	U_w/U_c	Re_c	Re_w
1	SB	CO	0.210	-	-	0.226	-	-	90225	-
2	SB	WO	-	0.18	2	-	0.412	-	-	54031
3	SB	WO	-	0.12	2	-	0.325	-	-	33621
4	SB	WO	-	0.08	2	-	0.218	-	-	15127
5	SB	WO	-	0.08	1	-	0.124	-	-	2447
6	SB	WC	0.210	0.18	2	0.237	0.387	1.63	94814	47645
7	SB	WC	0.210	0.12	2	0.242	0.319	1.32	96923	32350
8	SB	WC	0.210	0.08	2	0.239	0.203	0.85	95520	13066
9	SB	WC	0.210	0.08	1	0.223	0.107	0.48	89255	1819
10	SB	CO	0.140	-	-	0.15	-	-	89726	-
11	SB	WC	0.140	0.08	2	0.152	0.146	0.96	91031	6791
12	SB	WC	0.140	0.12	2	0.157	0.219	1.39	94366	15236
13	SB	WC	0.140	0.18	2	0.159	0.313	1.97	95497	31276
14	SB	WC	0.140	0.08	1	0.137	0.053	0.39	81921	454
15	SB	WO	-	0.08	2	-	0.145	-	-	6696
16	SB	WO	-	0.08	1	-	0.041	-	-	270
17	SB	WO	-	0.12	2	-	0.212	-	-	14315
18	SB	WO	-	0.18	2	-	0.33	-	-	34713

regime parameter U_w/U_c has been computed as an indicator of the relative importance of the waves compared to the current. Moreover, the wave-current parameter is used to distinguish two wave-current regimes: the current-dominated regime ($U_w/U_c < 1$) and the wave-dominated regime ($U_w/U_c > 1$). This is done in order to be consistent with literature (Lodahl et al., 1998) and facilitate the comparison. A range of dimensional quantities and parameters for each run is listed in Table 4.4 (runs over sand bed) and Table 4.5 (runs over gravel bed).

The wave-current parameter U_w/U_c for all the WO and WC runs are plotted against the relative wave amplitude a/d_{50} in Figure 4.11.

Table 4.5: Dimensional and nondimensional parameters for the WINGS campaign runs over gravel bed: target current velocity U, wave height H, wave period T, current Reynolds number Re_c, wave Reynolds number Re_w, freestream current velocity U_c, orbital velocity U_w, wave-current regime parameter U_w/U_c.

Run	Bed	Type	U [m/s]	H [m]	T [s]	U_c [m/s]	U_w [m/s]	U_w/U_c	Re_c	Re_w
19	GB	CO	0.140	-	-	0.142	-	-	85063	-
20	GB	WC	0.140	0.05	1	0.146	0.027	0.19	87437	118
21	GB	WC	0.140	0.08	1	0.153	0.052	0.34	91973	425
22	GB	WC	0.140	0.08	2	0.144	0.147	1.02	86552	6900
23	GB	WC	0.140	0.12	2	0.168	0.218	1.30	100873	15136
24	GB	WO	-	0.05	1	-	0.042	-	-	281
25	GB	WO	-	0.08	1	-	0.061	-	-	592
26	GB	WO	-	0.08	2	-	0.143	-	-	6509
27	GB	WO	-	0.12	2	-	0.233	-	-	17281
28	GB	WC	0.210	0.05	1	0.246	0.058	0.24	98286	534
29	GB	WO	-	0.08	2	-	0.199	-	-	12605
30	GB	WO	-	0.08	1	-	0.116	-	-	2142
31	GB	WO	-	0.05	1	-	0.061	-	-	592
32	GB	CO	0.210	-	-	0.245	-	-	97957	-
33	GB	WC	0.210	0.08	2	0.281	0.186	0.66	112209	11002
34	GB	WC	0.210	0.12	2	0.28	0.293	1.05	111937	27253
35	GB	WC	0.210	0.08	1	0.262	0.11	0.42	104742	1915
36	GB	WO	-	0.12	2	-	0.259	-	-	21290

Current shear velocity (also referred as friction velocity) u^* and equivalent roughness k_s have been computed by best fit technique (Sumer, 2007). Such technique assumes that the shear velocity and equivalent roughness of a steady, fully developed boundary layer flow can be inferred by linear fitting the velocity profile in a certain region of the boundary layer, known as the logarithmic layer. The best fit procedure is different depending if the flow is hydraulically smooth, i.e. when the viscous sublayer thickness is larger than the bed grain size, or is hydraulically rough, when the viscous sublayer is destroyed as the grains are fairly larger than the supposed thickness of the viscous. In hydraulically smooth flow, the velocity profile in the logarithmic region follows the law of the wall

$$\frac{u}{u^*} = \frac{1}{\kappa} log(\frac{zu^*}{\nu}) + 5.0 \tag{4.3}$$

where κ is the von Karman constant ($= 0.4$).

In hydraulically rough flow, the near-bed velocity distribution follows the following logarithmic law:

$$\frac{u}{u^*} = \frac{1}{\kappa} \ln \frac{z}{z_o} \tag{4.4}$$

where $z_0 = k_s/30$, where k_s is the equivalent roughness. Shear velocity is obtained from the slope of the linear fitting of u and $\log z$, whereas k_s is obtained through its intercept. However, an hypothesis on the position of the theoretical bottom must be done. The procedure again follows the one suggested by Sumer (2007), which consists of the following steps. The first step is to make a series of hypothesis on the position of the theoretical bottom. According to Sumer (2007), the theoretical bottom should lie between $0.15 \div 0.30$ of the physical roughness from the top of the grain.

The second step is to plot the current velocity profile and distance from the bottom z in a semi-logarithmic plane, considering all the hypothetical positions of the theoretical bottom. Therefore here, an attempt to find the theoretical bottom is done by adding 0.05, 0.10, 0.15, 0.20, 0.25, 0.35, 0.4 of d_{50} to z. An example of the theoretical bottom position analysis for Run 32 (CO, GB, $U = 0.210$ m/s) is shown in Figure 4.12. A first attempt in looking for the logarithmic layer, as suggested

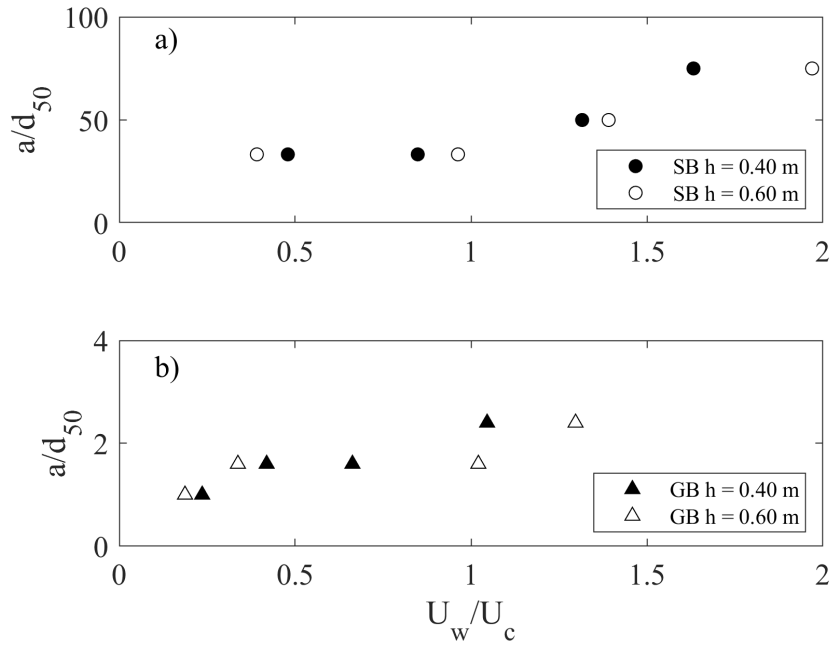

Figure 4.11: Wave-current regime parameter U_w/U_c versus the relative wave amplitude a/d_{50}: (a) sand bed, (b) gravel bed.

by Sumer, should be done below $0.1 \div 0.3\ h$. Between the hypotized profiles, the theoretical bottom position that ensures the larger logarithmic layer is chosen.

The third step is to proceed with a linear fitting of the points in the logarithmic layer and compute the slope α and intercept β, from which u^* ($= \kappa/\alpha$, where κ is the Von Karman constant) and k_s ($= 30 \exp \beta$) are obtained.

The fourth step, once the shear velocity is obtained, is to plot the velocity profile in wall units u^+ and z^+. Then a check of the limits of the chosen logarithmic profile is performed. For hydraulically rough flow, the logarithmic profile should lie between $0.2k_s^+$ and $0.3h^+$. Moreover, a check if the profile matches with theoretical profiles, i.e. the Van Driest profile and the logarithmic law is performed. If all these checks pass, the points are chosen as belonging to the logarithmic profile and u^* and k_s are kept as final, otherwise points are eventually removed or added until all the checks pass.

The computation of the shear velocity and related quantities are subject to some uncertainty. Especially k_s may be very different depending on the measurement chosen to be part of the logarithmic profile linear fitting. A 95% confidence interval for the slope is computed in order to assess the range of uncertainty of the slope

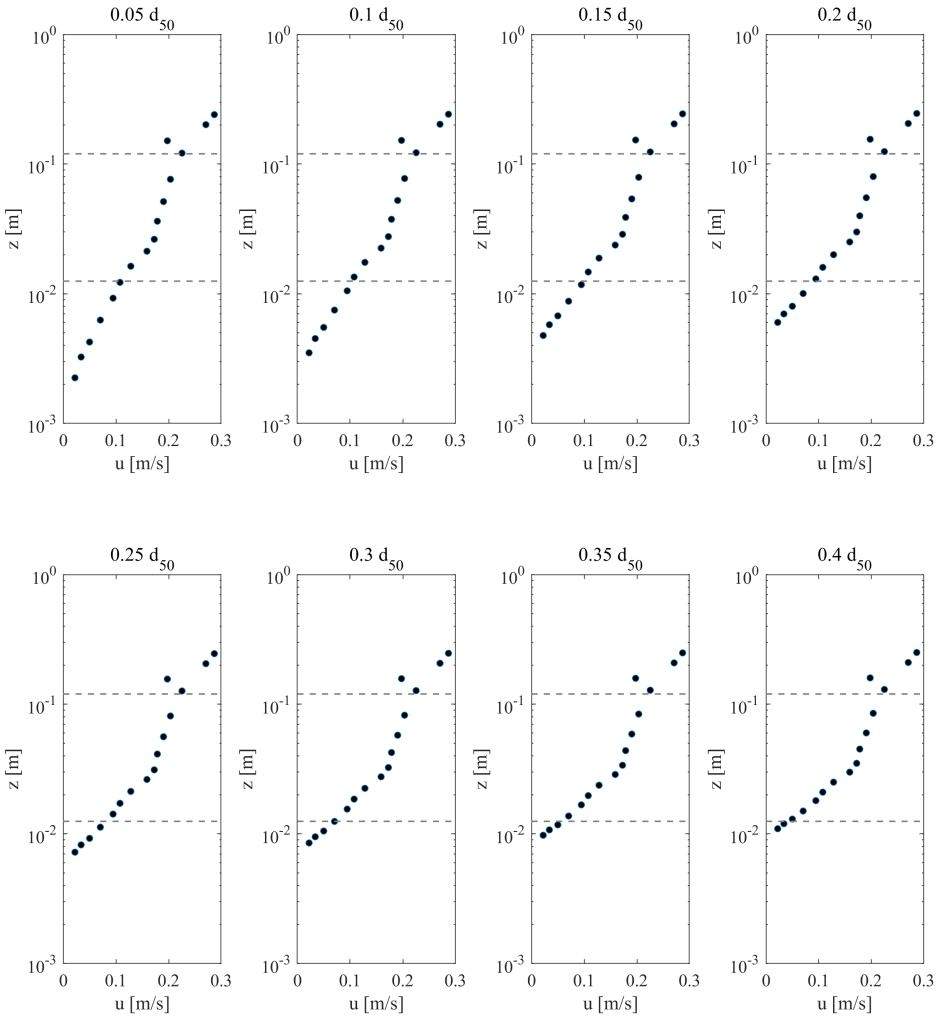

Figure 4.12: Example of the procedure to detect the theoretical bottom for Run 32 (CO, GB, $U = 0.210$ m/s) with different fractions of the grain diameter d_{50} as distance from the top of the grain. The dashed lines are the lower ($z = 0.2k_s$) and upper ($z = 0.3h$) limits of the logarithmic layer suggested by Sumer (2007)

is computed by means of a t-student distribution. Same has been done for the k_s. From the shear velocity the Reynolds shear number has been computed, following the relation

$$Re^* = \frac{u^* d_{50}}{\nu}; \tag{4.5}$$

Table 4.6 shows u^*, k_s alongside their confidence interval values for all CO and WC runs. Confidence interval for u^* is in the average 12% with a maximum of 28% for Run 32.

Table 4.6: Quantities obtained through best fit procedure (Sumer, 2007): shear velocity u^*, equivalent roughness k_s and Reynolds shear number Re^*. Confidence intervals for u^* and k_s are also reported.

Run	u^* [m/s]	k_s [m]	Re^*
1	0.0109 ± 0.0009	0.0004 ± 0.0001	13
6	0.0128 ± 0.0021	0.0029 ± 0.0011	17
7	0.0115 ± 0.0015	0.0012 ± 0.0004	15
8	0.0124 ± 0.0013	0.0022 ± 0.0006	15
9	0.0120 ± 0.0014	0.0022 ± 0.0006	14
10	0.0100 ± 0.0012	0.0141 ± 0.0034	12
11	0.0066 ± 0.0014	0.0008 ± 0.0005	8
12	0.0071 ± 0.0011	0.0011 ± 0.0005	9
13	0.0081 ± 0.0008	0.0027 ± 0.0007	10
14	0.0055 ± 0.0014	0.0003 ± 0.0002	7
19	0.0159 ± 0.0034	0.1418 ± 0.0372	398
20	0.0152 ± 0.0015	0.1299 ± 0.0161	381
21	0.0169 ± 0.0020	0.1535 ± 0.0219	421
22	0.0156 ± 0.0018	0.1316 ± 0.0183	390
23	0.0150 ± 0.0014	0.0900 ± 0.0118	375
28	0.0265 ± 0.0054	0.1006 ± 0.0214	662
32	0.0242 ± 0.0070	0.0645 ± 0.0212	606
33	0.0284 ± 0.0024	0.0877 ± 0.0072	710
34	0.0286 ± 0.0013	0.0844 ± 0.0036	716
35	0.0273 ± 0.0031	0.0698 ± 0.0072	682

4.3.1 Current only

In the present section the results for the experiments in current-alone conditions are presented. As a remainder, the main symbols and acronyms used in the following paragraphs are here recalled:

U	Nominal current velocity
U_c	Freestream current velocity
U_w	Wave orbital velocity
H	Wave height
T	Wave period
CO	Current Only
WO	Wave only
WC	Waves plus current
SB	Sand bed
GB	Gravel bed

Figure 4.13 shows the dimensionless double-averaged velocity profiles in the current direction $\langle\bar{u}\rangle/U_c$ (black line), along with the dimensionless time-averaged profiles $\bar{u}/U_c$ (markers) for every ADV from which the space average is obtained. Figure 4.13 shows also the standard deviation of the current turbulent velocity u' for each time-averaged velocity (grey error bars), which is an indicator of the intensity of the turbulent velocity fluctuation. Turbulent fluctuations are obtained by means of Reynolds averaging:

$$u = \bar{u} + \tilde{u} + u' \tag{4.6}$$

All quantities are made dimensionless by dividing by the freestream velocity U_c. Standard deviation of the turbulent fluctuation is also referred in the following as "time variability" of the current velocity, whereas the difference between the time-averaged and double-averaged velocities in absolute value, at a specific bed distance z and divided by U_c, is referred in the text as the "space variability" of the current velocity profile: $\frac{|\langle\bar{u}(z)\rangle-\bar{u}(z)|}{U_c}$. The double-averaged profile of Figure 4.13 have an average space variability of 0.04 with a maximum of 0.18. The error bars

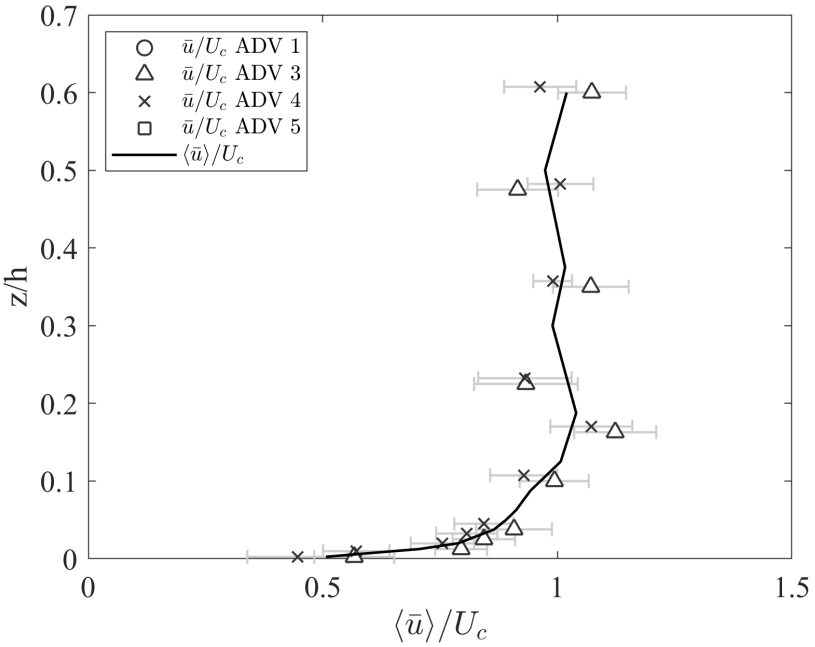

Figure 4.13: Dimensionless time-averaged $\bar{u}/U_c$ (markers) for every ADV and double-averaged $\langle\bar{u}\rangle/U_c$ (line) velocity profiles for Run 1 (CO, SB, $U = 0.210$ m/s).

show that the double-averaged profile is always within the time variability range of all the ADVs, which is 0.06 (depth-averaged).

Figure 4.14 shows the double-averaged $\langle\bar{u}\rangle/U_c$ velocity profile in wall units for Run 1 over sand bed (CO, SB, $U = 0.210$ m/s) and the Van Driest theoretical profile. Experimental measurements used for the linear fitting are highlighted in Figure with a grey marker face. The experimental velocity profile fits well with the Van Driest theoretical profile, showing that the flow is close to hydraulically smooth condition. The equivalent roughness in wall units $k_s^+ = k_s u^*/\nu$ is 4, therefore within the range of hydraulically smooth flow ($k_s^+ < 5$).

Figure 4.15 shows the time- and double-averaged velocity profiles Run 32 (CO, GB, $U = 0.210$ m/s). The depth-averaged space variability is 0.08, with maximum of 0.24. In comparison with Figure 4.13, results in Figure 4.15 show a larger time variability of the fluctuating velocities (0.12). The presence of the gravel bed enhances turbulent fluctuations in proximity of the wall, and leads to an increase in bottom resistance ($u^* = 0.0109$ m/s for Run 1, $u^* = 0.0242$ m/s for Run 32), compensated by an increase of the freestream velocity ($U_c = 0.226$ m/s for Run 1, $U_c = 0.245$ m/s for Run 32).

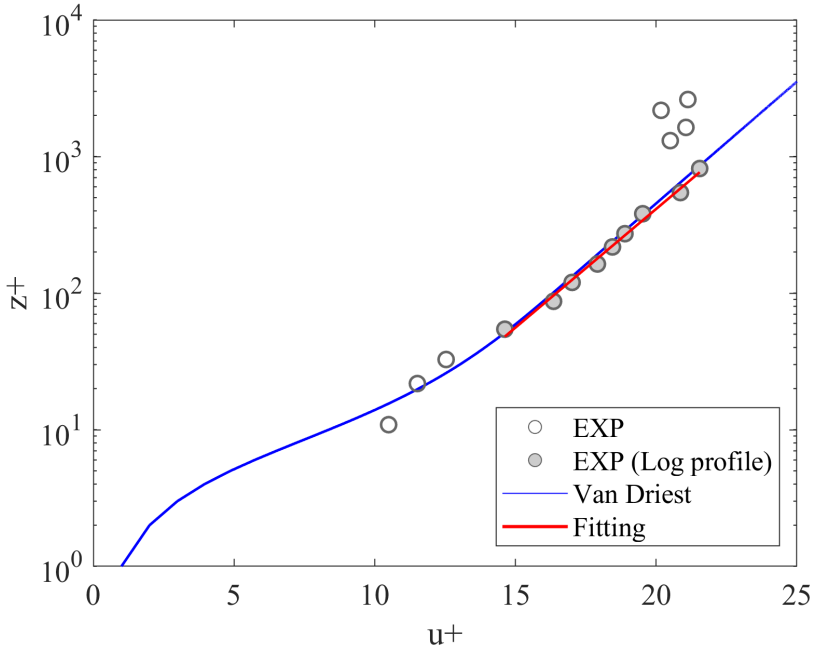

Figure 4.14: Double-averaged $\langle\bar{u}\rangle/U_c$ velocity profile in wall units for Run 1 (CO, SB, $U = 0.210$ m/s). Van Driest profile and fitting in the logarithmic layer are plotted aswell. Velocities used for the best fit are highlighted in grey.

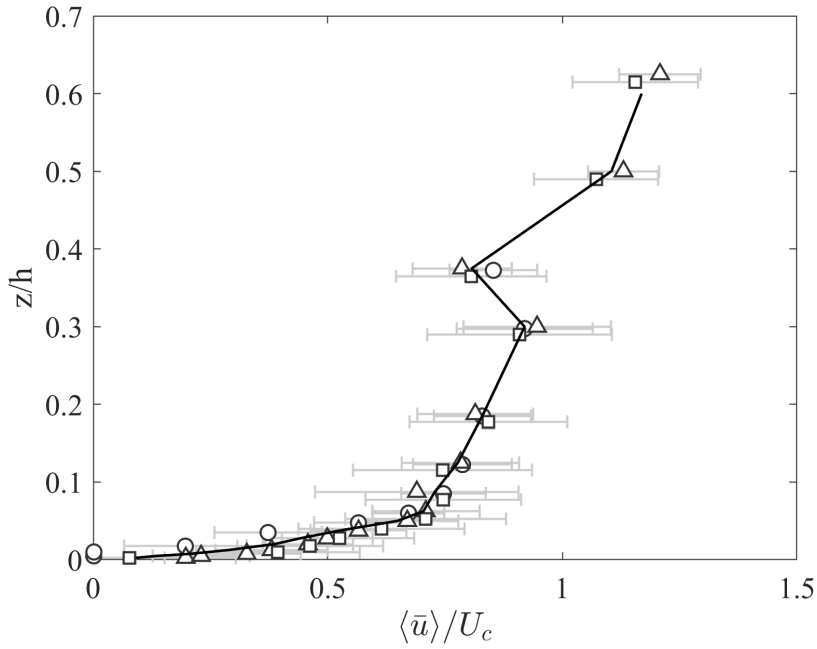

Figure 4.15: Dimensionless time-averaged $\bar{u}/U_c$ (markers) and double-averaged $\langle\bar{u}\rangle/U_c$ (line) velocity profiles for Run 32 (CO, GB, $U = 0.210$ m/s).

Figure 4.16 shows the double-averaged $\langle \bar{u} \rangle / U_c$ velocity profile in wall units for Run 32 (CO, GB, $U = 0.210$ m/s) and the Van Driest theoretical profile. The

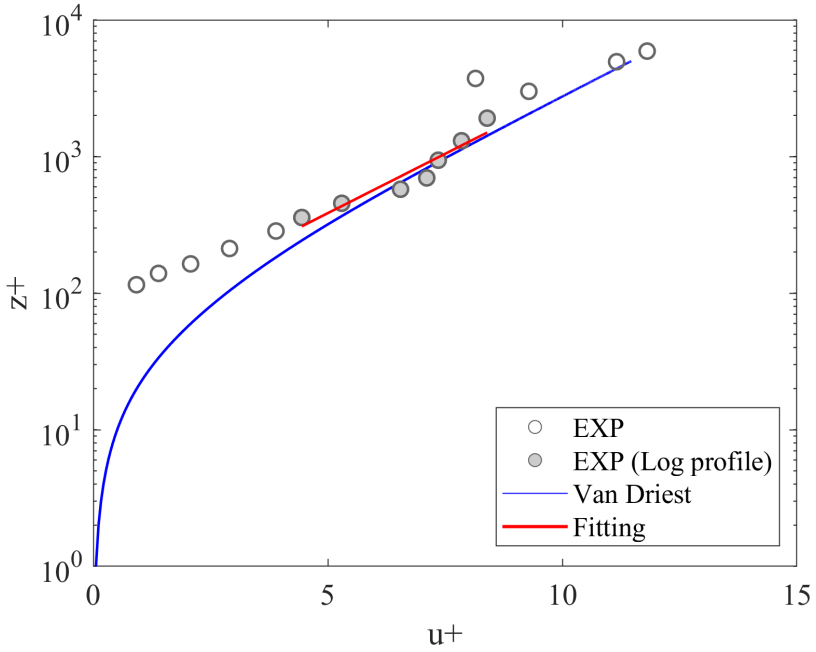

Figure 4.16: Double-averaged $\langle \bar{u} \rangle / U_c$ (circles) velocity profile in wall units for Run 32 (CO, GB, $U = 0.210$ m/s). Van Driest profile and fitting in the logarithmic layer are plotted aswell. Velocities used for the best fit are highlighted (grey circles).

theoretical bottom, found via the Sumer (2007) best fit method, explained in Section 4.2, has been found to be $0.15 d_{50}$. The best fit procedure show a value of the equivalent roughness k_s of 0.645 m, correspondent approximately to 2.5 d_{50}, which is in agreement with many studies of the equivalent roughness over gravel bed. The experimental velocity profile fits fairly well with both the Van Driest theoretical profile and the logarithmic law along the whole logarithmic layer, which suggests that the boundary layer is fully developed.

Figure 4.17 shows the dimensionless double-averaged velocity profiles in the wave direction $\langle \bar{v} \rangle / U_c$, along with the dimensionless time-averaged profiles $\bar{v}/U_c$ from which the space average is obtained, for Run 1 (CO, SB) and 32 (CO, GB). Both figures show the presence of a residual current in the y direction, showing that the current is not perfectly orthogonal. The depth-averaged freestream velocity in the wave direction is 0.0306 m/s (SB) for Run 1 and 0.0402 m/s for Run 32 (GB), which correspond to 0.14 and 0.16 of the respective U_c.

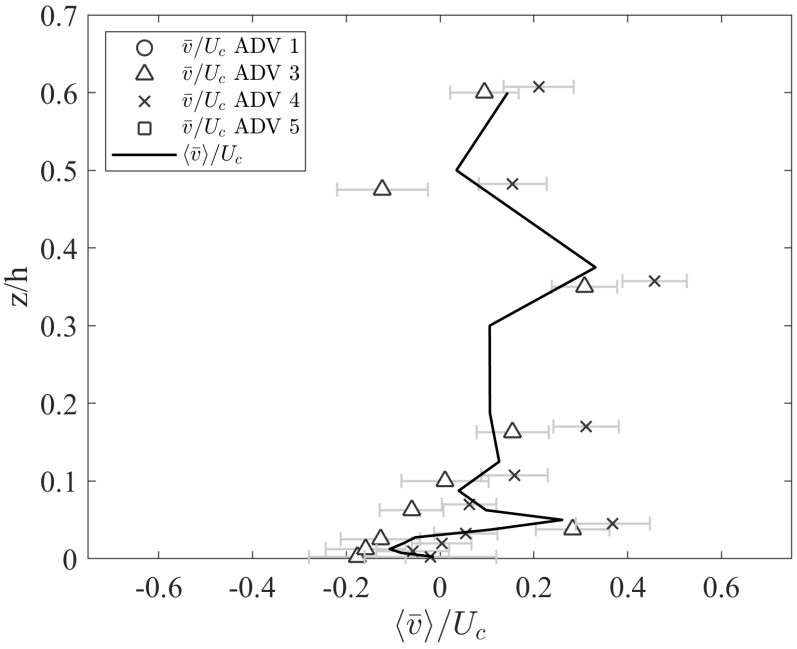

(a)

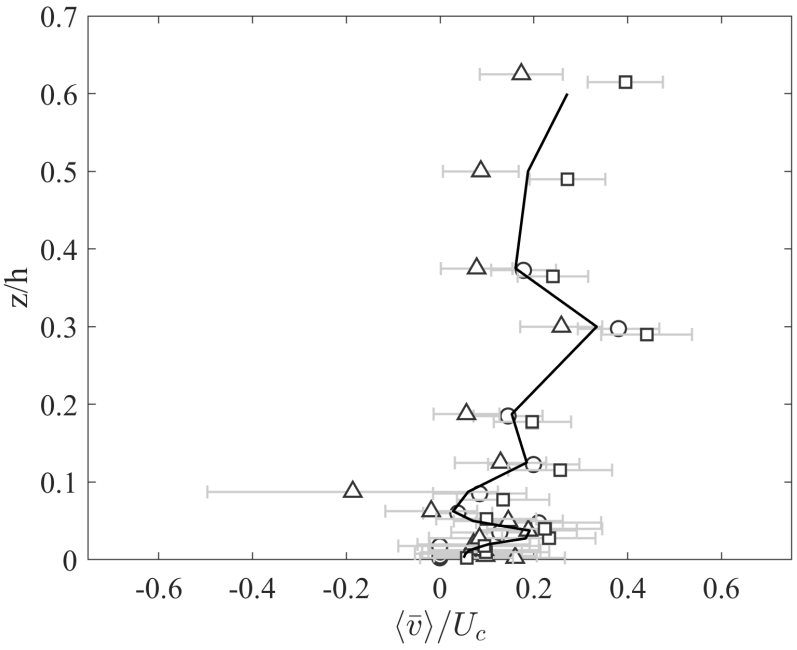

(b)

Figure 4.17: Dimensionless time-averaged $\bar{v}/U_c$ (markers) and double-averaged $\langle\bar{v}\rangle/U_c$ (line) current velocity profiles: (a) Run 1, CO, SB; (b) Run 32, CO, GB.

Time- and double-averaged velocity profiles have been computed also for CO runs with $U = 0.140$ m/s ($h = 0.60$ m), shown in Figure 4.16(a) and (b) for Run 10 (CO, SB) and Run 19 (CO, GB) respectively.

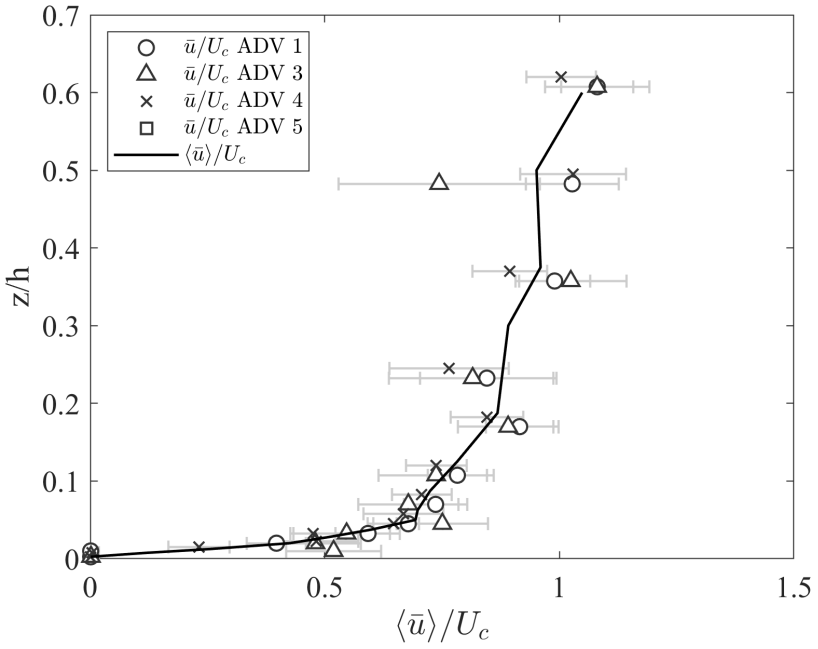

(a)

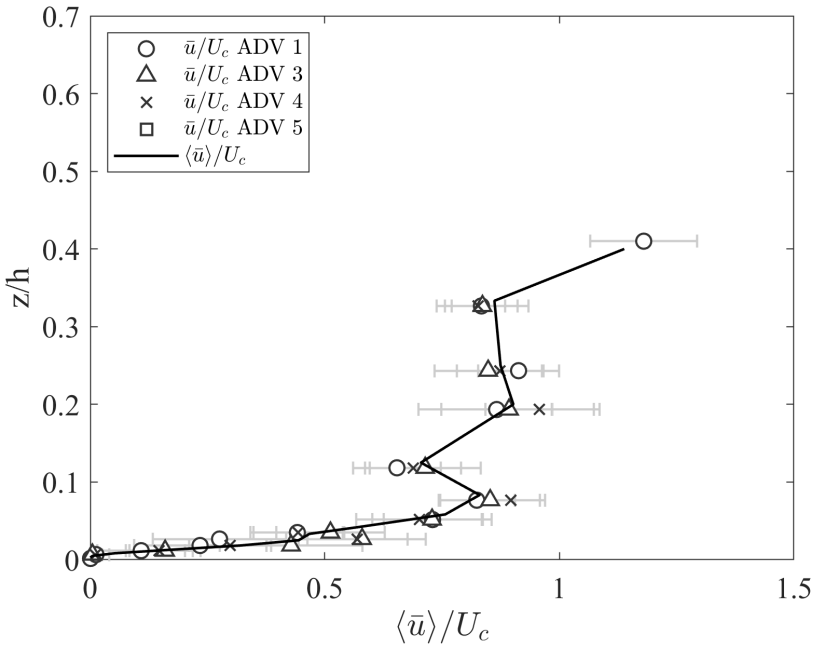

(b)

Figure 4.18: Dimensionless time-averaged $\bar{u}/U_c$ (markers) and double-averaged $\langle\bar{u}\rangle/U_c$ (line) current velocity profiles with $U = 0.140$ m: (a) Run 10 (CO, SB); (b) Run 19 (CO, GB).

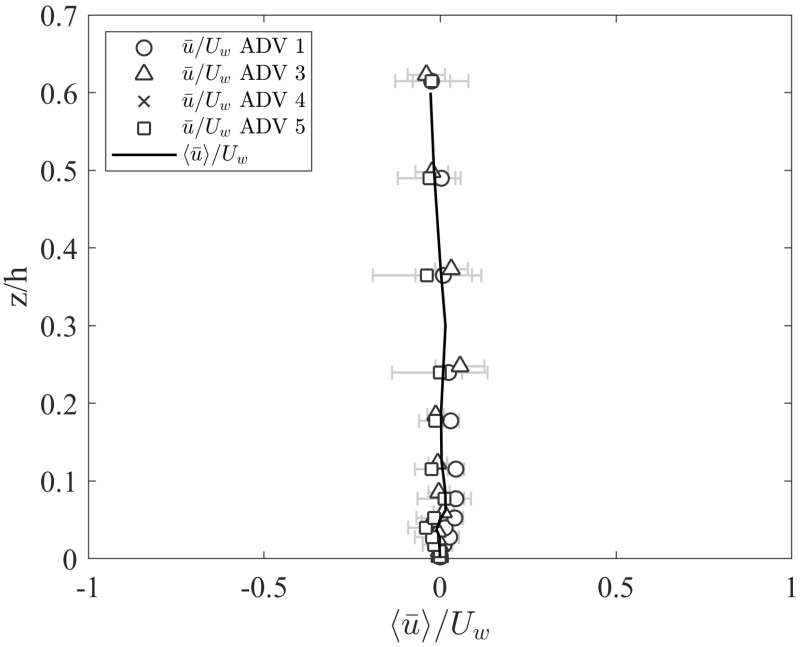

Figure 4.19: Dimensionless time-averaged $\bar{u}/U_w$ (markers) and double-averaged $\langle\bar{u}\rangle/U_w$ (line) current velocity profiles for Run 3 (WO, SB, $H = 0.12$ m, $T = 2.0$ s).

4.3.2 Wave only

In the following subsection a brief analysis of the velocity profiles for the wave-alone experiments is shown. Figure 4.19 shows the time- and double-averaged velocity profiles for Run 3 (WO, SB, $H = 0.12$ m, $T = 2.0$ s), thus over sand bed, whereas Figure 4.20 shows the time- and double-averaged velocity profiles for Run 29 (WO, GB, $H = 0.08$ m, $T = 2.0$ s).

The depth-averaged time-variability, expressed in this case as a percentage of U_w, for Run 3 ($U_w = 0.325$ m/s) is 0.01 with a maximum of 0.05, whereas it is 0.12 with a maximum of 0.25 for Run 29 ($U_w = 0.199$ m/s), over gravel bed. The comparison between Figures 4.19 and 4.20 shows that the increase in variability is one order of magnitude larger in presence of the gravel bottom, as already observed in the current only runs analysis.

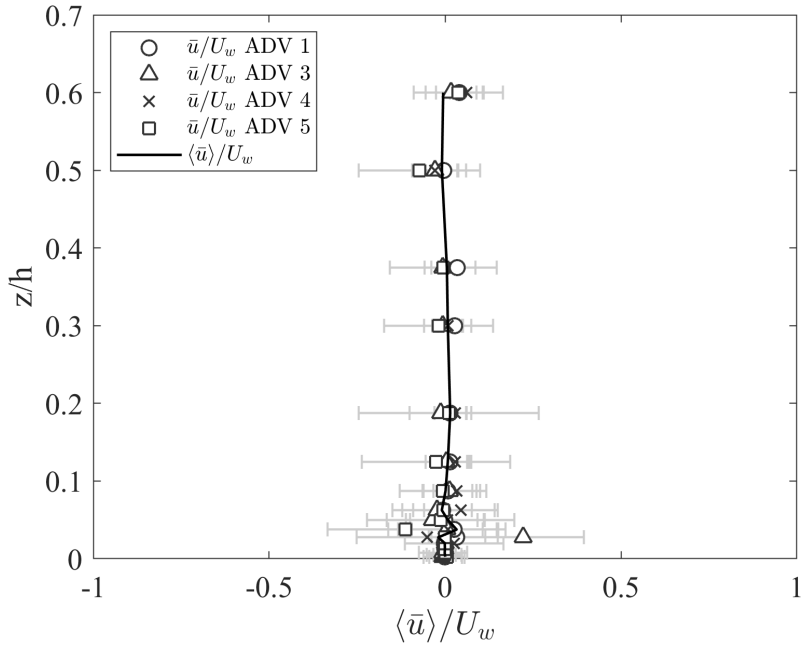

Figure 4.20: Dimensionless time-averaged $\bar{u}/U_w$ (markers) and double-averaged $\langle\bar{u}\rangle/U_w$ (line) current velocity profiles for Run 29 (WO, GB, $H = 0.08$ m, $T = 2.0$ s).

4.3.3 Waves plus current

In the present Section, the analysis of the WC mean velocity profiles is reported. Figure 4.21 shows the time- and double-averaged velocity profiles for Run 8 (WC, SB, $U = 0.210$ m/s, $h = 0.40$ m, $H = 0.08$ m, $T = 2.0$ s). The depth-averaged space variability is 0.04 with a maximum of 0.18. In comparison with the correspondent CO case (Run 1) shown in Figure 4.13, presence of waves seems to determine a larger turbulent fluctuation, corresponding to a depth-averaged value of 0.08 of the freestream velocity U_c, in comparison with a 0.06 of Run 1. Moreover, the superposition of waves seems to determine an increase in bottom resistance, shown by a decrease in velocity in the boundary layer (below $z = 0.3h$) and an increase of velocity in the freestream, with an increase of U_c from 0.226 m/s of Run 1 to 0.239 m/s for Run 8.

Figure 4.22 shows the time- and double-averaged velocity profiles for Run 6 (WC, SB, $U = 0.210$ m/s, $H = 0.18$ m, $T = 2.0$ s). This case is similar to Run 8, but with an increased wave height ($H = 0.18$ m). The presence of the waves determine a slight increase of the fluctuating velocities variability, reaching 0.07 of

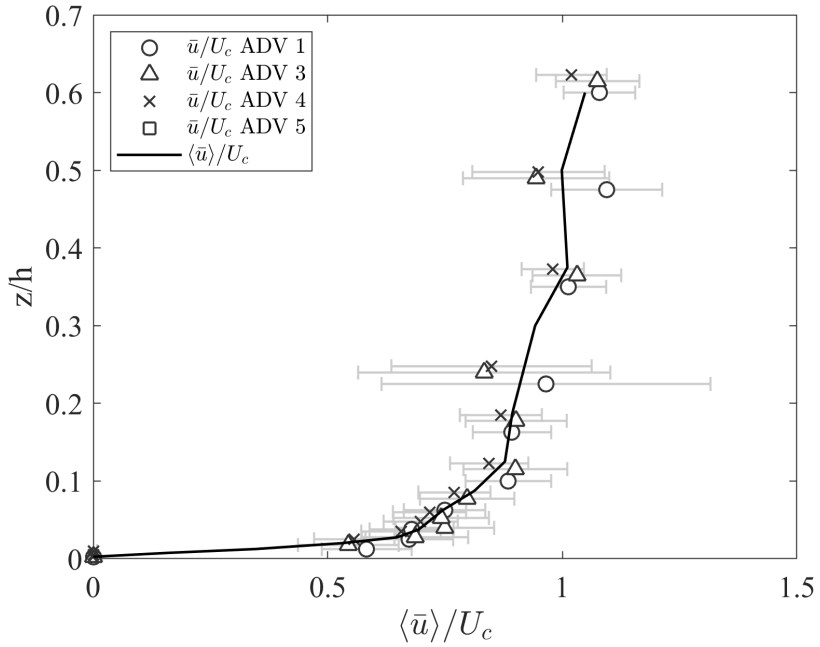

Figure 4.21: Dimensionless time-averaged $\bar{u}/U_c$ (markers) and double-averaged $\langle\bar{u}\rangle/U_c$ (line) velocity profiles for Run 8 (WC, SB, $U = 0.210$ m/s, $H = 0.08$ m, $T = 2.0$ s)

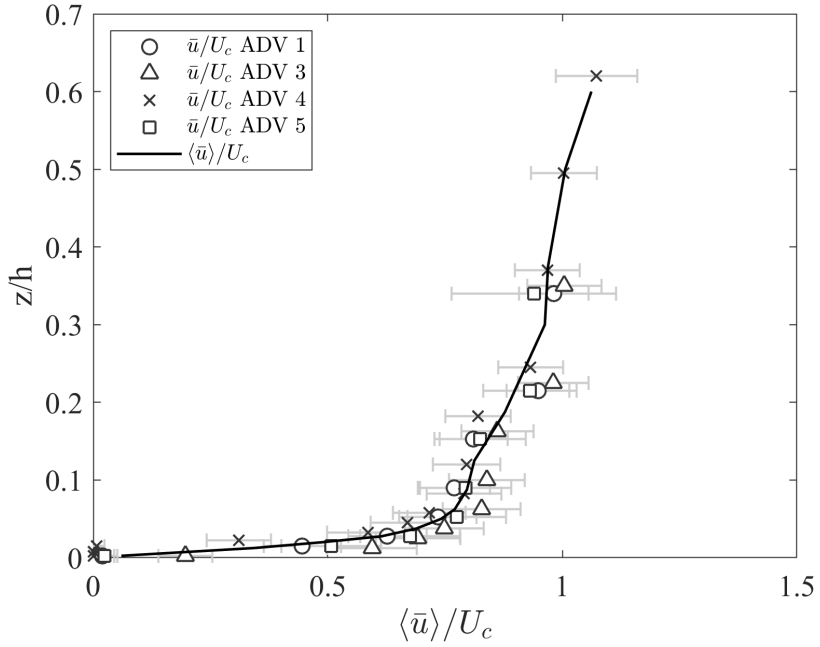

Figure 4.22: Dimensionless time-averaged $\bar{u}/U_c$ (markers) and double-averaged $\langle\bar{u}\rangle/U_c$ (line) velocity profiles for Run 6 (WC, SB, $U = 0.210$ m/s, $H = 0.18$ m, $T = 2.0$ s).

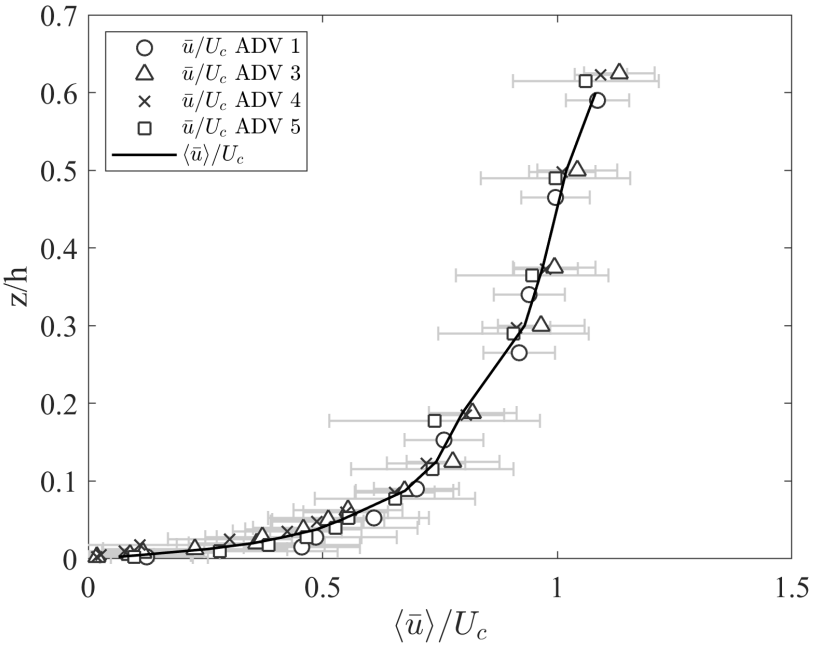

Figure 4.23: Dimensionless time-averaged $\bar{u}/U_c$ (markers) and double-averaged $\langle\bar{u}\rangle/U_c$ (line) velocity profiles for Run 33 (WC, GB, $U = 0.210$ m/s, $H = 0.08$ m, $T = 2.0$ s).

U_c, which however is slightly lower than the smaller wave case of Run 8. Freestream velocity in this case is equal to 0.237 m/s, very close to the 0.239 m/s of Run 8, but still higher than the corresponding CO case (0.226 m/s).

Figure 4.23 shows the time- and double-averaged velocity profiles for Run 33 (WC, GB, $U = 0.210$ m/s, $H = 0.08$ m, $T = 2.0$ s). The case has the same wave conditions of Run 8, but over gravel bed. The superposition of the oscillatory flow seems to determine an increase of bottom resistance experienced by the current and an increase of freestream velocity ($U_c = 0.245$ m/s for Run 32, $U_c = 0.281$ m/s for Run 33). In comparison with the CO and WC cases of Figures 4.13 and 4.21, the presence of waves in Run 33 does not seem to induce a visible increase in turbulent velocity depth-averaged variability (0.12 of U_c) in comparison with the correspondent CO case of Figure 4.15.

Figure 4.24 shows the time- and double-averaged velocity profiles for Run 34 (WC, GB, $U = 0.210$ m/s, $H = 0.12$ m, $T = 2.0$ s). Run 34 is similar to Run 33, except for a wave height, being $H = 0.12$ m rather than 0.08 m. Comparison between Run 33 and 34 shows very slight differences between the two cases, superposition of

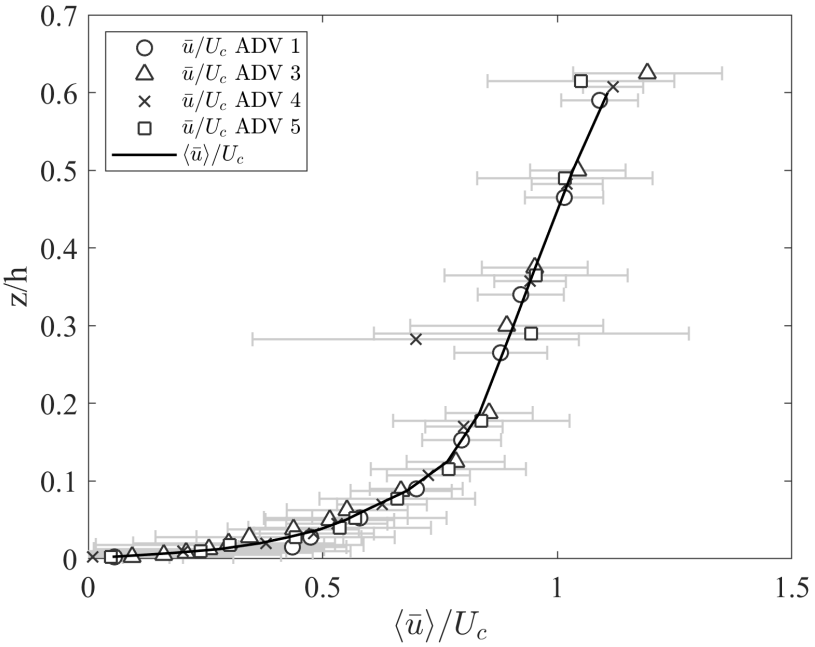

Figure 4.24: Dimensionless time-averaged $\bar{u}/U_c$ (markers) and double-averaged $\langle\bar{u}\rangle/U_c$ (line) velocity profiles for Run 34 (WC, GB, $U = 0.210$ m/s, $H = 0.12$ m, $T = 2.0$ s).

a larger wave determines a very similar value of U_c, which is 0.280 m/s in Run 33 and 0.281 m/s in Run 34.

Figure 4.25 shows the time- and double-averaged velocity profiles for Run 11 (WC, SB, $U = 0.140$ m/s, $H = 0.12$ m, $T = 2.0$ s). Superposition of the oscillatory flow in this case does not a determine a noticeable variation of U_c (0.152 m/s of Run 11, 0.150 m/s for the corresponding CO case of Run 10).

Figure 4.26 shows the time- and double-averaged velocity profiles for Run 22 (WC, GB, $U = 0.140$ m/s, $H = 0.12$ m, $T = 2.0$ s). In comparison with the CO case of Figure 4.18(b), a larger time variability of the fluctuating velocity shown by the error bars is observed. Analogously to the case with $U = 0.140$ m/s the superposition determines a slight variation of U_c (0.146 m/s for Run 22, 0.142 for Run 19).

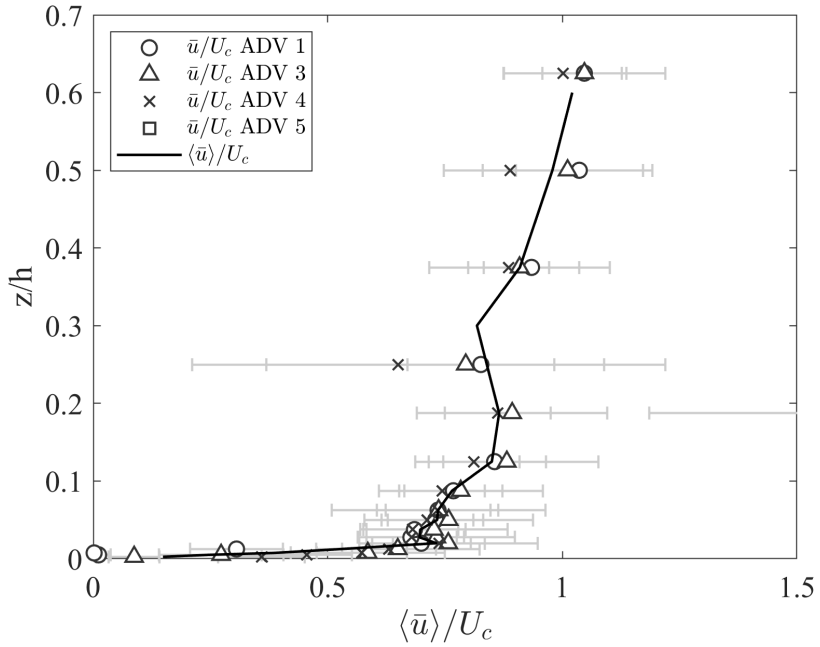

Figure 4.25: Dimensionless time-averaged $\bar{u}/U_c$ (markers) and double-averaged $\langle\bar{u}\rangle/U_c$ (line) velocity profiles for Run 11 (WC, SB, $U = 0.140$ m/s, $H = 0.08$ m, $T = 2.0$ s).

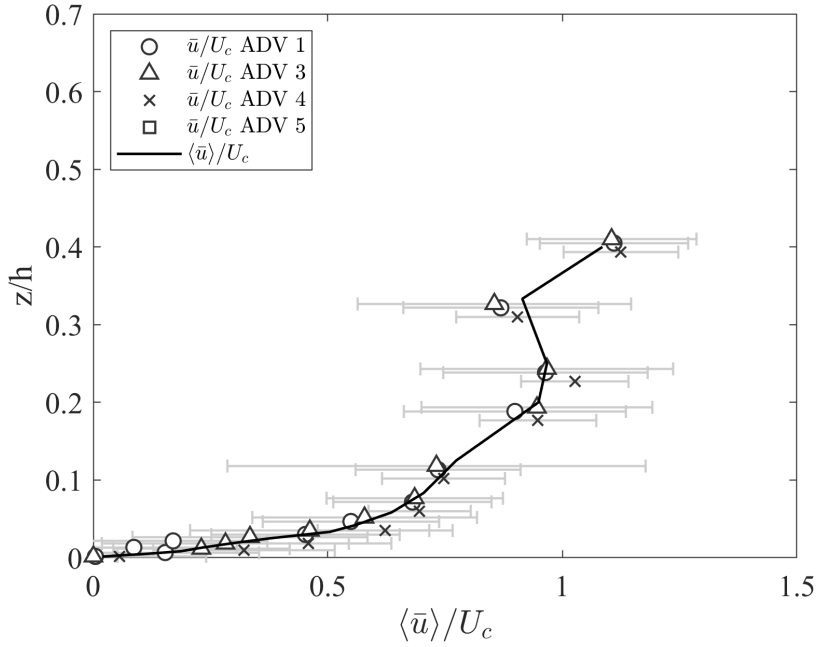

Figure 4.26: Dimensionless time-averaged $\bar{u}/U_c$ (markers) and double-averaged $\langle\bar{u}\rangle/U_c$ (line) velocity profiles for Run 22 (WC, GB, $U = 0.140$ m/s, $H = 0.08$ m, $T = 2.0$ s).

In order to investigate more closely the shear experienced by the current in proximity of the bed, the double-averaged profiles are analyzed specifically in the logarithmic layer region of the boundary layer.

Figure 4.27 shows a comparison between CO and WC dimensionless double-averaged velocity profiles, $\langle\bar{u}\rangle/U_c$ over sand bed with $U = 0.210$ m/s in wall distance units z^+. The lines denote the linear fitting used for the computation of u^* and k_s.

Figure 4.27(b), which reports a comparison between Runs 1 (CO) and 6 (WC, $H = 0.18$ m, $T = 2.0$), shows the same comparison but between Runs 1 (CO) and 6 (WC, $H = 0.12$ m, $T = 2.0$ s, a), thus with a larger wave height. Presence of larger wave height determines an increase of resistance experienced by the current in comparison with run 7, revealed by the increase of u^* (= 0.0128 m/s) and k_s (= 0.00290 m).

Figure 4.28 shows a comparison between CO and WC dimensionless double-averaged velocity profiles $\langle\bar{u}\rangle/U_c$ over gravel bed with $U = 0.210$ m/s in wall distance units z^+, for Runs 32 (CO) and (a) 33 (WC, $H = 0.08$ m, $T = 2.0$) and (b) Run 34 (WC, $H = 0.12$ m, $T = 2.0$). A similar behavior to the sand bed case is observed in Figure 4.28(a) over gravel bed, although the starting CO shear velocity is doubled in comparison with the sand bottom runs, due to the presence of the rough bottom ($u^* = 0.0242$ m/s, $k_s = 0.0644$ m). Also in this case shear velocity and equivalent roughness seem to increase as waves are superposed to the current, with $u^* = 0.0284$ m/s, $k_s = 0.0877$ m. Figure 4.28(b) shows that, as wave height increases from 0.08 to 0.12 m, shear velocity and equivalent roughness remain very similar, in the sense that their difference does not exceed their confidence interval, with $u^* = 0.0286 \pm 0.0013$ m/s and $k_s = 0.0843 \pm 0.0036$ m.

Figure 4.29 reports the dimensionless double-averaged logarithmic velocity profiles in wall distance units (z^+) over sand bed with $U = 0.140$ m/s. Figure 4.29(a), which shows a comparison between Run 10 (CO) with Run 11 ($H = 0.08$ m, $T = 2$ s), highlights an opposite behavior compared with the $U = 0.210$ m/s case. Superposition of waves determines a decrease in shear velocity, with an u^* decreasing from 0.0100 to 0.0066 m/s and k_s decreasing from 0.0141 m to 0.0008 m. This behavior is also observed in Figure 4.29(b) which shows a comparison between Run 10 (CO) with Run 12 ($H = 0.12$ m, $T = 2$ s), thus with a larger wave

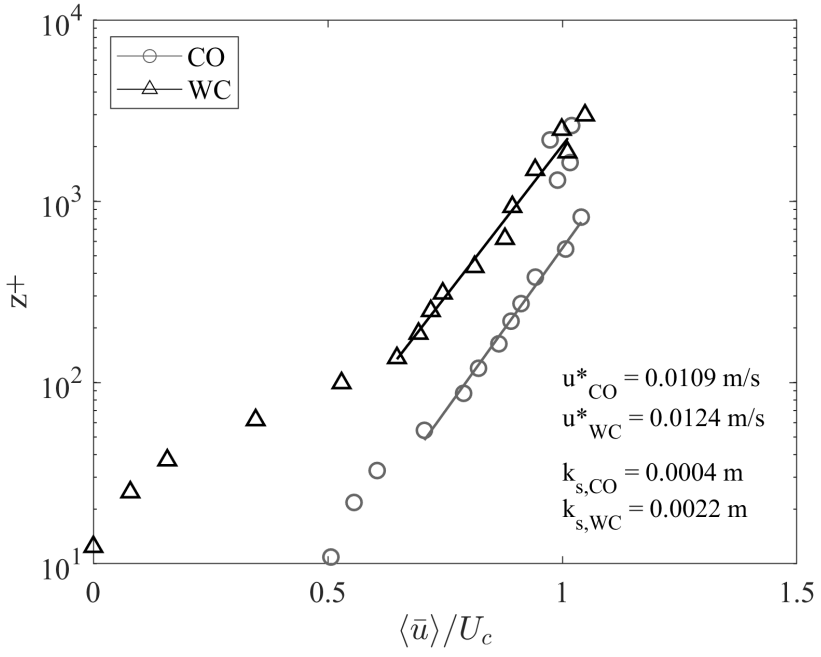

(a)

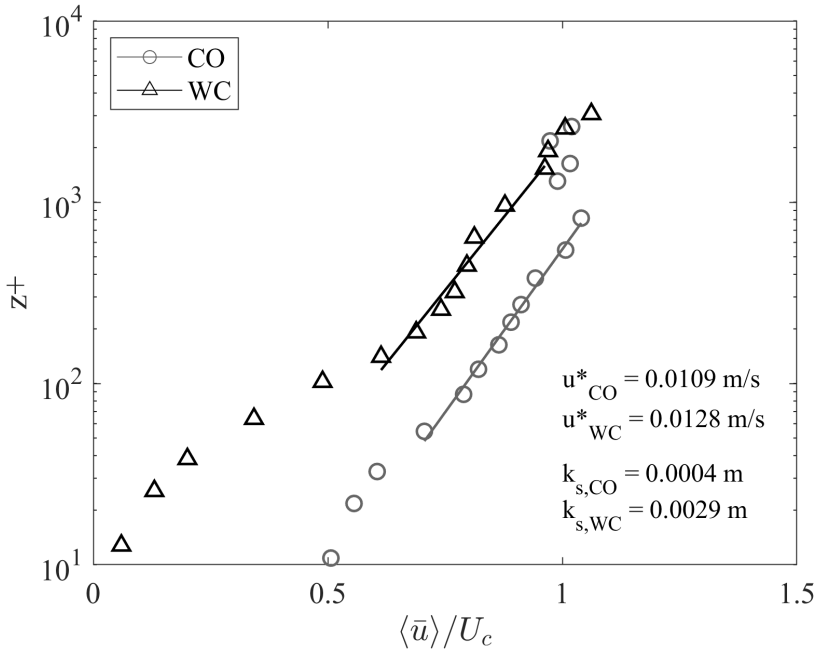

(b)

Figure 4.27: Logarithmic profiles in wall units with $U = 0.210$ m/s over sand bed: (a) Run 1 (CO, circles) and Run 8 (WC, triangles, $H = 0.08$ m, $T = 2.0$ s); (b) Run 1 (CO, circles) and Run 6 (WC, triangles, $H = 0.12$ m, $T = 2.0$ s).

height. The shear velocity of Run 12 ($u^* = 0.0071$ m/s) is larger than Run 11 but still smaller than the CO case of Run 10. The same happens with the equivalent

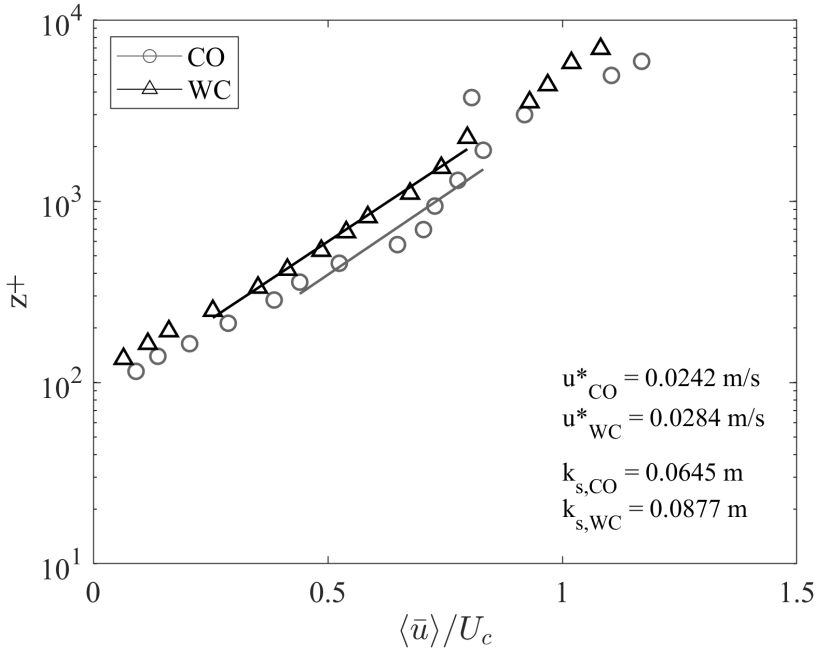

(a)

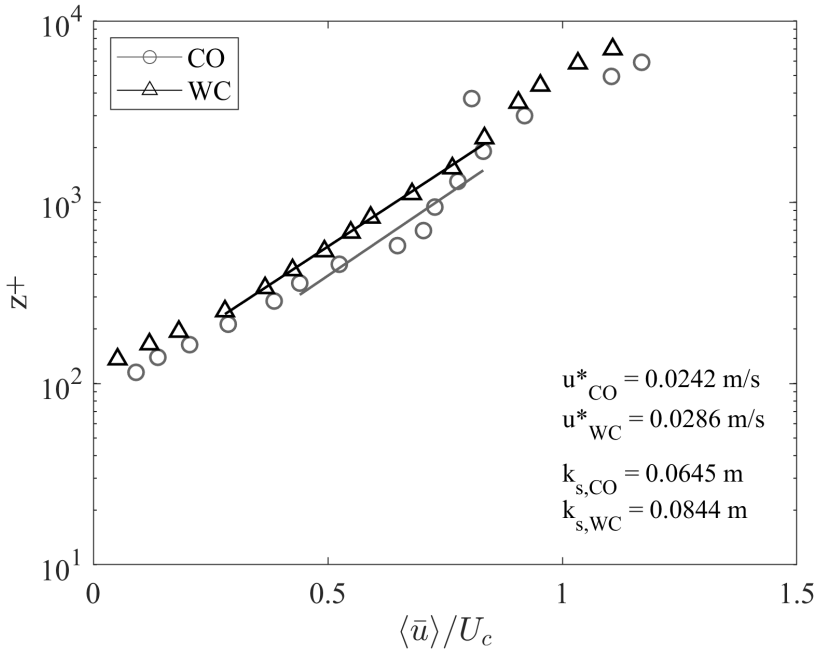

(b)

Figure 4.28: Logarithmic profiles in wall units with $U = 0.210$ m/s over gravel bed: (a) Run 32 (CO, circles) and Run 33 (WC, triangles, $H = 0.08$ m, $T = 2.0$ s); (b) Run 32 (CO, circles) and Run 34 (WC, triangles, $H = 0.12$ m, $T = 2.0$ s);

roughness k_s, which decreases by an order of magnitude (0.0141 m to 0.0011 m).

Figure 4.30 illustrates the dimensionless double-averaged logarithmic veloc-

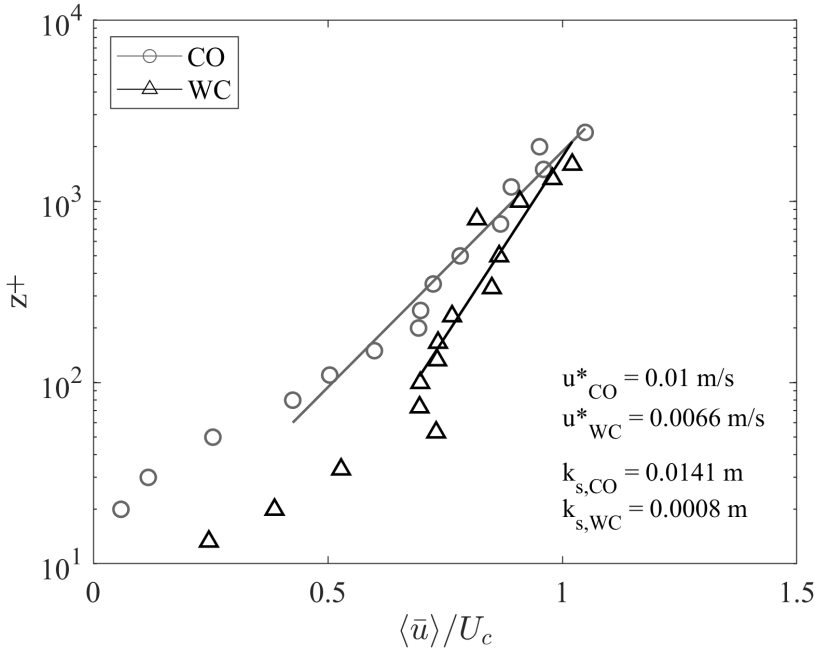

(a)

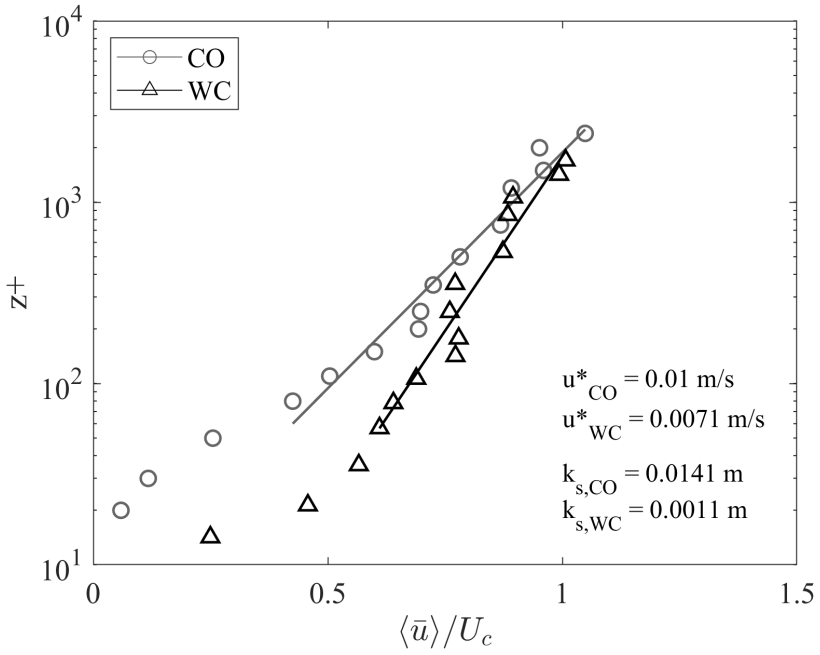

(b)

Figure 4.29: Logarithmic profiles in wall units with $U = 0.140$ m/s over sand bed: (a) Run 10 (CO, circles) and Run 11 (WC, triangles, $H = 0.08$ m, $T = 2.0$ s); (b) Run 10 (CO, circles) and Run 12 (WC, triangles, $H = 0.12$ m, $T = 2.0$ s).

ity profiles in wall distance units (z^+) over gravel bed with $U = 0.140$ m/s. The comparison between Run 19 (CO) and Run 22 (WC, $H = 0.08$ m, $T = 2$ s) logarith-

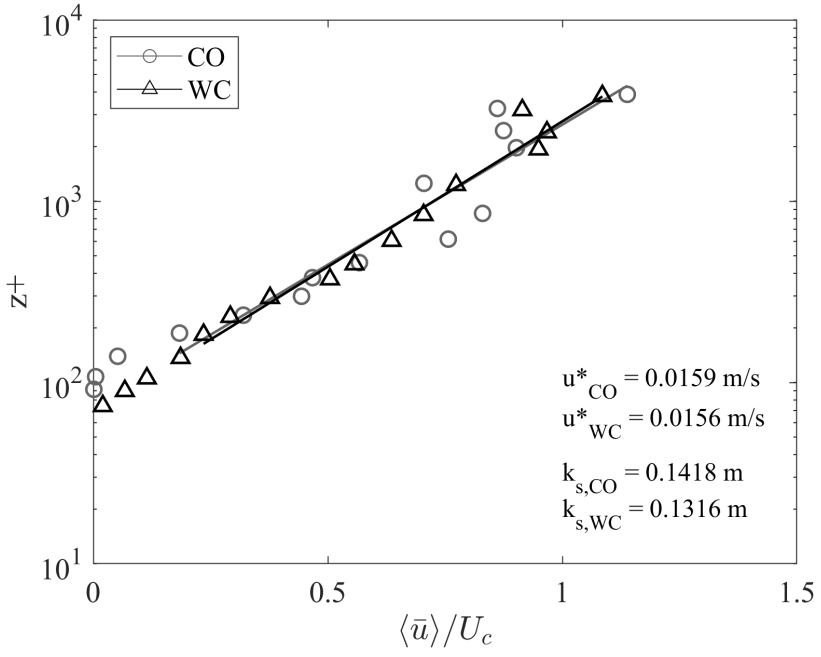

(a)

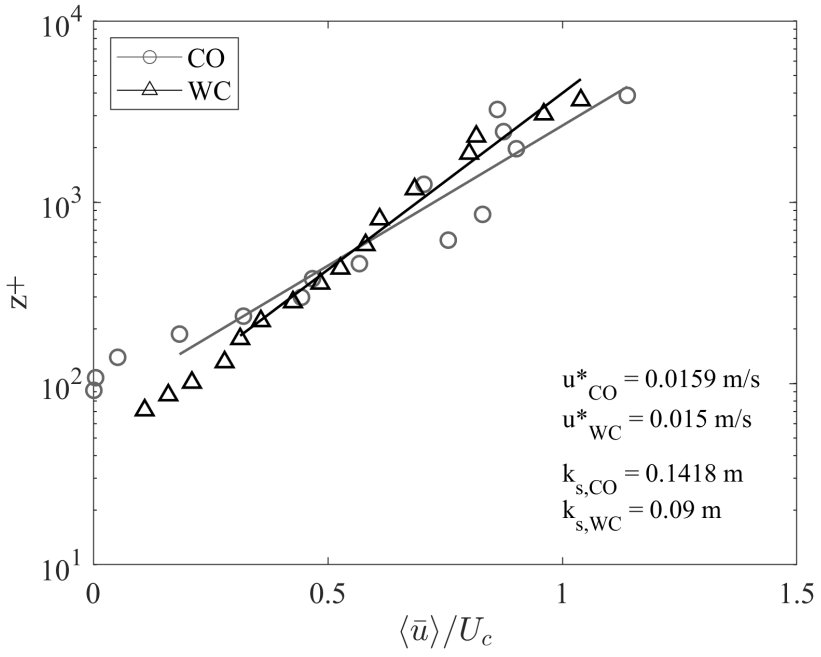

(b)

Figure 4.30: Logarithmic profiles in wall units with $U = 0.140$ m/s over gravel bed (a) Run 19 (CO, circles) and Run 22 (WC, triangles, $H = 0.08$ m, $T = 2$ s; (b) Run 19 (CO, circles) and Run 23 (WC, triangles, $H = 0.12$ m, $T = 2$ s;

mic profiles in Figure 4.30(a), shows that in the analyzed condition the presence of waves seems to not affect noticeably the current profile. A decrease of shear velocity

and apparent roughness is observed, although to a much lesser extent in comparison with the sand bed case. This behavior is observed also in Figure 4.30(b), in which the difference between CO and WC shear velocity seems to be larger, but still inside the shear velocity confidence interval (0.0014 m/s). In comparison with the gravel bed case with $U = 0.210$ m/s, k_s in the case of $U = 0.140$ m/s is more than doubled, and the k_s for the CO case is fairly larger than the literature value reference of $2.5d_{50}$. The reason for such a finding is unclear.

4.3.4 Comparison with literature models

The experimental velocity profiles from the combined flow experiments have been compared with a selection of wave-current models. In the following, the models by Grant and Madsen (1986, GM86), Soulsby (1997, SO97) and Styles et al. (2017, ST17) have been chosen to purse a validation with the WINGS experimental data. The GM86 is a two-layer eddy viscosity model, improved from the Grant and Madsen (1979) model, which assumes two linear eddy viscosities, in and out of the combined boundary layer. In the original model, the combined flow shear velocity u^*_{wc} is associated with the maximum bed shear velocity of wave–current combined flow ($u^*_{wcm,wc}$). Instead, in the GM86 model, both the bottom shear stress due to current and the maximum shear stress of combined flow are considered. Within the wave boundary layer, the eddy viscosity is related to the maximum combined wave-current shear velocity, whereas above of it, the eddy viscosity depends only on the turbulence of the current:

$$\nu_t = \kappa u^*_{wc} z \qquad \text{for } z < \delta_{wc} \tag{4.7}$$

$$\nu_t = \kappa u^*_{c} z \qquad \text{for } z > \delta_{wc}. \tag{4.8}$$

where κ von Karman's coefficient ($= 0.4$), $u*_c$ is the pure current shear velocity and δ_{wc} is the combined flow boundary layer thickness.

The application of the GM86 model has been pursued according to the following procedure. A value of the combined flow friction factor f_{cw} is first assumed in order to compute the relative wave-current strength ratio C_r. The friction factor has been then obtained by iteration from:

$$1/(4f_{cw}^{0.5}) + \log(1/(4f_{cw}^{0.5})) = log(C_r U_w/\omega z_0) + 0.14((4f_{cw}^{0.5})) - 1.65 \tag{4.9}$$

Current, wave and combined flow shear velocities u_c^*, u_w^* and u_{wc}^* have been estimated using the C_r and f_{cw} values:

$$u_w^* = (C_r f_{cw} U_w^2)^{0.5} \tag{4.10}$$

$$u_{wc}^* = u_w^* C_r^{0.5} \tag{4.11}$$

Velocity $u(z)$ profiles are then obtained:

$$u(z) = (u_c^*/\kappa)(u_c^*/u_{wc}^*)\ln(z/z_0), \qquad \text{for } z \leq \delta_{wc} \tag{4.12}$$

$$u(z) = (u_c^*/\kappa)\ln(z/z_{0c}), \qquad \text{for } z \geq \delta_{wc} \tag{4.13}$$

where z_{0c} is the apparent roughness experienced by the current in the presence of waves. The computed shear velocities then have been used to compute a new C_r from the following:

$$C_r = [1 + 2(u_c^*/u_w^*)^2\cos(\phi_b) + (u_c^*/u_w^*)^4]^{0.5} \tag{4.14}$$

where ϕ_b is the attack angle between waves and current inside the boundary layer. Then, this new value of C_r has been used again until convergence is achieved and the final shear velocity value is obtained.

The Soulsby (1997) method follows an empirical formulation. The expression for the mean bottom shear stress is:

$$\tau_m = [1 + 1.2(|\tau_w|/(\tau_c + \tau_w)] \tag{4.15}$$

where τ_c is the current alone bed shear-stress and τ_w is the wave alone shear stress. The velocity profile is given then by:

$$u(z) = \tau_m^{0.5}/\kappa \log z/z_0; \tag{4.16}$$

The ST17 model is an extension of the Styles and Glenn (2000), which is a version of the Grant and Madsen (1979) model but has been modified to include

different eddy viscosity profiles. For conditions in which the height of the roughness elements are small in comparison to the wave boundary layer thickness, the three-layers eddy viscosity profile proposed by Glenn (1983) is used:

$$u(z) = u_c^*/\kappa \ln(z/z_2) + u(z_2), \qquad \text{for } z_2 < z, \tag{4.17}$$

$$u(z) = u_c^{*2}/(\kappa u_{wc}^*) \ln(z - z_1)/z_1) + u(z_1), \qquad \text{for } z_1 < z < z_2 \tag{4.18}$$

$$u(z) = u_c^{*2}/(\kappa u_{wc}^*) \ln(z/z_0), \qquad \text{for } z_0 < z < z_1, \tag{4.19}$$

where z_1 is an arbitrary constant scale height, and $z_2 = z_1 u_{wc}^*/u_c^*$, which is obtained by matching the eddy viscosities at $z = z_2$.

If the roughness length is larger than the wave boundary layer and consequently the condition is fully rough turbulent z_0 becomes larger than z_1 and the no-slip condition is applied in the range $z_1 < z_0 < z_2$. The solution for the current becomes:

$$u(z) = u_c^*/\kappa \ln(z/z_2) + u(z_2), \qquad \text{for } z_2 < z, \tag{4.20}$$

$$u(z) = u^*2_c/(\kappa u_{wc}^*) \ln((z - z_0/z_1), \qquad \text{for } z_1 < z_0 < z < z_2 \tag{4.21}$$

The predicting ability of the velocity profile is assessed by means of a deviation term $D_{u,model} = |u_{model} - \langle \bar{u} \rangle|/U_c$ where u_{model} is the velocity predicted by the model at a certain distance from the bed z, the velocity profile is then depth-averaged for the u values in the logarithmic layer. An analogous approach has been adopted for the shear velocity ($D_{u*,model}$) and apparent roughness ($D_{k_s,model}$).

Figures 4.31 (a) and (b) show the experimental velocity profiles for $U = 0.210$ m/s, $H = 0.08$ m and $T = 2.0$ s, over sand (Run 8) and gravel (Run 33) bed, compared with the velocity profiles estimated by the selected wave-current models. In the case shown in Figure 4.31(a) the best performance in terms of predicting the velocity profile is given by the GM86 model with a depth averaged velocity deviation in the logarithmic profile of 2%, SO97 and ST17 follows with a deviation both around 9%. Shear velocity deviation is 5% for GM86, 40% for SO97 and 1% for ST17. Figure 4.31(b) shows the models comparison with experimental data for Run 33 (WC, GB,

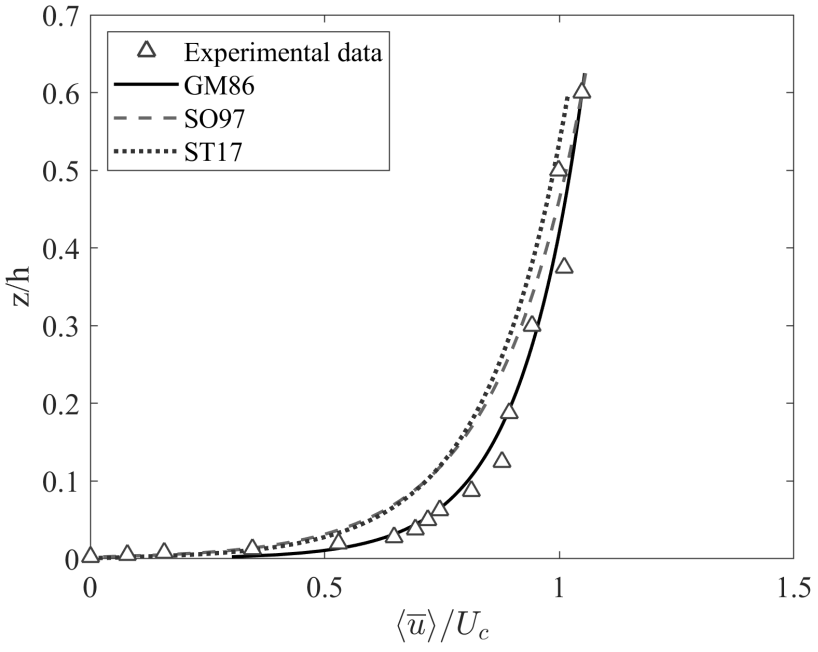

(a)

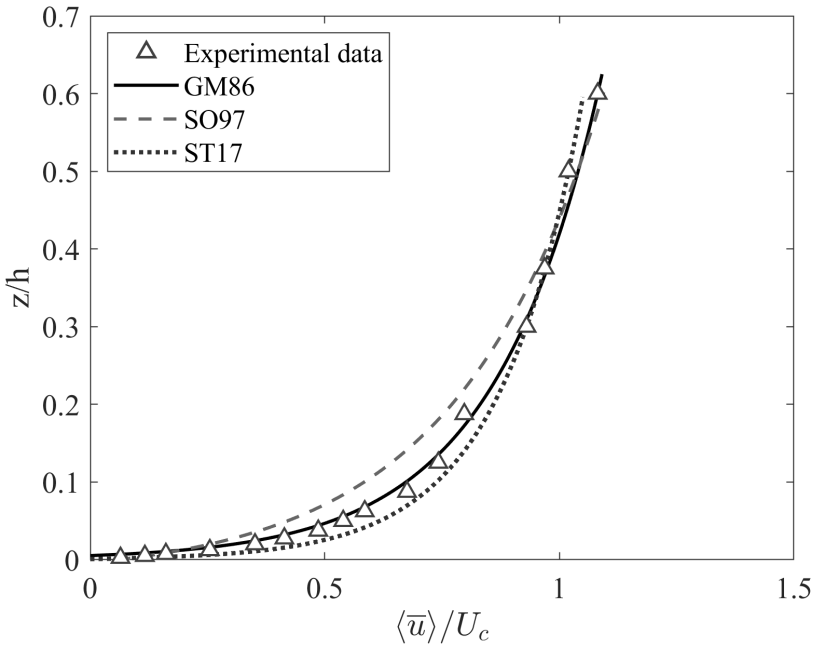

(b)

Figure 4.31: Current velocity profiles models comparison for WC cases: (a) Run 8 (SB, $U = 0.210$ m/s, $H = 0.08$ m, $T = 2.0$ s), (b) Run 33 (GB, $U = 0.210$ m/s, $H = 0.08$ m, $T = 2.0$ s),

$U = 0.210$ m/s, $H = 0.08$ m, $T = 2.0$ s). Again, the best performance is given by the GM86 model with a depth-averaged velocity deviation of 3%, followed by

ST17 which overestimates velocity by 7% and SO97, which instead underestimates by 22%. Shear velocity deviation for GM86 is 9%, whereas the SO19 and ST17 under and overestimates shear velocity greatly by 43% and 65% respectively. Figure 4.32 shows the experimental velocity profiles with $U = 0.140$ m/s, $H = 0.12$ m and $T = 2.0$ s, over sand (Run 12, a) and gravel (Run 23, b) bed, compared with the velocity profiles estimated by the wave-current models. Again, in the case of sand bed of Figure 4.32(a) the GM86 model performs best with a depth-averaged velocity deviation of 4%, followed by ST17 (10%) and SO97 (11%). Shear velocity deviation is overestimated by ST17 model by 17%, followed by GM86 (18%) and SO97 (65%). In the case of gravel bed in Figure 4.32(b), the depth-averaged velocity predicted by GM86 model deviates by 2% from the experimental data, followed by ST17 (10%) and SO97 (12%). Shear velocity deviation is 2% for GM86 model, whereas SO97 and ST17 largely either over or underestimates shear velocity respectively by 43 and 38% respectively. All the depth-averaged, shear velocity and apparent roughness deviations are reported in Table 4.7.

Table 4.7: Depth-averaged velocity deviation, shear velocity deviation and equivalent roughness deviation of the wave-current models.

Run	$D_{u,GM86}$	$D_{u,SO97}$	$D_{u,ST17}$	$D_{u*,GM86}$	$D_{u*,SO97}$	$D_{u*,ST17}$	$D_{k_s,GM86}$	$D_{k_s,SO97}$	$D_{k_s,ST17}$
6	0.028	0.106	0.085	0.039	0.427	0.215	0.5096	8.8991	0.1849
7	0.034	0.111	0.089	0.208	0.677	0.126	2.1892	25.3822	8.3257
8	0.019	0.098	0.096	0.049	0.435	0.007	0.4731	10.6597	4.0521
9	0.029	0.088	0.082	0.087	0.471	0.105	0.4293	9.7962	3.9914
11	0.038	0.104	0.093	0.221	0.709	0.236	3.0605	35.1110	12.7114
12	0.040	0.115	0.100	0.183	0.656	0.169	2.5473	29.7459	9.6016
13	0.032	0.114	0.099	0.061	0.454	0.013	0.7977	11.8627	3.1430
14	0.071	0.145	0.141	0.339	0.799	0.350	8.4832	68.0424	33.4725
21	0.060	0.160	0.093	0.315	0.010	0.560	0.6521	0.5753	0.9264
22	0.043	0.140	0.104	0.157	0.223	0.475	0.5293	1.0632	0.9141
23	0.045	0.125	0.102	0.018	0.433	0.389	0.3065	2.0848	0.8744
28	0.026	0.127	0.063	0.133	0.112	0.585	0.3801	0.7648	0.8964
33	0.032	0.219	0.076	0.099	0.259	0.651	0.2816	1.7581	0.8904
34	0.031	0.200	0.075	0.087	0.206	0.647	0.2572	1.3562	0.8860
35	0.091	0.326	0.027	0.122	0.275	0.663	0.1170	2.8893	0.8626

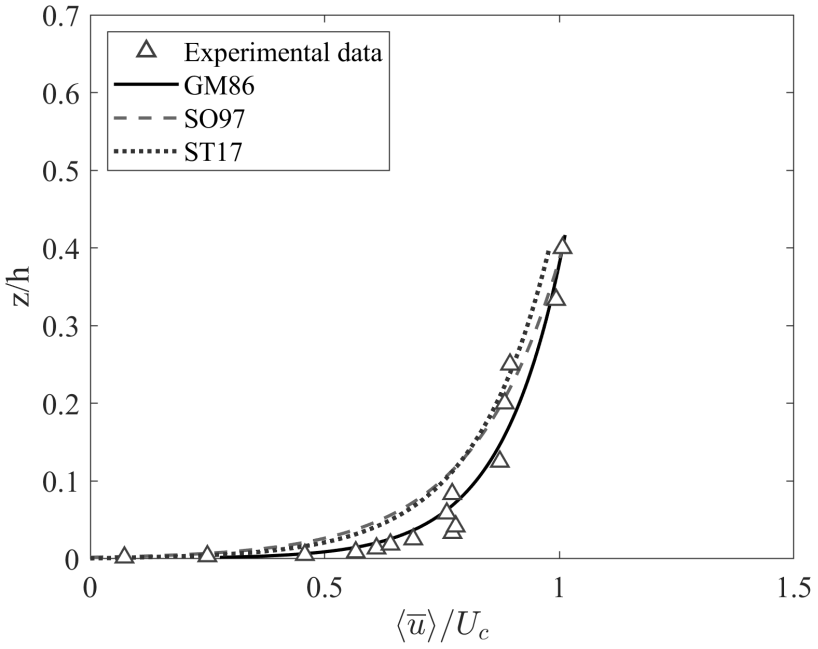

(a)

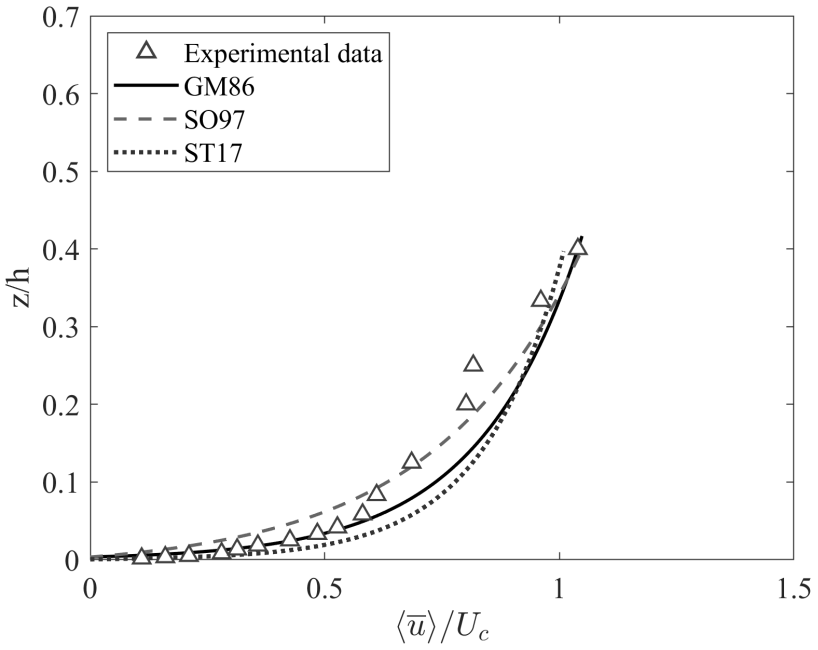

(b)

Figure 4.32: Current velocity profiles models comparison for WC cases: (a) Run 12 (SB, $U = 0.140$ m/s, $H = 0.12$ m, $T = 2.0$ s), (b) Run 23 (GB, $U = 0.140$ m/s, $H = 0.12$ m, $T = 2.0$ s),

4.4 Phase-averaged flow analysis

Phase-averaged velocities in the current direction, $\tilde{u}$, and wave direction, $\tilde{v}$, have been computed as follows:

$$\tilde{u} = \frac{1}{N_w} \sum_{i=1}^{N_w} u_i - \bar{u} \tag{4.22}$$

$$\tilde{v} = \frac{1}{N_w} \sum_{i=1}^{N_w} v_i - \bar{v} \tag{4.23}$$

where N_w is the number of waves used for the phase-average. The phase-averaged velocities are then space-averaged for each ADV in order to obtain phase- and space-averaged velocities $\langle\tilde{u}\rangle$ and $\langle\tilde{v}\rangle$ in the x and y direction respectively.

Figure 4.33 shows the phase- and space-averaged profiles for Run 4 (SB, WO, $H = 0.08$ m, $T = 2.0$ s), thus a Wave Only run over sand bed. Each profile in the plots corresponds to a certain phase of the wave. The figure features the profiles from $t/T = 0$ to $t/T = 1$ with a phase interval $\Delta t/T$ of $0.05t/T$ between each phase and the successive, therefore each panel shows a total of 21 profiles per wave phase. Profiles are plotted in shades of grey to recognize the t/T corresponding to each profile. To each space- and phase-averaged velocity, the double-averaged velocities $\langle\bar{u}\rangle$ and $\langle\bar{v}\rangle$ have been summed to $\langle\tilde{u}\rangle$ and $\langle\tilde{v}\rangle$ in order to consider both the effects of the phase-averaged and mean flow.

Both panels in the figures, reveal the presence of an oscillatory flow in both x and y directions, showing that the wave motion does not propagate perfectly in the y direction. In the correspondence of the crest ($0.25t/T$) a depth-averaged velocity of $0.10\ U_w$ is observed in the negative x direction, showing that wave direction seems to be directed to the hydraulic left side with respect of the y direction. This inclination of the wave motion is probably related to the velocity measurement position is not perfectly aligned along the center of the wavemaker, which lies at $x = 20.60$ m, whereas the velocity measurement have been performed at $x = 17.88 \div 18.12$ m.

As observed in Figures 4.3(a) and 4.4(a) in the preliminary study on the spatial variability of the wave field, a wave diffraction pattern is observed during the WO tests, determined by the three-dimensional basin setup. Diffraction determines a variability of the wave field in terms of wave height, as already observed in the wave height contour plots, and in the inclination of the wave motion with respect

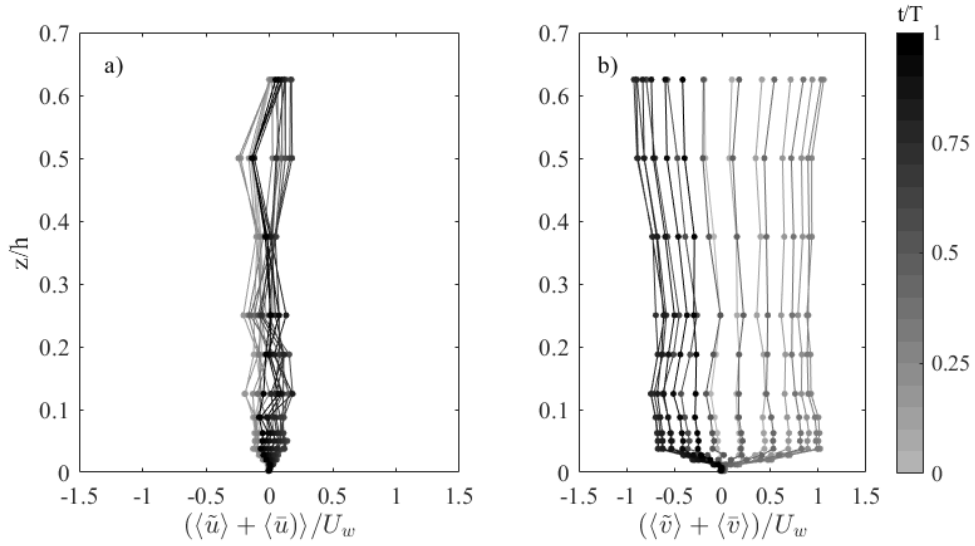

Figure 4.33: Phase- and space-averaged velocity profiles for Run 4 (SB, WO, H = 0.08 m, T = 2.0 s): (a) in the x direction, (b) in the y direction.

to the y direction, as observed in Figure 4.33.

Figure 4.34 shows the phase- and space-averaged profiles for Run 8 (SB, WC, U = 0.21 m/s, H = 0.08 m, T = 2.0 s), with the same wave condition of Figure 4.33 but with a superimposed current. The figure reveals that the presence of the current seems to suppress the oscillating component in the x direction, as observed in Figure 4.34(a), operating a realignment of the oscillatory flow in the y direction. This seems to occur regardless of the roughness of the bed, demonstrated by the results in Figures 4.35 (Run 29) and 4.36 (Run 33), which features the same wave and current conditions of Figures 4.33 and 4.34 respectively, but over gravel bed.

The veering effect operated by the current on the wave motion is represented ina different way in Figures 4.37 and 4.38, which show the phase- and space-averaged velocity ensembles for Run 3 (SB, WO, H = 0.12 m, T = 2.0 s) and Run 7 (SB, WC, U = 0.21 m/s, H = 0.12 m, T = 2.0 s) in the x (subpanel a) and y (subpanel b) directions.

The two Runs share the same wave conditions, with Run 3 being with pure waves and Run 7 featuring a superimposed current with U = 0.21 m/s. The distance from the bottom of the measurement point is indicated in shades of grey. The comparison between velocities in the x directions of Figures 4.37(a) and 4.38(a) shows the veering effect observed in the phase- and space-averaged velocity profiles,

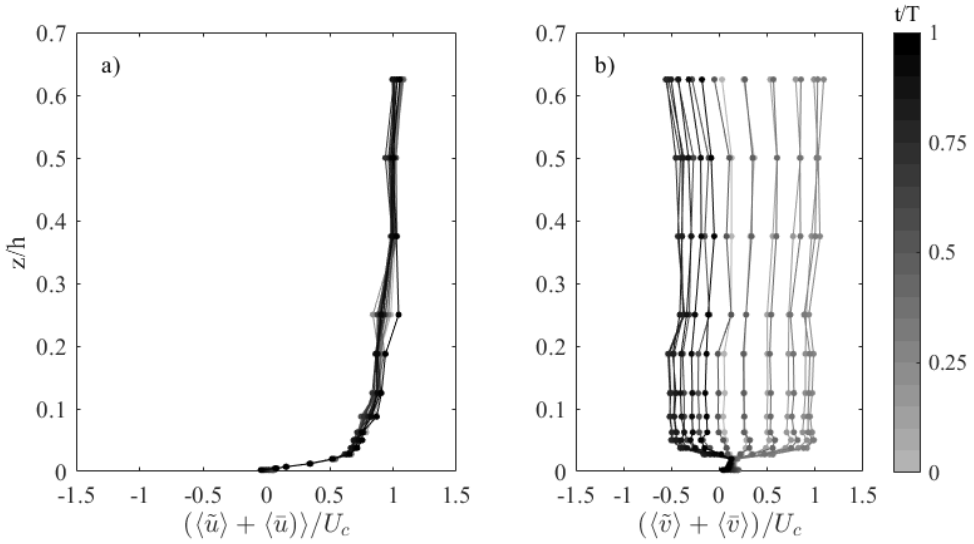

Figure 4.34: Phase- and space-averaged velocity profiles for Run 8 (SB, WC, U = 0.21 m/s, H = 0.08 m, T = 2.0 s): (a) in the x direction, (b) in the y direction.

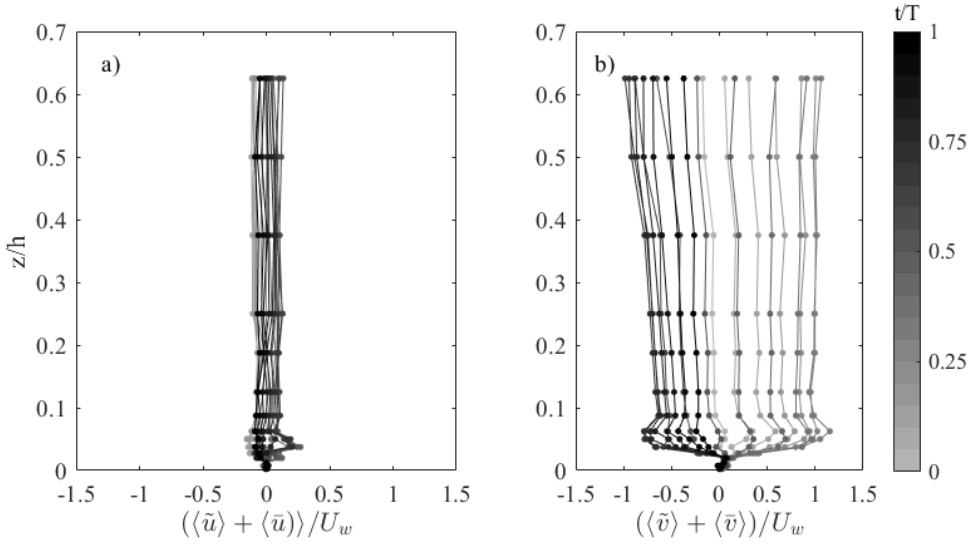

Figure 4.35: Phase-averaged velocity profiles for Run 29 (GB, WC, U = 0.21 m/s, H = 0.08 m, T = 2.0 s): (a) in the x direction, (b) in the y direction.

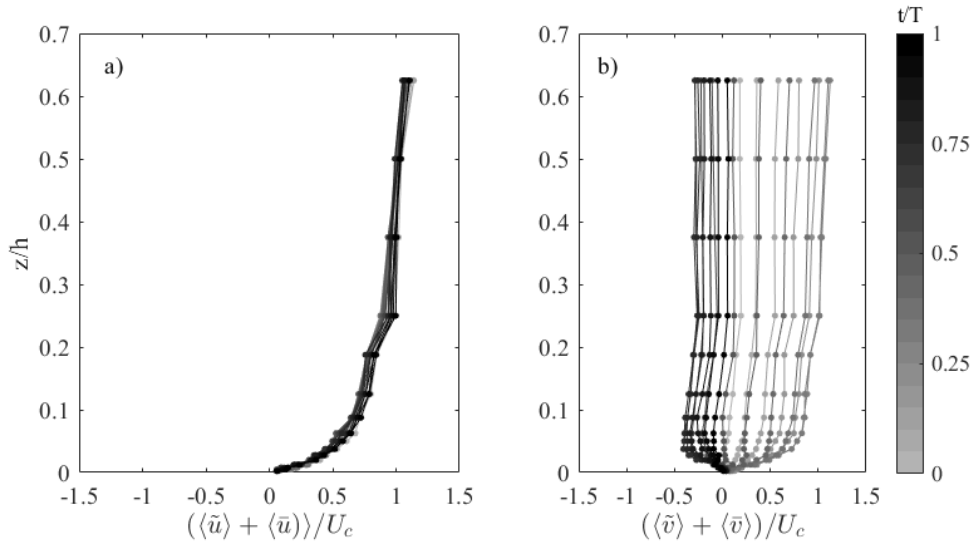

Figure 4.36: Phase-averaged velocity profiles for Run 33 (GB, WC, $U = 0.21$ m/s, $H = 0.08$ m, $T = 2.0$ s): (a) in the x direction, (b) in the y direction.

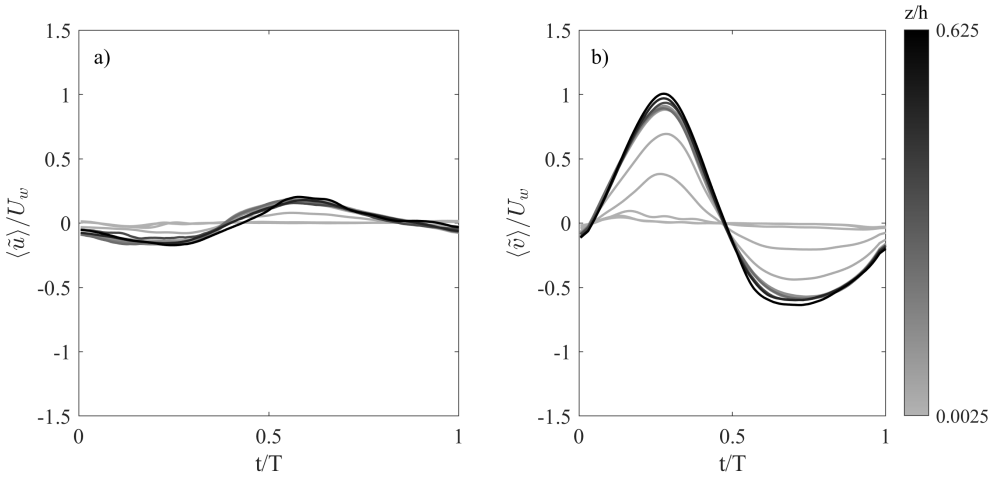

Figure 4.37: Phase- and space-averaged velocity wave ensembles for Run 3 (SB, WO, $H = 0.12$ m, $T = 2.0$ s): (a) in the x direction, (b) in the y direction.

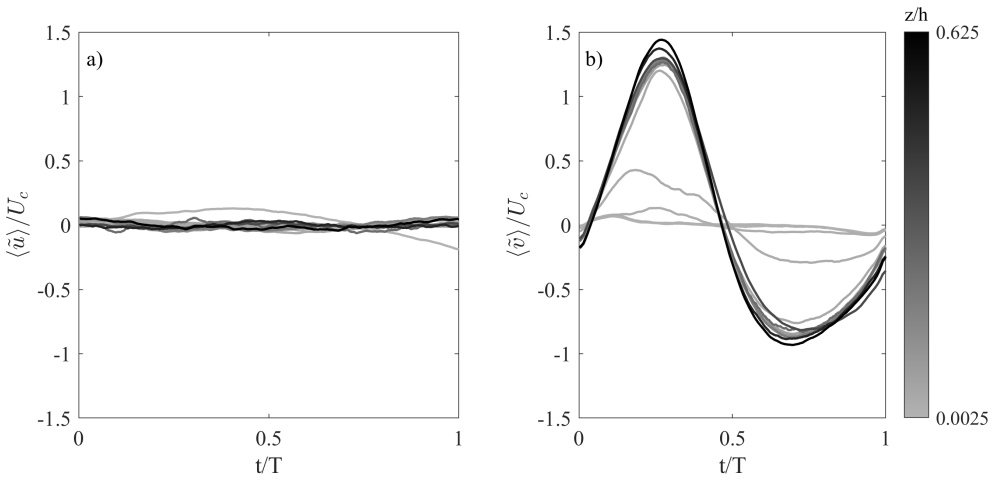

Figure 4.38: Phase- and space-averaged velocity wave ensembles for Run 7 (SB, WC, $U = 0.21$ m/s, $H = 0.12$ m, $T = 2.0$ s): (a) in the x direction, (b) in the y direction.

with the oscillatory flow being suppressed by the superposition of the current, which apparently operates a momentum transfer to the wave motion, that in turn tends to veer closer to the y direction. Considering a reference system in which the x direction corresponds to 0° and the y direction is at -90° anti-clockwise with respect to the x direction, the veering of the waves with respect to the reference system operated by the current, computed as $\theta = -\arctan \bar{v}/\bar{u}$ is from -96 ° to roughly -90°.

In some cases the direction of the waves has been observed to veer in the positive x direction due to the presence of the current. Figures 4.39 and 4.40 show the phase- and space-averaged wave ensembles for Run 27 (GB, WO, $H = 0.12$ m, $T = 2.0$ s) and Run 23 (GB, WC, $U = 0.14$ m/s, $H = 0.12$ m, $T = 2.0$ s) respectively. In this case, the wave direction of the wave only case is aligned with the y direction (-90°), current can make the wave motion to veer by a freestream depth-averaged of 10°.

Figures 4.41 and 4.42 provide an overview of the veering process on the current by showing the vertical profile of the angle between current and the x direction θ for all the CO and WC Runs, with $U = 0.210$ m/s and $U = 0.140$ m/s respectively, computed as $\theta = -\arctan \langle\bar{v}\rangle/\langle\bar{u}\rangle$.

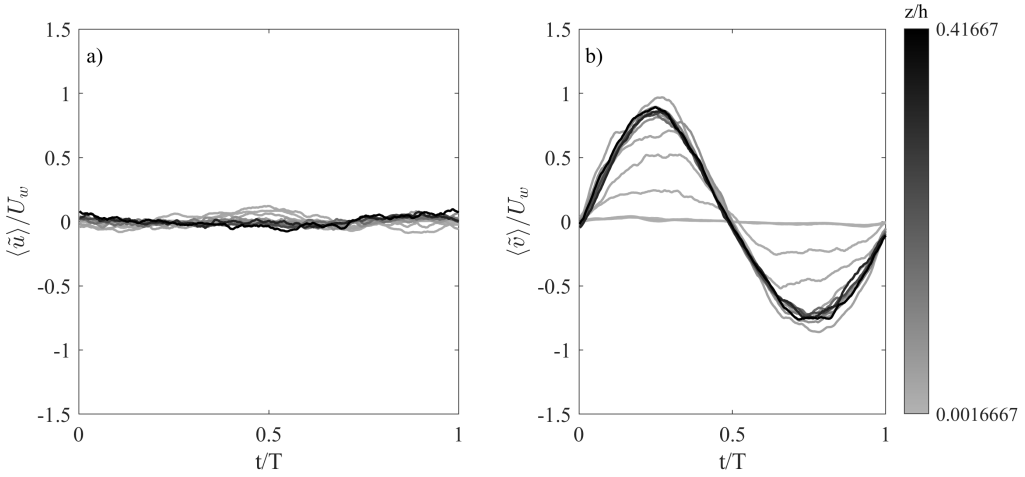

Figure 4.39: Phase- and space-averaged velocity wave ensembles for Run 27 (GB, WO, $H = 0.12$ m, $T = 2.0$ s): (a) in the x direction, (b) in the y direction.

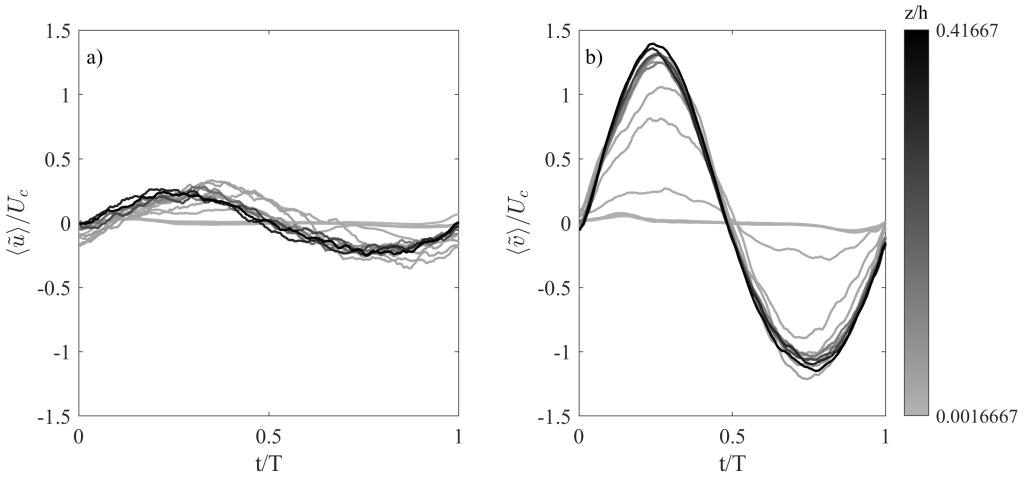

Figure 4.40: Phase- and space-averaged velocity wave ensembles for Run 23 (SB, WC, $U = 0.14$ m/s, $H = 0.12$ m, $T = 2.0$ s): (a) in the x direction, (b) in the y direction.

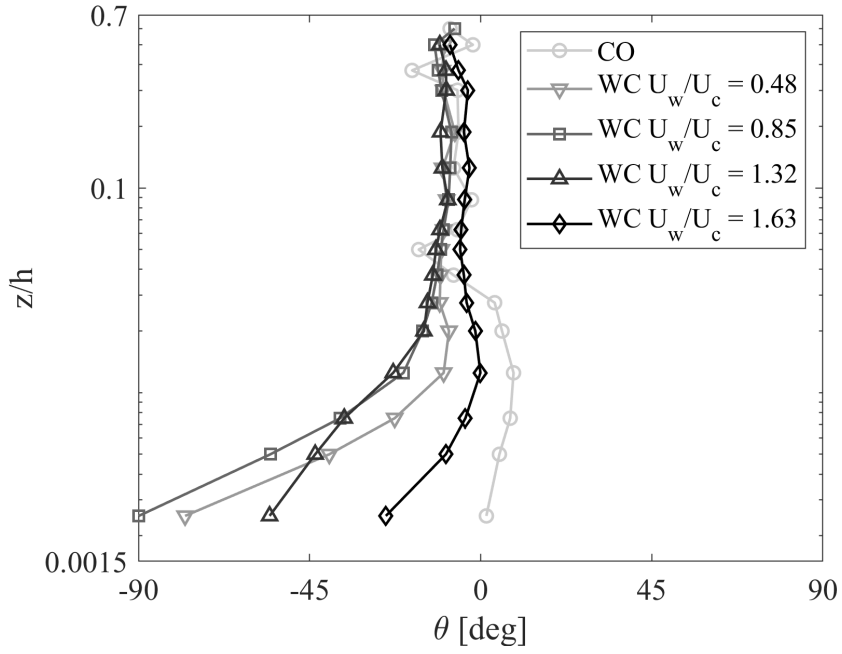

(a)

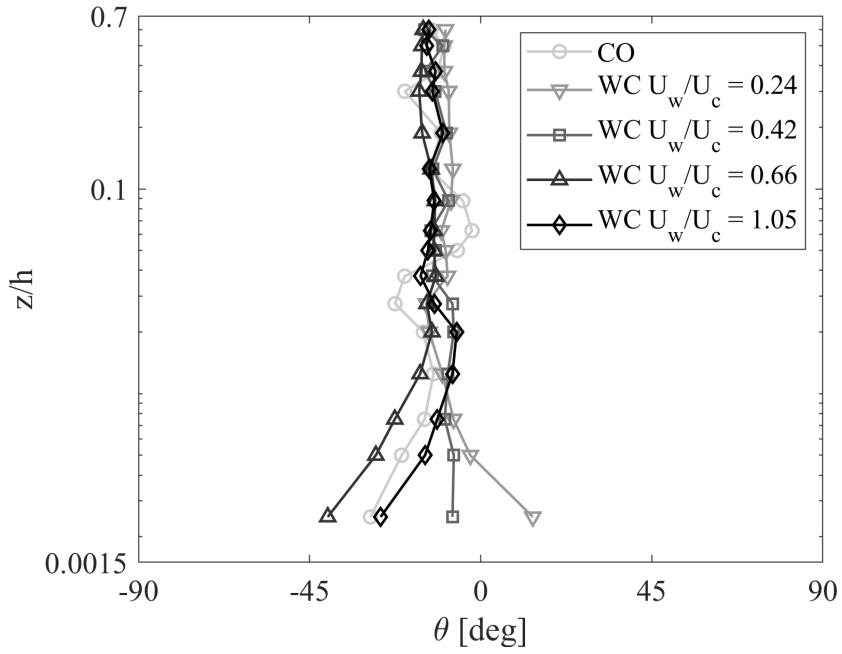

(b)

Figure 4.41: Angle between current and the x direction vertical profile of CO and WC runs with increasing U_w/U_c: (a) SB, $U = 0.210$ m/s: Run 1 (CO) and Run 9, 8, 7, 6 (WC) (b) GB, $U = 0.210$ m/s: Run 32 (CO) and Run 28, 35, 33, 34 (WC).

Figure 4.41(a) shows Runs with $U = 0.210$ m/s over sand bed. The larger deviation from the x direction (correspondent in the plot to 0°) seems to happen in

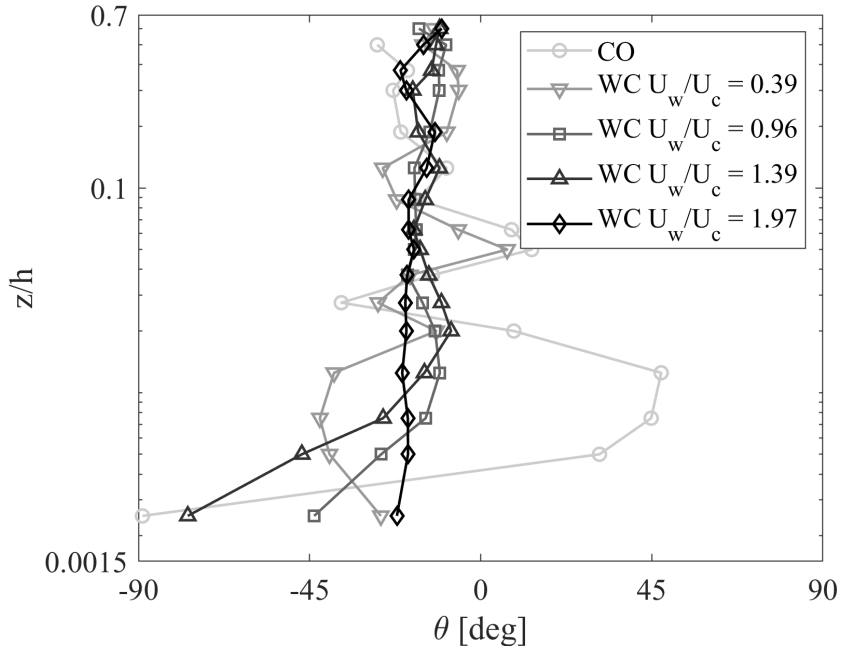

(a)

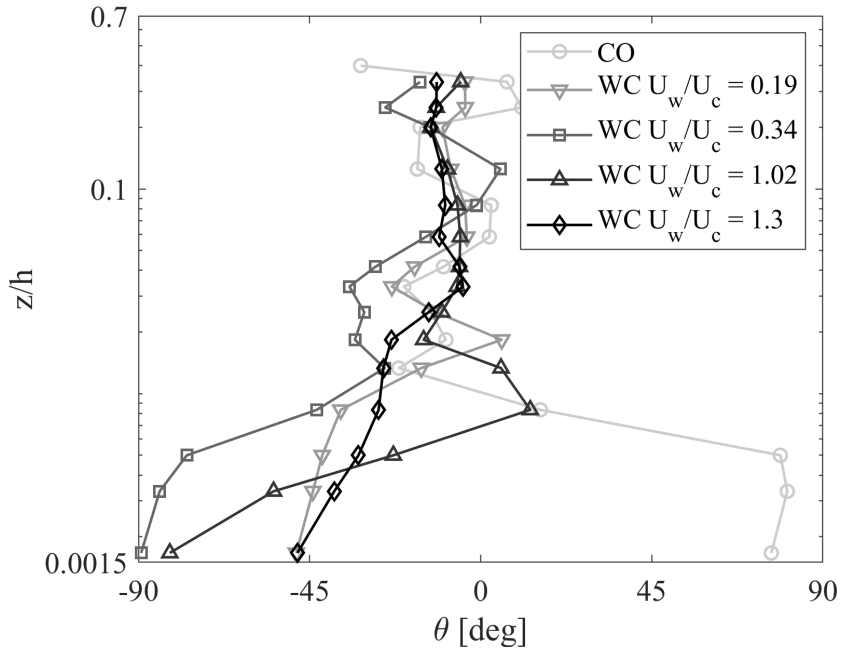

(b)

Figure 4.42: Angle between current and the x direction vertical profile of CO and WC runs with increasing U_w/U_c: (a) SB, $U = 0.140$ m/s: Run 10 (CO) and Run 14, 11, 12, 13 (WC). (b) GB, $U = 0.140$ m/s: Run 19 (CO) and Run 20, 21, 22, 23 (WC).

the proximity of the bed. The superposition of the oscillatory flow always determines a deviation from the direction of the current. However, such an effect seems to become more intense as the relative importance of the waves on the current decreases (i.e. U_w/U_c). This behavior is not observed with the same U in the runs over gravel bed, as it can be observed in 4.41(b), in which the behavior of the angle change does not have an easily readable pattern. Veering angle profiles for runs with U = 0.140 m/s, are shown in Figure 4.42(a), over sand bed, and 4.42(b) over gravel bed. Analogously to the U = 0.210 m/s case, the larger U_w/U_c runs seems to determine the veering angle to decrease the most, over both sand and gravel bed, nevertheless the data does not seem to have a clear pattern as the wave-current parameter increases.

4.5 Turbulent flow analysis

An attempt in analysing the turbulent velocity data of the WINGS campaign has been carried out and the results are shown in the following Section. Turbulent (or fluctuating) velocities u', v' and w', respectively in the x (current), y (wave), and w (vertical upward) directions, have been recovered from instantaneous velocity timeseries u, v and w through Reynolds averaging, as explained in Section 4.3.1. Once the turbulent velocities are recovered, they are employed to obtain turbulence related quantities.

4.5.1 Turbulence intensities and Reynolds stresses

Figure 4.43 shows turbulence intensities I_u ($= \sqrt{u'^2}/\bar{u}$) and I_v ($= \sqrt{v'^2}/\bar{v}$) in the current (a) and wave (b) direction respectively, of Run 1 (CO), Run 7 (WC, H = 0.12 m, T = 2.0 s) and Run 8 (WC, H = 0.08 m, T = 2.0 s). All runs are over sand bed with U = 0.210 m/s.

The Figure illustrates that the presence of waves always enhances turbulence intensity both close and far from the bottom. Moreover, the profiles manifest an overall gradient increase in comparison with the lone current, which is associated with larger turbulence production. Nevertheless, as the relative importance of the waves to the current increases, in terms of the parameter U_w/U_c, turbulence intensity

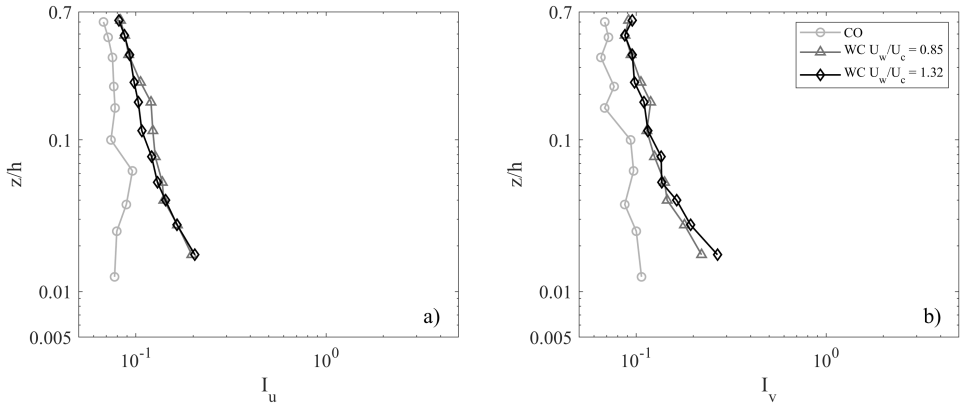

Figure 4.43: Turbulence intensities I_u (a) and I_v (b) of Run 1 (CO), Run 7 (WC, $H = 0.12$ m, $T = 2.0$ s) and Run 8 (WC, $H = 0.08$ m, $T = 2.0$ s), all runs are over sand bed with $U = 0.210$ m/s.

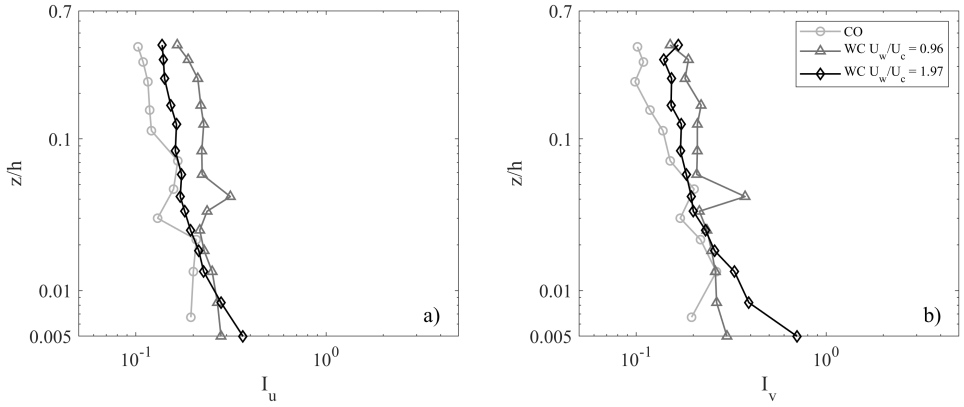

Figure 4.44: Turbulence intensities I_u (a) and I_v (b) in the current and wave direction respectively of Run 10 (CO), Run 11 (WC, $H = 0.08$ m, $T = 2.0$ s) and Run 13 (WC, $H = 0.18$ m, $T = 2.0$ s) over sand bed with $U = 0.140$ m/s.

profiles in the case of wave plus current seems to have a very similar behavior. Moreover, no noticeble difference is observed between turbulence intensities in the current I_u and in the wave I_v direction.

Figure 4.44 shows turbulence intensities I_u and I_v in the current (a) and wave (b) direction respectively of Run 10 (CO), Run 11 (WC, $H = 0.08$ m, $T = 2.0$ s) and Run 13 (WC, $H = 0.18$ m, $T = 2.0$ s) over sand bed with $U = 0.140$ m/s. As U_w/U_c increases, a turbulence intensity enhancement is observed in proximity of the bed, while a decrease in the upper part of the water column. The increase of the parameter U_w/U_c seems also to affect the profile gradient in the very proximity

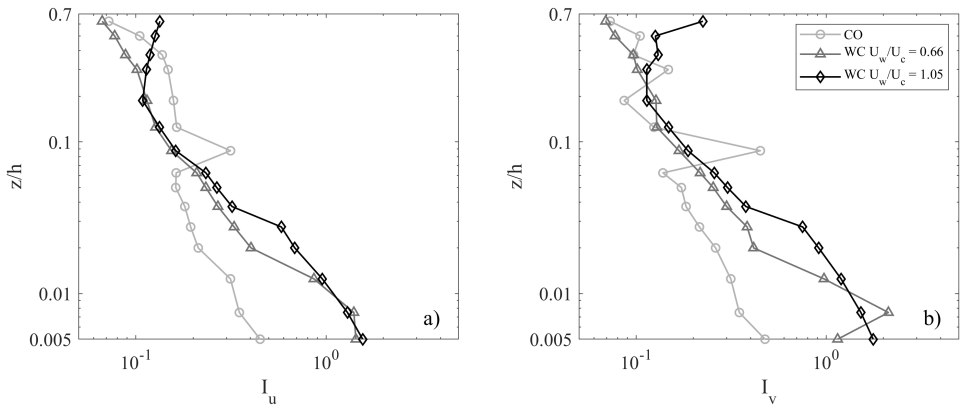

Figure 4.45: Turbulence intensities I_u and I_v of Run 32 (CO), Run 33 (WC, H = 0.08 m, T = 2.0 s) and Run 34 (WC, H = 0.12 m, T = 2.0 s) over gravel bed with U = 0.210 m/s.

of the bottom boundary, with an increment of U_w/U_c determining an increase of the bottom turbulence intensity gradient.

Figure 4.45 shows turbulence intensities in the current direction I_u (a) and wave direction I_v (b) of Run 32 (CO), Run 33 (WC, H = 0.08 m, T = 2.0 s) and Run 34 (WC, H = 0.12 m, T = 2.0 s) over gravel bed with U = 0.210 m/s. Presence of the gravel bottom determines larger gradients of turbulence intensities, in comparison with the corresponding SB case (Figure 4.43) with the same U = 0.210 m/s. Notwithstanding the different U_w/U_c, the two WC profiles share a very similar behavior, analogously to the velocity profiles of Figure 4.28. However, the increment of turbulence intensity in the larger U_w/U_c examined case (Run 34) seems to involve a larger part of the water column (approximately up to 0.03 $\div$ 0.04 z/h).

Figure 4.46 shows turbulence intensities I_u and I_v of Run 19 (CO), Run 21 (WC, H = 0.08 m, T = 2.0 s) and Run 22 (WC, H = 0.12 m, T = 2.0 s), thus over gravel bed with U = 0.140 m/s. Figure shows larger gradient in comparison with the corresponding sand bed case with the same U of Figure 4.44, approximately up to z/h = 0.10 m. The CO case shows a larger turbulent intensity very close to the bottom boundary, compared with all the correspondent WC cases. This could confirm the results of Figure 4.30, which shows a slightly larger shear experienced by the current in the absence of waves. However, such a behavior has not been observed with the sand bed case in Figure 4.44. Moreover, slightly larger gradients of the turbulence intensity profiles are observed in the CO case.

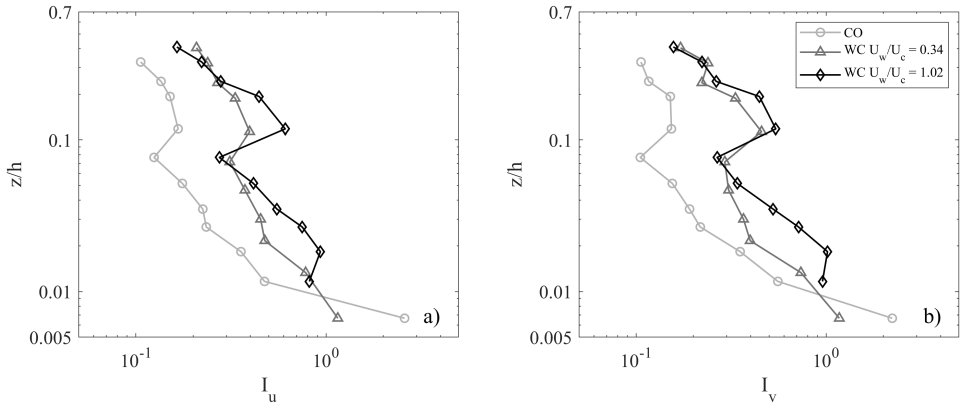

Figure 4.46: Turbulence intensities I_u (a) and I_v of Run 19 (CO), Run 21 (WC, H = 0.08 m, T = 2.0 s) and Run 22 (WC, H = 0.12 m, T = 2.0 s), thus over gravel bed with U = 0.140 m/s.

Reynolds stresses ($\overline{u'w'}$) are an indicator of the friction experienced by a flow due to the presence of coherent structures in proximity of a wall boundary. Figure 4.47 shows Reynolds stress profiles of Run 1 (CO), Run 7 (WC, H = 0.12 m, T = 2.0 s) and Run 8 (WC, H = 0.08 m, T = 2.0 s), all runs are over sand bed with U = 0.210 m/s. The superposition of waves always induces an increment of bottom Reynolds stress. The Reynolds stress maximum is very close in values for both the WC cases, although the two peaks lies at a difference distance from the bed.

Figure 4.48 shows Reynolds stress profiles of Run 32 (CO), Run 33 (WC, H = 0.08 m, T = 2.0 s) and Run 34 (WC, H = 0.12 m, T = 2.0 s) over gravel bed with U = 0.210 m/s. The two WC Reynolds stress profile show a very similar behavior close to the surface. A greater shear stress maximum is associated with larger U_w/U_c case.

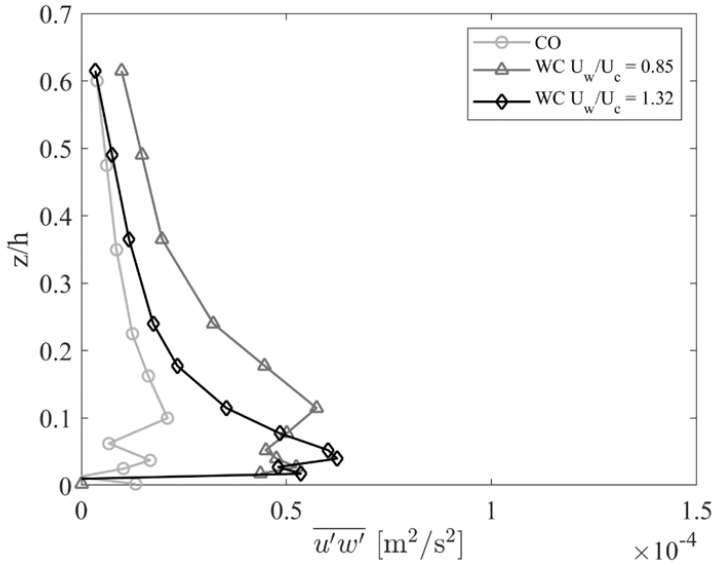

Figure 4.47: Reynolds stress profiles of Run 1 (CO), Run 7 (WC, $H = 0.12$ m, $T = 2.0$ s) and Run 8 (WC, $H = 0.08$ m, $T = 2.0$ s), all runs are over sand bed with $U = 0.210$ m/s.

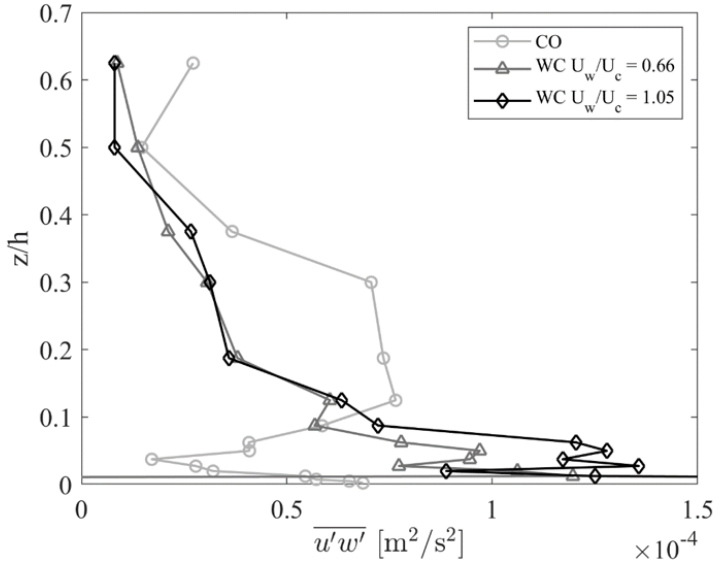

Figure 4.48: Reynolds stress profiles of Run 32 (CO), Run 33 (WC, $H = 0.08$ m, $T = 2.0$ s) and Run 34 (WC, $H = 0.12$ m, $T = 2.0$ s) over gravel bed with $U = 0.210$ m/s.

4.5.2 Quadrant analysis

Wall turbulence in a fully developed steady flow manifests with the presence of coherent structures determined by velocity gradients in the boundary layer. Their presence heavily affects mean flow velocity and alters momentum transport, determining an increase of bottom shear resistance. Turbulence production at a wall boundary is generated by the succession of two cyclic events: ejections (or bursts) and sweeps (Corino and Brodkey, 1969). These events are the main responsible for turbulent vertical momentum transport and they determine the most of the generation of the Reynolds shear stress (Wallace, 2016). Quadrant analysis is a well-established technique to observe the behavior of the ejection-sweep cycle (Wallace et al., 1972; Lu and Willmarth, 1973; Kim et al., 1987). Turbulent events, defined as the fluctuating velocities $(u'(t), w'(t))$ of a timeseries, where u' and w' are the streamwise and vertical upward direction turbulent velocities, are subdivided into four quadrants depending on the signs of u' and w'. The first quadrant (Q1), where $u' > 0$, $w' > 0$, is called the outward interaction quadrant, the second quadrant (Q2), where $u' < 0$ and $w' > 0$, is the ejections quadrant, the third quadrant (Q3), where $u' < 0$ and $w' < 0$, is the inward interaction quadrant and the fourth quadrant (Q4), where $u' > 0$ and $w' < 0$, is the sweeps quadrant. In a steady flow, the contribution of the i-th quadrant at any point, excluding an hyperbolic region of size Ω, is

$$(u'w')_{i,\Omega} = \lim_{T\to\infty} \int_0^{T_{end}} u'(t)w'(t)I_{i,\Omega}(u', w')dt \tag{4.24}$$

where T_{end} is the last instant of the time series, and the indicator function $I_{i,\Omega}$ is

$$I(u', w') = \begin{cases} 1, & \text{if } (u', w') \text{ is the } i\text{-th quadrant and if} |u'w'| > \Omega|\overline{u'w'}|; \\ 0, & \text{otherwise.} \end{cases}$$

In particular, Ω is a threshold parameter which allows to consider as ejections-sweep events only the values of $(u'w')$ that are larger than Ω times $|\overline{u'w'}|$ (Wallace, 2016). The threshold parameter is used to observe the relative importance of the quadrant events in generating significantly strong shear stress. Figure 4.49 shows the correlation plot of u' and v' for for Current Only Runs 1 (CO, SB, $U = 0.210$ m/s, Figures a, c, e) and 32 (CO, GB, $U = 0.210$ m/s, Figures b, d, f) for ADV 3, measured in the lower part of the logarithmic profile (a, b), in the upper part (c, d) and in the

freestream (e, f). Results are shown for a threshold Ω of 4. Figure 4.49(a) shows that, the quantity of ejection and sweep events (Q2 and Q4) is larger in comparison with outward and inward interactions (Q1 and Q3) in the lower part of the logarithmic layer. The ratio of Q2 and Q4 events to the Q1 and Q3 events outside of the hyperbolic hole, which comprehend the 31% of all turbulent events, is in the range of $1.62 \div 1.83$. Figure 4.49(b) shows that the presence of a gravel bed determines an increase of intensity of the turbulent fluctuations, shown by the increased dispersion of the turbulent events. Nevertheless, the proportion of ejections and sweep events in comparison with inward/outward interactions are similar to the sand bed case of Figure 4.49(a), with a slight increase in the case of gravel bed (events ratio in the range $2.0 \div 2.25$). This seem to suggest that the presence of the gravel bed induces an increase of intensity of turbulent events, alongside an increase of the relative number of ejections and sweeps. Figure 4.49(c) shows that, over sand bed, in the upper part of the logarithmic layer the distribution of turbulent events in the quadrants changes. Percentage of events inside the hyperbolic hole decreases and more events are distributed in the quadrants. Ejections and sweeps slight increases, but in comparison the larger increase is in the inward/outward quadrants, with a decreasing events ratio of $1.47 \div 1.64$. Moreover, the turbulent events distribution in the quadrants is less elliptical, which indicates a decrease of correlation of u' and w'. This seems to suggest that, farther from the bed, the ejection-sweep cycles as a mechanism of turbulent momentum transfer progressively decreases in favor of a more "isotropic" behavior. Figure 4.49(d) shows that, over gravel bed, closer to the upper limit of the logarithmic layer, the relative number of ejections and sweeps increases to the lower logarithmic limit case of Figure 4.49(b), with an events ratio of $1.90 \div 2.75$. This seem to suggest, alongside with the shape of the turbulent events distribution, that in comparison with the sand bed case of Figure 4.49(c), ejection and sweep events seem to be the main mechanism of turbulent vertical momentum transport even in the upper part of the logarithmic layer. Figure 4.49(e) shows that, in the freestream of the sand bed case, the distribution of turbulent events in the quadrants changes in favour of the inward/outward quadrants. Percentage of events inside the hyperbolic hole decreases and more events are distributed in all the quadrants. Events ratio drops to $1.14 \div 1.47$. Figure 4.49(f) shows that in

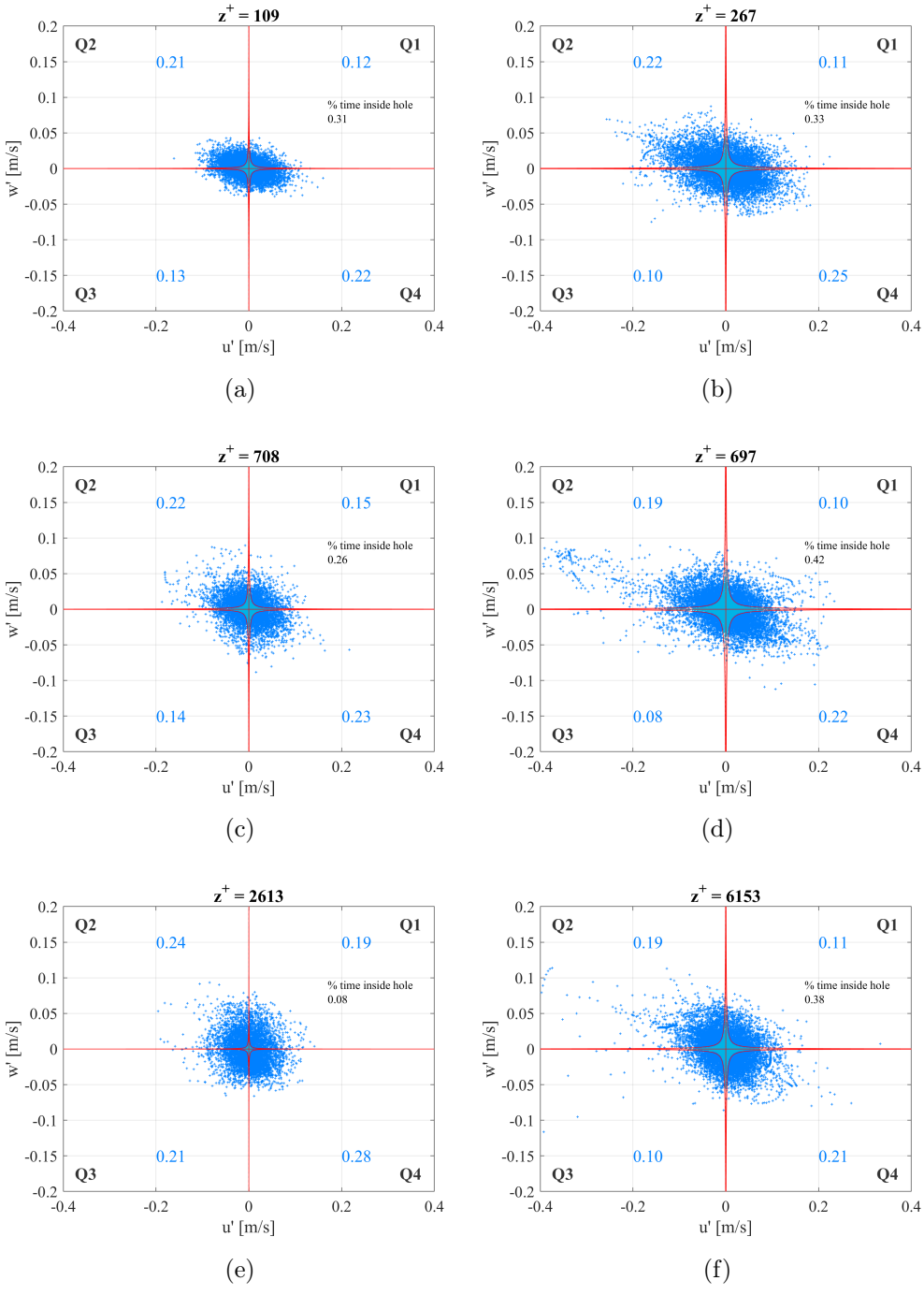

Figure 4.49: Correlation plot of u' and v' measured by ADV 3 at different z^+: (a, c, e) Run 1 (CO, SB, $U = 0.210$ m/s; (b, d, f) Run 32 (CO, GB, $U = 0.210$ m/s.

the freestream of the gravel bed case, the distribution of events is similar inside the logarithmic layer of Figure 4.49(d), with an events ratio of 1.73 ÷ 2.10. However, the overall shape of the events distribution is slightly less elliptical, showing a loss of correlation. Figure 4.50 shows the correlation plot of u' and v' for the waves plus current Run 8 (WC, SB, $U = 0.210$ m/s, Figures a, c, e) and Run 33 (WC, GB, $U = 0.210$ m/s, Figures b, d, f) for ADV 3, measured in the lower part of the logarithmic profile (a, b), in the upper part (c, d) and in the freestream (e, f). Wave condition for both Run 8 and Run 33 is: $H = 0.08$ m, $T = 2.0$ s. Figure 4.50(a) shows the quadrant analysis for the sand bed case, close to the lower limit of the logarithmic layer. In comparison with the current only case of Figure 4.49(a), presence of waves determines an increase in intensity of turbulent events (u', w'), which are more dispersed. The events ratio is larger (2.17) than the current only case (1.62 ÷ 1.83), but the number of turbulent events above the hyperbolic threshold almost halved, and with a number of events inside the hyperbolic hole reaching the 62%. It appears that, the presence of the waves determines a decrease in number of ejections and sweeps, but at the same time an increase in their intensity. A similar situation is observed over the gravel bed in Figure 4.50(b), with an events ratio of 2.11, and a slight decrease of the number of the events above the hyperbolic hole threshold in comparison with Figure 4.49(b). In the upper logarithmic layer (Figures 4.50(c) and d) the overall distribution of extreme events is similar, with an events ratio which slight decreases for the sand bed case (1.89 ÷ 2.25) and has a very slight increase for the gravel bed (2.25). Figures 4.50(e) and f show the quadrant analysis in the freestream, with a larger dispersion in comparison with Figures 4.49e and f.

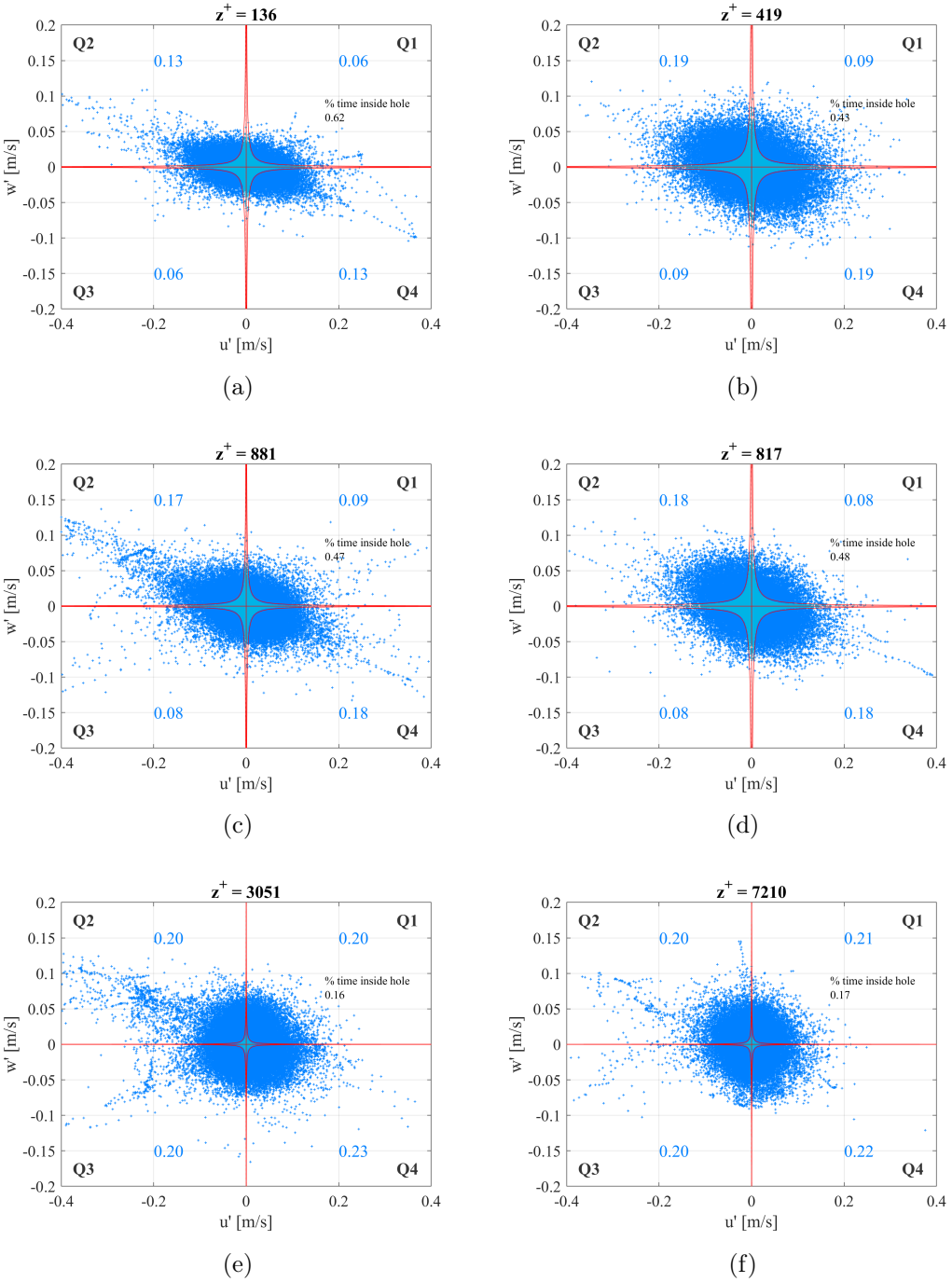

Figure 4.50: Correlation plot of u' and v' measured by ADV 3 at different z^+.: (a, c, e) Run 8 (WC, SB, $U = 0.210$ m/s, $H = 0.08$ m, $T = 2.0$ s; (b, d, f) Run 33 (WC, GB, $U = 0.210$ m/s, $H = 0.08$ m, $T = 2.0$ s).

4.6 Discussion of results

The mean flow analysis showed that the current flow is always significantly modified by the presence of waves. In order to provide an overall insight on how superposition of the oscillatory flow affects the bottom friction experienced by the current, Figures 4.51 and 4.52 show the wave-current parameter U_w/U_c, plotted against the shear Reynolds number ratio Re^*_{CO}/Re^*_{WC}, which instead is an indicator of the shear experienced by the current in the combined flow relative to the current only case. Figure 4.51 resumes what already observed by the logarithmic profiles and described above, in terms on how the shear in the current direction is influenced by the presence of waves. The grey continuous line indicates the boundary between current- and wave-dominated regimes, at the left and right side of the line respectively.

Two cases can be distinguished depending on the strength of the current, expressed in the form of the Froude number Fr $(= U/\sqrt{gh})$. In the presence of a "stronger" current ($Fr = 0.106$, $U = 0.210$ m/s), the superposition of the oscillatory flow always determines an increase of bed resistance, as shown by the Re^*_{WC}/Re^*_{CO} being always above unity. The generation of the wave boundary layer seems to determine a turbulence enhancement, proved by the increase in shear velocity and apparent roughness. This is in accordance with most of experimental evidence in the literature (Grant and Madsen, 1979; Fernando et al., 2011). Nevertheless, as the relative importance of the waves increases, i.e. as the parameter U_w/U_c increases, shear seems to be enhanced in a non-monotonous fashion. Specifically, three regions can be identified. A first region, approximately where $U_w/U_c < 0.6$, thus where current dominates, in which shear seems to increase. A second region, approximately in between $0.8 < U_w/U_c < 1.35$, in which a constant trend is observed as U_w/U_c increases, and a third region, where waves dominates ($U_w/U_c < 1.35$) and in which shear experienced by the current seems to increase again. Apparently these regions are observed regardless of the characteristics of the bottom, although there are only sand bed runs in the third wave-dominated region.

This behavior recalls what has been already observed by Lodahl et al. (1998), who performed experiments of co-linear waves and currents in an oscillating water tunnel with a broad range of Re_c ($1500 \div 160000$) and Re_w ($200 \div 940000$), therefore

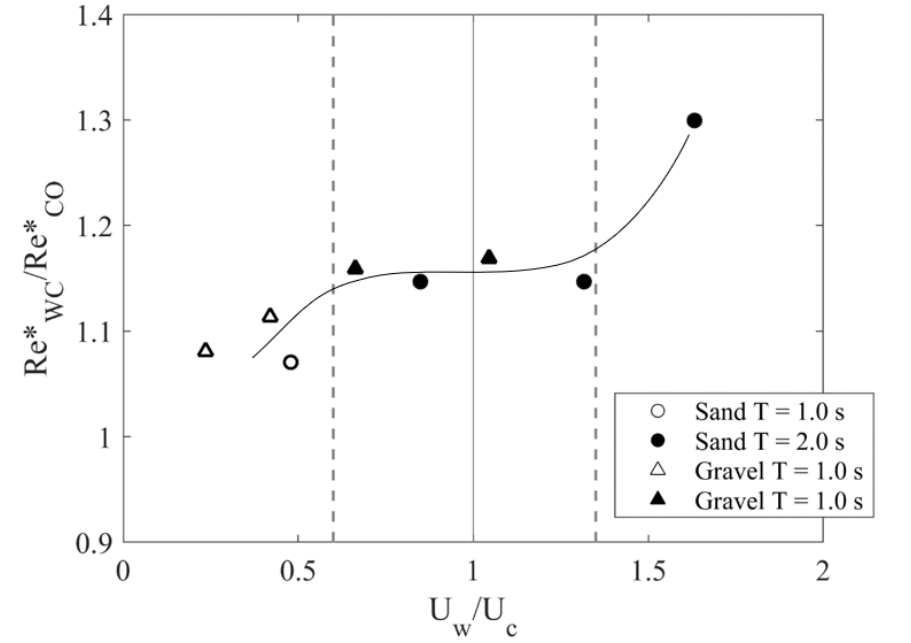

Figure 4.51: Wave-current regime parameter U_w/U_c vs the shear Reynolds number ratio Re^*_{WC}/Re^*_{CO} for WC runs with $Fr = 0.106$ ($U = 0.210$ m/s).

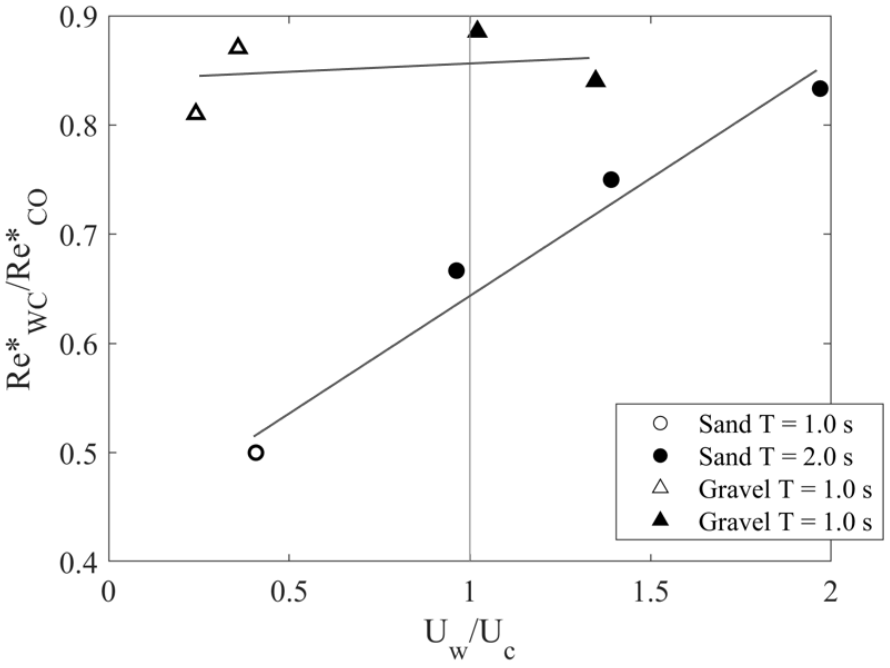

Figure 4.52: Wave-current regime parameter U_w/U_c vs the shear Reynolds number ratio Re^*_{WC}/Re^*_{CO} for WC runs with $Fr = 0.058$ ($U = 0.140$ m/s).

including the range of our experiments ($Re_c = 81921 \div 111937$) They found that, in the current dominated regime, i.e. where $U_w/U_c < 1$, the relation between the shear stresses of the combined flow and the lone current are constant, whereas in the wave dominated regime ($U_w/U_c > 1$) two behaviors have been observed. If both boundary layers are turbulent, the shear stresses ratio increases linearly, whereas if the wave boundary layer instead is laminar a relaminarization process, intended as a local decrease of the bed shear stress ratio, may occur. Nevertheless, some differences can be observed between our findings and the ones by Lodahl et al. (1998). First of all, in the study by Lodahl and authors, in the constant region no increase of shear is observed, whereas in our case we always observe an increase in bottom friction when waves are superposed onto the current. Moreover, when the current dominates, a friction gradient is observed in our experiments, which is never observed by Lodahl et al. It must be take into account that the ones by Lodahl and authors are very different experiments, carried out in a oscillating water tunnel, therefore without any free surface effect and with colinear waves and current, thus with no three-dimensional wave-current interaction.

In presence of a "weaker" current ($Fr = 0.058$, $U = 0.140$ m/s), a very different trend is observed, in which the superposition of waves determines a decrease of flow resistance, observed by the ratio Re^*_{WC}/Re^*_{CO} which is always below 1. Such results have not been observed commonly in wave-current experiments. A similar process has been observed by (Musumeci et al., 2006), in which the presence of waves over rough bottom, determined a decrease in the apparent roughness. Their experiments were however in the wave dominated regime ($U_w/U_c = 2.02 \div 4.76$) with very different ranges of Re_c ($13252 \div 14192$) Re_w ($1123 \div 12260$). Moreover, in our waves plus current experiments apparent roughness decrease is also accompained with a shear velocity decrease, whereas a shear velocity increase is always observed in (Musumeci et al., 2006). In the present tests, the shear increase is apparently linear in the sand bed case, and the flow resistance experienced by the current increases as the orbital velocity U_w increases. With the same Fr but over a gravel bed the behaviour is different. In the current dominated regime the current experiences a larger flow resistance in comparison with the sand bed with the same current, although as U_w increases the shear experienced by the current seems to remain

constant.

The comparison of the combined flow experimental velocity profiles with a selection of models showed that, for the performed wave-current conditions, the best performance is achieved by the Grant and Madsen (1986) model, which estimated satisfactorily the experimental combined flow velocity profiles and shear velocity. The empirical formulation by Soulsby (1997) and the Styles et al. (2017) three-layers eddy viscosity model both underestimated velocity profile of sand bed cases, whereas respectively under- and overestimating velocity profiles in gravel bed experiments.

The phase-averaged flow analysis showed a mutual veering effect in the combined flow. The superposition of the current seems to determine a veering of the wave motion in the current direction, which seems to occur regardless of the roughness of the bottom. In turn, the wave motion seems more effective in operate a current deviation in the lower part of the water column, which characteristics seems to be related to the wave-current parameter U_w/U_c and the bottom roughness.

An attempt to investigate wave-current turbulent flow has been carried out by analysing turbulent velocity related quantities. Results show that combined flow turbulence intensity profiles may show very different patterns depending on the bed and current velocity condition.

In the presence of a stronger current, the superposition of the waves always determined an increase of turbulent activity with respect to the current only case, which confirms what already observed in the mean flow analysis of the corresponding cases. Moreover, results of the cases closer to the limit between current- and wave-dominated regimes ($U_w/U_c = 1$) reveals very similar turbulent intensity profiles and gradients, which is an agreement with what overall trend observed in Figure 4.51.

When waves are superposed to a weaker current over gravel bed, a decrease of bottom turbulence intensity is observed in the very proximity of the bed, while an increase occurs in the rest of the water column. The superposition the of waves also seems to determine a slight reduction of the turbulence intensity profile gradient. The combination of this occurrences may be related to the decrease of shear observed in the mean flow analysis. Nevertheless, the same has not been observed in the sand bed case with the same Fr current.

Quadrant analysis showed that, in presence of a pure current, rough bed

determines the ejection-sweep mechanism to involve a larger part of the water column, which recalls the behavior already observed in the turbulent intensity profiles. Superposition of the oscillatory flow seems to determine an increase of turbulent events intensity, which is eventually responsible for the shear stress increase at the bottom observed in the mean flow analysis. Such increase is however accompanied with an absolute decrease of number of ejection and sweep events, which suggest a suppression of ejection-sweep events and an enhancement of their intensity. A possible explanation could be that in certain phases of the wave, the ejections-sweeps events may be enhanced or suppressed, depending on the stage of the wave boundary layer generation. However, this conclusion should be supported by a phase-averaged quadrant analysis, which is not included in the current work.

Chapter 5

Wave-current interaction at a right angle over sloping beds

5.1 Overview

In this Chapter the results of the ACCLIVE campaign data analysis are presented and discussed. First, a preliminary investigation on the surface elevation and flow velocity time series has been conducted in order to characterize the experimental conditions, in terms of their time and space variability. Subsequently, time-, phase-averaged and turbulent velocity data of Current Only and Waves plus Current runs are compared and the results are discussed for mean, phase-averaged and turbulent flow.

5.2 Preliminary data analysis

In this Section a preliminary investigation on the surface elevation and velocity time series is presented. Figure 5.1 shows the phase-averaged wave surface elevation for Run 9, measured in the correspondence of the flat bottom (x = 1.70 m, y = -1.00 m, $h = h_0$ = 0.30 m), close to the wavemaker. The number of wave cycles used to compute the ensemble averaged wave is 600, which is much larger than the 50 wave cycles minimum recommended by Sleath (1987) to compute phase-averaged wave quantities. A larger variability of the wave surface elevation time series compared to the phase-averaged wave is observed in correspondence of the wave crest,

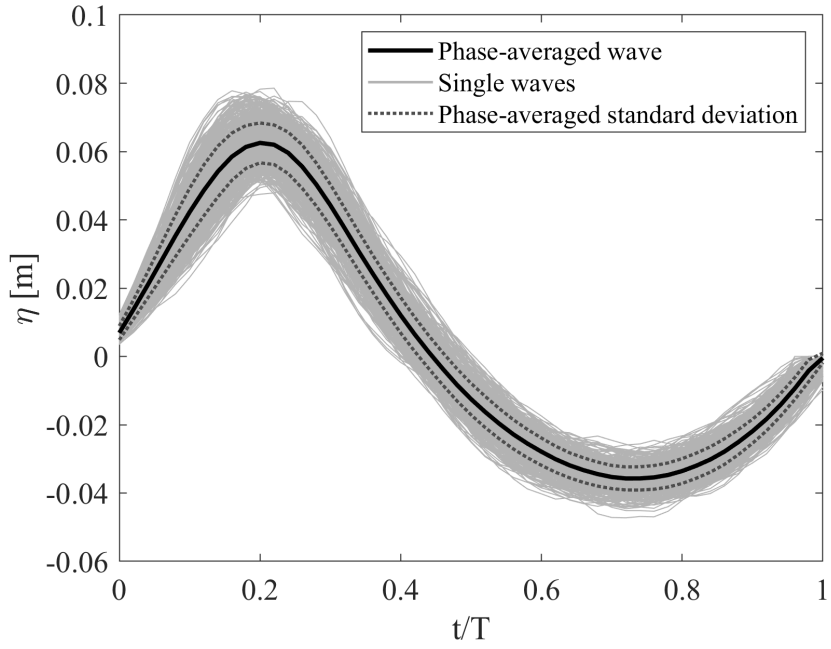

Figure 5.1: Phase-averaged wave surface elevation $\tilde{\eta}$ superposed to the surface elevation η time series for Run 17.

being equal to $\pm$ 0.0058 m, and corresponding to 7% of the wave height. Average standard deviation at the wave crest for all the runs is 7%, with a maximum of 15% for Run 12. Wave peak period satisfactorily corresponds to the target of 1.0 s, with an average deviation of 2% and a maximum of 4% for Run 9. Shallowness h/gT^2 and wave height H/gT^2 parameters have been computed in order to characterize the generated wave field (Dean, 1970). Over the horizontal bottom of the wave tank ($h_0 = 0.3$ m), the average shallowness parameter for all runs is 0.030, whereas average nonlinear parameter is 0.012, therefore generated waves can be considered weakly nonlinear waves propagating in intermediate depth, in the range of validity of Stokes 5^{th}-order wave theory, relatively close but never exceeding the wave breaking limit, $H/h = 0.8$. In the acquisition area, over the sloping bed, the shallowness parameter ranges from to 0.028 to 0.024 as depth decreases along the beach slope, therefore wave shoaling is expected, although also here the waves never reach the wave breaking limit.

A time-variability analysis has been conducted in order to assess the capability to reproduce a steady current using the ACCLIVE experimental setup. Velocity time series have been subdivided into smaller intervals and a statistical analysis has

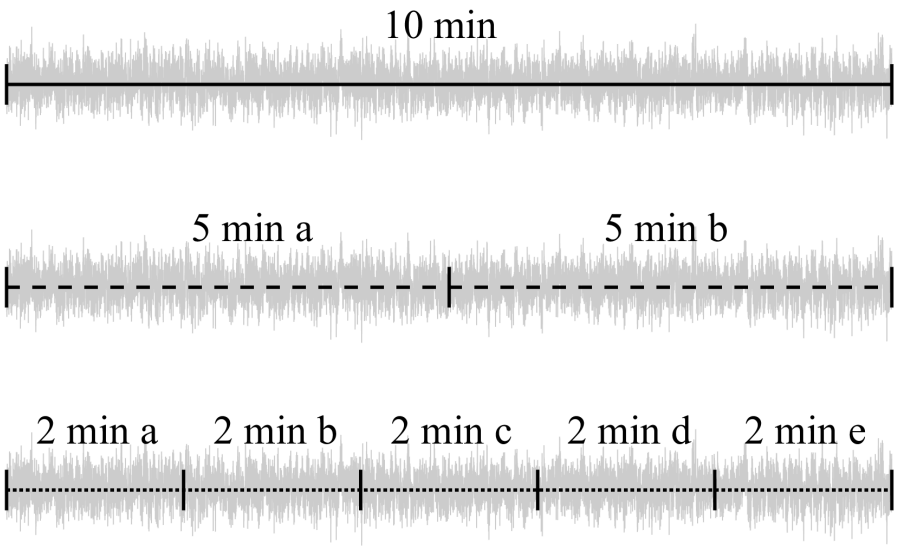

Figure 5.2: Subdivision in time segments of the original 10 minutes time series.

been performed in order to assess the time series variability considering different time spans. Similar approaches have been adopted by Lim and Madsen (2016) and Mathisen and Madsen (1996b). Duration of the measured velocity time series is 10 minutes, which has been divided in 2 segments of 5 minutes each (respectively called: 5 min a, 5 min b) and in 5 segments of 2 minutes (respectively called: 2 min a, 2 min b, 2 min c, 2 min d, 2 min e) as shown in Figure 5.2. Time-averaged velocities $\bar{u}$ and $\bar{v}$ have been computed from the original 10 minutes time series. The time-averaged velocities of the smaller time segments (5 and 2 minutes) have been computed, namely: $\bar{u}_{5,s}$ and $\bar{v}_{5,s}$ which are the 5 minutes segment time-averages of the dimensionless streamwise and crosswise velocities, where s is a specific time segment (namely a or b); and $\bar{u}_{2,s}$ and $\bar{v}_{2,s}$, which are the 2 minutes time-averages of the dimensionless streamwise and crosswise velocities, where s indicates a specific time segment (namely a, b, c, d, or e). In order to compare the variability of the different time spans, the deviation of the time-averaged velocities computed from a shorter time series compared to the one computed from the whole 10 minutes time series have been calculated:

$$\Delta\bar{u}_{10-5s} = \bar{u} - \bar{u}_{u,5,s}; \tag{5.1}$$

$$\Delta\bar{u}_{10-2s} = \bar{u} - \bar{u}_{u,2,s}. \tag{5.2}$$

Deviations of the time-averaged velocities for crosswise and vertical velocities

are computed as well using the same notation. In a similar way, the variability of the standard deviation has been computed as:

$$\Delta\sigma_{u,10-5s} = \sigma_u - \sigma_{u,5,s}; \tag{5.3}$$

$$\Delta\sigma_{u,10-2s} = \sigma_u - \sigma_{u,2,s}; \tag{5.4}$$

where σ_u is the standard deviation of u for the 10 minutes time series, $\sigma_{u,5,s}$ is the standard deviation of the 5 minutes time series for the segment s (a or b), $\sigma_{u,2,s}$ is the standard deviation of the 2 minutes time series for the segment s (a, b, c, d, or e). Standard deviation differences for crosswise velocities are computed as well using the same notation.

Figure 5.3 shows the dimensionless time-averaged velocities for Run 3 (CC, CO, $U = 0.14$ m/s) $\bar{u}/U$ (5.3a) and $\bar{v}/U$ (5.3b) for the following timespans: 10 minutes (continuous line), 5 minutes (dashed lines), 2 minutes (dotted lines); error bars indicate dimensionless standard deviation for the 10 minutes time series σ_u/U. Figure 5.3a shows that the time-averaged velocity profiles are quite similar for all the considered timespans. This suggests that the steadiness of the current is mantained fairly well for the entire duration of each experiment even for the smallest examined time segment, with depth-averaged deviations $\Delta\bar{u}_{5,s}/U < 0.01$, $\Delta\bar{u}_{2,s}/U < 0.02$ and a maximum of 0.06. Dimensionless standard deviation σ_u/U shown by the error bars is quite similar at every measuring position z, with a depth-averaged mean of 0.23 ($\pm$ 0.02).

The dimensionless time-averaged velocity profiles of $\bar{v}/U$ in Figure 5.3b show a behavior similar to the one of $\bar{u}/U$, with depth-averaged $\Delta v_{5,s}/U < 0.01$ and $\Delta v_{2,s}/U < 0.02$ and a maximum of 0.05. Dimensionless standard deviation σ_u/U shown by the error bars is again quite similar at every measuring position z with a depth-averaged value of 0.24 ($\pm$ 0.01). Figure 5.3c shows the dimensionless variability of standard deviation of the 10 minutes time series versus the 5 minutes one ($\Delta\sigma_{u,10-5s}/U$, dashed line) and the 2 minutes one ($\Delta\sigma_{u,10-2s}/U$, dotted lines) for Run 3 (CO, CC, $U = 0.14$ m/s) for streamwise (5.3c) and crosswise (5.3d) velocity. Results indicate that $\Delta\sigma_u/U$ is always below 0.01, with larger deviation peaks observed at the bottom below $z/h_0 = 0.1$. The proximity of the bed may determine local turbulent fluctuations which disappear as a result of the time average as

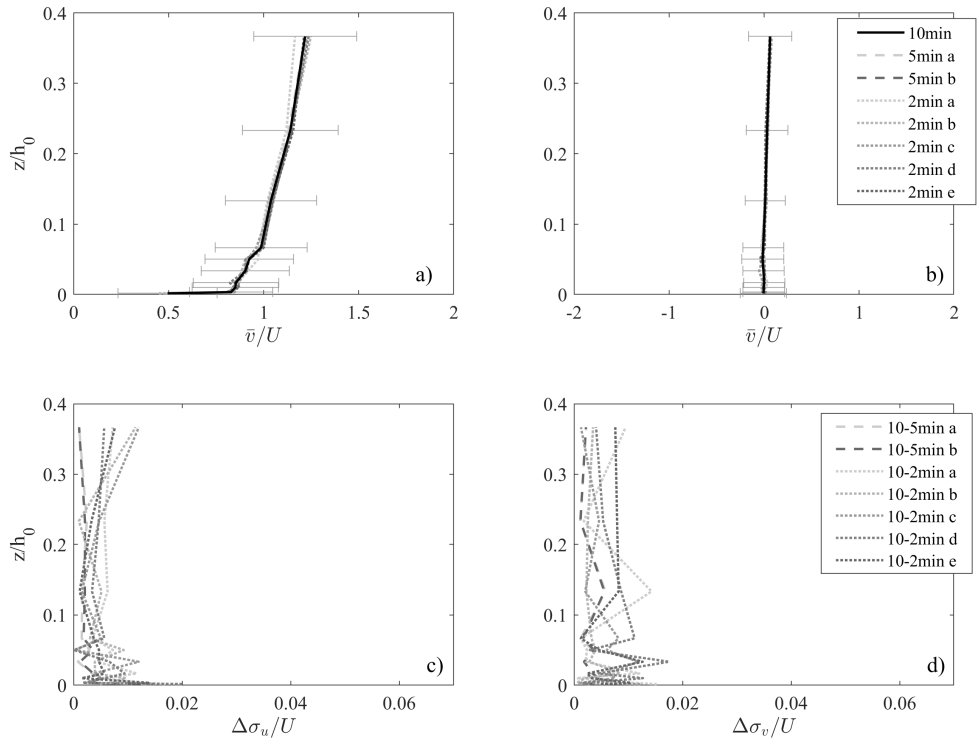

Figure 5.3: Velocity time variability for Run 3 (CO, CC, $U = 0.14$ m/s): Dimensionless time-averaged velocity profiles with the different timespans for streamwise (a) and crosswise (b) velocities; dimensionless standard deviation relative to differences with the 10 minutes timespan for streamwise (c) and crosswise (d) velocities.

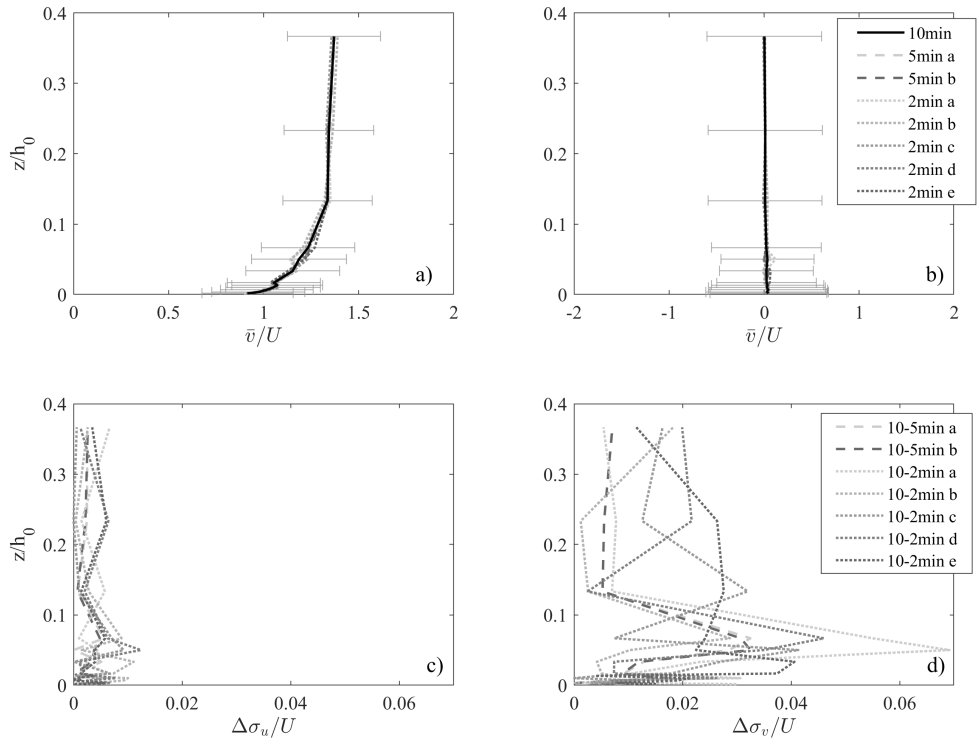

Figure 5.4: Velocity time variability for Run 9 (WC, CC, $U = 0.14$ m/s): Dimensionless time-averaged velocity profiles with the different timespans for streamwise (a) and crosswise (b) velocities, dimensionless standard deviation relative to differences with the 10 minutes timespan for streamwise (c) and crosswise (d) velocities.

the run duration increases. Nevertheless, the difference between the two 5 minutes runs is relatively small for all the considered time spans. Dimensionless standard deviation differences of the crosswise velocity in Figure (5.3d) show a very similar behavior, which is below 0.02 all along the water column and for all the time spans.

Figure 5.4 shows the dimensionless time-averaged velocity profiles for Run 9 (WC, CC, $U = 0.14$ m/s) of streamwise (5.4a) and crosswise (5.4b) velocity for the following time spans: 10 minutes (continuous line), 5 minutes (dashed line) and 2 minutes (dotted line); error bars indicate dimensionless standard deviation of the 10 minutes time series. Measuring position and current mean velocity U are the same of Run 3, but in Run 9 waves are superposed to the current. Error bars in Figure 5.4a shows that the presence of waves does not induce a significant change of variability, since the depth-averaged σ_u is 0.24 ($\pm$ 0.01), i.e. equal to the one in the absence of waves. Difference in time-averaged velocity $\Delta u_{5,s}/U$ and $\Delta u_{2,s}/U$ are below 0.01

and 0.02 respectively, as for Run 3. Figure 5.4b shows that the presence of the superposed oscillatory motion determines an increase of variability in terms of σ_v/U (depth-averaged 0.08 $\pm$ 0.01) in comparison with Figure 5.3b. Variability between time spans $\Delta u/U$ is however lower than the current only case ($<$ 0.01 for both 5 and 2 minutes time spans). Figure 5.4 shows dimensionless standard deviation differences for streamwise (5.4c) and crosswise (5.4d) velocity profiles for Run 9. Comparison between Figures 5.3c and 5.4d indicates that the variability between time spans is quite similar to the ones already observed in the current only case. On the other hand, Figure 5.4d shows instead a significant increase in dimensionless standard deviation variability between time spans in the crosswise direction, which may reach 0.07 close to the bottom.

An investigation aimed at studying the flow field at different positions in the wave tank for the CO cases, i.e. at different water depth and along the current, has been performed. As a remainder from the experimental setup Section 3.3, the acronyms used to indicate the ADV positions in the tank are the following (refer to Figure 3.7b): central position (CC, x = 2.50 m, y = 1.00 m; h = 0.26 m); upstream position (US, x = 2.25 m, y = 1.00 m; h = 0.26 m); downstream position (DS, x = 2.75 m, y = 1.00 m; h = 0.26 m); shoreward position (SH, x = 2.50 m, y = 1.50 m; h = 0.24 m); seaward position (SE, x = 2.50 m, y = 0.50 m; h = 0.28 m). Figure 5.5a and 5.5b shows the dimensionless time-averaged $\bar{u}/U$ and $\bar{v}/U$ velocity profiles in the streamwise and crosswise directions for the CO Runs 2, 4 and 5, (CC, US and DS respectively), thus at measuring positions all aligned in the current direction (y = 1.00 m), having the same local water depth h = 0.26 m. Figure 5.5a shows that a steady unidirectional current in the x direction is satisfactorily achieved, as the velocity profiles aligned in the x direction have the same velocity distribution along the water column. The upper part of the velocity profile at DS shows an increase in velocity in comparison with the other two positions. As this position is closer to the current outlet, the flow may be affected by the presence of a slightly faster current downstream of the outflow section, which may determine the upper part of the profile to be accelerated. Nevertheless, depth-averaged difference between dimensionless time averaged velocities is less than 0.01 of U.

Figure 5.5b shows the dimensionless time-averaged velocity profiles $\bar{u}/U$ and

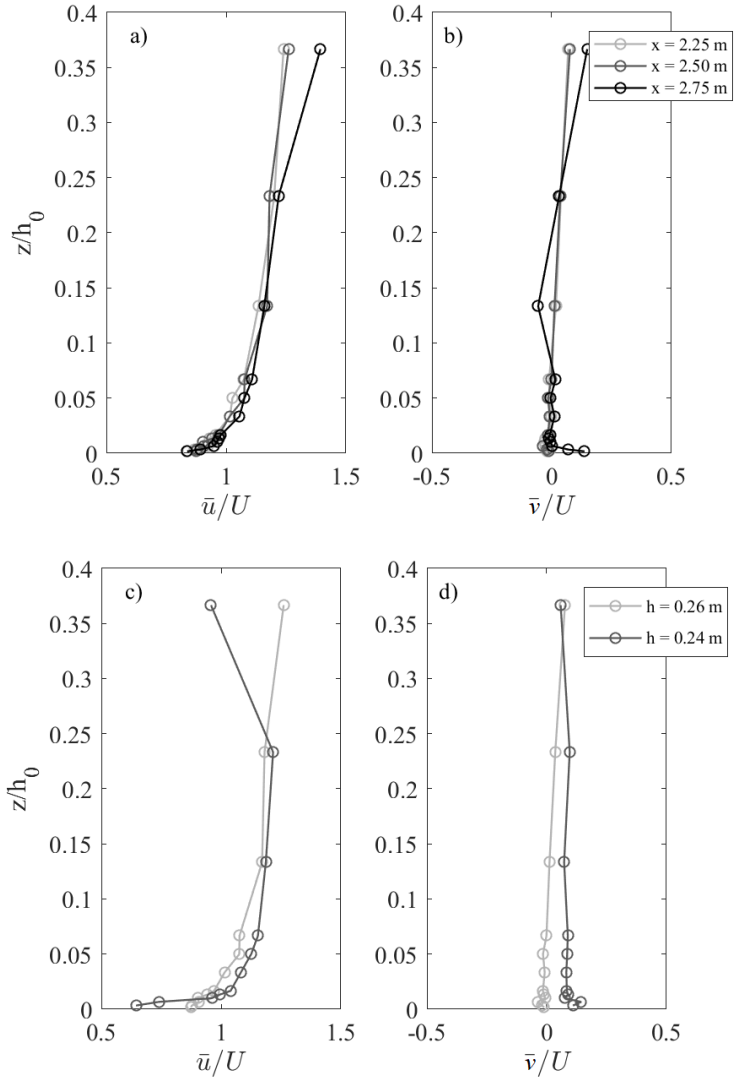

Figure 5.5: Dimensionless time-averaged $\bar{u}/U$ and $\bar{v}/U$ velocity profiles in the streamwise and crosswise directions: (a) velocity profiles for the CO Runs 2, 4 and 5, (CC, US and DS respectively) thus all aligned in the x direction ($y = 1.00$ m) having the same local water depth $h = 0.26$ m; (b) velocity profiles for Runs 2 and 6, (CC and SH respectively) thus both aligned in the y direction ($x = 2.50$ m) with local water depth of $h = 0.26$ m and 0.24 m respectively.

$\bar{v}/U$ for Runs 2 and 6, (CC and SH respectively) thus both aligned in the y direction ($x = 2.50$ m), with local water depth $h = 0.26$ m and 0.24 m respectively. Figure 5.5b shows that $\bar{u}/U$ velocity profile of Run 6 (SH, $h = 0.24$ m), which is more shoreward and at a shallower depth in comparison with Run 2 (CC, $h = 0.26$ m), presents a velocity decrease close to the bed and an increase in the central part of the water column. Indeed, as the discharge of the mean current velocity is constant and the local water depth is shallower, the current shows an overall velocity increase as an effect of mass continuity. Due to the increase of velocity, an increased bottom resistance is experienced by the current, which shows a more turbulent velocity distribution close to the bottom, compensated by a velocity increase over the rest of the water column. Velocity profiles of $\bar{v}/U$ highlight the existence of a shoreward directed mean flow all along the water column. This suggests that at the positions shoreward from the central axis of the inflow/outflow sections ($y = 1.00$ m), a recirculation region may be generated inside the tank, determining the current to veer in the shoreward direction. This veering effect is indeed not observed along the central axis while may reach a maximum value of 10% of U at SH.

Figure 5.6 presents the dimensional time-averaged velocities $\overline{u}$ and $\overline{v}$ for CO Runs 1, 2 and 3 which are at the same position in the tank (CC) but with different mean current velocity U, equal to 0.06, 0.11 and 0.14 m/s respectively. Velocity have been plotted dimensionally in order to appreciate the differences in the velocity profile between runs with different U. It can be observed that the $\bar{u}$ velocity distribution follows the increase of mean velocity U. The increase of the mean current velocity determines the velocity distribution to be altered, determining progressively larger turbulence-induced flow resistances at the bottom as U increases, as proven by the increase of the velocity gradient in the vertical direction. Velocity profiles in the crosswise direction $\bar{v}$ show values close to zero for all runs along the whole water column, indicating that the current remain unidirectional at $y = 1.00$ m even with increasing mean current velocity. Moreover no veering in the crosswise direction is observed, showing that the velocity field at $y = 1.00$ m (CC, US and DS) is not affected by the recirculation region for all the considered mean current velocities.

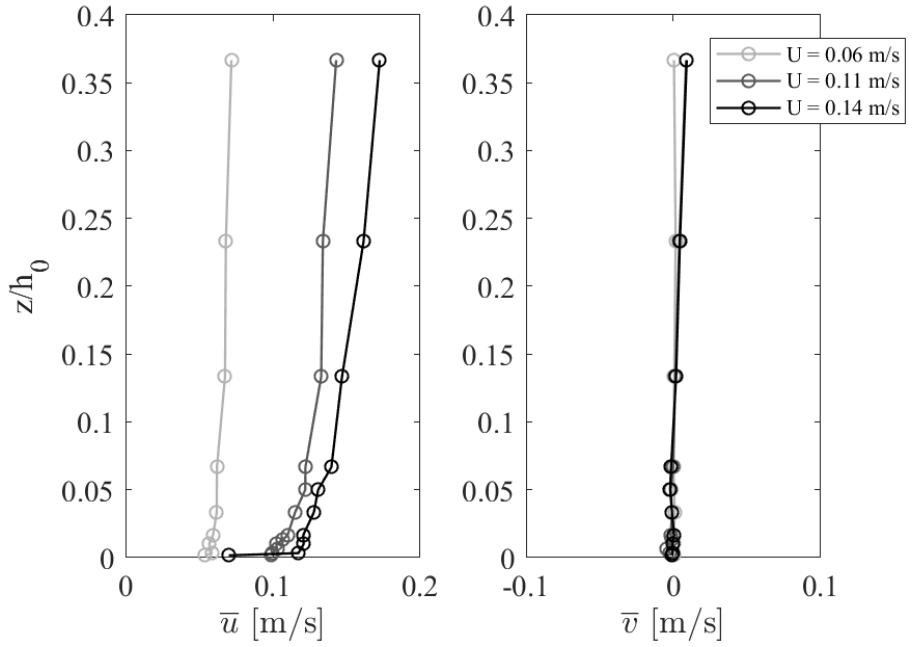

Figure 5.6: Dimensional time-averaged velocity profiles $\overline{u}$ (a) and $\overline{v}$ (b) directions for Runs 1, 2 and 3 (CO). All the runs share the same ADV position (CC, $h = 0.26$ m) but have different U.

5.3 Mean flow analysis

A comparative analysis of CO and WC time-averaged velocity profiles is carried out in the following, in order to investigate how the mean current flow is affected by the superposition of waves.

Hydrodynamics quantities and nondimensional parameters have been computed from the velocity profiles. Current freestream velocity U_c have been computed by depth-averaging the time-averaged velocity outside the current boundary layer. Wave orbital velocity has been computed by considering the phase-averaged velocity maximum at the first measurement point above the wave boundary layer thickness, computed according to Sleath (1987) as:

$$\delta_w = 3\sqrt{\frac{2\nu}{\omega}}. \tag{5.5}$$

where here ω is the wave angular frequency. Current and wave Reynolds number (Re_c and Re_w respectively) are then computed:

$$Re_c = \frac{U_c h}{\nu}; \qquad Re_w = \frac{U_w a}{\nu}; \tag{5.6}$$

Table 5.1: Hydrodynamic quantities and parameters for all runs: current freestream velocity U_c, wave orbital velocity U_w, shear velocity u^*, current boundary layer thickness δ_c, wave-current regime parameter U_w/U_c, current Reynolds number Re_c, wave Reynolds number Re_w, and relative water depth Kh, where K is the wave number.

Run	U_c [m/s]	U_w [m/s]	u^* [m/s]	k_s [m]	δ_c [m]	U_w/U_c	Re_c	Re_w	Kh
1	0.07	-	0.019	$3.0 \cdot 10^{-10}$	0.086	-	18694	-	-
2	0.14	-	0.031	$3.6 \cdot 10^{-7}$	0.081	-	37184	-	-
3	0.17	-	0.034	$4.0 \cdot 10^{-6}$	0.080	-	44857	-	-
4	0.14	-	0.030	$2.7 \cdot 10^{-7}$	0.074	-	36550	-	-
5	0.14	-	0.031	$2.7 \cdot 10^{-7}$	0.089	-	35952	-	-
6	0.14	-	0.034	$6.8 \cdot 10^{-7}$	0.081	-	33120	-	-
7	0.12	-	0.009	$1.1 \cdot 10^{-2}$	0.082	-	33983	-	-
8	0.17	0.22	0.038	$5.4 \cdot 10^{-7}$	0.080	1.36	42991	9549	0.19
9	0.19	0.23	0.043	$4.3 \cdot 10^{-6}$	0.079	1.17	50436	9637	0.19
10	0.15	0.21	0.028	$3.6 \cdot 10^{-9}$	0.073	1.38	39912	8988	0.19
11	0.16	0.31	0.058	$4.5 \cdot 10^{-5}$	0.088	1.93	41303	13029	0.19
12	0.16	0.27	0.041	$2.1 \cdot 10^{-6}$	0.080	1.72	37405	11379	0.18
13	0.11	0.24	0.006	$2.4 \cdot 10^{-4}$	0.083	2.23	30719	10379	0.20

Shear velocity u^* and equivalent roughness k_s are estimated by the time-averaged velocity profiles by means of best fit method (Sumer, 2007). The main hydrodynamic quantities and nondimensional parameters are shown in Table 5.1.

Figure 5.7 shows the local wave steepness H/L as a function of the relative depth h/L_∞, where L_∞ is the wavelength at infinite depth according to linear wave theory:

$$L_\infty = \frac{gT^2}{2\pi}. \tag{5.7}$$

As no resistive wave gauges could not be deployed in the correspondence of the velocity measurement points, the wave height of the ACCLIVE experiments has been computed considering the linear shoaling coefficient K_s and the wave height at infinite depth H_∞. The shoaling coefficient is equal to the ratio between the incident shoaling wave height and the wave height at infinite depth H_∞, and it can be com-

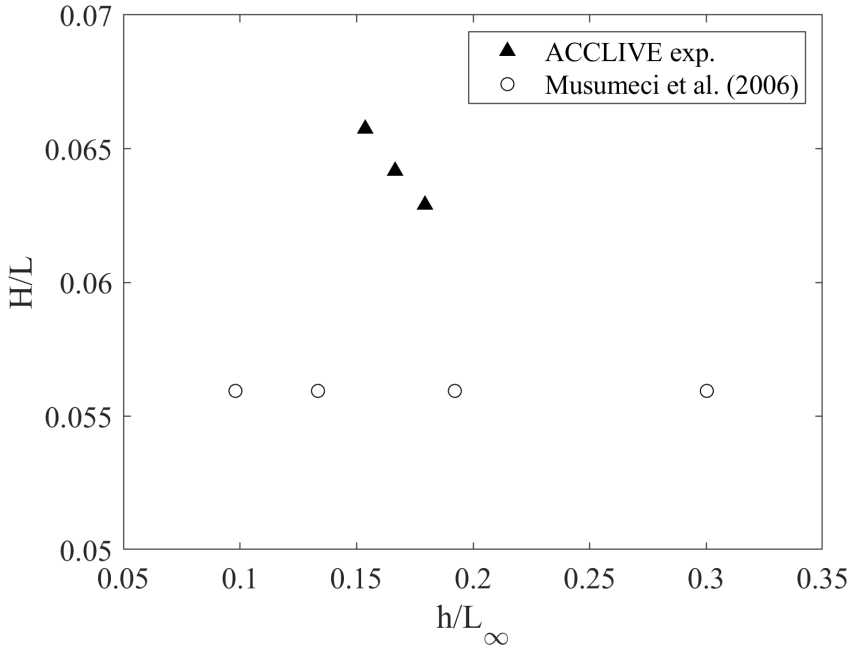

Figure 5.7: Wave steepness H/L_∞ as a function of relative depth for ACCLIVE (a) and Musumeci et al. (2006) (b) combined flow experiments.

puted by the following:

$$K_s = \sqrt{\frac{2\cosh^2 Kh}{\sinh 2Kh + 2Kh}}, \tag{5.8}$$

where K is the wave number estimated by using the linear dispersion relationship.

Wave steepness of Musumeci et al. (2006) experiments, which have been conducted in the same experimental facility but over a flat fixed sand bottom, has been also plotted in Figure 5.7. Water depth of Musumeci's experiments is equal to 0.30 m, wave height is $0.083 \div 0.106$ m and wave period is $0.8 \div 1.4$ s. Although there are some differences between ACCLIVE and Musumeci's in terms of experimental setup and performed wave conditions, the two experiments are comparable, as the ACCLIVE wave condition ($H = 0.085$ m, $T = 1.0$ s) lies within the wave height and period of Musumeci's and the bottom physical roughness of Musumeci's ($d_{50} = 0.24$ mm) is close to the one of smooth concrete of the ACCLIVE experiments The current discharge in Musumeci et al. experiments is 0.033 m^3/s, only the ACCLIVE experiments with the same current discharge (Runs 2, 4, 5, 6, 7, 8, 10, 11, 12, 13) have been considered here for the comparison. The figure reveals that the ACCLIVE experiments lie within the range of Musumeci's experiments relative depth, although

wave steepness increases in the ACCLIVE experiments as the relative depth decreases, which indicate the occurrence of wave shoaling.

Figure 5.8a shows the logarithmic profiles of $\bar{u}/U$ and the velocity profiles of $\bar{v}/U$ for Runs 2 (CO) and 8 (WC), at CC with mean current velocity $U = 0.11$ m/s. Velocities are plotted versus the bed distance in wall units $z^+ = z\nu/u^*$, where u^* is the shear velocity. Dashed lines indicate the current boundary layer thickness δ_c for the CO (grey) and WC (black) conditions, continuous lines show the linear fitting of the velocities inside the logarithmic layer. In comparison with the CO case, superposition of waves determines a velocity increase in the logarithmic layer (depth-averaged $\Delta u = u_{WC} - u_{CO} = 0.18$) and a decrease in proximity of the bed. This suggests the occurrence of an increased bottom resistance due to the superposition of the wave boundary layer on the current, which enhances turbulence mixing in the proximity of the bed. This observation is confirmed by the increase of the shear velocity u^* from 0.031 m/s to 0.038 m/s (18%) and the increase in apparent roughness from 3.6 to 5.4 $\cdot 10^{-7}$ m (33%).

Figure 5.8b shows the logarithmic profiles of $\bar{u}/U$ and $\bar{v}/U$ for Runs 3 (CO) and 9 (WC) with $U = 0.14$ m/s. Both runs are at CC. The position is the same as Runs 2 and 8, whose logarithmic profiles are reported in Figure 5.8a, but in the presence of a stronger current, a larger velocity difference between CO and WC profiles is observed in the x direction (depth-averaged $\Delta\bar{u}/U = 0.30$). Presence of waves induces an increase in bottom friction which leads to the increase in shear velocity u^* from 0.034 to 0.043 m/s of the WC case (21%). The sole current is stronger than the case shown in Figure 5.8a ($Re_c = 37184$ for Run 2, $Re_c = 44857$ for Run 3). No significant increase of apparent roughness k_s is observed, from 4.0 to 4.3 $\cdot 10^{-6}$ m, which is however an order of magnitude larger of the case with current mean velocity $U = 0.11$ m/s. Figure 5.8c shows the logarithmic profiles of $\bar{u}/U$ and $\bar{v}/U$ for Runs 6 (CO) and 12 (WC) with $U = 0.11$ m/s at SH, thus at a shallower water depth than the runs shown in Figure 5.8a and 5.8b, but with the same U of the run shown in Figure 5.8a. The presence of waves still determines an overall velocity increase of the current ($\Delta u = 0.08$) but to a lesser extent than the case of Figure 5.8a with a larger h. The superposition of waves induces an increase of turbulence at the bottom, proved by the increase of shear velocity u^* from 0.034 m/s for the

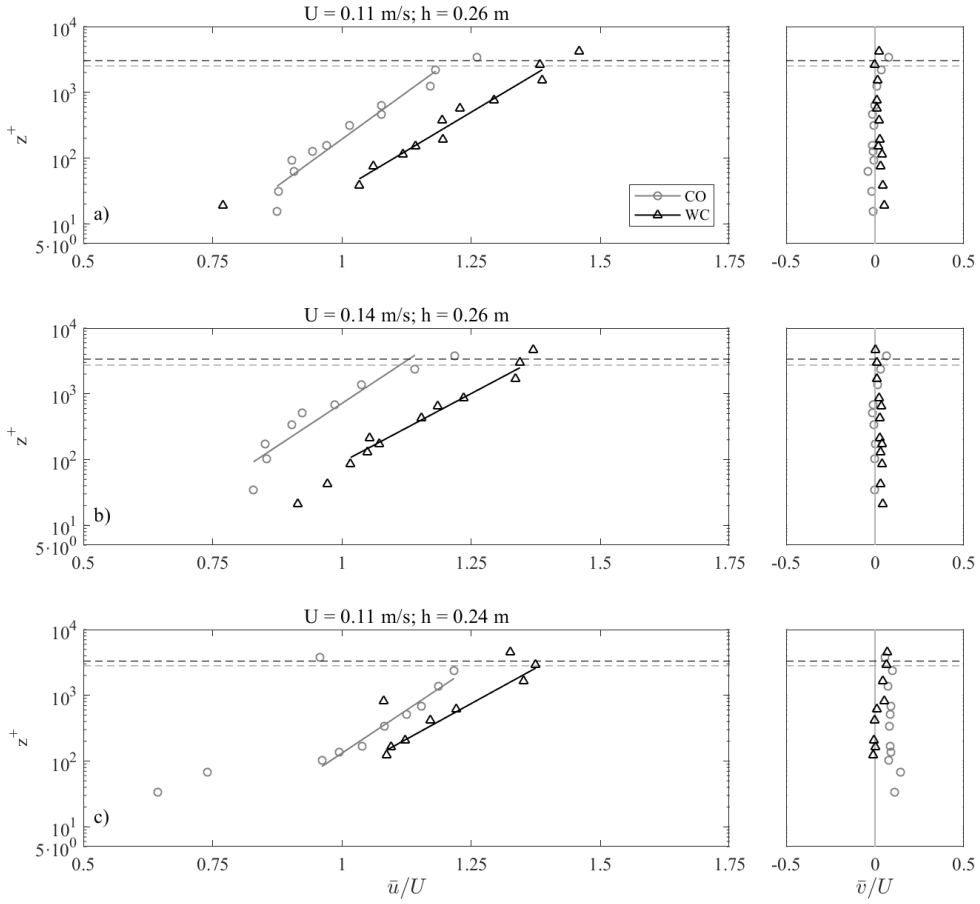

Figure 5.8: Dimensionless time-averaged logarithmic velocity profiles in the streamwise (left panels) and crosswise (right panels) direction: (a) Runs 2 (CO) and 8 (WC) at CC with $U = 0.11$ m/s; (b) Runs 3 (CO) and 9 (WC) at CC with $U = 0.14$ m/s; (c) Runs 6 (CO) and 12 (WC) at SH with $U = 0.11$ m/s. Measuring station is at CC ($x = 2.50$ m, $y = 1.00$ $h = 0.26$ m). Dashed lines indicate the current boundary layer thickness δ_c for the CO (grey) and WC (black) cases.

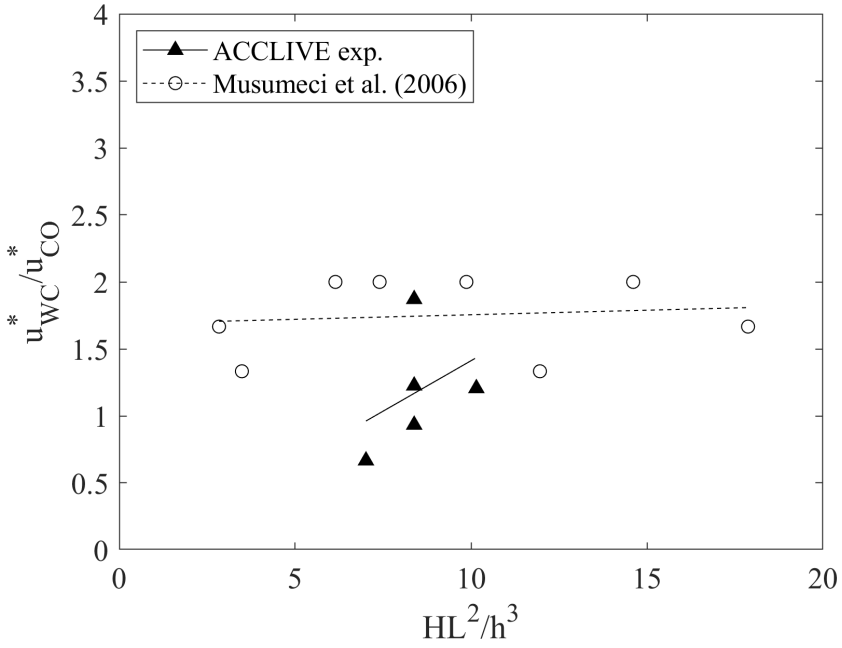

Figure 5.9: The friction velocity ratio u^*_{WC}/u^*_{CO} versus the Ursell number HL^2/h^3 for ACCLIVE and Musumeci et al. (2006) experiments.

CO case to 0.041 m/s for the WC case. Velocity profiles of $\bar{v}/U$ in Figure 5.8c show that the CO case presents a mean flow in the shoreward direction, as an effect of the recirculating flow, as already observed in Section 5.2. Nevertheless, with the waves superposed on the current, this effect is reduced. The reason may be that the presence of waves determines the generation of an undertow current in the seaward direction, which probably opposes the above recirculating effect.

Figure 5.9 shows the shear velocity ratio u^*_{WC}/u^*_{CO} versus the Ursell number HL^2/h^3, which is here used as an indicator of the nonlinearity of the wave. The experiments of the present work are compared with the shear velocity data of Musumeci et al. (2006). Results indicate that as the wave nonlinearity increases, the shear velocity ratio of the Musumeci experiments reveals a constant trend, whereas the ACCLIVE experiments seems to be characterized by an increasing trend of the relative shear, although in a narrower range of the Ursell number. Although the data are characterized by a certain scattering, this seems to suggest that the presence of the sloping bottom determine a larger gradient of relative shear, compared to the case of waves propagating over flat bottom.

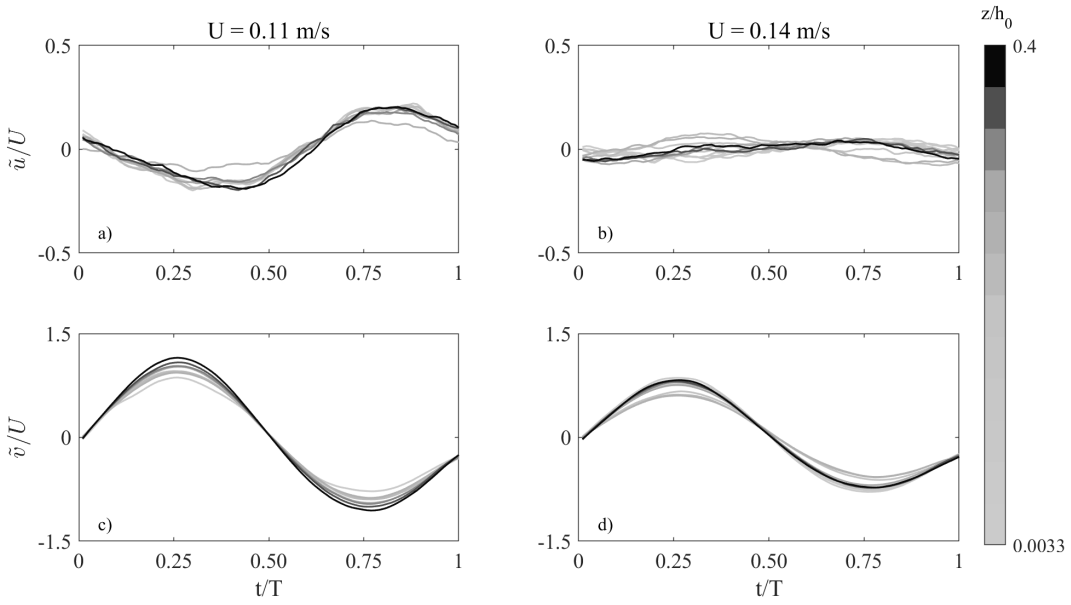

Figure 5.10: Phase-averaged velocities for Runs 9 and 10 (WC, $H = 0.085$ m, $T = 1.0$ s) in the crosswise (a, b) and streamwise (c, d) direction. Both runs have the same local water depth $h = 0.26$ m but different mean current velocity: $U = 0.11$ m/s (a, c) and $U = 0.14$ m/s (b, d).

5.4 Phase-averaged flow analysis

Dimensionless phase-averaged current and wave velocities $\tilde{u}$ and $\tilde{v}$ have been computed for the ACCLIVE dataset as follows:

$$\tilde{u}(z, t/T) = \frac{1}{U}\Big(\frac{1}{N_w}\sum_{i=1}^{N_w} u_i(z, t/T) - \bar{u}\Big) \tag{5.9}$$

$$\tilde{v}(z, t/T) = \frac{1}{U}\Big(\frac{1}{N_w}\sum_{i=1}^{N_w} v_i(z, t/T) - \bar{v}\Big) \tag{5.10}$$

where N_w is the number of waves used for the computation of the phase average. Figure 5.10 shows the dimensionless phase-averaged velocities $\tilde{u}$ (5.10a, 5.10b) and $\tilde{v}$ (5.10c, 5.10d) for Runs 9 and 10. The two runs share the water same depth ($h = 0.26$ m) but have different mean current velocity: $U = 0.11$ m/s (5.10a, 5.10c), $U = 0.14$ m/s (5.10b, 5.10d) respectively. The wave height and period are $H = 0.085$ m, $T = 1.0$ s respectively. Figure 5.10a shows that the presence of waves determines an oscillatory flow to occur in the current direction. During the crest phase, defined as the half-cycle between 0 and $0.5T$, a current velocity decrease is observed, whereas during the trough phase, defined as the half-cycle between $0.5T$ and 1, an increase

of velocity of the current is observed. The oscillatory flow in the current direction is found to be out of phase with respect to the wave motion. The phase shift of the crests of $\tilde{u}$ and $\tilde{v}$ can be quantified by the absolute value of the difference between the instant t/T corresponding to the maximum of $\tilde{u}$ and t/T corresponding to the maximum of $\tilde{v}$:

$$\Delta(t/T)_{max} = |(t/T)_{max(\tilde{u})} - (t/T)_{max(\tilde{v})}|. \tag{5.11}$$

Comparison between Figures 5.10a and 5.10b suggests that the presence of a stronger current ($U = 0.14$ m/s) determines the wave motion to induce a less significant oscillation of $\tilde{u}$, i.e. the amplitude of $\tilde{u}$ is reduced in comparison with the weaker current case. Moreover, phase-averaged current velocities show a smaller phase shift at the bottom in comparison with the rest of the water column (Figure 5.10b). As the current experiences a larger bottom resistance ($u^* = 0.041$ m/s) than the case with a weaker current ($u^* = 0.031$ m/s, Figure 5.10a). Figure 5.11 shows the phase-averaged velocities $\tilde{u}$ (5.11a, 5.11b) and $\tilde{v}$ (5.11c, 5.11d) for Runs 9 and 12, the two runs share the same mean current velocity ($U = 0.11$ m/s) but measurements were obtained at different water depths: $h = 0.26$ m (5.11a, 5.11c), $h = 0.24$ m (5.11b, 5.11d), respectively. The wave characteristics are $H = 0.085$ m, $T = 1.0$ s. The data in Figures 5.11b and 5.11d reflect the fact that wave shoaling is occurring between the two positions (CC and SH, respectively). A larger oscillation is observed as an effect of wave shoaling all along the measured water column. Moreover, a larger phase shift is observed (depth-averaged $\Delta(t/T)_{max} = 0.60$) in comparison with Run 9 ($\Delta(t/T)_{max} = 0.38$).

In order to observe how phase shift varies along the water column at different depths, the phase shift profiles of $\Delta(t/T)_{max}$ for Runs 13, 11 and 12 ($h = 0.28$ m, 0.26 m and 0.24 m respectively) are shown in Figure 5.12. As depth decreases, the depth-averaged phase shift of maximums $\Delta(t/T)_{max}$ increases from 0.15 (for $h = 0.28$ m) to 0.60 (for $h = 0.24$ m). The current respond to the increasing nonlinearity of the wave velocity distribution with an inertial effect which induces a delay in the phase shift between current and wave oscillations. Moreover, in the lower part of the water column a decrease of phase shift is observed for every $\Delta(t/T)_{max}$ profile, although progressively less significant as depth decreases.

Figure 5.13 shows the dimensionless phase-averaged and time-averaged ve-

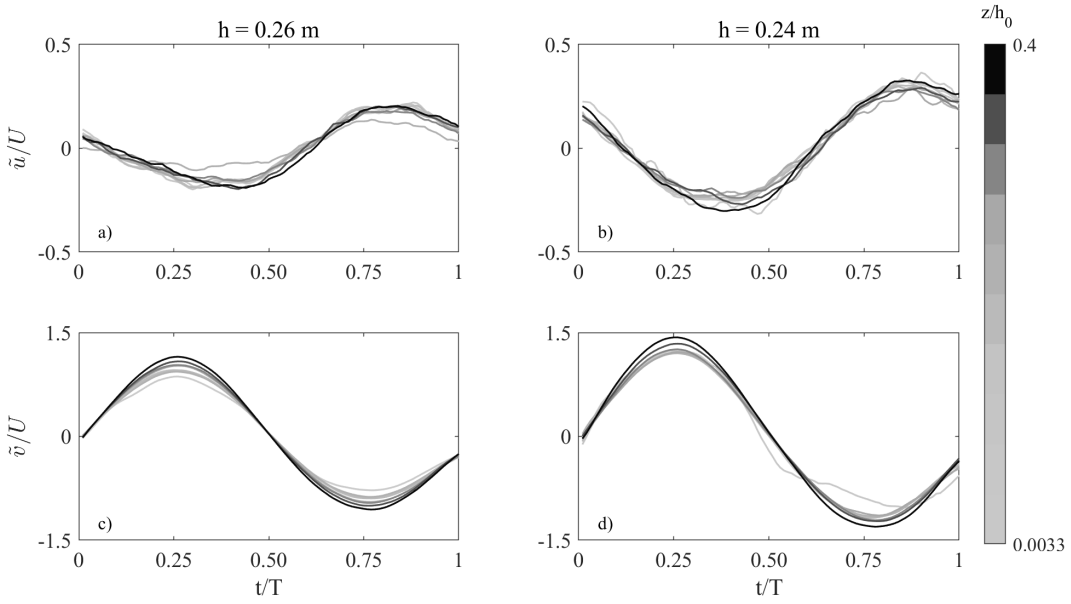

Figure 5.11: Phase-averaged velocities for Runs 9 and 10 (WC, $H = 0.085$ m, $T = 1.0$ s) in the crosswise (a, b) and streamwise (c, d), with local water depth $h = 0.26$ m (a, c) and $h = 0.24$ m (b, d): $U = 0.11$ m/s (a, c) and $U = 0.14$ m/s (b, d).

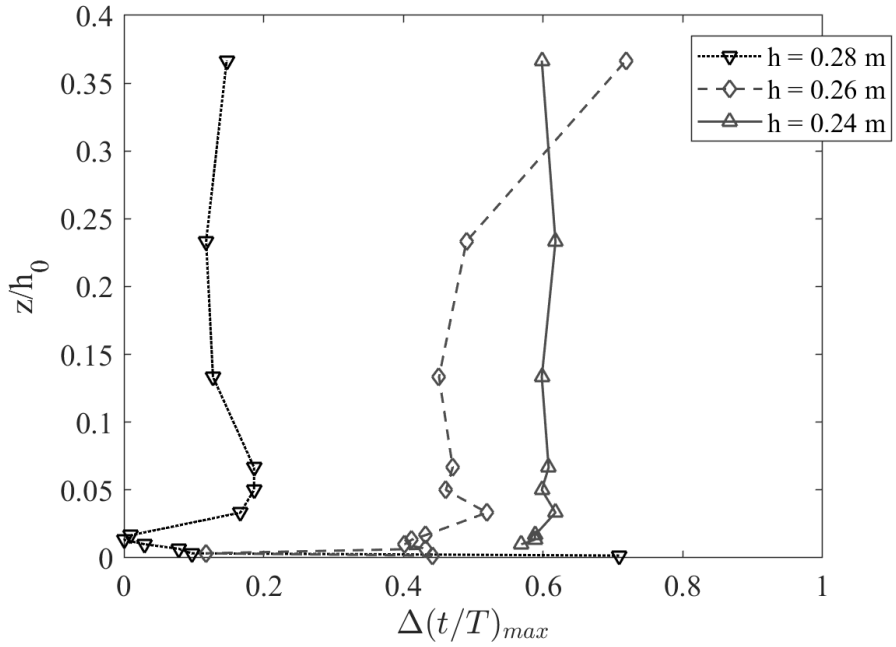

Figure 5.12: Phase shift between maximums of phase-averaged velocities $\tilde{u}$ and $\tilde{v}$ for Runs 13, 11 and 12 ($h = 0.28$ m, 0.26 m and 0.24 m respectively).

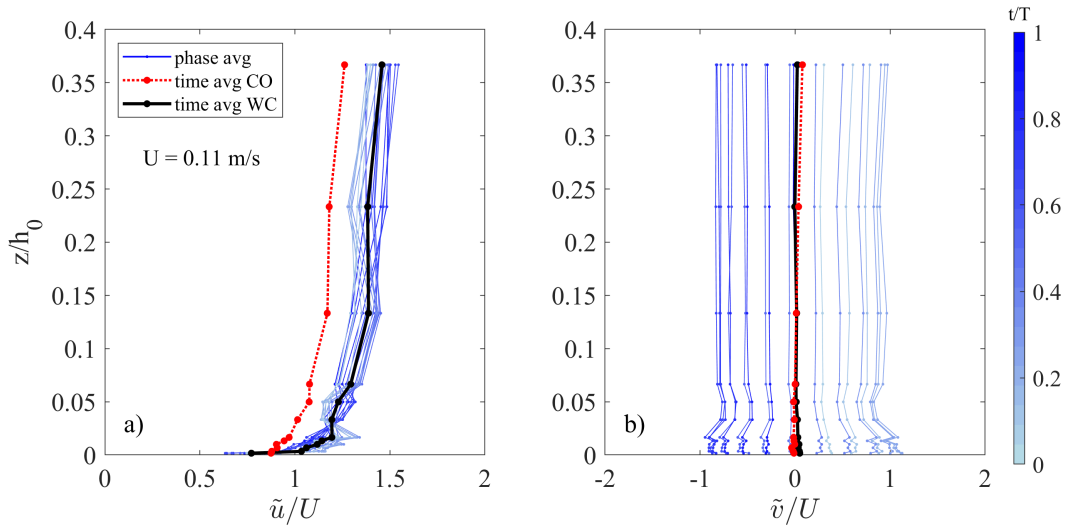

Figure 5.13: Phase-averaged velocities for Runs 2 and 8 (CO and WC respectively) in the streamwise (a) and crosswise (b) directions. Time-averaged CO profile (red dashed line, red dot marker), time-averaged WC profile (black thick continuous line, black dot marker) and phase-averaged WC profile (see color bar). Mean velocity U = 0.11 m/s, local water depth h = 0.26 m.

locity profiles for Run 8 (WC) and the dimensionless time-averaged velocity profile for Run 2 (CO) in the current (5.13a) and wave (5.13b) direction. Both profiles are measured at central position and mean current velocity U = 0.11 m/s.

The results indicate that the presence of waves induces current velocities to oscillate around their time-averaged $\bar{u}/U$. The upper part of the velocity profile experiences a decrease in velocity during the crest phase, and an increase of velocity during the trough phase, as already observed in Figure 5.10 and Figure 5.11.

Figure 5.14 shows the dimensionless phase-averaged and time-averaged velocity profiles for Run 12 (WC) and the dimensionless time-averaged velocity profile for Run 6 (CO) in the current (5.14a) and wave (5.14b) direction. Both runs are at SH position and mean current velocity is U = 0.11 m/s. By comparing Figure 5.14a and Figure 5.13a, a more intense oscillatory motion of the current is observed as waves are superposed, as wave shoaling at this position is determining wave velocity amplitude to increase. This again induces a decrease of velocity during the crest phase and an increase during the trough phase. Such a decrease of velocity forces the current to slow down below the CO measured velocities. Therefore, the current experiences an overall (depth-averaged) velocity increase, but slows down during the

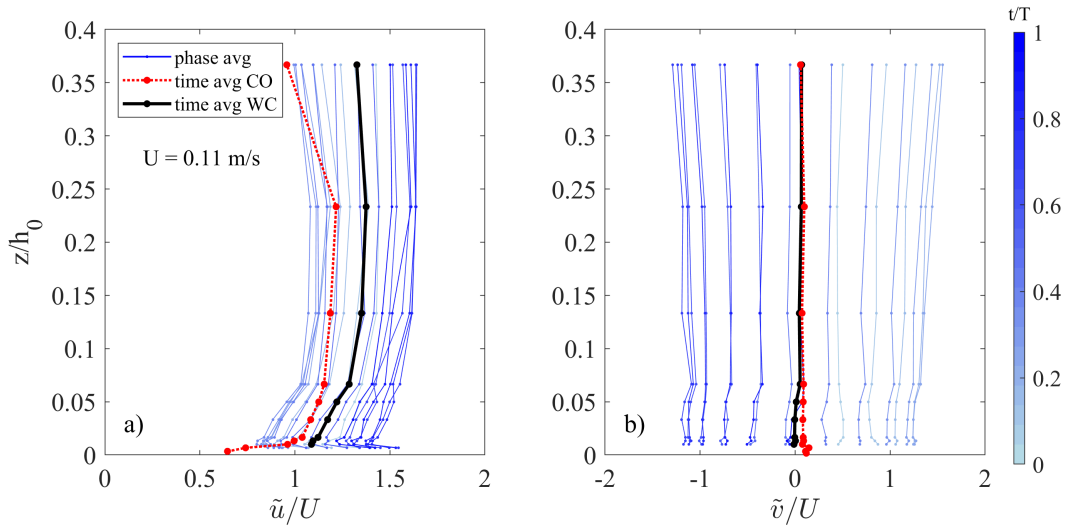

Figure 5.14: Phase-averaged velocities for Runs 6 and 12 (CO and WC respectively) in the streamwise (a) and crosswise (b) directions. Time-averaged CO profile (red dashed line, red dot marker), time-averaged WC profile (black thick continuous line, black dot marker) and phase-averaged WC profile (see color bar). Mean velocity U = 0.11 m/s, local water depth h = 0.24 m.

crest phase below the CO $\bar{u}/U$ profile.

5.5 Turbulent flow analysis

An attempt to operate a quadrant analysis to observe the behavior of ejections and sweeps at different distances from the bed is carried out. The methodology is analogous to the one performed in the turbulent flow analysis section of the WINGS campaign data analysis chapter, Section 4.5.

Figure 5.15a, 5.15c and 5.15e shows the correlation plots for u' and w' for Run 3 (CO, CC, U = 0.14 m/s) whereas Figure 5.15b, 5.15d and 5.15f shows the correlation plots for Run 9 (WC, CC, U = 0.14 m/s), at different distances from the bottom: z/h_0 = 0.007 (5.15a, 5.15b), z/h_0 = 0.133 (c,d), z/h_0 = 0.233 (5.15e, 5.15f). The percentage of events occurring in each quadrant are indicated (light blue), excluding a central hyperbolic region with threshold $\Omega|\overline{u'w'}|$. The study has been carried out by varying the threshold parameter Ω, although in Figure 5.15 only the hole region with Ω = 5 is shown. Comparison between CO (Figure 5.15a, 5.15c and 5.15e) and WC (Figure 5.15b, 5.15d and 5.15f) shows that, at every

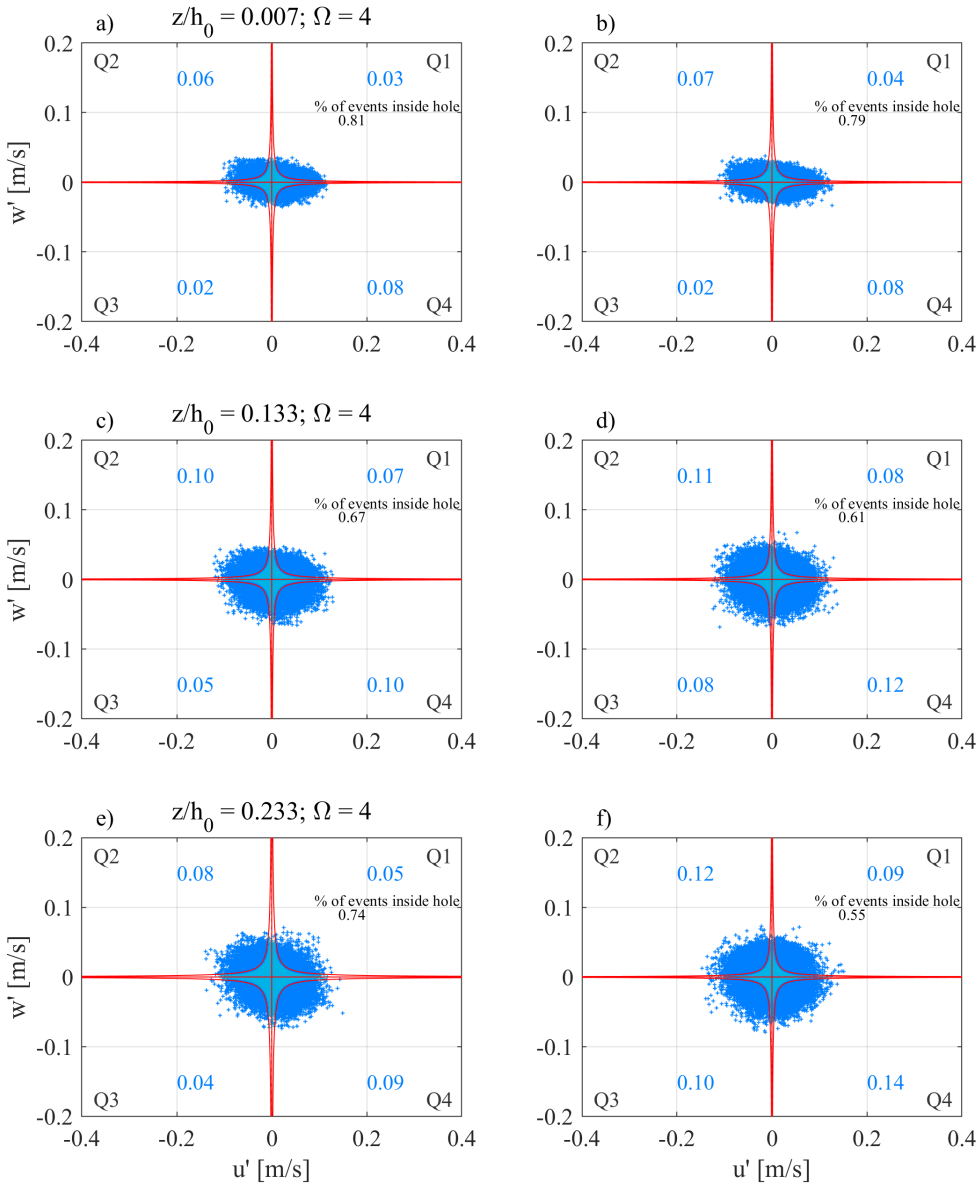

Figure 5.15: Correlation plots for u' and w' for Run 3 (CO, a, c and e) and Run 9 (WC, b, d and f), at different distance from bottom: $z/h_0 = 0.007$ (a, b), $z/h_0 = 0.133$ (c, d), $z/h_0 = 0.233$ (e, f). Measurements of both Runs are at CC and have same mean current velocity $U = 0.14$ m/s. Hyperbolic hole $\Omega = 4$.

considered z/h_0, an increase in the relative number of ejection events is always observed when waves are added. This suggests that the presence of waves enhances turbulent mixing all along the water column. In the lower part of the water column (Figure 5.15e and 5.15f) the overall shape of the correlation plot is fairly elliptical in the direction of the Q2 and Q4 quadrants. This suggests that turbulent events distribution is skewed in the direction of the Q2 and Q4, showing that turbulent momentum transfer at the wall is mainly driven by ejection (Q2) and sweep (Q4) events, only a slight difference can be observed between CO and WC case. As distance from bottom increases (Figure 5.15c and 5.15d) the overall shape of the turbulent events turns from elliptical to almost circular. Turbulent events relatively diminishes in the Q2 and Q4 quadrants in favour of quadrants Q1 and Q3. The turbulent momentum transfer progressively leaves the ejections-sweeps cycle as a main mechanism of turbulent mixing to a more isotropic behavior. The presence of waves enhances turbulent ejections, but also outward and inward interactions. Moreover, the hole region associated with the Reynolds stress $|\overline{u'w'}|$ decreases in size, and the number of events inside the hole decreases likewise. In the upper part of the water column (Figure 5.15e and 5.15f) turbulent events distribution is even less elliptical. Here, the presence of waves determines an overall increase of turbulent fluctuations in all quadrants. Moreover, the presence of waves leads to a smaller Reynolds stress value, as the hyperbolic threshold is lower in the WC case.

5.6 Discussion of results

The preliminary analysis on the velocity time series showed that, in the presence of a sole current, steady flow conditions are satisfactorily achieved in the experimental tank, and the time variability, in terms of difference of standard deviation, of the smallest acquisition time (2 minutes) did not exceed 2%. Presence of waves determines an increase in the time variability in the wave direction, with a maximum difference of standard deviation of 7% for the 2 minutes long time series. The following data analysis have been then carried out time-averaging the whole 10 minute time series, in which difference of standard deviation is below 2% for both CO and WC cases. A spatial characterization of the flow field for the sole current

has been conducted in order observe how the current velocity profile is altered by the presence of the sloping bed. Vertical velocity profiles showed slight differences between the measured velocities close to the inflow/outflow central axis, nevertheless a mean flow is observed in the shoreward direction farther from the central axis. This suggests the presence of a recirculation region, which conveys part of the current away from the outlet. However, such recirculation region does not seem to affect the flow field close to the inlet/outlet central axis. Moreover, the space variability analysis showed that as local depth decreases in the shoreward direction, current velocity distribution features a more turbulent profile along with an increase of Re_c.

The data analysis of the time- and phase-averaged flow showed a complex interaction between the shoaling waves and the steady current in terms of shear production, momentum transfer and turbulent mixing. Comparison between CO and WC experiments showed that the superposition of waves determines the current to experience a larger shear at the bottom, which suggests the occurrence of an enhanced turbulent mixing induced by the oscillatory motion. Conversely, the upper part of the measured profile experiences a velocity increase. As waves shoal, a mean momentum transfer in the upper part of the flow is observed as well, however the presence of waves does not seem to enhance significantly turbulent shear, as demonstrated by a very similar shear velocity determined by the wave from the central to the shoreward position. A possible explanation is that, in the presence of a current with a larger Re_c, wave motion may be less effective in inducing an increase of turbulent mixing.

A comparison with the experiments of Musumeci et al. (2006), which have been carried out in the same facility but over a flat bottom, showed a different trend of the combined flow shear velocities with respect to the experiments over sloping bottom of the present study. Indeed, as the Ursell number, used as a wave nonlinearity indicator, increases the presence of a sloping bottom seems to enhance the combined flow shear velocity increase with respect to the current only case, whereas in the presence of a flat bottom, seems to be characterized by a constant trend.

Analysis of phase-averaged velocities showed that superposition of waves induces the current to oscillate around its mean velocity. Moreover a phase shift

between current and wave phase-averaged velocity maximums has been observed. Such a phase shift seems to be enhanced gradually as the waves shoal. A possible explanation is the following: as waves shoal, the wave velocity distribution during a wave phase becomes more skewed, i.e. the absolute value of the wave acceleration during the crest phase increases. On the other hand, as the mean current velocity increases with decreasing depth, the current opposes to the acceleration induced by the wave motion. Indeed, as the momentum carried by the current increases as depth decreases, it is less prone to be affected by the change of velocity induced by the shoaling waves, determining the oscillating effect on the current to be delayed. Therefore, while shoaling waves induce the amplitude of the current oscillation to increase, a larger momentum current opposes to the wave increased acceleration, determining the occurrence of a delay in the oscillatory motion of the current. Quadrant analysis applied to turbulent flow showed that the presence of waves induces an increase of the ejection-sweep cycle events, which determines turbulent mixing to be enhanced. Moving farther from the bottom, turbulent field progressively abandon the ejection-sweep cycle as main mechanism of turbulent momentum transfer, in favour of a more isotropic turbulence mixing.

Chapter 6

Numerical modelling of the wave-current interaction

6.1 Overview

In the present Chapter, the setup and results of the numerical simulations of wave-current orthogonal flow are presented. The following investigation is a complementary study, aimed at assessing the ability of the examined CFD numerical models to correctly reproduce the shear effects determined by the superposition of waves on the current. Specifically, two models have been considered: a three-dimensional (3D) and a one-dimensional (1D) one.

The 3D model is meant to investigate three-dimensional effects of the waves on current, in terms of velocity distribution, bottom friction stress and other turbulent shear related quantities, in the presence of a rough bed. The procedure employed to build the numerical setup and an attempt of model validation is described in the present chapter. The numerical setup is designed in order to reproduce a selection of experiments from the WINGS laboratory campaign (Chapter 4) with waves and currents propagating over a gravel bed. In order to accurately replicate the experimental conditions of the laboratory campaign, the model features a reconstruction of the real gravel bed, used in the CFD model as bottom boundary.

The 1D model served as a preliminary setup to investigate the capabilities of the internal field and boundary conditions for the 3D model, and the overall feasibility of the numerical setup. As the computational cost is significantly lower

in comparison with the 3D model, thanks to a reduced domain and a significantly smaller amount of cells, the 1D model served as a prompt testing ground for flow conditions and for the numerical setup in general. Moreover, The output flow field of the 1D model simulations can be used as internal or boundary conditions within larger models, in order to account for the superposition of waves on the current since the first timestep. The two models differ mainly by the computational domain and mesh, whilst sharing the same governing equations, boundary conditions and numerical solving algorithms, with slight differences highlighted in the respective numerical setup description sections.

The 1D model has been setup and tested against a selection of the WINGS experiments, as well as the 3D model. Two types of 1D simulations have been performed, one featuring a smooth bottom boundary, and one having a rough bottom boundary. The rough bed condition is modelled through the use of a rough wall function at the bottom boundary. Smooth bed simulations are then compared with the results of the WINGS experiments over sand bed, whereas rough bed simulations are compared with gravel bed experiments. Simulations in the presence of a lone current, waves only, and combined flow have been performed, for the 1D model, whereas the 3D model has been tested for current only condition.

First, the numerical models, in terms of governing equations, boundary conditions and computational mesh, are presented in the next Section. Then, the results of the testing of both models and the comparison with the laboratory data, are shown and analyzed. A discussion Section closes the Chapter.

6.2 Description of the numerical models

6.2.1 Governing equations

The CFD model solves the incompressible Reynolds-averaged Navier-Stokes (RANS) equations:

$$\frac{\partial u_i}{\partial t} + u_j \frac{\partial u_i}{\partial x_j} = -\frac{1}{\rho}\frac{\partial p}{\partial x_i} + \frac{\partial}{\partial x_j}\left[2\nu S_{ij} + \frac{\tau_{ij}}{\rho}\right] \tag{6.1}$$

and the continuity equation

$$\frac{\partial u_i}{\partial x_i} = 0; \tag{6.2}$$

where the mean strain tensor is

$$S_{ij} = \frac{1}{2}(\frac{\partial u_i}{\partial x_j} - \frac{\partial u_j}{\partial x_i}). \tag{6.3}$$

u_i are the mean velocities, x_i are the coordinates, t is time, p is pressure, ν is the kinematic viscosity, ρ is fluid density and τ_{ij} is the Reynolds stress tensor, which accounts for both normal and shear stresses due to turbulent fluctuation momentum transfer. The Reynolds stress tensor is defined by the constitutive relation

$$\frac{\tau_{ij}}{\rho} = -\overline{u_i' u_j'} = 2\nu_t S_{ij} - \frac{2}{3}k\delta_{ij} \tag{6.4}$$

where δ_{ij} is the Kronecker delta, ν_t is the turbulent eddy viscosity and k is the turbulent kinetic energy.

Turbulence closure is achieved by means of a $k-\omega$ Shear Stress Transport (SST) model (Menter, 1993), which is a popular variant of the well-known $k-\omega$ (Wilcox, 2006). The $k-\omega$ SST is a two-equation turbulence closure model, which couples the continuity and momentum RANS equations with transport equations for turbulent kinetic energy k and the specific rate of dissipation of turbulent kinetic energy ω, which both enter the momentum equation through the eddy viscosity ν_t.

The SST model features a 'zonal' formulation, which combines a $k-\omega$ in the inner parts of the boundary layer, and switches to a $k-\epsilon$ behaviour in the free-stream, therefore avoiding a common $k-\omega$ sensitivity issue to free-stream inlet turbulence properties (Menter et al., 2003). Moreover, the $k-\omega$ SST model shows good behaviour in the presence of adverse pressure gradients and separating flows. On the other hand, it may produce too large turbulence levels in regions with large normal strain, like stagnation regions and regions with high accelerations. However, this tendency is much less pronounced than with a normal $k-\epsilon$ model (Menter et al., 2003). Conversely, the $k-\epsilon$ model is known to lead to numerical instabilities in the occurrence of large time steps or under-relaxation factors in iterative methods (Ferziger et al., 2020). The SST zonal formulation is based on blending functions, which ensure a proper selection of the $k-\omega$ and $k-\epsilon$ zones without user interaction depending on the wall distance. The eddy viscosity in the k-ω_{SST} model is:

Table 6.1: $k-\omega$ SST model coefficients and auxiliary relationships.

F_1	$\tanh\left\{\left\{\min\left[\max\left(\frac{\sqrt{k}}{\beta^*\omega z}, \frac{500\nu}{z^2\omega}\right), \frac{4\sigma_{\omega 2}k}{CD_{k\omega}z^2}\right]\right\}^4\right\}$
F_2	$\tanh\left[\left(\max\left(\frac{2\sqrt{k}}{\beta^*\omega z}, \frac{500\nu}{z^2\omega}\right)\right)^2\right]$
P_k	$\min\left(\tau_{ij}\frac{\partial \bar{u}_i}{\partial x_i}, 10\beta^* k\omega\right)$
$CD_{k\omega}$	$\max\left(2\rho\sigma_{\omega 2}\frac{1}{\omega}\frac{\partial k}{\partial x_i}\frac{\partial \omega}{\partial x_i}, 10^{-10}\right)$
α_1	$5/9$
β_1	$3/40$
β^*	$9/100$
σ_k	0.85
σ_ω	0.5
$\sigma_{\omega 2}$	0.856

$$\nu_t = \frac{a_1 k}{\max\left(a_1\omega, SF_2\right)} \tag{6.5}$$

whereas the two transport equations for k and ω are

$$\frac{\partial k}{\partial t} + \bar{u}_j\frac{\partial k}{\partial x_j} = P_k - \beta^* k\omega + \frac{\partial}{\partial x_j}\left[\left(\nu + \sigma_k\nu_t\right)\frac{\partial k}{\partial x_j}\right] \tag{6.6}$$

$$\frac{\partial \omega}{\partial t} + \bar{u}_j\frac{\partial k}{\partial x_j} = \alpha_1 S_{ij}^2 - \beta_1\omega^2 + \frac{\partial}{\partial x_j}\left[\left(\nu + \sigma_\omega\nu_t\right)\frac{\partial \omega}{\partial x_j}\right] + 2(1-F_1)\sigma_{\omega 2}\frac{1}{\omega}\frac{\partial k}{\partial x_i}\frac{\partial \omega}{\partial x_i} \tag{6.7}$$

where k and ω are computed by means of the following

$$k = \frac{1}{2}\overline{u_i' u_i'} \tag{6.8}$$

$$\omega = \frac{\epsilon}{k\beta^*} \tag{6.9}$$

in which the dissipation of turbulent kinetic energy ϵ is

$$\epsilon = \nu\overline{\frac{\partial u_i'}{\partial x_k}\frac{\partial u_i'}{\partial x_k}} \tag{6.10}$$

F_1 and F_2 are blending coefficients; α_1, β_1 and β^*, σ_k, σ_ω and $\sigma_{\omega 2}$ are model coefficients. Values of the model coefficients are shown in Table 6.1

The equations are solved numerically by means of the open source CFD toolbox OpenFOAM, which is a well-established and largely used CFD modelling

software for both research and commercial use in marine and coastal applications (Jacobsen et al., 2012; Higuera et al., 2013, 2014; Baykal et al., 2017). The solver application used for solving the equations for WO and WC simulations is pimpleFoam, which is a large time-step transient solver for incompressible flow using the PIMPLE (merged PISO-SIMPLE) algorithm (Issa, 1986). For the current only case the SIMPLE (Semi-Implicit Method for Pressure-Linked Equations) algorithm is used instead, which is a steady-state solver for incompressible turbulent flow (Patankar and Spalding, 1983), through the simpleFoam application.

6.2.2 Boundary conditions

Both 1D and 3D models are subject to the following boundary conditions. At friction wall boundaries, a no-slip condition is imposed hence velocities are set equal to zero. Pressure boundary condition at the bottom is defined as zero gradient (Neumann condition). The lid at the top boundary holds a slip condition. The application of a lid at the top boundary rather than a free surface solver is a commonly used and valid approach for the flow conditions without large free surface disturbances as the wave modeling cases (Baykal et al., 2017). A Neumann condition at the top boundary is set for k and ω.

Waves and current inlets and outlets for both 1D and 3D models are defined as cyclic boundaries. There are a total of four cyclic boundaries, two normal to the current direction x and two normal to the wave direction y, with each one being coupled with its 'twin' cyclic boundary in front. Whatever field quantity 'crosses' a cyclic boundary, it 'outflows' during the next timestep from its coupled boundary. Cyclic boundaries can either be inlets or outlets.

The CFD simulation is a High-Re type, i.e. it makes use of wall functions to model the flow close to the bed, rather then resolving the boundary layer by the mesh itself. This has been done for reasons concerning computational costs, as the mesh resolution increases at the bottom, needed to resolve high velocity field gradients, would have slowed down the simulation. Moreover, OpenFOAM implements wall functions that gives the possibility to reproduce bottom roughness. This feature offers the possibility to include roughness effects in the 1D model. Two types of wall functions have been used: smooth and rough wall functions, meant to reproduce

sand bed and gravel bed conditions respectively of the WINGS experiments. Bottom boundary condition for the wall function in rough condition requires an equivalent roughness values, which was chosen to be $2.5d_{50}$ (Baykal et al., 2017; Lim and Madsen, 2016; Sumer, 2007), corresponding to the values of the WINGS experimental campaign.

Steady and oscillatory flows are imposed as source terms in the momentum equation, which generate body forces at the cell centroids in the x and y direction, in order to simulate current and waves, respectively. The steady momentum source S_c is based on the experimental freestream velocity U_c from the CO WINGS laboratory experiments. Oscillatory momentum source S_w generates a regular oscillatory body force based on the the orbital velocity U_w of the WO WINGS laboratory campaign experiments

$$S_w = U_w \omega \cos \omega t \tag{6.11}$$

Current only (CO) and Wave Only simulations (WO) have been carried out in order to validate the cases in the absence of the combined flow. In CO condition, the two cyclic boundaries normal to the wave direction have been substituted with 'empty' OpenFOAM boundaries, which allows to have only zero velocities in the direction normal to the empty boundary. In a similar manner, in WO condition, the two cyclic boundaries normal to the current direction have been substituted with 'empty' OpenFOAM boundaries. The Waves plus Current (WC) simulations are generated summing together the steady and oscillatory momentum sources in orthogonal direction.

The numerical domain and the boundary conditions of the combined flow model are schematized in Figure 6.1.

It is important to stress out that the 1D model is defined one-dimensional as it solves the governing equations along the vertical direction, i.e. considering a certain number of cells along the z direction, while having only one cell in the x and y directions. Nevertheless, velocities in the internal field can be non-zero in all directions, thus the present simulations are actually three-dimensional simulations, but solved along the water column. In the case of CO and WO simulations empty boundaries makes the simulation two-dimensional, allowing non-zero velocities in

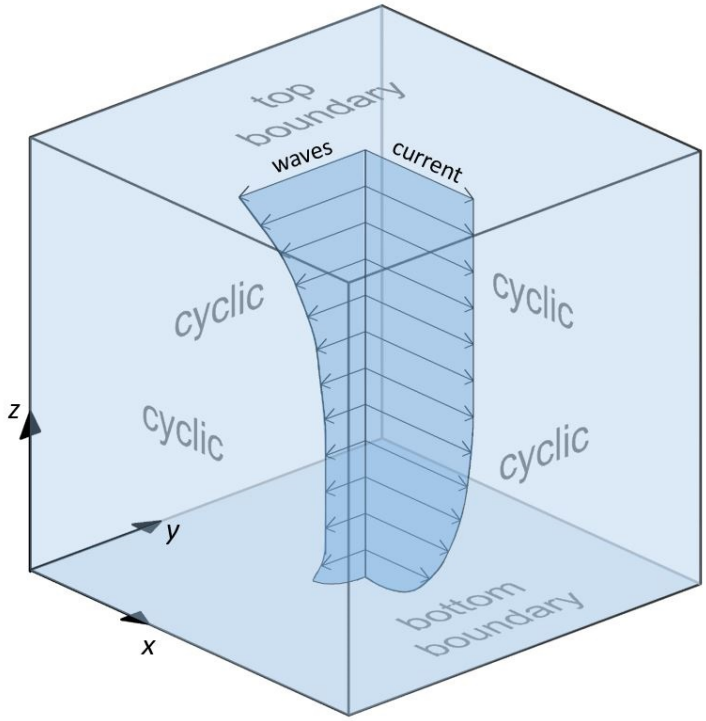

Figure 6.1: Schematization of the numerical domain and boundary conditions.

the vertical and in the current direction (in the case of CO) or the wave direction (in the case of WO). The name '1D model' is used only to denote that the solution domain is subdivided in multiple cells only in the vertical direction, having no more then one cell in the x and y direction.

6.2.3 Computational mesh

6.2.3.1 Setup of the 1D model

The domain is 0.015 m in the x direction, 0.015 in the y direction and 0.400 m in the z direction. The domain height has been chosen to be 0.400 m, as the water level of the WINGS experiments. As mentioned before, the mesh has one cell in the x (current) and in the y (wave) directions, while being subdivided in several cells in the vertical z direction. The number of cells of the mesh in the z direction is related to the expected position of the lower limit of the logarithmic profile. Indeed, in order for the wall function to work properly, the first cell centroid closer to the wall needs to fall within the logarithmic layer, therefore the cell in contact with the bottom boundary needs to be at least 2 times the lower limit of the logarithmic layer in the z direction. For the smooth bed case the total number of cells is 70, in

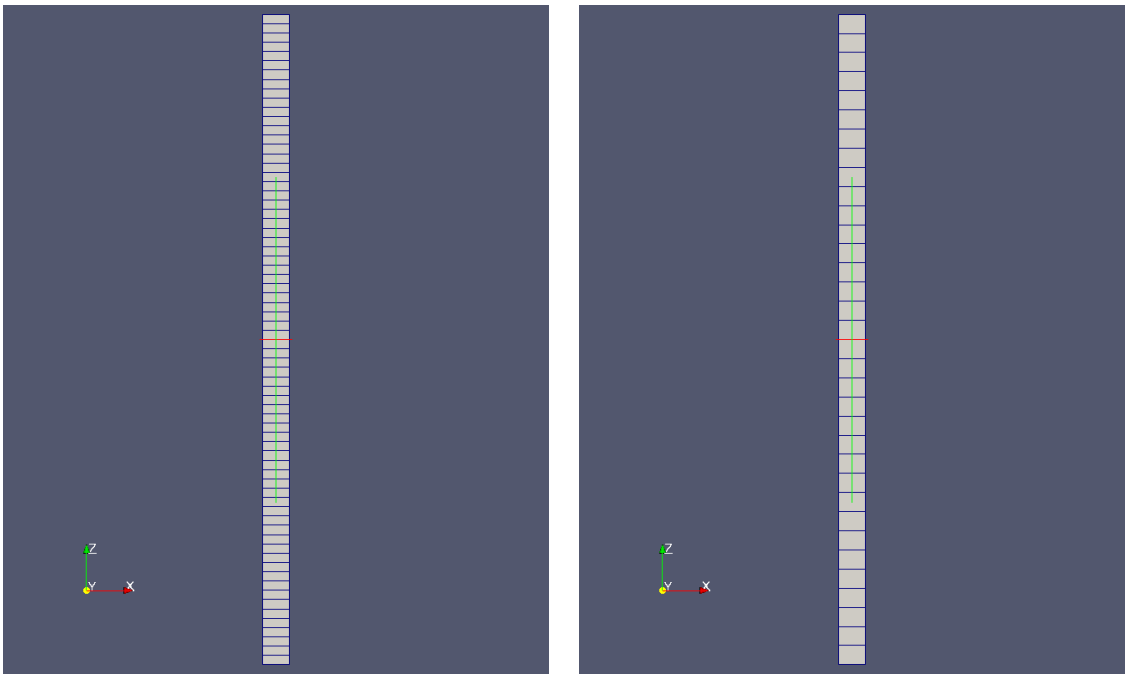

(a) (b)

Figure 6.2: Side view of the 1D model in the OpenFOAM simulation environment: smooth simulation (a), rough simulation (b).

order to have the first cell center at the bottom above the logarithmic layer lower boundary $z^+ = 30$ (correspondent to $z = 0.0028$ m). Such a volume is based on the WINGS Run 1 shear velocity u^* (= 0.0109 m/s), hence the first cell center lies at 0.0029 m from the bed. The number of cells for the rough case is instead 34, in order to have the first point above the lower limit of the logarithmic layer for rough flow $z^+ = 0.2k_s^+$, based on the Run 32 WINGS shear velocity u^* (= 0.0245 m/s) and equivalent roughness k_s (= 0.0645 m). The meshes of the 1D model, for both smooth and rough cases, are shown in Figure 6.2.

Current only simulations lasted until friction velocity was satisfactorily stable, i.e. the difference between last and second-to-last friction velocities was lesser than 0.00001 m/s, wave only and combined flow simulations lasted until satisfying variability of the velocity time series and bed shear stresses is reached.

A similar approach has been used for waves plus current simulation. After a series of preliminary experiments, the duration for waves plus current experiments has been chose to be 400 s, which gives enough time to the current to stabilize, and to have the same number of waves (120 with $T = 2.0$ s) used within the WINGS for

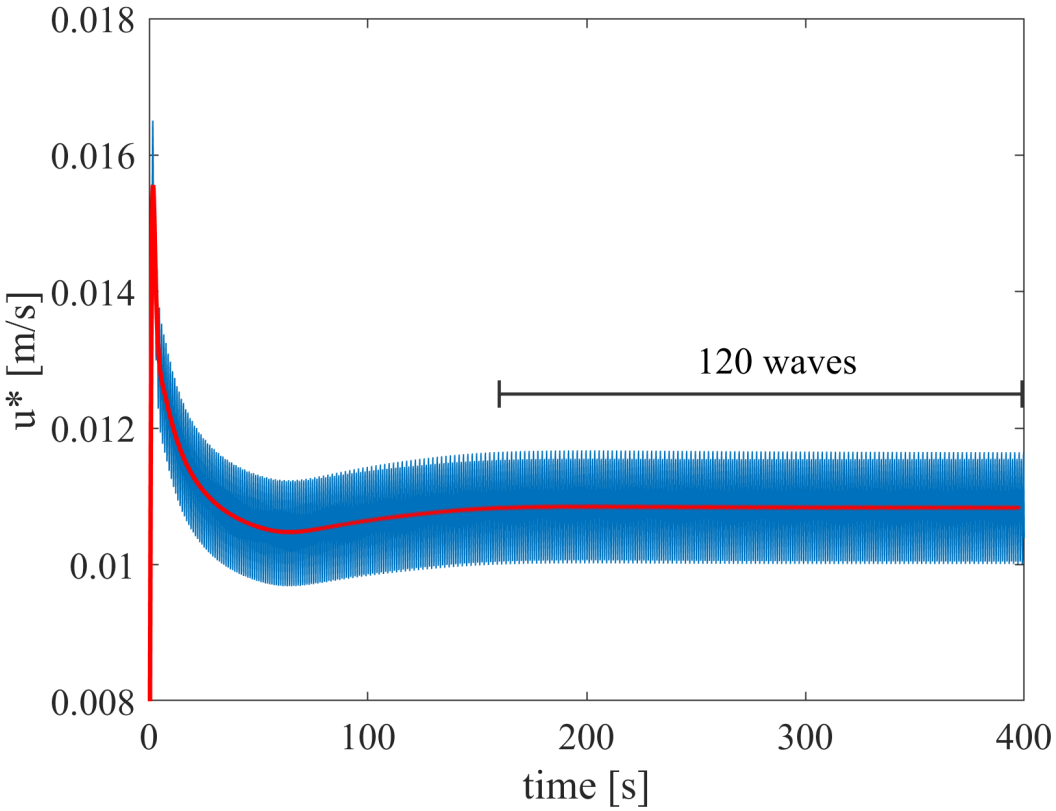

Figure 6.3: Example of CFD shear velocity time series. The time interval used for velocity time-averaging and the trend of the time series (red line) is also highlighted.

time-average. Then, time-averaged CFD current velocity profiles are obtained by considering only the last 240 s of the time-series.

Figure 6.3 shows an example of a shear velocity time series, with highlighted the time interval used within the time-averaging.

Velocity time series are probed at each cell centre with a sampling frequency 100 Hz. In all the calculations, the time step is kept variable to ensure that a certain Courant is not exceeded for numerical stability purposes. Courant number is capped to 0.5.

6.2.3.2 Setup of the 3D model

The domain size is 0.140 x 0.140 x 0.400 m, in the x (current) direction, in the y (wave) and in the vertical (z) direction respectively. The domain vertical extension has been chosen to be 0.400 m, also in this case equal to the water level of the WINGS experiments. The domain extension in the x and y direction has been

changed several times at different stages during the development of the numerical setup, due to computational cost and stability considerations, ranging from 0.60 to 0.07 m of edge length in the x and y directions. The larger domain setup tested (0.60 m), featured a prohibitive number of cells (4.3 mln cells) which led to large computational times, the smaller one was instead too small to consider more than the bed grain d_{50} (= 0.025 m) and therefore largely dependent on the gravel bed reconstruction portion chosen as the bottom boundary. In the end, a 0.140 x 0.140 m in the x and y directions area has been chosen as a trade-off between computational cost and having a sufficient numbers of gravel grains in the bottom boundary, which correspond to approximately 5-6 grains per direction.

The computational domain is then discretized into finite volumes of quadrilateral blocks in varying shapes and dimensions.

The 3D reconstruction of the gravel bottom obtained within the WINGS campaign has been snapped into the mesh in order to run simulations on a replica of the bed used in the experiments through the snappyHexMesh OpenFoam tool. Resolution, elevation distribution and other relevant quantities about the surface reconstruction have been already discussed in Section 4.2.

A first attempt is done in snapping a portion of the surface reconstruction area to the mesh, by selecting the area below which the ADVs have been positioned in the laboratory experiments. Once the surface reconstruction is snapped, the cells beneath the surface reconstruction have been removed by the snapping algorithm, with the snapped surface becoming the new bottom boundary. By doing so, the domain decreases in size in the vertical direction, thus the mesh height is adjusted so that the distance between the upper boundary and the average elevation of the surface reconstruction is equal to the desired water level (= 0.4 m). The mesh is refined in proximity of the bed using 3 levels of refinement. For each level of refinement, hexahedrical cells are splitted in 8 subcells. Level of refinement 1 means that the 0.010 x 0.010 x 0.010 m is splitted in 8 cells of size 0.005 x 0.005 x 0.005 each, a level of refinement 2 means that the original cell is divided into 32 cells of 0.0025 x 0.0025 x 0.0025, and so on. Refinement is operated below $z = 0.300h$, where h is the domain vertical extension (= 0.400 m), up to the bottom boundary. A smoothing iterative algorithm in snappyHexMesh ensures that cell in contact with

the bottom boundary follow the shape of the bed surface reconstruction, although keeping convergence criteria under control (Gisen, 2014).

Preliminary simulations have been carried out on two-dimensional slice of the three-dimensional mesh, in order to analyze mesh sensitivity and perform numerical stability checks. Indeed, mesh resolution at the bottom has a significant influence on the generation of the correct wall shear stresses.

A range of levels of refinement on the original cell size mesh has been tested. The selection criteria were (i) optimal matching of the wall friction velocity relative to the reference WINGS Run, (ii) the overall number of cells for computational cost reason. Wall shear stresses have been measured by a post processing OpenFOAM tool for shear stresses measurement at the wall.

After meshing boundary conditions are defined, side domain boundaries are defined as cyclic boundaries. An issue arised with the definition of cyclic boundary conditions, indeed cyclic boundaries in OpenFoam require the coupled boundary to have identical number and spatial distribution of cell faces. The snapping of the rough bed reconstruction makes all the faces irregular on the bottom edge, making the side boundaries different in terms of number and area distribution of cells. In order to overcome this issue, an attempt with cyclic Arbitrary Mesh Interface (cyclicAMI) boundaries has been carried out. This boundary condition allows to couple cyclic boundaries of different size and shape by recomputing the mass flux crossing the faces at each time step. However, the cyclicAMI mass flux computing algorithm is someway sensitive to the refinement level operated by the snappyHexMesh tool, incurring often in error of the weight assignment for each outlet face, which is basically how the flux of a field quantity exiting from an outlet is redistributed during the next timestep through the inlet, which has a different number and distribution of cell faces. In order to outflank the problem, once the mesh is snapped and adjusted over the height, it is mirrored two times: first in the current direction, thus reflected on a plane of normal (1,0,0). Then, the mesh is mirrored again on a plane of normal (0,1,0), thus it extends in the wave direction. However, in order to have a 0.140 x 0.140 m domain, a preliminary structured grid mesh with size 0.070 x 0.070 x 0.400 m is generated, then the surface reconstruction is snapped and the mesh mirrored.

The final mesh is then 0.140 x 0.140 x 0.400 m in size having all the side

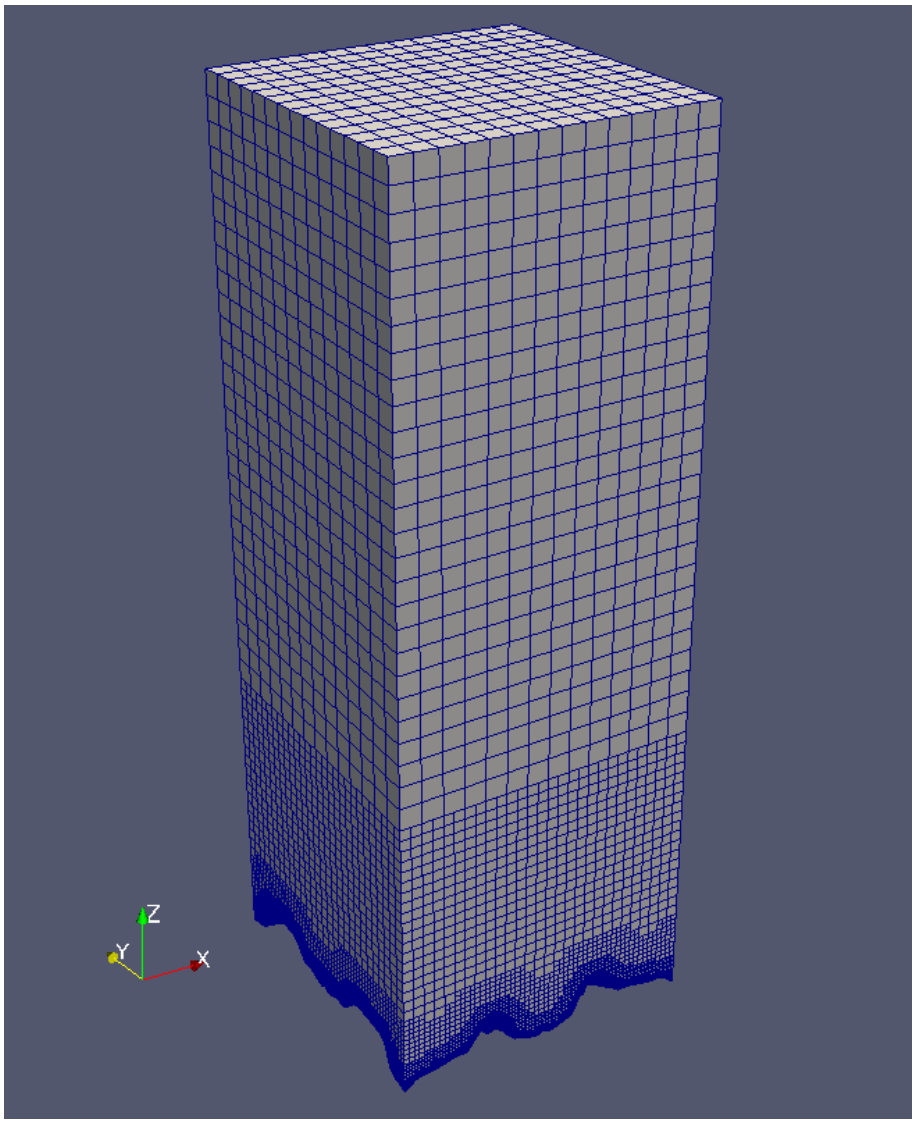

Figure 6.4: Lateral view of the three-dimensional model mesh.

boundaries identical in terms of size, refinement level, number of faces. The original cells are 0.01 x 0.01 x 0.01 m hexahedrical cells, after the refinement the total number of cells is of 529,988.

The final mesh is shown in Figure 6.4. CO and WO tests have been carried out on half of the domain (0.070 x 0.140 cm) in order to save computational time, two of the four coupled cyclic boundaries have been replaced with slip boundaries for velocity and Neumann boundaries for pressure, turbulent kinetic energy k and dissipation ω.

The simulations have been carried out until a stable velocity profile and bottom shear stresses, in terms of time variability, has been achieved. The stabilization time is different for every simulation but is roughly around 1000 s. Considering the

fourth level refinement, the z^+ reached by the cell centres at the bottom ranges 12 $\div$ 30. However, the snappyHexMesh algorithm smooths the cells in order to better contour/surround the reconstructed gravel grains, thus cells at the bottom may be smaller then level 4 refined cells. The bottom boundary is shown in Figure 6.5.

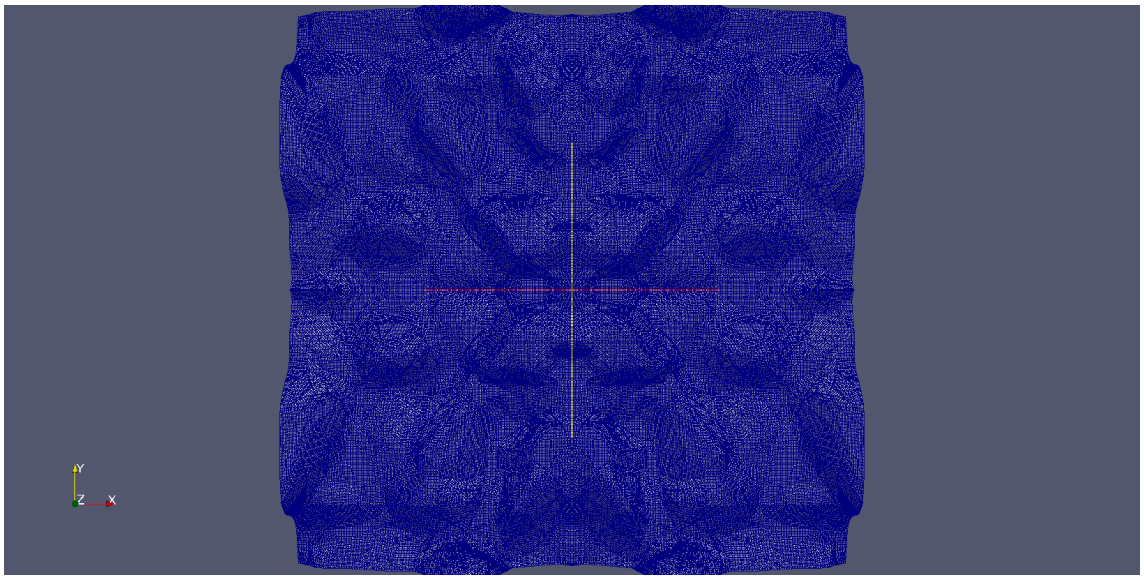

(a)

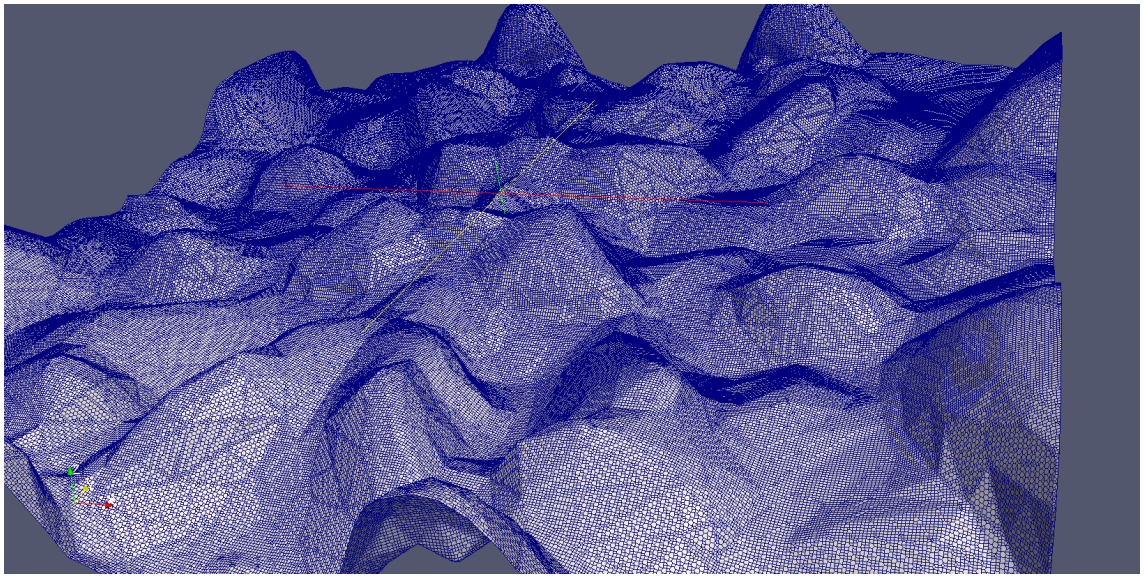

(b)

Figure 6.5: Top view (a) and detail (b) of the 3D mesh bottom boundary.

Higher levels of refinement have not been tested as CPU times increased significantly.

The size has been chosen also considering the fact that as the oscillatory flow is applied with the same magnitude for each time step for each cell, there is

no need to extend the mesh in the wave direction in order to include a whole wave phase, as there is no orbital velocity distribution in the wave direction. To make an analogy to a physical device, the model works more as an oscillating water tunnel rather than a wave flume.

In order to drive the flow conditions within the model, steady and oscillatory pressure gradients are imposed in the domain as body forces to simulate current and waves, as already described in the boundary conditions subsection 6.2.2. The current steady flow is driven by a source term in the momentum equation, which however is not a velocity source based on experimental freestream velocity U_c as in the 1D model, but rather on a pressure gradient based on the desired friction velocity (Baykal et al., 2017), which is taken from the WINGS experiments. The current source term is based on the following:

$$u^* = \sqrt{-\frac{h}{\rho}\frac{\partial p}{\partial x}}, \tag{6.12}$$

from which the current source term S_c

$$S_c = u_*^2/h. \tag{6.13}$$

The oscillatory flow is driven by a momentum source term S_w based on a pressure gradient considering the expression:

$$S_w = U_w \omega \cos \omega t \tag{6.14}$$

where U_w is the same of the correspondent WO WINGS Run.

The total physical time covered in the simulations presented is 1000 s. As an indication of computational cost, the calculation lasting 200 seconds of physical time for the three-dimensional wave-current interaction problem requires approximately 1.5 days of CPU time, when simulated in parallel on eight modern CPUs.

In all the calculations, the time step is kept variable to ensure that a certain Courant number is not exceeded. Courant number is capped to 0.5.

The no slip condition at the bottom determine the flow to experience a resistance in proximity of the bed and a consequent development of a boundary layer, until eventually a steady state is reached between forces exerted by the flow and the resistance opposed at the bottom. Over a smooth bottom, forces exerted

by the bed are only due to shear, whereas over a rough bottom, bottom stresses are made of both normal and tangential components. Wall stress is then computed as the area integral of the sum of normal and shear stresses experienced by each cell face of the bottom boundary.

6.3 Numerical results

In the following section the results of the validation of the 1D and 3D model are presented.

6.3.1 Results of the 1D Model

Table 6.2 lists the performed 1D simulations. Runs 1-4 are carried out preliminarly in CO and WO conditions, for both smooth and rough bottom, Runs 5-6 are WC Runs over smooth bottom, whereas Runs 7-8 are over rough bottom. Table 6.2 indicates the corresponding CO and WO WINGS Runs from which the freestream current and wave orbital velocities are taken as input of the model for setting the steady and oscillatory momentum sources respectively. The table includes the WINGS WC Runs used to compare experimental velocity profiles, shear velocity and equivalent roughness with the CFD model. Freestream current velocities are taken from CO WINGS Runs, whereas orbital velocities are taken from WO WINGS Runs, with the exception of CFD Run 6, which considers the orbital velocity of the WC WINGS Run 6 rather than the corresponding WINGS WO Run 2, since the results of the latter one are flawed due to an experimental error, as explained in

Table 6.2: List of the 1D simulations alongside current velocity U, orbital velocity U_w.

CFD Run	Type	Bed	WINGS CO Run	WINGS WO Run	WINGS WC Run	U_c [m/s]	U_w [m/s]
1	CO	smooth	1	-	-	0.226	-
2	CO	rough	32	-	-	0.245	-
3	WO	smooth	-	4	-	-	0.218
4	WO	rough	-	29	-	-	0.199
5	WC	smooth	1	4	8	0.226	0.218
6	WC	smooth	1	6	6	0.226	0.387
7	WC	rough	32	29	33	0.245	0.199
8	WC	rough	32	36	34	0.245	0.293

Section 4.2.

Figure 6.6a shows the dimensionless time-averaged velocity profile for CFD Run 1 (CO, smooth wall, $U_c = 0.226$ m/s) with dimensionless experimental double-averaged velocity profile of the correspondent WINGS Run (Run 1, CO, SB).

Figure 6.6a shows a good agreement of the velocity profile closer to the wall. However, above approximately $0.3h$, a noticeable overestimation of the current profile in the freestream is observed. A depth-averaged velocity deviation is computed, as the difference between the CFD velocity at a certain distance from the bed z and the experimental double-averaged velocity closest to that z, nondimensionalized by experimental freestream velocity U_c. A depth-averaged velocity deviation of 0.04 is observed below $z = 0.3h$, while a 0.13 deviation is observed above in the freestream.

Figure 6.6b shows the same velocity profile but in wall units alongside the Van Driest velocity profile, showing a good agreement between the two profiles in the logarithmic layer, which share a very close value shear velocity value of shear velocity (u^*_{EXP} and u^*_{CFD} both equal to 0.011 m/s) and $k_{s,EXP} = 4.09 \cdot 10^{-4}$ m and $k_{s,CFD} = 4.13 \cdot 10^{-4}$ m.

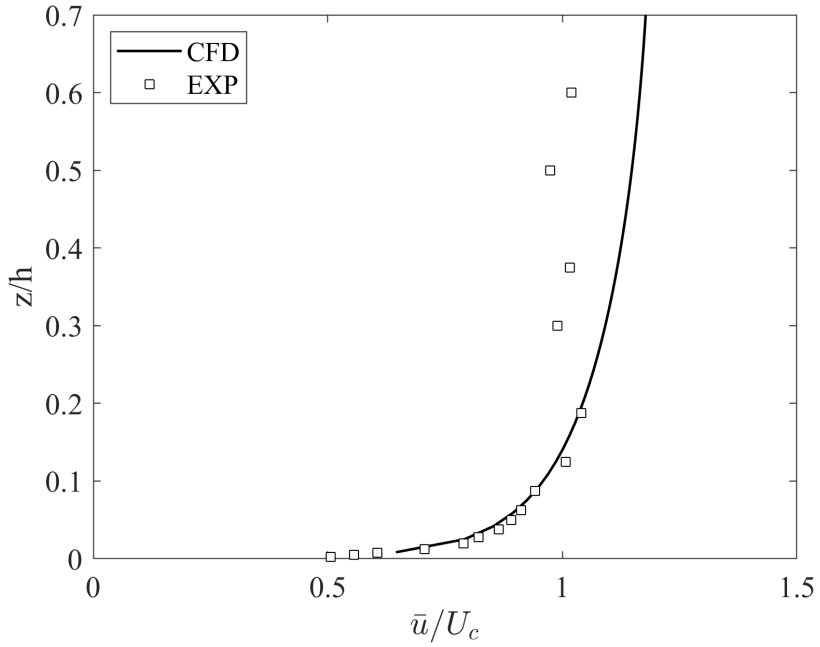

(a)

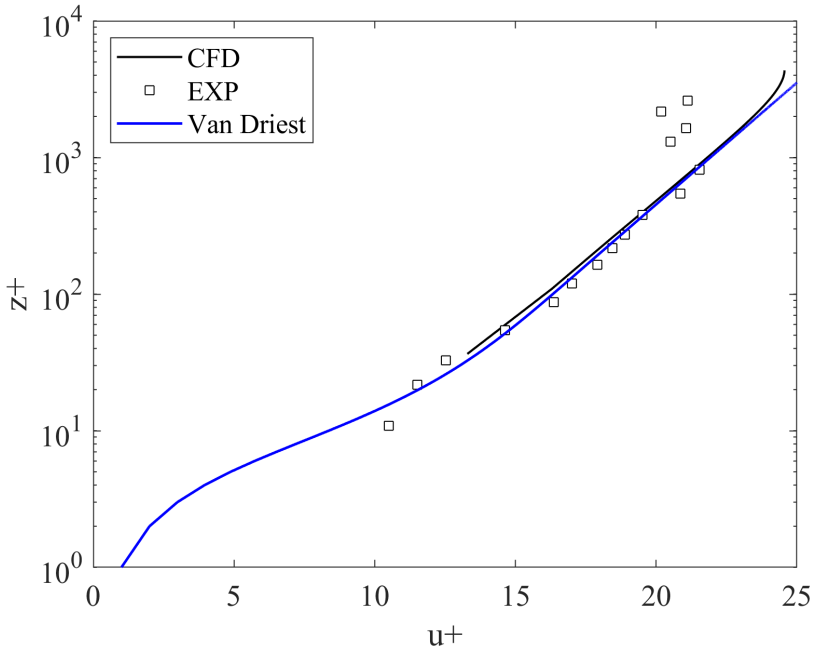

(b)

Figure 6.6: Comparison between CFD Run 1 (smooth wall function) and WINGS Run 1 velocity profiles (a), the same profiles but in wall units (b).

In Figure 6.7a the dimensionless time-averaged velocity profile for CFD Run 7 ($U_c = 0.245$ m/s, rough wall) is compared with the dimensionless double averaged velocity profile of WINGS Run 32 (CO, GB).

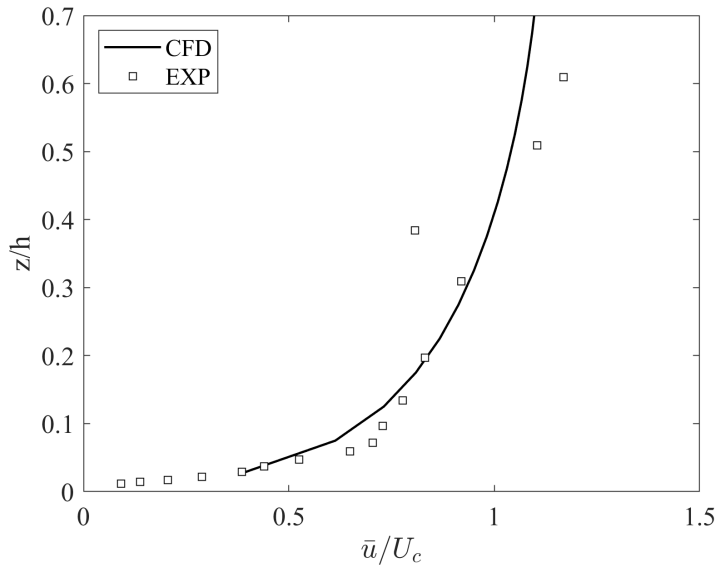

(a)

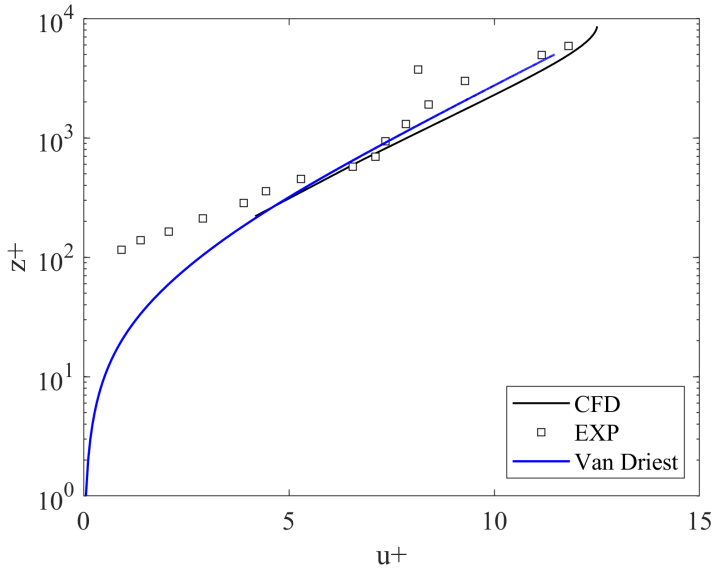

(b)

Figure 6.7: Comparison between CFD Run 2 (rough wall function) and WINGS Run 32 velocity profiles (a), the same profiles but in wall units (b).

The velocity profile deviates by 0.04 in the lower part of the water column ($z < 0.30$ m), while deviating by 0.08 in the upper part. In this case the shear velocity predicted by the model is equal to 0.0220 m/s compared to the WINGS $u^* = 0.0242$ m/s, and the equivalent roughness predicted by the model is 0.0575 m, compared to $k_s = 0.0645$ m of the WINGS Run.

Figure 6.8 shows the phase-averaged velocity profile during the crest (a) and

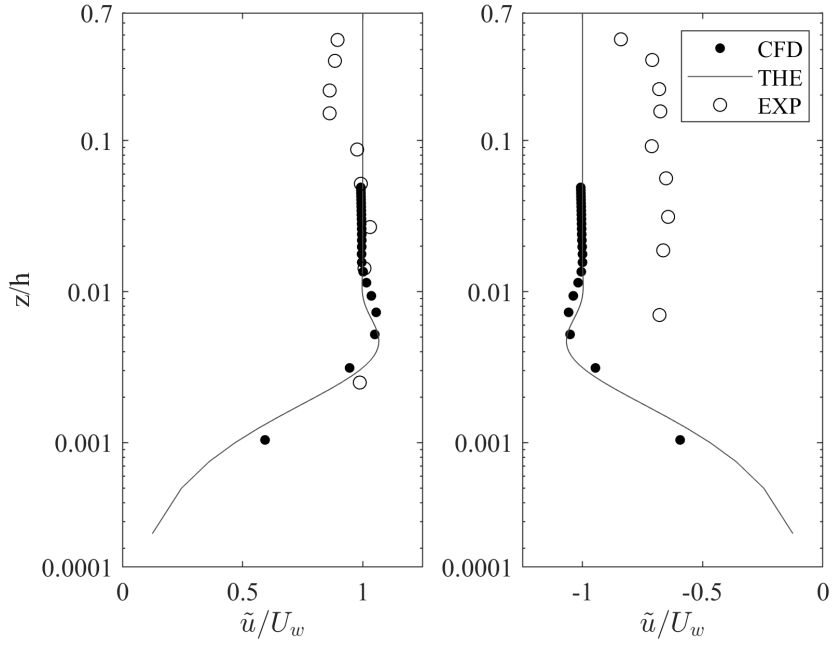

Figure 6.8: Comparison of computed (CFD), theoretical (THE) and experimental (EXP) phase-averaged velocity profiles for 1D Wave Only rough bed CFD Run 3: crest (a), trough (b).

trough (b) wave phases for both experiments (WINGS Run 4, $U_w = 0.20$ m/s, empty markers) and CFD simulation (CFD Run 3, full markers).

In addition, the analytical solution for the wave boundary layer velocity profile over smooth bed is also plotted (Jensen et al., 1989). Indeed, the experimental setup did not allow to have a proper reconstruction of the wave boundary layer, as only few points were measured inside wave boundary layer. In order to check if the simulated profile determines the reconstruction of a proper boundary layer, the analytical solution is plotted. As no shear velocity has been computed from the experiments, the resolution of the mesh has been set by means of a trial and error technique, by increasing the size of the mesh and best fitting the results of the numerical simulation to the analytical solution and experimental data. Figure 6.8a shows a good agreement of the CFD simulation with the analytical solution at the crest profile. A mesh sensitivity analysis showed that an increase of mesh resolution led to numerical instabilities in proximity of the top boundary. In the end, a mesh of 480 cells has been used.

However, Figure 6.8b shows a disagreement between experimental and sim-

ulation data. This is clearly determined by the fact that the one in the simulation are linear waves, instead the experimental ones are wave in intermediate waters with a skewed velocity distribution along the phase, in the range of validity of streamfunction-5th order stokes solution wave theory (Figure 4.5). An issue arised during the first timesteps of the 1D WO simulations. Indeed, the oscillatory flow somehow developed through time into a steady current profile, showing a mean non-zero velocity value, which involved the whole water column. The numerical model has been set in order to keep the Courant number under a certain value, which in the first attempt of this simulation was set to 0.25. At the very beginning of the simulation, the Courant number exceeded that value, subsequently the model 'forces' the Courant number to go below the 0.25 threshold. After that instability, and even if the Courant number was back in the set range after a few timesteps, a steady current profile started to develop. A possible explanation could be the presence of the two very close cyclic boundaries, this configuration may repeatedly loop instabilities that may occur during the simulation. A solution has been found by setting the oscillatory body force to start from its maximum value in order to avoid high velocity gradient right at the beginning of the simulation, therefore having the oscillatory momentum source $S_w = U_w\omega\cos(\omega t)$ rather than $U_w\omega\sin(\omega t)$. As a further precaution, the Courant number has been set to 0.50.

In the wave boundary layer freestream velocities and bottom shear stresses experience a phase shift, which is determined by the different reactions to the oscillatory motion of the low momentum fluid close to the wall and the large momentum fluid closer to the surface. An attempt to quantify the phase-shift in the CFD simulations has been carried out.

Figure 6.9a shows the phase-averaged wave velocity time series outside the wave boundary layer, compared with the phase-averaged bottom shear stress τ/ρ. Figure shows that freestream wave velocity and bed shear stresses are phase-shifted by 37 degrees. Solution is close to the laminar solution (45 degrees).

Similarly to Figure 6.8, Figure 6.10 shows the phase-averaged crest (left) and trough (right) for CFD Run 4 (WO, rough wall function). Analogously to the smooth bottom case, Figure a and b show a good velocity profile agreement in the crest phase, and a poor agreement during the trough phase, determined by the linear

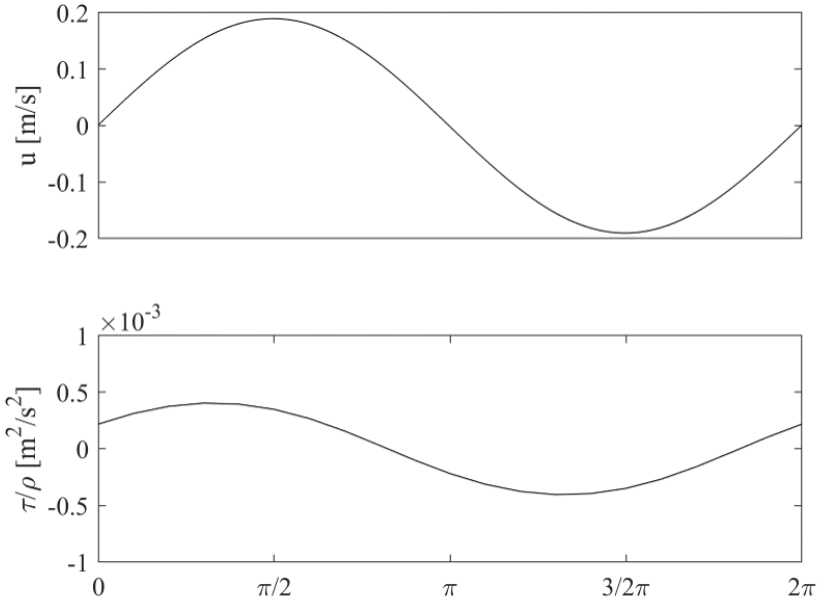

(a)

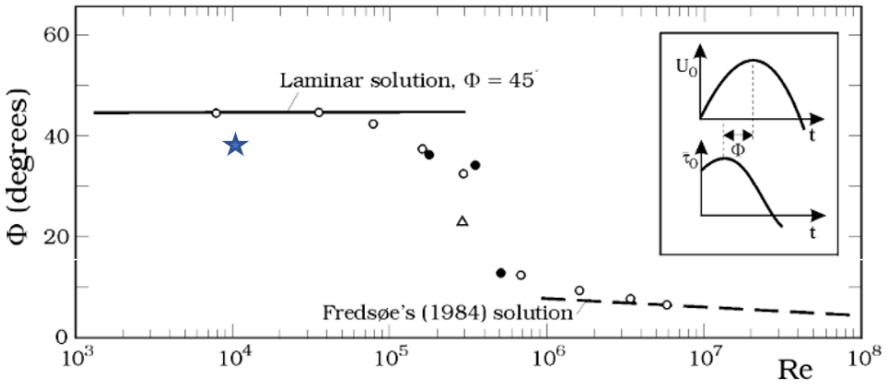

(b)

Figure 6.9: Phase shift of the shear stresses in respect to freestream velocities for the 1D Wave Only simulation Run 3 (a), phase shift versus wave Reynolds number Re_w (Jensen et al., 1989).

oscillatory flow.

Figure 6.11a shows the phase-averaged wave velocity time series outside the wave boundary layer, compared with the phase-averaged bottom shear stress τ/ρ. Figure shows a 37 degrees between the tau and freestream velocity crests, which is close to the laminar solution expected phase-shift.

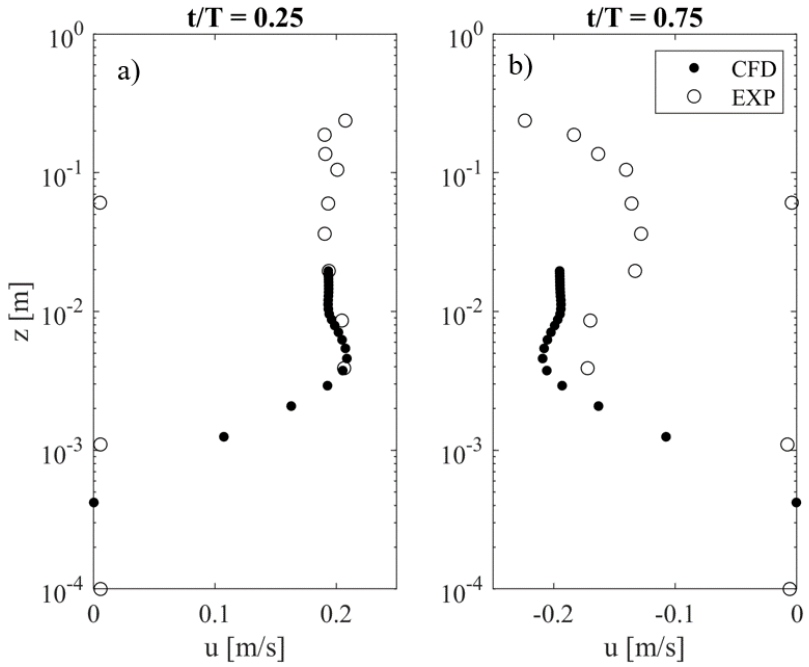

Figure 6.10: Comparison of computed (CFD), theoretical (THE) and experimental (EXP) phase-averaged velocity profiles for 1D Wave Only rough bed Run 4: crest (a), trough (b)

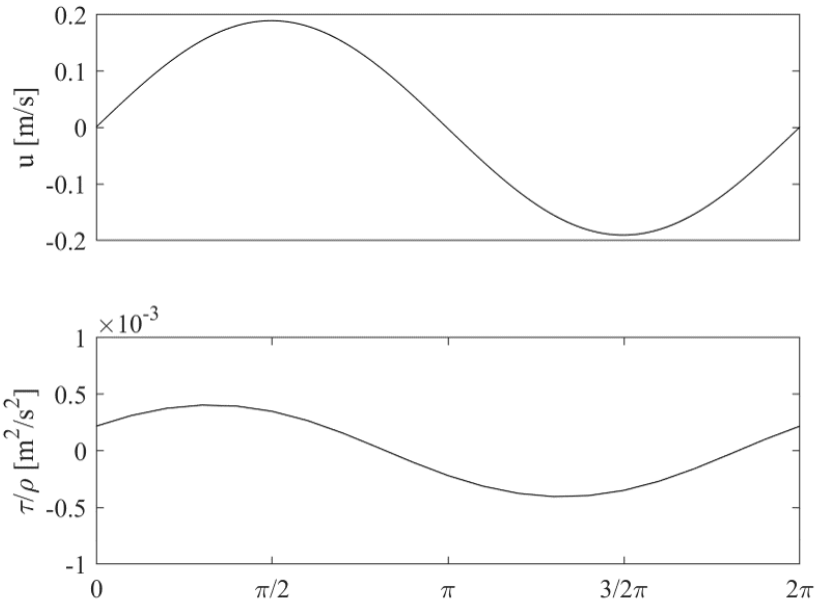

(a)

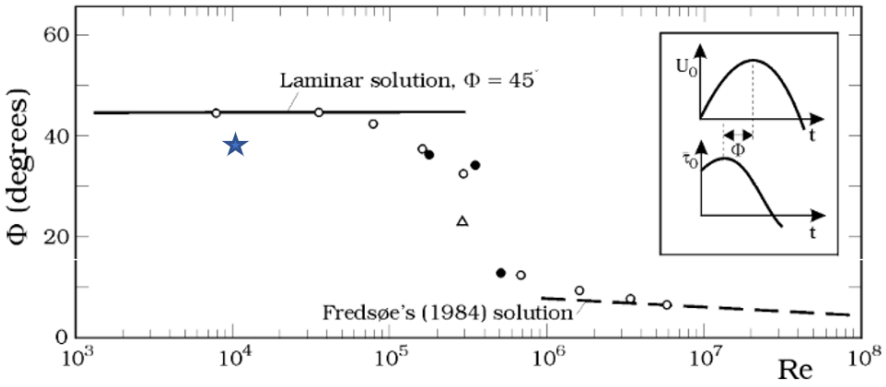

(b)

Figure 6.11: Phase shift of the shear stresses in respect to freestream velocities for the 1D Wave Only simulation Run 3 (a), phase shift versus wave Reynolds number Re_w (Jensen et al., 1989).

In the following, the results for the CFD simulations of the combined flow are presented.

Figure 6.12a shows the dimensionless time-averaged velocity profile for CFD Run 5 (WC, smooth wall function, $U_c = 0.226$ m/s, $U_w = 0.218$ m/s) with dimensionless experimental double-averaged velocity profile of the correspondent WINGS Run 8 (WC, SB). The velocity profile comparison shows a good agreement between experimental data and simulations, with a slight overestimation of bottom current velocity, with a depth-averaged deviation of 0.03 below $z < 0.30$ m, and an underestimation in the upper part of the profile of 0.04. This result suggest an underestimation of shear stress, and a correspondent overestimation of the velocity profile in proximity of the bed. Figure 6.12b shows the same profiles of Figure 6.12a but in wall units. Shear velocity obtained from the best fit of the CFD velocity profile slightly underestimates the experimental ones, with a shear velocity equal to 0.0117 m/s against the 0.0124 m/s of experimental Run 8. The same happens for equivalent roughness which is predicted as $9.0 \cdot 10^{-4}$ m by the model, against an experimental WINGS value of k_s equal to 0.0022 m.

The lower part of the CFD velocity profiles in Figure 6.12b does not agree with the experimental data. This is probably due to the use of the wall function, which assumes the cell centroid closer to the wall boundary lies in the logarithmic layer, which seems not be the case if one looks at the WINGS velocity profile. Such discrepancy is due to the fact that the mesh used in this Run has been designed in order to have the first cell centroid in the logarithmic layer for the Current Only case. This, combined with the use of wall function, makes the model assume that the first cell centroid is already in the logarithmic layer. However, the superposition of waves determines an increase in u^*, which determines the lower limit of the logarithmic layer to be shifted upwards. This occurrence is probably responsible for the underestimation of the shear related quantities and the overall deviation from the freestream velocity profile, which however is below 5%.

Figure 6.13a shows the dimensionless time-averaged velocity profile for CFD Run 5 (WC, smooth wall function, $U_c = 0.226$ m/s, $U_w = 0.387$ m/s) with dimensionless experimental double-averaged velocity profile of the correspondent WINGS Run 6 (WC, SB), Figure 6.13b shows the same profiles but in wall units. The simulation

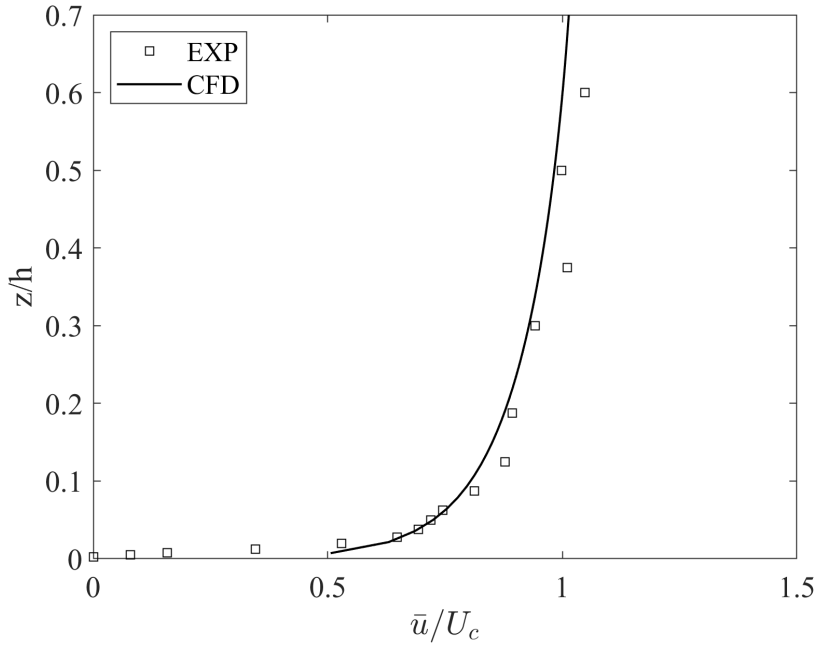

(a)

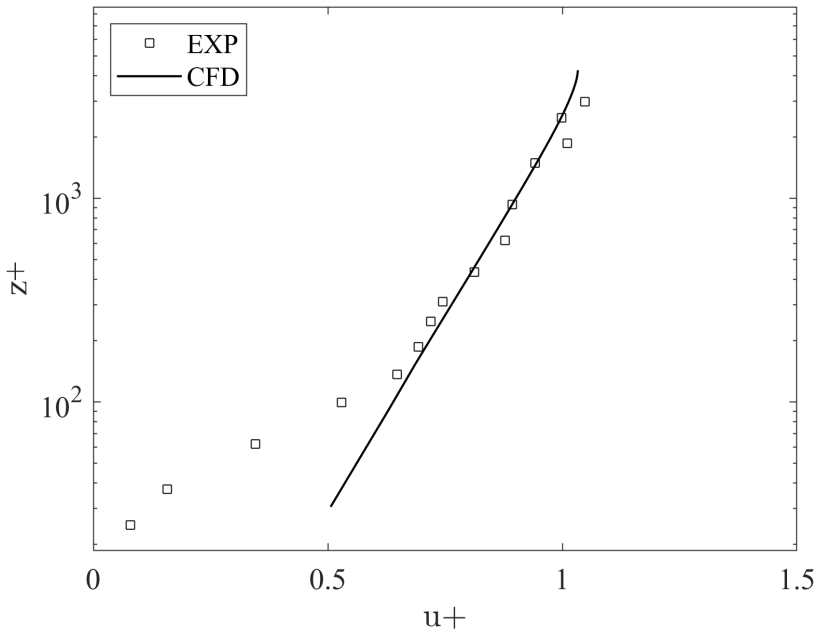

(b)

Figure 6.12: Comparison between of CFD Run 5 (WC, smooth wall function, U_c = 0.226 m/s, U_w = 0.218 m/s) and the correspondent WINGS Run 8 (WC, SB) (a), the same profiles but in wall units (b).

differs from the case of Figure 6.12 by having the same input freestream velocity but an almost doubled wave orbital velocity. As wave orbital velocity increases,

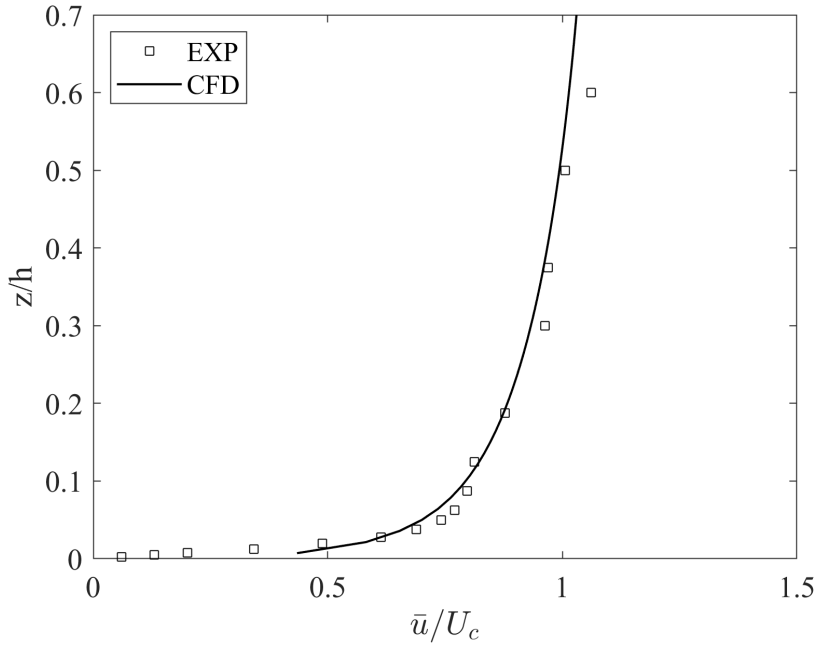

(a)

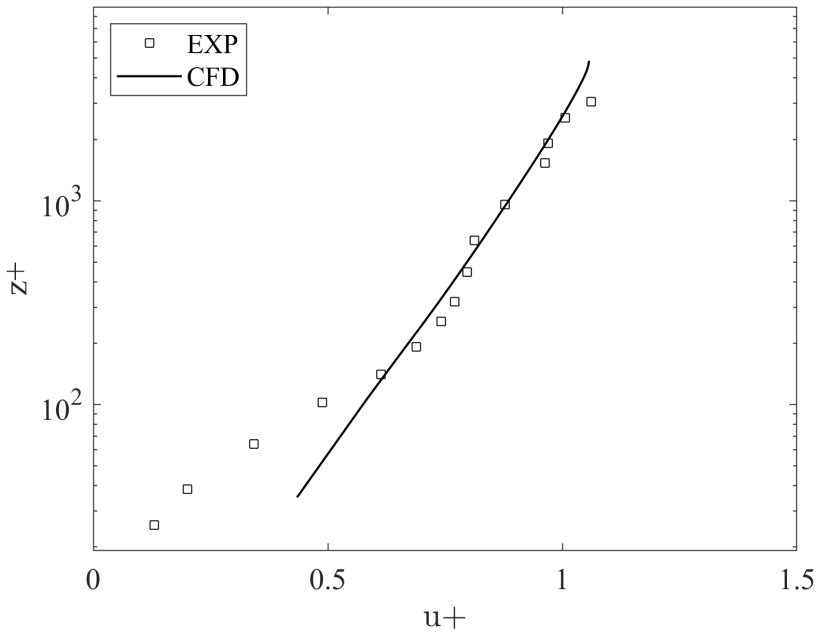

(b)

Figure 6.13: Comparison between CFD Run 6 (WC, smooth wall function, $U_c = 0.226$ m/s, $U_w = 0.387$ m/s) and the correspondent WINGS Run 6 (WC, SB) velocity profiles (a), the same profiles but in wall units (b).

the model seems to predict fairly well the velocity profile, with a depth-averaged deviation of 0.04 and 0.02, below and below $z < 0.30$ m respectively. Nevertheless,

shear velocity is slightly underestimated by the model, predicting a value of 0.0122 m/s against the experimental u^* of 0.0128 m/s. Equivalent roughness is 0.0026 m, very similar to the experimental value of 0.0029 m.

Figure 6.14a shows the dimensionless time-averaged velocity profile for CFD Run 7 (WC, rough wall function, $U_c = 0.245$ m/s, $U_w = 0.199$ m/s) with dimensionless experimental double-averaged velocity profile of the correspondent WINGS Run 33 (WC, GB), Figure 6.13b shows the same profiles but in wall units. It is evident from the comparison of the WINGS and CFD velocity profiles that the model significantly underestimates velocity profile by 0.10 of U_c below $z < 0.30$ m and by 0.07 above. A significant overestimation of the shear related quantities is indeed observed, with a shear velocity of 0.0309 m/s and an equivalent roughness of 0.1601 m, against the respective WINGS campaign values of $u^* = 0.0284$ m/s and $k_s = 0.0877$ m.

Figure 6.15a shows the dimensionless time-averaged velocity profile for CFD Run 8 (WC, rough wall function, $U_c = 0.245$ m/s, $U_w = 0.293$ m/s) with dimensionless experimental double-averaged velocity profile of the correspondent WINGS Run 34 (WC, GB). This results differ from the ones shown in Figure 6.14 only by the input wave orbital, velocity being $U_w = 0.293$ m/s instead of 0.199 m/s. The increase of orbital velocity determines an even larger discrepancy between experimental and model values, with an underestimation in proximity and far from the bottom of 0.11 and 0.08 respectively. This is probably related to a significant overestimation of the shear velocity and equivalent roughness by the model, with a shear velocity of 0.0326 m/s against an experimental u^* of 0.286 m/s, and an equivalent roughness of 0.2004 m compared to an experimental of 0.0844 m.

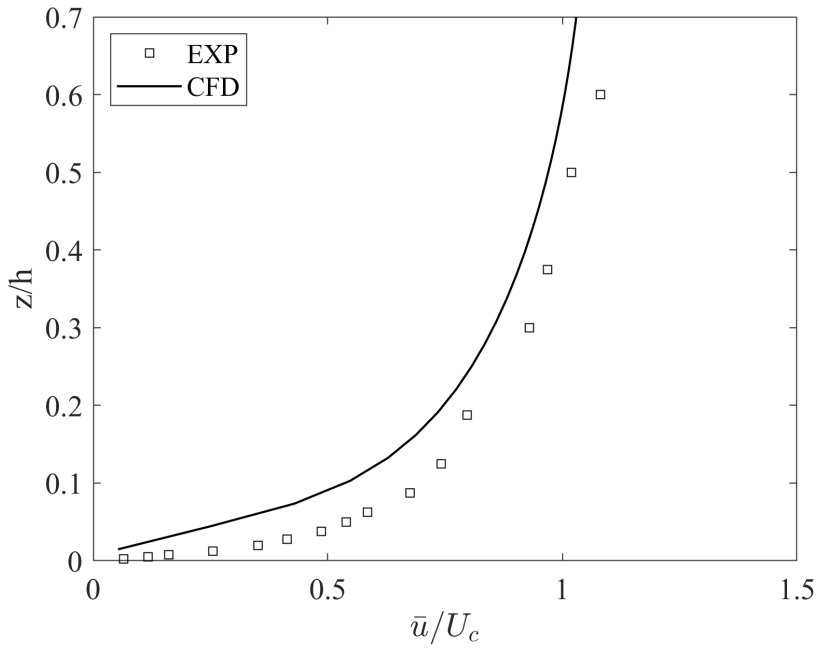

(a)

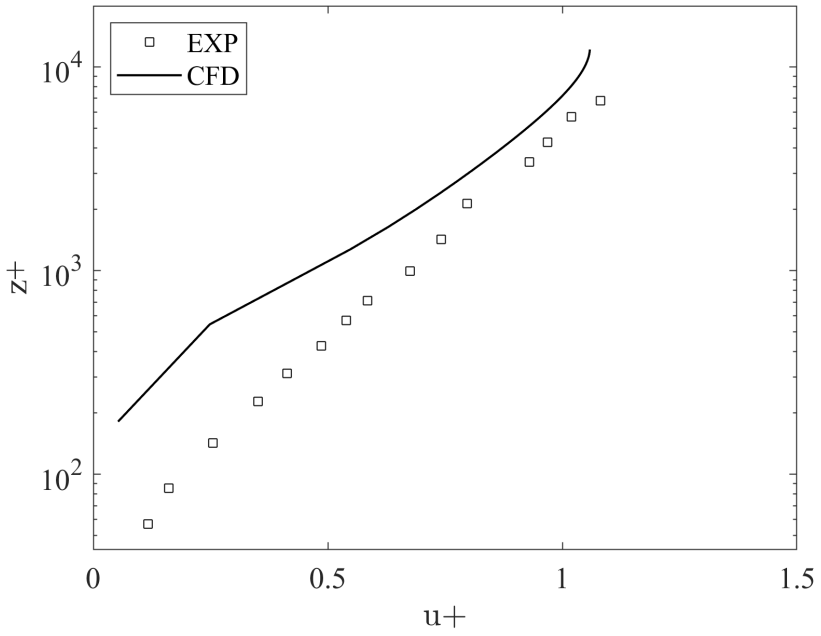

(b)

Figure 6.14: Comparison between CFD Run 7 (WC, rough wall function, $U_c = 0.245$ m/s, $U_w = 0.199$ m/s) and the correspondent WINGS Run 33 (WC, GB) velocity profiles (a), the same profiles but in wall units (b).

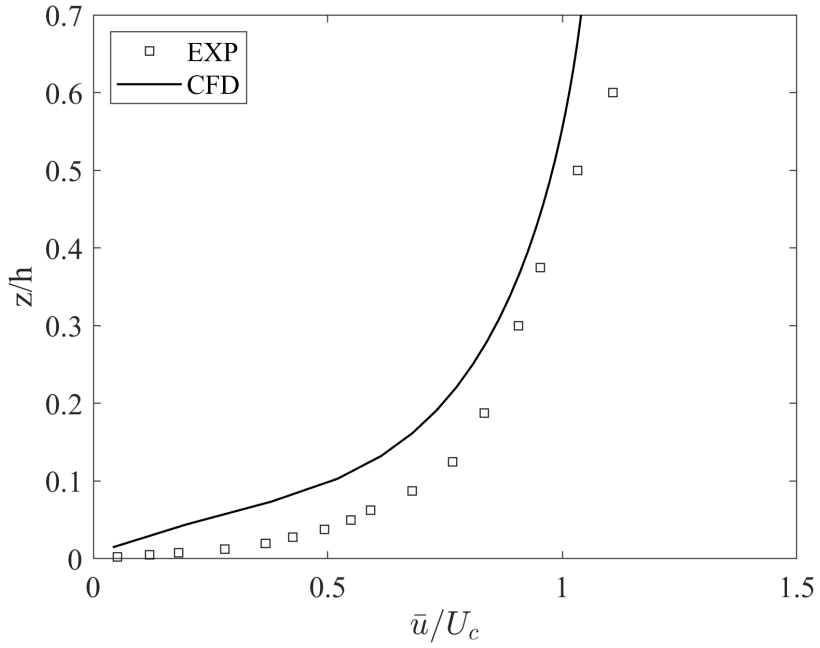

(a)

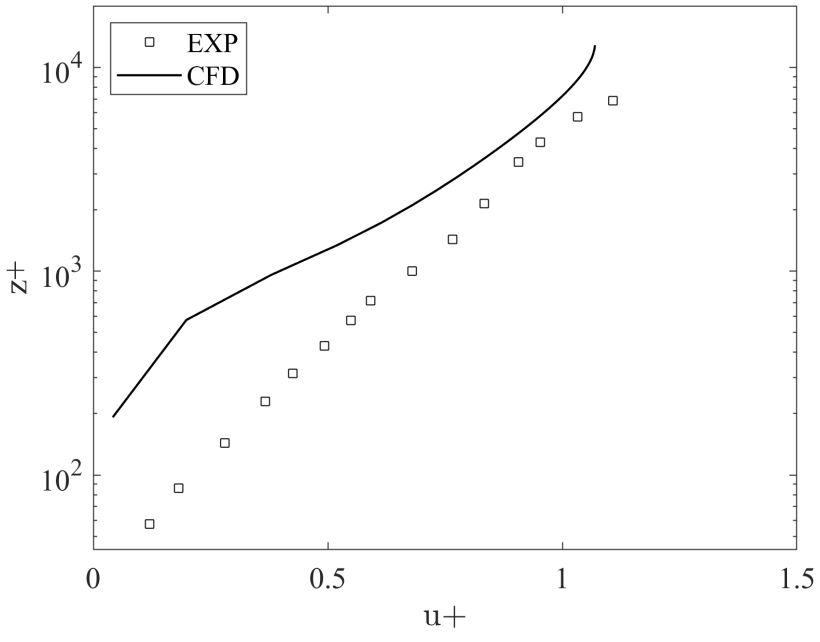

(b)

Figure 6.15: Comparison between time-averaged and double-averaged experimental WINGS velocity profiles for CFD Run 8 (WC, rough wall function, $U_c = 0.245$ m/s, $U_w = 0.293$ m/s) and the correspondent WINGS Run 34 (WC, GB) (a), the same profiles but in wall units (b).

6.3.2 Results of the 3D Model

The results of the 3D simulation are presented here. A series of numerical velocity gauges have been positioned in the domain in order to probe flow velocity in x, y and z directions. A total of 192 probes have been set, subdivided into 4 profiles, with each profile having 48 probes. The probes in each profile share the same x and y position in the domain, while having a different z in order to reconstruct a velocity vertical distribution for each profile. Considering a reference system like the one in Figure 6.1, the probes x and y positions are the following: probe 1 ($x = 0.035$ m, $y = 0.035$ m); probe 2 ($x = 0.115$ m, $y = 0.035$ m); probe 3 ($x = 0.035$ m, $y = 0.115$ m); probe 4 ($x = 0.115$ m, $y = 0.115$ m). The velocities time series are then time-averaged for each profile for a 240 s time interval, and then space-averaged for all the profiles, in order to obtain a final double-averaged profile.

Figure 6.16 shows the velocity profile of the 3D Run. The simulation is in CO condition, with a pressure gradient based on WINGS Run 32 shear velocity ($\partial p/\partial x = u^{*2}/h = 0.0015$ m^2/s). The Figure shows that the CFD model results differ from the measured velocity profile in both the freestream and proximity of the bed. Indeed, in the upper part of the water column, the CFD simulation reaches the freestream at a distance closer to the bed, by showing rather smaller velocity gradients in comparison with the experimental velocity profile. Presence of the rough flow boundary layer seems to affect a larger portion of the water column in the WINGS velocity profile, rather than in the model. In the very proximity of the bottom, the bed shear stress seems to induce an underestimation of the velocity profile, which however it has not been probed in the very vicinity of the bottom. Nevertheless, the bottom stress experienced by the current in the model, which is given by the sum of normal and shear components integrated for all the faces in the bottom boundary, apparently matches the experimental one, reaching a steady condition at $\partial p/\partial x = 0.0015$ m^2/s, as it has been imposed by the pressure gradient in the momentum source term. Although the present results should be considered as preliminary, they highlight that the discrepancy between the shear experienced by the current, which is apparently correctly reproduced by the model, and the measured velocity profile deserves future investigations.

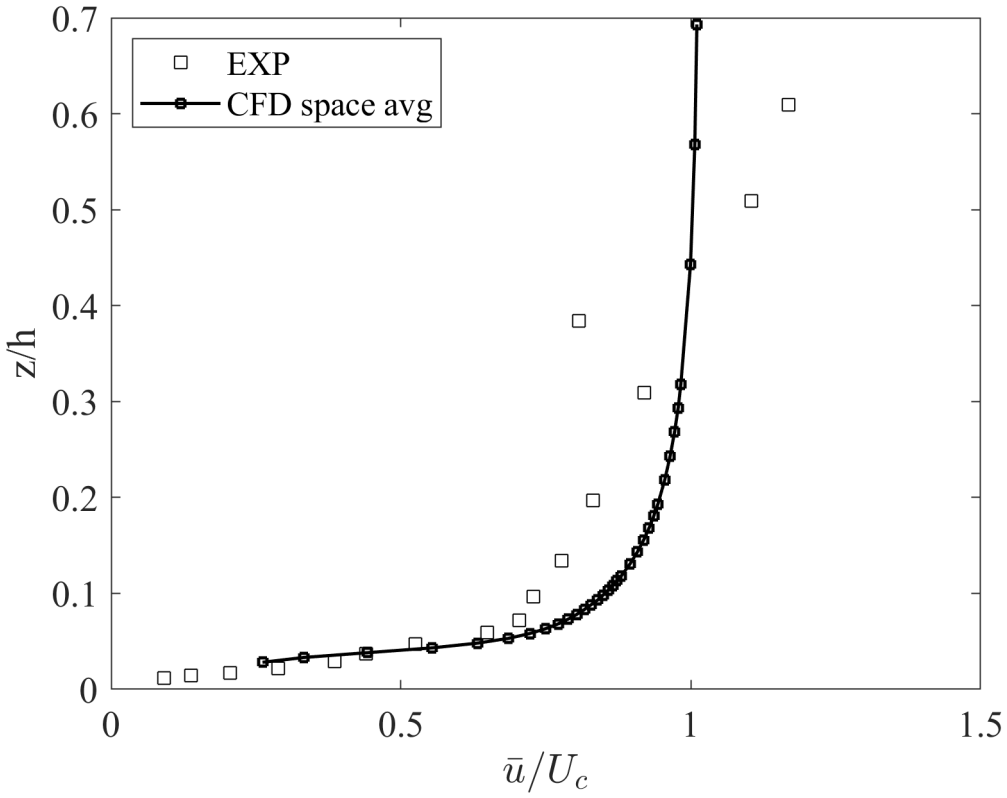

Figure 6.16: Velocity profile in wall units of a Current Only 3D simulation.

6.4 Discussion of results

The results of the 1D model, with smooth wall function implemented in the bottom boundary, showed a good agreement with the experimental velocity data in the presence of a lone current, the experimental setup is satisfactorily able to reproduce the velocity profile and shear stesses in the logarithmic layer. A larger deviation of the velocity profile is observed when the oscillatory flow is superposed on the current. By means of the comparison with the experimental data, the results showed an overall underestimation of the velocity profile in the freestream, and an overestimation of the velocity in proximity of the bed, probably related to an overall underestimation of the bed shear stresses operated by the model. This occurrence could be related to the inability of the numerical setup to follow the change in the logarithmic layer limits due to the increase in shear determined by the presence of waves. Indeed, the mesh has been set based on the shear velocity of the the lone current experimental run, in order to have the first point in the logarithmic layer, but with the lower limit of the logarithmic layer shifting up due to the increase

of the shear velocity, therefore the first cell centroid falls below that limit when the oscillatory flow is superposed. The problem may be also related to the use of wall functions in presence of an oscillatory flow. As it is known that this bottom boundary conditions may not perform well in presence of adverse pressure gradients, their use is questionable in the first place. Unfortunately, the literature in this regard is rather limited. (Mcdonald, 1969; Panara et al., 2006). A possible solution could be to increase the size of the first cell according to the shear velocity increase only. However, that would need an estimation of the value of the shear velocity *a priori* in order to sizing the mesh accordingly. A straightforward solution could be the use of Low-Re simulations, therefore without the use of wall functions, which would eventually work for smooth bed simulations. On the other hand, in such a setup the roughness should be resolved by the mesh, by means of a reproduction of a physically rough bottom boundary. The use of wall function has been chosen in order to take advantage of the possibility to include equivalent bottom roughness effects. Notwithstanding the above critical issues, the results are interestingly close to the experimental data and, with some modifications, the model could be used for preliminary estimates of the flow field to use as an input for larger models in which the combined flow occurs, or used as a standalone predictive tool for wave-current combined flow, not only for velocity profiles but also for turbulent production and dissipation profiles, which would however eventually need a proper validation, not provided in the present work. From another viewpoint, the investigation highlights the limits of the use of wall functions for the modeling of the current velocity profile close to the bottom boundary, when used in combination with an oscillatory flow. Wall functions are indeed largely used in both scientific and commercial contexts in coastal engineering, therefore the topic deserves further investigations.

For what concerns the rough wall function 1D simulations, results showed a significant overestimation of both freestream and boundary layer velocities. Such an occurrence is probably related to a large overestimation of the effect of the equivalent roughness set in the wall function.

A 3D numerical setup has been developed and a preliminary validation has been presented. The numerical setup has an interesting feature, as it is provided with a 3D reconstruction of the gravel bed used as bottom boundary. A series of technical

issues related to the building of the model have been highlighted, and the solutions to solve or outflank those problems have been presented. The model is, indeed, able to reproduce the correct shear conditions at the bottom of a lone current, as they are imposed in the current momentum source term, however the current velocity does not match the experimental one. Indeed, this model is known to produce large turbulence kinetic energy production when normal strain are large (Menter et al., 2003), which is the case when the bed roughness is physically reproduced in the model. The problem with this kind of configuration is not only the significantly large computational times related to the domain size and number of cells, but rather the large times for the model to reach a steady state. Indeed, as for the 1D model the 400 s of physical time were sufficient, with the 3D model the steadiness of the current and the desired value of shear velocity are reached after approximately 1000 s. Unfortunately, due to the above mentioned computational costs, the model itself does not give much possibility to test different turbulence closures or other numerical setup configurations, or at least not within the time frame and the scope of the present work.

The present results, however, suggest that further investigations should focus on: (i) for the smooth 1D model, setting a setup in a Low-Re condition, hence with the boundary layer fully resolved by the mesh, and with the cell centroid closest to the bed lying in the viscous layer, at least for the sand bed case; (ii) for the 3D model, testing of different turbulence closure models, and comparisons not only with velocity profiles, but also k and ω vertical distributions.

Chapter 7

Conclusions

In the present work, an investigation on the hydrodynamics of orthogonal wave-current combined flow has been carried out. Specifically, the work has been focused on the effects of waves on the current boundary layer, and on how the oscillatory flow affects the current velocity distribution. Two laboratory campaigns have been carried out. One with waves and currents propagating over sand and gravel flat beds, the WINGS campaign, and one over a sloping profile fixed bed, the ACCLIVE campaign. Flow velocity measurements have been carried out by means of Acoustic Doppler Velocimeters, both inside and outside of the boundary layer. Wave surface elevation time series have been measured by means of resistive wave gauges.

Mean flow has been investigated by computing double-averaged velocity profiles, by means of time- and space-averaging of the velocity time series for the WINGS dataset, and time-averaged profiles for the ACCLIVE dataset. Friction velocity and equivalent equivalent roughness have been inferred from the velocity profile by best fit method (Sumer, 2007).

The hydrodynamics of the combined flow has been investigated by means of a comparison of the experiments of pure current with the ones in the presence of superposed waves. Instantaneous velocities have been Reynolds-averaged in order to obtain turbulent fluctuations time series, from which turbulence intensities and Reynolds stresses, have been computed.

The mean current velocity profiles of the WINGS dataset have been compared with a selection of analytical models in order to assess their validity for the case of

wave-current orthogonal flow for the considered wave-current conditions.

Moreover, a series of CFD investigations have been carried out. Specifically, two numerical setups have been set, a one-dimensional one and a three-dimensional one. The models solve for Reynolds-averaged Navier Stokes equations for incompressible fluids, boundary conditions are cyclic and dynamic conditions are imposed through steady and oscillatory body forces at the cell centroids, in order to simulate the current and the waves respectively. Validation is carried out by means of the WINGS mean velocity profiles. The 1D model solves the bottom roughness through the use of wall functions, whereas the 3D setup features a reconstruction of the gravel bed used within the WINGS campaign. Current only, wave only and waves plus current tests where conducted for the 1D model, whereas a preliminary current only flow for 3D model has been carried out.

The data analysis of the laboratory and numerical data provided the following results:

Mean flow

- In the presence of a stronger current ($Fr = 0.106$), the shear experienced by the flow in the current direction is always enhanced by the presence of the waves, as observed by the increment of friction velocity(up to 30%) and equivalent roughness (up to an order of magnitude). The combined flow shear increment with respect to the lone current case, expressed by the ratio Re^*_{WC}/Re^*_{CO}, appears to increase in a non-monotonous fashion, as the relative importance of the waves with respect to the current, expressed by the wave-current parameter U_w/U_c, increases. Specifically, for values of U_w/U_c close to 1, thus in proximity of the limit between current- and wave-dominated regimes, the shear seems to feature a constant trend. Whereas, for relatively low and high values of U_w/U_c, the shear experienced by the current due to the presence of waves increases with a similar trend. This behavior seems to be consistent for both sand and gravel bed experiments. This occurrence may be related to the the presence of the laminar wave boundary layer which may determine a suppression of turbulent momentum transport in the region inbetween $U_w/U_c = 1$. A similar behavior has been observed by Lodahl et al. (1998), although such Authors

report a decrease of shear in that region, rather than a constant trend.

- In the presence of a weaker current ($Fr = 0.058$) a decrease of friction velocity up to 50%, alonside a decrease of equivalent roughness up to an order of magnitude, have been always observed due to the superposition of the oscillatory flow. Similar occurrences have been observed in past experimental and numerical investigations (Musumeci et al., 2006; Olabarrieta et al., 2010), although in those studies only a decrease of equivalent roughness was observed. In experiments over sand bed, a close-to-linear behavior of Re^*_{WC}/Re^*_{CO} has been observed here as the wave-current parameter increases, whereas over gravel bed results show a constant trend.

- The superposition of shoaling waves induces the current to experience a larger bottom friction, as observed by the increment up to 20% of the friction velocity, which suggests the occurrence of an enhanced turbulent mixing induced by the oscillatory motion. As waves shoal, the presence of waves does not seem to enhance significantly turbulent shear. This is shown by a very similar shear velocity determined by the wave in the more shoreward position. Indeed, Although wave orbital velocity increases as the wave shoals, in the presence of a current with a larger Re_c wave motion may be less effective in inducing an increase of turbulence shear.

- Analysis of the phase-averaged velocity profiles showed that superposition of waves induces the current to oscillate around its mean velocity. Moreover a phase shift between current and wave phase-averaged velocity maximums has been observed. Such a phase shift seems to be gradually enhanced as the waves shoal. Indeed, as wave shoaling progresses, the skewness of the wave velocity distribution increases, and the absolute value of the wave acceleration during the crest phase increases. Conversely, as the mean current velocity increases with decreasing depth as an effect of continuity, the current opposes to the acceleration induced by the wave motion. Indeed, as the momentum carried by the current increases as water depth decreases, it is less subject to the presence of the the shoaling waves, determining the oscillating effect on the current to be delayed. in other words, while shoaling waves induce the

amplitude of the current oscillation to increase, a larger momentum current opposes to the wave increased acceleration, determining the occurrence of a delay in the oscillatory motion of the current. The phase-shift, expressed as the shift between the maximums phase-averaged velocities in the current and wave direction, increases as the waves shoal, from 20% at the most seaward position to 60% at the most shoreward position.

- The comparison of the combined flow experimental velocity profiles with a selection of models showed that, for the performed wave-current conditions, the best performance is achieved by the Grant and Madsen (1986) model, which estimated satisfactorily the experimental combined flow velocity profiles and shear velocity, with deviations of velocities up to 6%. The empirical formulation by Soulsby (1997) and the Styles et al. (2017) three-layers eddy viscosity model both underestimated velocity profile of sand bed cases, reaching velocity deviations of 15%, whereas under- and overestimating velocity profiles in gravel bed experiments up to 30%.

Turbulent flow

- Turbulent flow analysis partly confirmed what already observed for the mean flow. In the presence of a stronger current over sand bed, combined flow turbulence intensity profiles are characterized by larger values and vertical gradients up to 3-4 times with respect with the pure current case. A similar behavior has been observed also on gravel bed, with turbulence intensities involving a larger portion of the water column in comparison with the sand bed case. In the presence of a weaker current, the superposition of waves always induces an increase of turbulence intensity profile values, except over gravel bed in which a decrease is observed in the very proximity of the bottom. However, over gravel bed the presence of the oscillatory flow determines a decrease of the turbulent intensity gradient, which may be related to the decrease of bottom friction observed in the mean flow analysis. This result however has not been observed in the sand bed case.

- Quadrant analysis showed that, in the presence of a lone current over a flat

gravel bed, the ejection-sweep mechanism reaches parts of the water column closer to the water surface, similar to what has been observed in the turbulence intensity profiles. The superposition of the oscillatory flow appears to induce an increment of ejections and sweeps intensity, which is associated with the shear stress increase at the bottom observed in the mean flow analysis. Moreover, a decrease of the number of ejection and sweep events has been recorded, which suggests a suppression of the ejection-sweep events alongside an enhancement of their intensity. In the presence of shoaling waves, an increase of the ejection-sweep cycle events, which determines turbulent mixing to be enhanced, is induced by the oscillatory flow. Moving farther from the bottom, as expected, turbulent field progressively abandon the ejection-sweep cycle as main mechanism of turbulent momentum transfer, in favour of a more isotropic turbulent mixing.

Numerical analyses

- The simulations using the the one-dimensional setup, with smooth wall function implemented in the bottom boundary, showed a good agreement with the experimental velocity data in the presence of a pure current. A larger deviation of the velocity profile is observed when the oscillatory flow is superposed on the current. By means of the comparison with the experimental data, the results showed a slight underestimation of the velocity profile in the freestream, and an overestimation of the velocity in proximity of the bed, probably related to an overall underestimation of the friction velocity operated by the model, which is around 6%.

  This occurrence is probably associated to the inability of the numerical setup to follow the logarithmic layer limit shift determined by the wave-induced bottom friction enhancement. The numerical mesh has been set in order to have the wall function to properly model the lowest velocity point of the current logarithmic layer. However, in the presence of waves, the lower limit of the logarithmic layer shifts up due to the increase of the shear velocity determined by the oscillatory flow, making the centroid of the lowest cell of the mesh to fall below the logarithmic layer limits. This occurrence determines a

significant overestimation of the velocity profile close to the bed, and a consequent decrease in the freestream. In the presence of a rough wall function, the results of the 1D setup model showed a significant underestimation of both freestream and boundary layer velocities, reaching deviations of 40% from the experimental velocity profile. This occurrence is probably associated to a large overestimation of the effect of the equivalent roughness set in the wall function.

- The result of a first attempt of a 3D simulation of a lone current has been presented, although not validated by the experimental results. The model is not able to correctly simulate the current flow velocity profile, which does not match the experimental profiles. A possible explanation could be the use of the $k-\omega$ SST turbulence closure model, which has been reported to generate large turbulence kinetic energy production when large normal strain are present (Menter et al., 2003), which is our case as the bed roughness is physically reproduced in this model.

In the present work, a comprehensive investigation of the nonlinear and turbulent interaction of waves and currents occurring in the near region has been presented, considering both wave-dominated and current-dominated conditions, different bottom roughness, horizontal and sloping beds. The problem has been tackled from different viewpoints (e.g. mean flow, phase-averaged and turbulent flow), complementing the capabilities of different experimental facilities and numerical models. However, the present analysis highlighted also the need for further analyses.

In particular, future experimental studies should focus on: (i) extend the range of the experiments for the current Fr, in order to investigate how the shear velocity change behaves in between the examined Fr values $0.058 \div 0.106$; (ii) recover direct measurements of bottom shear stresses rather than inferring via indirect methods, for instance by using innovative techniques, such as the one of Musumeci et al. (2018); (iii) further analysis on turbulence, including a phase-averaged turbulence intensity study and quadrant analysis, in order to better understand how the current ejection-sweep mechanism is altered during the different phases of the wave cycle; (iv) in the presence of a sloping bottom, extend the cases to conditions closer to breaking, in order to investigate the effects of waves for cases with larger orbital velocities and skewer phase-averaged velocities distribution.

With respect to the CFD wave-current models, further investigations should concentrate on: (i) performing other conditions with the same numerical setups, in order to test the validity of the cyclic boundaries coupled with body forces method in a larger range of cases; (ii) for the smooth 1D model, considering a setup in a Low-Re condition, with the boundary layer fully resolved by the mesh; (iii) investigating the error determined by the underestimation of the current velocity in the freestream, especially for its effect on the wave surface elevation alterations; (iv) for the 3D model, testing other turbulence closure models, and compare with velocity profile of the presented model, observing also the behavior of k and ω vertical distributions.

Acknowledgements

A	Inlet section area
A_{bm}	Wave orbital amplitude ($= U_w/\omega$)
C_r	Wave-current strength ratio
d_{50}	Nominal 50%-percentile grain diameter
$D_{u,model}$	Current velocity deviation of a model with respect to the experimental data
$D_{u^*,model}$	Shear velocity deviation of a model with respect to the experimental data
$D_{k_s,model}$	Equivalent roughness deviation of a model with respect to the experimental data
f_{cw}	Combined flow friction factor
Fr	Froude number
F_1	First $k-\omega$ SST (Menter et al., 2003) blending coefficient
F_2	Second $k-\omega$ SST (Menter et al., 2003) blending coefficient
g	Gravity acceleration
h	Local water depth
h_0	Flat bottom water depth (for ACCLIVE dataset)
h^+	Water depth in wall units
H	Nominal wave height
H_m	Measured wave height
I_u	Turbulence intensities in the current direction
I_v	Turbulence intensities in the wave direction
$I_{i,\Omega}$	Indicator function of quadrant analysis

k	Turbulent kinetic energy
k_r	Reflection coefficient
k_s	Equivalent roughness
k_s^+	Equivalent roughness in wall units
K	Wave number
K_s	Shoaling coefficient
Ku	Frequency distribution kurtosis
N_w	Number of waves used for the phase average
N_z	Number of surface bed elevations
p	Pressure
Re_c	Reynolds number of the current
Re_w	Reynolds number of waves
Re^*	Shear Reynolds number
Re^*_{CO}	Shear Reynolds number (Current only)
Re^*_{WC}	Shear Reynolds number (Waves plus current)
s	Time segment of the 10 minute time series
Sk	Frequency distribution skewness
S_c	Steady flow momentum source term
S_c	Oscillatory flow momentum source term
t	Time
T	Wave period
T_{end}	Last instant of the turbulent time series
u	Instantaneous velocity in the current direction
$\bar{u}$	Time-averaged velocity in the current direction
$\tilde{u}$	Phase-averaged velocity in the current direction
u'	Turbulent velocity in the current direction
u^*	Current bottom friction (or shear) velocity
u^*_c	Current shear velocity in the Grant and Madsen (1986) model
u^*_w	Wave shear velocity in the Grant and Madsen (1986) model
u^*_{wc}	Combined flow shear velocity in the Grant and Madsen (1986) model
$u^*_{wcm,wc}$	Combined flow maximum bed shear velocity

u_{model}	Velocity predicted by GM86, SO97 or ST17 model
$u_{5,s}$	streamwise velocity of the 5 minutes segment
$u_{2,s}$	Dimensionless time-averaged streamwise velocity of the 2 minutes segment
u^+	Current velocity in wall units
U	Nominal current velocity
U_c	Freestream velocity
U_w	Wave orbital velocity
v	Instantaneous velocity in the wave direction
$\bar{v}$	Time-averaged velocity in the current direction
$\tilde{v}$	Phase-averaged velocity in the wave direction
v'	Turbulent velocity in the wave direction
$v_{5,s}$	Dimensionless time-averaged crosswise velocity of the 5 minutes segment
$v_{2,s}$	Dimensionless time-averaged crosswise velocity of the 2 minutes segment
w	Instantaneous velocity in the vertical upward direction
$\bar{w}$	Time-averaged velocity in the vertical upward direction
$\tilde{w}$	Phase-averaged velocity in the vertical upward direction
w'	Turbulent velocity in the vertical upward direction
$w_{5,s}$	Dimensionless time-averaged vertical upward velocity of the 5 minutes segment
$w_{2,s}$	Dimensionless time-averaged vertical upward velocity of the 2 minutes segment
x	Current direction coordinate
y	Crosswise direction coordinate
z	Vertical upward direction coordinate (bottom distance)
z^+	Bottom distance in wall units
α	slope of the linear fitting in the logarithmic velocity profile
α_1	$k-\omega$ model coefficient

β	intercept of the linear fitting in the logarithmic velocity profile
β_1	$k-\omega$ model coefficient
β^*	$k-\omega$ model coefficient
δx	Geostatistic spatial correlation lag in the x direction
δy	Geostatistic spatial correlation lag in the y direction
δ_c	Current boundary layer thickness
δ_w	Wave boundary layer thickness
ϵ	Turbulent dissipation
η	Wave surface elevation
$\tilde{\eta}$	Phase-averaged surface elevation
κ	Von Karman number
ν	Kinematic viscosity
ν_t	Turbulent (or eddy) viscosity
ρ	Water density
σ_H	Standard deviation of the measured wave height
σ_u	Standard deviation of dimensionless time-averaged streamwise velocity
$\sigma_{u,5,s}$	Standard deviation of dimensionless time-averaged streamwise velocity of the 5 minutes segment
$\sigma_{u,2,s}$	Standard deviation of dimensionless time-averaged streamwise velocity of the 2 minutes segment
σ_v	Standard deviation of dimensionless time-averaged crosswise velocity
$\sigma_{v,5,s}$	Standard deviation of dimensionless time-averaged crosswise velocity of the 5 minutes segment
$\sigma_{v,2,s}$	Standard deviation of dimensionless time-averaged crosswise velocity of the 2 minutes segment
θ	Angle between waves and currents
ω	Rate of turbulent kinetic energy dissipation
Ω	Hyperbolic hole region factor

List of symbols

A	Inlet section area
A_{bm}	Wave orbital amplitude ($= U_w/\omega$)
C_r	Wave-current strength ratio
d_{50}	Nominal 50%-percentile grain diameter
$D_{u,model}$	Current velocity deviation of a model with respect to the experimental data
$D_{u^*,model}$	Shear velocity deviation of a model with respect to the experimental data
$D_{k_s,model}$	Equivalent roughness deviation of a model with respect to the experimental data
f_{cw}	Combined flow friction factor
Fr	Froude number
F_1	First $k-\omega$ SST (Menter et al., 2003) blending coefficient
F_2	Second $k-\omega$ SST (Menter et al., 2003) blending coefficient
g	Gravity acceleration
h	Local water depth
h_0	Flat bottom water depth (for ACCLIVE dataset)
h^+	Water depth in wall units
H	Nominal wave height
H_m	Measured wave height
I_u	Turbulence intensities in the current direction
I_v	Turbulence intensities in the wave direction
$I_{i,\Omega}$	Indicator function of quadrant analysis

k	Turbulent kinetic energy
k_r	Reflection coefficient
k_s	Equivalent roughness
k_s^+	Equivalent roughness in wall units
K	Wave number
K_s	Shoaling coefficient
Ku	Frequency distribution kurtosis
N_w	Number of waves used for the phase average
N_z	Number of surface bed elevations
p	Pressure
Re_c	Reynolds number of the current
Re_w	Reynolds number of waves
Re^*	Shear Reynolds number
Re^*_{CO}	Shear Reynolds number (Current only)
Re^*_{WC}	Shear Reynolds number (Waves plus current)
s	Time segment of the 10 minute time series
Sk	Frequency distribution skewness
S_c	Steady flow momentum source term
S_c	Oscillatory flow momentum source term
t	Time
T	Wave period
T_{end}	Last instant of the turbulent time series
u	Instantaneous velocity in the current direction
$\bar{u}$	Time-averaged velocity in the current direction
$\tilde{u}$	Phase-averaged velocity in the current direction
u'	Turbulent velocity in the current direction
u^*	Current bottom friction (or shear) velocity
u^*_c	Current shear velocity in the Grant and Madsen (1986) model
u^*_w	Wave shear velocity in the Grant and Madsen (1986) model
u^*_{wc}	Combined flow shear velocity in the Grant and Madsen (1986) model
$u^*_{wcm,wc}$	Combined flow maximum bed shear velocity

u_{model}	Velocity predicted by GM86, SO97 or ST17 model
$u_{5,s}$	streamwise velocity of the 5 minutes segment
$u_{2,s}$	Dimensionless time-averaged streamwise velocity of the 2 minutes segment
u^+	Current velocity in wall units
U	Nominal current velocity
U_c	Freestream velocity
U_w	Wave orbital velocity
v	Instantaneous velocity in the wave direction
$\bar{v}$	Time-averaged velocity in the current direction
$\tilde{v}$	Phase-averaged velocity in the wave direction
v'	Turbulent velocity in the wave direction
$v_{5,s}$	Dimensionless time-averaged crosswise velocity of the 5 minutes segment
$v_{2,s}$	Dimensionless time-averaged crosswise velocity of the 2 minutes segment
w	Instantaneous velocity in the vertical upward direction
$\bar{w}$	Time-averaged velocity in the vertical upward direction
$\tilde{w}$	Phase-averaged velocity in the vertical upward direction
w'	Turbulent velocity in the vertical upward direction
$w_{5,s}$	Dimensionless time-averaged vertical upward velocity of the 5 minutes segment
$w_{2,s}$	Dimensionless time-averaged vertical upward velocity of the 2 minutes segment
x	Current direction coordinate
y	Crosswise direction coordinate
z	Vertical upward direction coordinate (bottom distance)
z^+	Bottom distance in wall units
α	slope of the linear fitting in the logarithmic velocity profile
α_1	$k-\omega$ model coefficient

β	intercept of the linear fitting in the logarithmic velocity profile
β_1	$k-\omega$ model coefficient
β^*	$k-\omega$ model coefficient
δx	Geostatistic spatial correlation lag in the x direction
δy	Geostatistic spatial correlation lag in the y direction
δ_c	Current boundary layer thickness
δ_w	Wave boundary layer thickness
ϵ	Turbulent dissipation
η	Wave surface elevation
$\tilde{\eta}$	Phase-averaged surface elevation
κ	Von Karman number
ν	Kinematic viscosity
ν_t	Turbulent (or eddy) viscosity
ρ	Water density
σ_H	Standard deviation of the measured wave height
σ_u	Standard deviation of dimensionless time-averaged streamwise velocity
$\sigma_{u,5,s}$	Standard deviation of dimensionless time-averaged streamwise velocity of the 5 minutes segment
$\sigma_{u,2,s}$	Standard deviation of dimensionless time-averaged streamwise velocity of the 2 minutes segment
σ_v	Standard deviation of dimensionless time-averaged crosswise velocity
$\sigma_{v,5,s}$	Standard deviation of dimensionless time-averaged crosswise velocity of the 5 minutes segment
$\sigma_{v,2,s}$	Standard deviation of dimensionless time-averaged crosswise velocity of the 2 minutes segment
θ	Angle between waves and currents
ω	Rate of turbulent kinetic energy dissipation
Ω	Hyperbolic hole region factor

List of Figures

List of Tables

Bibliography

J Aberle and V Nikora. Statistical properties of armored gravel bed surfaces. *Water Resources Research*, 42(11), 2006.

Mohammad Saud Afzal, Lars Erik Holmedal, and Dag Myrhaug. Three-dimensional streaming in the seabed boundary layer beneath propagating waves with an angle of attack on the current. *Journal of Geophysical Research: Oceans*, 120(6):4370–4391, 2015.

Ken Haste Andersen and Carla Faraci. The wave plus current flow over vortex ripples at an arbitrary angle. *Coastal engineering*, 47(4):431–441, 2003.

MM Arnskov, J Fredsøe, and BM Sumer. Bed shear stress measurements over a smooth bed in three-dimensional wave-current motion. *Coastal Engineering*, 20 (3-4):277–316, 1993.

Toshiyuki Asano and Yuichi Iwagaki. Bottom turbulent boundary layer in wave-current co-existing systems. In *Coastal Engineering 1984*, pages 2397–2413. 1985.

Ralph Alger Bagnold. Motion of waves in shallow water. interaction between waves and sand bottoms. *Proceedings of the Royal Society of London. Series A. Mathematical and Physical Sciences*, 187(1008):1–18, 1946.

Willem T Bakker and Th Van Doorn. Near-bottom velocities in waves with a current. In *Coastal Engineering 1978*, pages 1394–1413. 1978.

WT Bakker. Sand concentration in an oscillatory flow. In *Coastal Engineering 1974*, pages 1129–1148. 1975.

Cüneyt Baykal, B Mutlu Sumer, David R Fuhrman, Niels Gjøl Jacobsen, and Jørgen

Fredsøe. Numerical simulation of scour and backfilling processes around a circular pile in waves. *Coastal engineering*, 122:87–107, 2017.

Eco Wiebe Bijker. The increase of bed shear in a current due to wave action. In *Coastal Engineering 1966*, pages 746–765. 1967.

Zdravko I Botev, Joseph F Grotowski, Dirk P Kroese, et al. Kernel density estimation via diffusion. *The annals of Statistics*, 38(5):2916–2957, 2010.

David A Cacchione and David E Drake. Measurements of storm-generated bottom stresses on the continental shelf. *Journal of Geophysical Research: Oceans*, 87 (C3):1952–1960, 1982.

L Cea, J Puertas, and L Pena. Velocity measurements on highly turbulent free surface flow using adv. *Experiments in fluids*, 42(3):333–348, 2007.

John B Christoffersen and Ivar G Jonsson. Bed friction and dissipation in a combined current and wave motion. *Ocean Engineering*, 12(5):387–423, 1985.

Felicity C Coffey and Peter Nielsen. Thb influence of waves oh current profiles. *Coastal Engineering Proceedings*, (20):7–7, 1986.

Hugh W Coleman and W Glenn Steele. Engineering application of experimental uncertainty analysis. *AIAA journal*, 33(10):1888–1896, 1995.

ER Corino and RS Brodkey. A visual study of turbulent shear flow. *J. Fluid Mech*, 37(1):30, 1969.

AG Davies, RL Soulsby, and HL King. A numerical model of the combined wave and current bottom boundary layer. *Journal of Geophysical Research: Oceans*, 93 (C1):491–508, 1988.

Robert G Dean. Relative validities of water wave theories. *Journal of the Waterways, Harbors and Coastal Engineering Division*, 96(1):105–119, 1970.

David L Donoho and Jain M Johnstone. Ideal spatial adaptation by wavelet shrinkage. *biometrika*, 81(3):425–455, 1994.

C Faraci, E Foti, and RE Musumeci. Waves plus currents at a right angle: The rippled bed case. *Journal of Geophysical Research: Oceans*, 113(C7), 2008.

C Faraci, P Scandura, RE Musumeci, and E Foti. Waves plus currents crossing at a right angle: near-bed velocity statistics. *Journal of Hydraulic Research*, 56(4): 464–481, 2018.

Carla Faraci and Yong Liu. Analysis of wave forces acting on combined caissons with inner slope rubble mound. *Coastal Engineering*, 34, 2014.

Pradeep C Fernando, Junke Guo, and Pengzhi Lin. Wave–current interaction at an angle 1: experiment. *Journal of hydraulic research*, 49(4):424–436, 2011.

Joel H Ferziger, Milovan Perić, and Robert L Street. *Computational methods for fluid dynamics, 4th Ed.* Springer, 2020.

JJ Finnigan. Turbulent transport in flexible plant canopies. In *The forest-atmosphere interaction*, pages 443–480. Springer, 1985.

Jørgen Fredsøe. Turbulent boundary layer in wave-current motion. *Journal of Hydraulic Engineering*, 110(8):1103–1120, 1984.

Luis A Giménez-Curto and Miguel A Corniero Lera. Oscillating turbulent flow over very rough surfaces. *Journal of Geophysical Research: Oceans*, 101(C9):20745–20758, 1996.

David Gisen. Generation of a 3d mesh using snappyhexmesh featuring anisotropic refinement and near-wall layers. In *ICHE 2014. Proceedings of the 11th International Conference on Hydroscience & Engineering*, pages 983–990, 2014.

Bruce Glavovic, Mick Kelly, Robert Kay, and Ailbhe Travers. *Climate change and the coast: building resilient communities*. CRC Press, 2014.

Derek G Goring and Vladimir I Nikora. Despiking acoustic doppler velocimeter data. *Journal of hydraulic engineering*, 128(1):117–126, 2002.

William D Grant and Ole S Madsen. The continental-shelf bottom boundary layer. *Annual review of fluid mechanics*, 18(1):265–305, 1986.

William D Grant and Ole Secher Madsen. Combined wave and current interaction with a rough bottom. *Journal of Geophysical Research: Oceans*, 84(C4):1797–1808, 1979.

FJ Havinga. Sediment concentrations and sediment transport in case of irregular non-breaking waves with a current. 1992.

Pablo Higuera, Javier L Lara, and Inigo J Losada. Simulating coastal engineering processes with openfoam®. *Coastal Engineering*, 71:119–134, 2013.

Pablo Higuera, Javier L Lara, and Inigo J Losada. Three-dimensional interaction of waves and porous coastal structures using openfoam®. part i: Formulation and validation. *Coastal Engineering*, 83:243–258, 2014.

Bas Hofland, Paulo Rosa-Santos, Francisco Taveira-Pinto, Ermano de Almeida, Rute Lemos, Ana Mendonça, and Conceição Juana Fortes. Measuring damage in physical model tests of rubble mounds. In *Coasts, Marine Structures and Breakwaters 2017: Realising the Potential*, pages 929–940. ICE Publishing, 2018.

Lars Erik Holmedal, Dag Myrhaug, and Håvard Rue. Seabed shear stresses under irregular waves plus current from monte carlo simulations of parameterized models. *Coastal engineering*, 39(2-4):123–147, 2000.

Lars Erik Holmedal, Dag Myrhaug, and Håvard Rue. The sea bed boundary layer under random waves plus current. *Continental Shelf Research*, 23(7):717–750, 2003.

S Hyunh Thanh and Andre Temperville. A numerical model of the rough turbulent boundary layer in combined wave and current interaction. In *EUROMECH colloquium on sand transport in rivers, estuaries and the sea. 262*, pages 93–100, 1991.

Md Rashedul Islam and David Z Zhu. Kernel density–based algorithm for despiking adv data. *Journal of Hydraulic Engineering*, 139(7):785–793, 2013.

Raad I Issa. Solution of the implicitly discretised fluid flow equations by operator-splitting. *Journal of computational physics*, 62(1):40–65, 1986.

Niels G Jacobsen, David R Fuhrman, and Jørgen Fredsøe. A wave generation toolbox for the open-source cfd library: Openfoam®. *International Journal for numerical methods in fluids*, 70(9):1073–1088, 2012.

BL Jensen, BM Sumer, and J Fredsøe. Turbulent oscillatory boundary layers at high reynolds numbers. *Journal of Fluid Mechanics*, 206:265–297, 1989.

PH Kemp and RR Simons. The interaction between waves and a turbulent current: waves propagating with the current. *Journal of Fluid Mechanics*, 116:227–250, 1982.

PH Kemp and RR Simons. The interaction of waves and a turbulent current-waves propagating against the current. *J Fluid Mech*, 130(MAY):73–89, 1983.

Ali Khelifa and Yvon Ouellet. Prediction of sand ripple geometry under waves and currents. *Journal of waterway, port, coastal, and ocean engineering*, 126(1):14–22, 2000.

John Kim, Parviz Moin, and Robert Moser. Turbulence statistics in fully developed channel flow at low reynolds number. *Journal of fluid mechanics*, 177:133–166, 1987.

G Klopman. Vertical structure of the flow due to waves and currents-laser-doppler flow measurements for waves following or opposing a current. *WL report H840-30, part II, for Rijkswaterstaat,*, 1994.

Kian Yew Lim and Ole Secher Madsen. An experimental study on near-orthogonal wave–current interaction over smooth and uniform fixed roughness beds. *Coastal Engineering*, 116:258–274, 2016.

CR Lodahl, B Mutlu Sumer, and Jørgen Fredsøe. Turbulent combined oscillatory flow and current in a pipe. *Journal of Fluid Mechanics*, 373:313–348, 1998.

SS Lu and WW Willmarth. Measurements of the structure of the reynolds stress in a turbulent boundary layer. *Journal of Fluid Mechanics*, 60(3):481–511, 1973.

Helge Lundgren. Turbulent currents in the presence of waves. In *Coastal Engineering 1972*, pages 623–634. 1973.

Ole Secher Madsen. Spectral wave-current bottom boundary layer flows. In *Coastal Engineering 1994*, pages 384–398. 1995.

Paul Peter Mathisen and Ole Secher Madsen. Waves and currents over a fixed rippled bed: 2. bottom and apparent roughness experienced by currents in the presence of waves. *Journal of Geophysical Research: Oceans*, 101(C7):16543–16550, 1996a.

Paul Peter Mathisen and Ole Secher Madsen. Waves and currents over a fixed rippled bed: 1. bottom roughness experienced by waves in the presence and absence of currents. *Journal of Geophysical Research: Oceans*, 101(C7):16533–16542, 1996b.

Henry Mcdonald. The effect of pressure gradient on the law of the wall in turbulent flow. *Journal of Fluid Mechanics*, 35(2):311–336, 1969.

Stuart J McLelland and Andrew P Nicholas. A new method for evaluating errors in high-frequency adv measurements. *Hydrological processes*, 14(2):351–366, 2000.

Florian R Menter, Martin Kuntz, and Robin Langtry. Ten years of industrial experience with the sst turbulence model. *Turbulence, heat and mass transfer*, 4(1): 625–632, 2003.

Florianr Menter. Zonal two equation kw turbulence models for aerodynamic flows. In *23rd fluid dynamics, plasmadynamics, and lasers conference*, page 2906, 1993.

RE Musumeci, L Cavallaro, E Foti, P Scandura, and P Blondeaux. Waves plus currents crossing at a right angle: Experimental investigation. *Journal of Geophysical Research: Oceans*, 111(C7), 2006.

Rosaria Ester Musumeci, Vincenzo Marletta, Agustin Sanchez-Arcilla, and Enrico Foti. A ferrofluid-based sensor to measure bottom shear stresses under currents and waves. *Journal of Hydraulic Research*, 56(5):630–647, 2018.

Dag Myrhaug, Lars Erik Holmedal, Richard R Simons, and Ruairi D MacIver. Bottom friction in random waves plus current flow. *Coastal engineering*, 43(2):75–92, 2001.

Day Myrhaug and Olav H Slaattelid. A rational approach to wave-current friction coefficients for rough, smooth and transitional turbulent flow. *Coastal Engineering*, 14(3):265–293, 1990.

Robert J Nicholls and Anny Cazenave. Sea-level rise and its impact on coastal zones. *science*, 328(5985):1517–1520, 2010.

Vladimir Nikora and Jeremy Walsh. Water-worked gravel surfaces: High-order structure functions at the particle scale. *Water Resources Research*, 40(12), 2004.

Vladimir Nikora, Derek Goring, Ian McEwan, and George Griffiths. Spatially averaged open-channel flow over rough bed. *Journal of Hydraulic engineering*, 127 (2):123–133, 2001.

Vladimir I Nikora, Derek G Goring, and Barry JF Biggs. On gravel-bed roughness characterization. *Water Resources Research*, 34(3):517–527, 1998.

AS Nortek. Vectrino velocimeter user guide. *Nortek AS, Vangkroken, Norway*, 621, 2009.

Maitane Olabarrieta, Raul Medina, and Sonia Castanedo. Effects of wave–current interaction on the current profile. *Coastal Engineering*, 57(7):643–655, 2010.

D Panara, M Porta, R Dannecker, and B Noll. Wall-functions and boundary layer response to pulsating and oscillating turbulent channel flows. In *Turbulence Heat and Mass Transfer 5. Proceedings of the International Symposium on Turbulence Heat and Mass Transfer*. Begel House Inc., 2006.

Mehran Parsheh, Fotis Sotiropoulos, and Fernando Porté-Agel. Estimation of power spectra of acoustic-doppler velocimetry data contaminated with intermittent spikes. *Journal of Hydraulic Engineering*, 136(6):368–378, 2010.

Suhas V Patankar and D Brian Spalding. A calculation procedure for heat, mass and momentum transfer in three-dimensional parabolic flows. In *Numerical prediction of flow, heat transfer, turbulence and combustion*, pages 54–73. Elsevier, 1983.

Dubravka Pokrajac, Ian McEwan, and Vladimir Nikora. Spatially averaged turbulent stress and its partitioning. *Experiments in Fluids*, 45(1):73–83, 2008.

Jie Qin, Jochen Aberle, Pierre-Yves Henry, Teng Wu, and Deyu Zhong. Statistical significance of spatial correlation patterns in armoured gravel beds. *Journal of Hydraulic Research*, 57(1):90–106, 2019.

Michael R Raupach and RH Shaw. Averaging procedures for flow within vegetation canopies. *Boundary-Layer Meteorology*, 22(1):79–90, 1982.

MR Raupach, RA Antonia, and S Rajagopalan. Rough-wall turbulent boundary layers. 1991.

Richard R Simons, Tony J Grass, and Mehrdad Mansour-Tehrani. Bottom shear stresses in the boundary layers under waves and currents crossing at right angles. In *Coastal Engineering 1992*, pages 604–617. 1993.

RR Simons, AG Kyriacou, RL Soulsby, and AG Davies. Predicting the nearbed turbulent flow in waves and currents. IAHR, 1988.

JFA Sleath. Turbulent oscillatory flow over rough beds. *Journal of Fluid Mechanics*, 182:369–409, 1987.

JFA Sleath. Velocities and bed friction in combined flows. In *Coastal Engineering 1990*, pages 450–463. 1991.

J Dungan Smith and SR McLean. Spatially averaged flow over a wavy surface. *Journal of Geophysical research*, 82(12):1735–1746, 1977.

Richard Soulsby. Dynamics of marine sands. 1997.

RL Soulsby, L Hamm, G Klopman, D Myrhaug, RR Simons, and GP Thomas. Wave-current interaction within and outside the bottom boundary layer. *Coastal engineering*, 21(1-3):41–69, 1993.

Richard Styles, Scott M Glenn, and Mitchell E Brown. An optimized combined wave and current bottom boundary layer model for arbitrary bed roughness. Technical report, US Army Engineer Research and Development Center, Coastal and Hydraulics ..., 2017.

BM Sumer. Lecture notes on turbulence/technical university of denmark, 2007, 2007.

H Tanaka and N Shuto. Friction laws and flow regimes under wave and current motion. *Journal of Hydraulic Research*, 22(4):245–261, 1984.

JH Trowbridge and YC Agrawal. Glimpses of a wave boundary layer. *Journal of Geophysical Research: Oceans*, 100(C10):20729–20743, 1995.

Motohiko Umeyama. Reynolds stresses and velocity distributions in a wave-current coexisting environment. *Journal of waterway, port, coastal, and ocean engineering*, 131(5):203–212, 2005.

Marcel RA van Gent and Ivo M van der Werf. Rock toe stability of rubble mound breakwaters. *Coastal Engineering*, 83:166–176, 2014.

Leo C Van Rijn and Fred J Havinga. Transport of fine sands by currents and waves. ii. *Journal of Waterway, Port, Coastal, and Ocean Engineering*, 121(2):123–133, 1995.

Paul J Visser. Wave basin experiments on bottom friction due to current and waves. In *Coastal Engineering 1986*, pages 807–821. 1987.

Tony L Wahl. WinADV: A Windows-based viewing and post- processing utility for ADV files. `https://www.usbr.gov/tsc/techreferences/computer%20software/software/winadv/index.html`, 2013.

James M Wallace. Quadrant analysis in turbulence research: history and evolution. *Annual Review of Fluid Mechanics*, 48:131–158, 2016.

James M Wallace, Helmut Eckelmann, and Robert S Brodkey. The wall region in turbulent shear flow. *Journal of Fluid Mechanics*, 54(1):39–48, 1972.

David C Wilcox. *Turbulence modeling for CFD. La Canada, CA: DCW Industries*. 2006.

N Robert Wilson and Roger H Shaw. A higher order closure model for canopy flow. *Journal of Applied Meteorology*, 16(11):1197–1205, 1977.

Jing Yuan and Ole S Madsen. Experimental study of turbulent oscillatory boundary layers in an oscillating water tunnel. *Coastal engineering*, 89:63–84, 2014.